Dedicated Sequences for Auditory fMRI

Inauguraldissertation
zur Erlangung der Würde eines Doktors der Philosophie
vorgelegt der
Philosophisch-Naturwissenschaftlichen Fakultät
der Universität Basel

von
Christian Boller
aus Zürich ZH
Basel, 16.4.2007

Genehmigt von der Philosophisch-Naturwissenschaftlichen Fakultät

auf Antrag von:

Prof. Dr. Klaus Scheffler
Dissertationsleiter

Prof. Dr. Jürgen Hennig
Korreferent

Prof. Dr. Joachim Seelig
Fakultätsverantwortlicher

Basel, den 19.12.2006

Prof. Dr. Hans-Peter Hauri
Dekan

Preface

Since its inception in 1990, functional magnetic resonance imaging (fMRI) based on the blood oxygenation level dependent (BOLD) effect has become a key technique in the research on human brain function. Of the primary sensory systems in humans, the visual system is probably the most thoroughly studied and has been a popular target region for human fMRI studies since the early days. The auditory system, on the other hand, has received much less attention. While several reasons can be listed for this, one of the most basic complications that arise when using fMRI to study auditory perception is that the image acquisition process itself produces intense acoustic noise. This scanner sound originates from the rapidly switched magnetic field gradients, which in the presence of the very large main magnetic field of the MR machine cause vibrations that are transmitted to the entire MR system. Echo planar imaging, which is the established standard imaging sequence for fMRI, produces particularly loud acoustic noise. This leads to a severely reduced acoustic contrast for experimental acoustic stimuli in auditory fMRI studies, even when they are presented using acoustically damping headphones. In addition to the sound intensity, the pulsating temporal pattern of the scanner acoustic noise during echo planar imaging can be shown to make the scanner sound an especially salient stimulus for the auditory system.

The main objective of this thesis was to investigate the potential of modifications to fMRI imaging sequences in order to reduce the interference of the generated acoustic noise with auditory stimuli. The two major sources of interference between scanner sound and experimental stimuli have been addressed using two different imaging sequences. The pulsation in the scanner sound is removed (or made inaudible) by the Continuous EPI sequence, while a large reduction in sound intensity is achievable using BURST type sequences such as the URGE-EVI sequence here described. While the principles of both sequences have been published before, they both offered great potential for further research in the direction of characterization, development and optimization. In the design and practical application of any imaging sequence, there are a large number of parameters that can be chosen and many decisions that have to be taken. Apart from the design, implementation and testing of the two sequences on different clinical MR scanners,

the present work therefore attempts to characterize and discuss "optimal" sequence parameters for typical auditory fMRI experiments.

The structure of this thesis reflects this division into two main parts which focus on two different acquisition methods. It starts with a basic introduction to MR imaging principles and auditory fMRI in chapters 1 and 2. The two main parts are then formed by chapters 3 to 5, which concentrate on the Continuous EPI sequence and chapters 6 to 8, which describe my work on BURST and URGE-EVI. Of the two main parts, each begins with an introductory chapter describing the working principle of that sequence and previous work, followed by a short chapter with decisions and considerations made in the practical implementation on clinical MR scanners and a larger chapter listing the results of my experiments to characterize the sequences and apply them to auditory fMRI.

Contents

Chapter 1

Introduction to MR Imaging

1.1 History of MRI

1.1.1 Discovery of NMR

The discovery of nuclear magnetic resonance was independently made by Felix Bloch [1] and Edward Mills Purcell [2] in 1946. Their experiments were conducted in the context of a general interest in the size of the nuclear magnetic moment, which could be measured both in sign and magnitude since the development of the molecular beam method by Rabi [3], which earned him the 1944 Nobel prize in physics. The crucial idea in the experiments of Bloch and Purcell was to detect the induced nuclear transitions by the same resonant radio frequency field inducing the transitions (absorption in the case of Purcell, induction in a separate coil in Bloch's experiment), instead of using molecular beam deflection. Two earlier attempts by Gorter at measuring the same absorption effect had failed [4, 5], presumably because of the long relaxation times, which could not be foreseen at the time [6].

The subsequent papers by Bloch [7, 8] provided both a detailed theoretical description of all important aspects of the nuclear magnetic resonance (NMR) effect (still valid and readable today!) and careful experimental measurements in water (fig. 1.1a) and paraffin. It came to him as a complete surprise to find relaxation times as long as seconds in water and only 1/100 s in paraffin.

Bloch and Purcell were awarded the Nobel prize in physics in 1952 "for their development of new methods for nuclear magnetic precision measurements and discoveries in connection therewith".

1.1.2 Pulsed NMR and Fourier spectroscopy

While the first NMR spectra were all acquired by slowly changing (sweeping) the RF frequency through resonance, it very soon became apparent that it

was also possible (and even advantageous) to acquire NMR spectra using a short, broadband pulse to excite the magnetization and then generate a spectrum from the freely decaying signal by means of a digital Fourier transform.

The possibility of measuring the NMR signal after switching off a strong on-resonant RF pulse was already recognized by Felix Bloch in the introduction to his famous "Nuclear Induction" paper in 1946 [7]. The first experiments using pulsed NMR were conducted by Torrey in 1949 [9, 10], who advocated the technique because it allowed for a more rapid search for unknown resonance frequencies and the direct measurement of relaxation times.

In 1950, Hahn also measured this pulsed NMR signal "due to free Larmor precession" [11] which soon became known as the "free induction decay" (FID). Even more important was his discovery of the "spin echo" following a two-pulse sequence, which arises from the reversed dephasing in an inhomogeneous field [12]. For many years, this became the dominant method to generate and measure the NMR signal.

However, it was only with Richard Ernst's introduction of the digital Fourier transform to generate resonance frequency spectra [13] that the full power of the pulsed NMR technique was realized. He was able to show his method to be of superior sensitivity and to allow for a simpler adjustment procedure compared to frequency-swept NMR. Especially convincing was his direct comparison of the spectra of ethylbenzene using the two methods (fig. 1.1b).

1.1.3 Chemical shifts

NMR soon became an indispensable tool in chemistry, when it was discovered that the nuclear resonance frequencies depend on the chemical compound measured. The first experimental measurements of such an effect were conducted in 1950 by Dickinson [14], who "most unexpectedly" found that the ^{19}F resonance frequency depended upon chemical compound, and Proctor and Yu [15], who measured two resonance frequencies in the proton spectra of NH_4NO_3, separated by a frequency proportional to the B_0 field. The theoretical explanation for this "chemical shift" and the mathematical framework to describe it were developed by Ramsey in a series of papers between 1950 and 1952 [16–18]. He found that the chemical shift arises from the partial shielding of the nuclei by the electrons, whose mobility clearly depends on the chemical compound.

1.1.4 MR Imaging

The possibility to generate images using NMR was discovered in 1973 independently by Paul Lauterbur and Peter Mansfield. Lauterbur [19] described

a projection reconstruction MR imaging technique he called "zeugmatography" (as sub-wavelength imaging technique based on the interaction of two fields, the homogeneous main field and the gradient field). He was able to show simple phantom images (fig. 1.1c) and anticipated the usefulness of this technique to detect tumors (which were known to have different relaxation properties [20]), chemical shift imaging and diffusion imaging. Mansfield at that time aimed at a NMR lattice structure measurement much like x-ray diffraction [21]. He was able to show simple 1D section images of three and five layered planar structures by Fourier transforming their NMR signals. Lauterbur and Mansfield were awarded with the Nobel Prize in Physiology or Medicine in 2003 "for their discoveries concerning magnetic resonance imaging".

These were rather preliminary results, however, and the road to the medical application of magnetic resonance imaging (MRI) was long and steep. At first, it seemed that mapping the MR signal from only one point in the sample was the easiest way to generate MR images.

In 1976, Damadian proposed an imaging method using NMR termed field focusing nuclear magnetic resonance (FONAR) [22], with the main aim of eventually enabling the in vivo detection of malignant tumors by MRI. His principle was based on shaping the main magnetic field as well as the resonant RF field in such a way that the resonance condition was met for one point in the sample only and then generating an image by mapping the FID amplitudes. He succeeded to generate images of the human body using his technique one year later [23]. A similar approach was taken by Hinshaw [24]. Although he was aware of Lauterbur's paper [19], he took a different approach at image generation, he used rapidly modulated gradients and a lowpass filter to measure only the NMR signal from a single point (the "sensitive point").

However, in the end, a different approach won the race, the 2D Fourier imaging technique developed by Kumar et al. [25], who used the frequency-encoding property of linear field gradients to generate images via a 2D or 3D Fourier transform of suitably encoded FID signals. They already noted the sensitivity gain that was possible with this technique and were able to show images of a two-bottle phantom in their paper. The main concerns at the time were the search for a suitable method to excite the magnetization of only a single slice for 2D imaging and the amount of computer time needed and image artifacts. It was Garroway et al. [26] who pioneered the use of spatially selective excitation pulses, at the time meant to form the basis of an imaging method consisting of pencil-beam excitation and Fourier reconstruction of the acquired line (which can also be seen as the 1D ancestor to Kumar's technique). Mansfield and Maudsley [27] similarly used selective irradiation of a thin strip of magnetization and a one-dimensional Fourier transform to generate images. Using this technique, they were able to produce images of biological structures (turkey bone and plant stems)

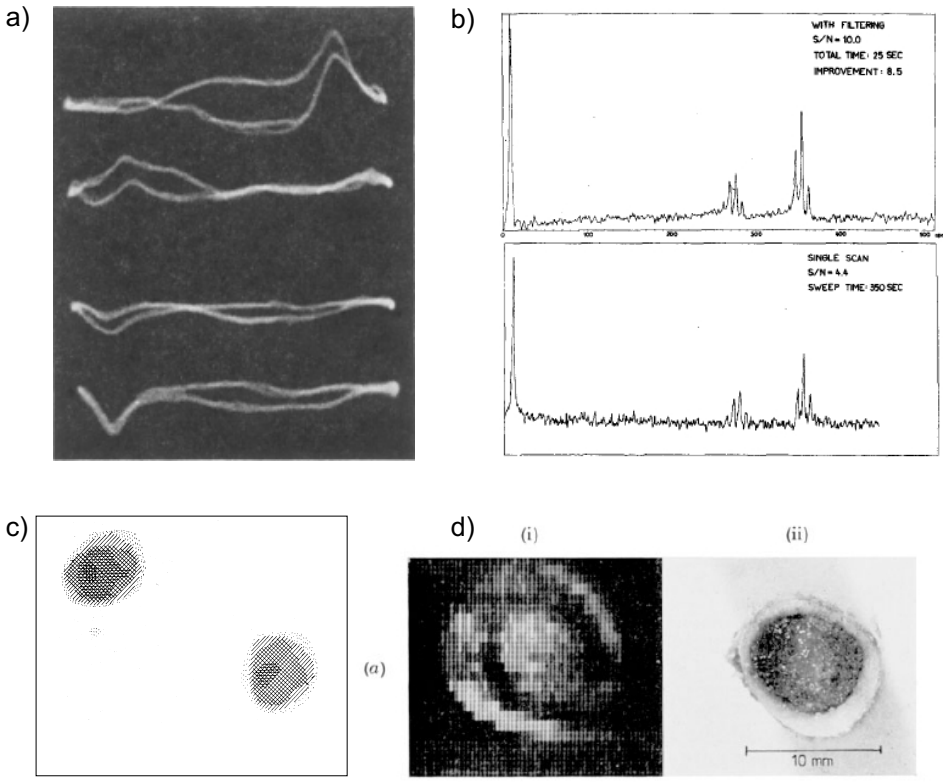

Figure 1.1: Historic milestones in magnetic resonance: (a) Bloch's first measurement of nuclear magnetic resonance signals in water in 1946 [7], (b) Ernst's 1966 demonstration of the advantages of pulsed (upper figure, SNR = 10, acquisition time 25 s) versus frequency swept spectroscopy (lower figure, SNR = 4.4, acquisition time 350 s) [13], (c) Lauterbur's first MR image of a two-bottle phantom in 1973 [19] and (d) Mansfield's line-scan image of a piece of turkey bone compared to the photographed section in 1976 [27].

with good resemblance to photographic sections of the same specimens (see fig. 1.1d)

In a Physics Today article [28] following the 2003 Nobel Prize award, Herman Carr claims to have demonstrated one-dimensional imaging already in 1952, which is probably true, but his work never reached the public acclaim the other works mentioned above had gotten, for reasons difficult to reconstruct from today's perspective.

1.2 The MR Signal, Polarization and the Bloch Equations

1.2.1 MR Signal

In this section, we shall follow the lines of thought presented by Felix Bloch in his seminal paper on nuclear magnetic resonance [7] to describe the behavior of a macroscopic magnetization vector $\mathbf{M}$ in an external field $\mathbf{B}$. First, it shall be assumed that this dynamic change of magnetization $d\mathbf{M}/dt$ is solely due to the external field and that this field is homogeneous throughout the sample. Then, the rate of change is simply governed by the magnetic torque acting upon the magnetization and is described by:

$$d\mathbf{M}/dt = \gamma(\mathbf{M} \times \mathbf{B})$$

where γ is the Larmor constant. Quantum mechanical calculations show that in the case of a large ensemble of nuclear spins, this classical equation corresponds exactly to the expectation value of the quantum mechanical counterparts.

According to above equation, if a homogeneous $\mathbf{B_0}$ field along the $\mathbf{e_z}$ axis is the only magnetic field present, a magnetization vector not collinear with $\mathbf{e_z}$ will rotate around $\mathbf{e_z}$ with a frequency $w_0 = \gamma \mathrm{B}_0$. In a coil oriented along the $\mathbf{e_x}$ or $\mathbf{e_y}$ axes and placed near the rotating magnetization sample, this rotation will induce a current alternating with frequency w_0. This is the MR signal. In the following subsection, we shall find that this signal is of a magnitude easily detectable with standard RF technique.

1.2.2 Polarization and the Size of the MR Signal

The quantum mechanical distribution of the spin up and spin down states in a sample follows the Boltzmann distribution

$$\frac{N_\uparrow}{N_\downarrow} = \exp\left(\frac{\hbar\omega_0}{kT}\right)$$

where $\hbar\omega_0 = \gamma\hbar\mathrm{B}_0$ corresponds to the energy difference between the $N_\uparrow$ and $N_\downarrow$ states with $\hbar = 1.054\times10^{-34}$ Js Planck's constant and γ the Larmor constant ($\gamma = 2.675\times10^8$ 1/Ts for protons), $k = 1.381\times10^{-23}$ J/K the Boltzmann constant, and T the temperature in Kelvin.

Since $\exp\left(\frac{\gamma\hbar\mathrm{B}_0}{kT}\right) \approx 1 + \frac{\gamma\hbar\mathrm{B}_0}{kT}$ for $\gamma\hbar\mathrm{B}_0 \ll kT$ (which is always well satisfied at body temperature) and the number of spins in a sample N can be approximated as $N = N_\uparrow + N_\downarrow \approx 2N_\downarrow$ we get:

$$\frac{N_\uparrow - N_\downarrow}{N} \approx \frac{N_\uparrow - N_\downarrow}{2N_\downarrow} = \frac{1}{2}\left(\frac{N_\uparrow}{N_\downarrow} - 1\right) \approx \frac{1}{2}\frac{\gamma\hbar\mathrm{B}_0}{kT}$$

And thus for the total polarization (the excess magnetization parallel to the B_0 field) in the sample:

$$M = \sum_{n=1}^{N} \mu_n = \left(\frac{\hbar\gamma}{2}\right)(N_\uparrow - N_\downarrow) \approx N\left(\frac{\hbar\gamma}{2}\right)\left(\frac{\gamma\hbar B_0}{2kT}\right) = N\left(\frac{\hbar\gamma}{2}\right)^2 \frac{B_0}{kT}$$

where $\mu = \frac{\hbar\gamma}{2}$ was used. For water protons at room temperature, even though the polarization is only about 5 spins in every million, this result in a field of 4.9×10^{-9} T for 1 cm^3 of water at $B_0 = 1.5$ T. The field strength of this polarized magnetization is about ten thousand times smaller than the magnetic field of the earth and may seem exceedingly difficult to detect in the presence of a field almost nine orders of magnitude larger. If the orientation of this polarized magnetization can be diverted away from the direction of the B_0 field, however, it precesses around $\mathbf{B_0}$ at a megahertz frequency and thereby generates a radio frequency field that is readily detectable as an electrical signal induced in a receive coil (Bloch calculates a signal of 1 mV for a 10 turn receive coil picking up the MR signal of a 1 cm^3 water sample at 1 T field strength).

1.2.3 Relaxation and the Bloch Equations

For the moment, we shall leave away the question how the polarized magnetization can be oriented in a direction different from the B_0 field and continue along Felix Bloch's description of the nuclear magnetic resonance effect [7]. Now, we have to revise the above assumption that the only influence on the magnetization stems from the external field. This because with that assumption, we have neglected three major sources of internal interactions: the field generated by the atomic electrons, the interaction between neighboring nuclear moments and the thermal agitation of the nuclei.

The influence of electron magnetic moments (the para- or diamagnetic shielding leading to chemical shifts in resonance frequency) depends on the substance but can be safely ignored in water. The internuclear coupling and the thermal motion of the nuclei, however, are both of great importance for the observed MR signal behavior. They are different in one important aspect, namely that only the fluctuating longitudinal magnetization due to the thermal motion of the spins, but not the internuclear coupling can lead to an energy exchange of the nuclear moments with their surrounding. This is especially important in view of the question how the nuclear polarization can develop upon the application of an external field B_0, since then an energy difference of $E = -M_z B_0$ exists between the parallel (polarized) state versus a randomly oriented state.

This transition into the thermal equilibrium M_0 due to thermal agitation can be described by a single exponential relaxation time T_1, where the longitudinal magnetization follows the simple differential equation

$$d\mathrm{M_z}/dt = -(\mathrm{M_z} - \mathrm{M_0})/\mathrm{T_1}$$

The magnetic field generated by neighboring nuclei, on the other hand, is so small that its fluctuations due to thermal agitation do not have a considerable influence on the longitudinal magnetization. If we look at the transverse magnetization components $\mathrm{M_x}$ and $\mathrm{M_y}$, however, this leads to a loss of phase coherence between the nuclei. It can be likewise described by an exponential decay time $\mathrm{T_2}$, which needs not be the same as $\mathrm{T_1}$:

$$d\mathrm{M_x}/dt = -\mathrm{M_x}/\mathrm{T_2}$$

$$d\mathrm{M_y}/dt = -\mathrm{M_y}/\mathrm{T_2}$$

Putting these equations together, we have a complete phenomenological description of the behavior of the magnetization, now known as the "Bloch equations":

$$d\mathrm{M_x}/dt = -\gamma(\mathrm{M_y}B_z - \mathrm{M_z}B_y) + \frac{\mathrm{M_x}}{\mathrm{T_2}} = 0$$

$$d\mathrm{M_y}/dt = -\gamma(\mathrm{M_z}B_x - \mathrm{M_x}B_z) + \frac{\mathrm{M_x}}{\mathrm{T_2}} = 0$$

$$d\mathrm{M_z}/dt = -\gamma(\mathrm{M_x}B_y - \mathrm{M_y}B_x) + \frac{\mathrm{M_z}}{\mathrm{T_1}} = \frac{\mathrm{M_0}}{\mathrm{T_1}}$$

or in vector form:

$$d\mathbf{M}/dt = \gamma(\mathbf{M} \times \mathbf{B}) - \frac{\mathrm{M_x} + \mathrm{M_y}}{\mathrm{T_2}} - \frac{\mathrm{M_z} - \mathrm{M_0}}{\mathrm{T_1}}$$

These equations are the centerpiece of all calculations in MR imaging to this date. The only significant change was the addition of terms to account for molecular diffusion by Torrey in 1956 [29] (it is noteworthy that early attempts to include diffusion terms go back as far as Hahn's "Spin Echoes" paper [12], where the effect of diffusion was treated as an off-resonance frequency). Possible strategies to numerically solve these equations are discussed in section 6.3.

The phenomenological relaxation terms were explained in terms of the underlying physical processes by Bloembergen et al. [30] in 1948. They could show how the observed relaxation times depend on the correlation time of the thermal molecular motion. For short correlation times, as in isotropic liquids, the two relaxation times $\mathrm{T_1}$ and $\mathrm{T_2}$ are approximately equal, while for solids, where correlation times are long, $\mathrm{T_2}$ is much shorter than $\mathrm{T_1}$.

1.2.4 RF excitation and the rotating frame

Here, follow Hahn's "Spin Echoes" paper and return to the question omitted in the previous section how a polarized magnetization not parallel to the static external field can be generated.

It turns out that this can be achieved by using a second external field. If the total external field comprises both a large, constant field $\mathbf{B_0}$ oriented along $\mathbf{e_z}$ and a much smaller, circularly polarized radio frequency field $\mathbf{B_1} = \mathbf{e_x} \mathrm{B}_1 \cos(\omega_1 t) - \mathbf{e_y} \mathrm{B}_1 \sin(\omega_1 t)$ in the plane orthogonal to the main magnetic field $\mathbf{B_0}$, the situation is most easily analyzed in a coordinate system rotating around $\mathbf{e_z}$ with frequency ω_0 so that $\mathbf{B_1}'$ is stationary: $\mathbf{B_1}' = \mathrm{B}_1 \, \mathbf{e_x}'$ and $\mathbf{B_0}' = \mathrm{B}_0 \, \mathbf{e_z}'$ (where $\mathbf{e_z} = \mathbf{e_z}'$).

For such a rotating coordinate frame any vector valued function $\mathbf{V}(t)$ (laboratory frame of reference or $\mathbf{V}'(t)$ in the rotating frame) has the time derivative

$$d\mathbf{V}/dt = (d\mathbf{V}/dt)' + \boldsymbol{\omega_1} \times \mathbf{V}$$

Therefore, the transformed equation of motion reads (we use $\mathbf{M} \times \boldsymbol{\omega_1} = -\boldsymbol{\omega_1} \times \mathbf{M}$):

$$\left(\frac{d\mathbf{M}}{dt}\right)' = \frac{d\mathbf{M}}{dt} + \boldsymbol{\omega_1} \times \mathbf{M} = \gamma \mathbf{M} \times \mathbf{B} - \mathbf{M} \times \boldsymbol{\omega_1} = \gamma \mathbf{M} \times \left(\mathbf{B} - \frac{\boldsymbol{\omega_1}}{\gamma}\right)$$

And, if we define an "effective field" $\mathbf{B_{eff}} = \mathbf{B} - \boldsymbol{\omega_1}/\gamma$ we have

$$\left(\frac{d\mathbf{M}}{dt}\right)' = \gamma \mathbf{M} \times \mathbf{B_{eff}}$$

With the above $\mathbf{B} = \mathbf{B_0} + \mathbf{B_1} = \mathrm{B}_0 \, \mathbf{e_z}' + \mathrm{B}_1 \, \mathbf{e_x}'$ we derive

$$\mathbf{B_{eff}} = \mathbf{B} - \frac{\boldsymbol{\omega_1}}{\gamma} = \mathrm{B}_0 \, \mathbf{e_z}' + \mathrm{B}_1 \, \mathbf{e_x}' - \frac{\omega_1}{\gamma} \, \mathbf{e_z}' = \frac{\omega_0}{\gamma} \, \mathbf{e_z}' + \frac{\omega_1}{\gamma} \, \mathbf{e_x}' - \frac{\omega_1}{\gamma} \, \mathbf{e_z}'$$

$$= \frac{1}{\gamma} \left[(\omega_0 - \omega_1) \, \mathbf{e_z}' + \omega_1 \, \mathbf{e_x}' \right]$$

From this equation we see that in the case of $\omega_0 = \omega_1$, which is called the resonance condition, we have $(d\mathbf{M}/dt)' = \gamma \mathbf{M} \times \mathbf{B_{eff}} = \gamma \, \omega_1 \, \mathbf{M} \times \mathbf{e_x}'$, i.e. a rotation around $\mathbf{e_x}'$ with angular velocity ω_1, which "tips" the magnetization away from $\mathbf{e_z}$, the direction of the polarization in the thermal equilibrium.

1.3 MR Imaging Principles

1.3.1 Spin Echoes and Gradient Echoes

The formation of echoes can be illustrated using a simple vector model, already introduced in Hahn's "Spin Echoes" paper [12]. The basic spin echo

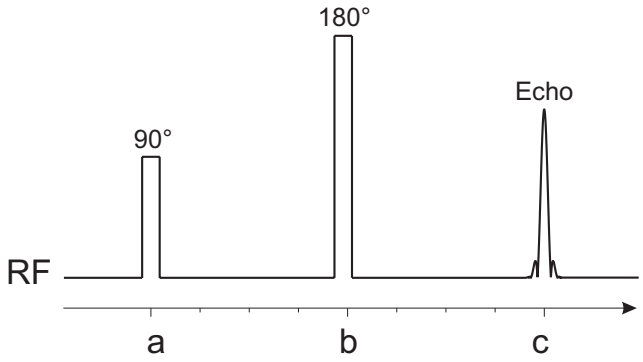

Figure 1.2: Schematic spin echo sequence

sequence is schematically shown in figure 1.2. It uses two RF pulses of 90° and 180° flip angle spaced by a time interval $\tau = b - a$. If the MR signal is measured beginning after the 180° (refocusing) pulse, it reaches maximal amplitude at time $c = b + \tau$. This is what we call the "spin echo" (of the 90° excitation pulse).

It can be explained in terms of a simple vector model (see figure 1.3) in which we follow the transverse part of the magnetization of nine exemplary spins in the rotating reference frame (in which a magnetization vector rotating around $\mathbf{B_0}$ with a frequency $\omega_0 = \gamma B_0$ is stationary). We assume these spins to be localized in microscopically different local fields, they therefore have different precession frequencies: $\omega_0 - \Delta\omega$ for spin 1, ω_0 for spin 5, and $\omega + \Delta\omega$ for spin 9. At time a, right after the 90° excitation pulse (applied along the vertical axis), they are all aligned, but due to their different precession frequencies, soon start to lose phase coherence. Assuming that $\tau \cdot \Delta\omega = \pi$, they are fully dephased at time b. At that time, the MR signal, which is the vector sum of the individual magnetizations, is zero. The 180° refocusing pulse, here assumed to be applied along the horizontal axis, then has the effect of vertically flipping the spins in the transverse plane. Now, the different precession frequencies of the individual spins has the opposite effect of rephasing the spins at the same rate, so that after a time τ (after the refocusing pulse) the magnetization is again aligned along the horizontal axis and the MR signal is maximal. This is the echo condition.

For the gradient echo sequence (illustrated in figure 1.4), the situation is similar, but with one important difference: In this case, the major source of dephasing is the applied gradient (which is assumed to be much stronger than the microscopic field inhomogeneities). If the polarity of this field gradient is inverted at time b, the spins are rephased even without a refocusing pulse, the gradient reversal has essentially the effect of a time reversal, in the sense that it reverses the precessional motion of each of the spins. The vector diagram of the gradient echo would therefore have to be read from time a to b, where the gradient is reversed, and then backwards from b to

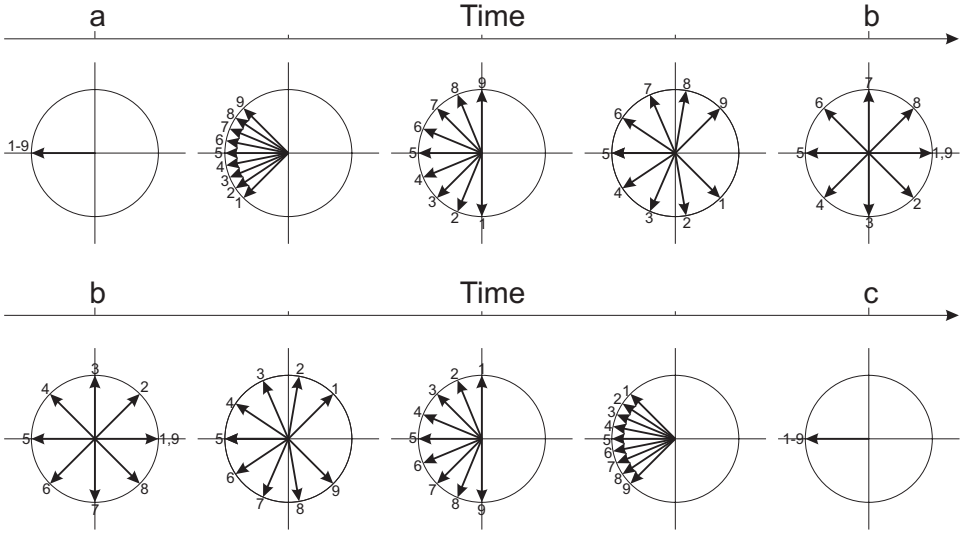

Figure 1.3: Echo formation process in a vector model

a (in the same row of figure 1.3). In practice, the microscopic field inhomogeneities cannot be neglected and the loss of phase coherence in the gradient echo sequence is a mixture of both effects, with the echo being only a partial refocusing of the total transverse magnetization.

1.3.2 Fourier Imaging and k-Space

In MR imaging, the locally different precession frequencies in the presence of a (linear) gradient filed is purposely used to Fourier encode the position within the sample. How this is done shall be explained in the following. The MR signal of a thin slice of a sample after a slice selective 90° pulse is

$$s(t) = \exp(i\omega_0 t) \int_x \int_y \rho(x,y)\, dxdy$$

where $\rho(x,y)$ is the proton density in the sample, and $\omega_0 = \gamma \mathrm{B}_0$ the Larmor frequency. In the presence of magnetic field gradients, this frequency is dependent on the spatial coordinates x and y: $\omega(x,y) = -\gamma \mathrm{B}(x,y) = -i\gamma(x\mathrm{G_x} + y\mathrm{G_y})t$ where $\mathrm{G_x}$ is the gradient field strength in T/m. If the gradient field strength is also time dependent, it is convenient to introduce k_x (analogous to the "wave number" in optics) as

$$k_x = -\gamma \int_0^t \mathrm{G_x}(\tau)\, d\tau$$

and k_y in the same manner. The signal in the sample then reads:

$$s(t) = \int_x \int_y \rho(x,y) \exp(ixk_x + iyk_y)\, dxdy$$

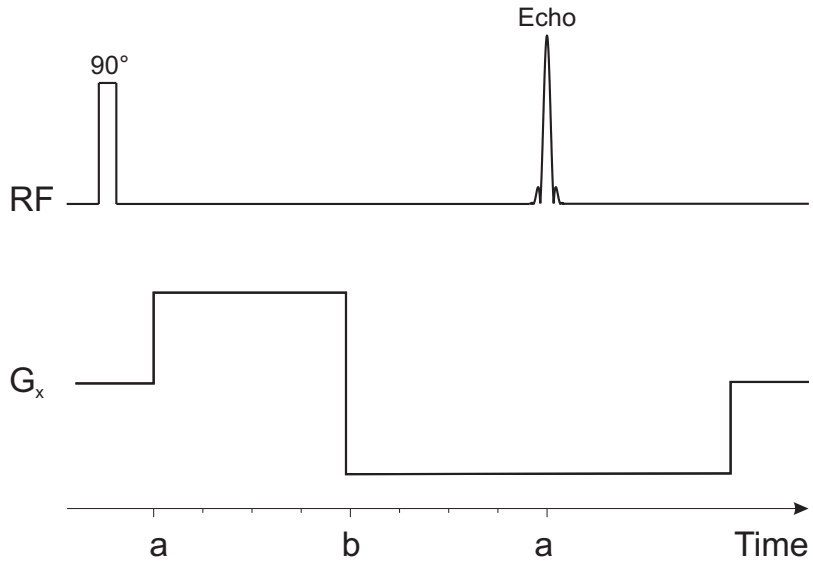

Figure 1.4: Schematic Gradient Echo Sequence

which is exactly the Fourier transform of ρ. Neglecting relaxation effects, we can therefore generate an image of the spin density in a sample by measuring the MR signal for a sufficient number of k_x and k_y combinations and Fourier transforming it. The number of gradient steps (or k_x and k_y points) to yield an image free from aliasing effects is given by the Nyquist criterion $\Delta k_i \leq 1/A_i$ where A_i is the object size along the spatial axis i.

1.3.3 Image contrast

The clinical relevance of the relaxation parameters T_1 and T_2 has been realized very early, even before MR imaging methods were developed. In 1971, Damadian [20] claimed, based on the measurements of NMR relaxation times of two kinds of malignant tumors, that malignant tumors in general could be distinguished from normal tissue or benign tumors based on their prolonged T_1 relaxation times due to their "decreased water structure". He patented the design and use of NMR methods to detect cancer in 1972 in US patent 3,789,832 (according to [22]), even though there were no imaging methods available at the time.

In today's clinical practice, the T_1 and T_2 weighted images are still the cornerstones of diagnostic MR imaging. Soft tissues in the human body have quite different relaxation times, which means that in such "weighted" images, where the main source of contrast is based on different T_1 or T_2 relaxation times, the anatomy of the body is well depicted. Still, we have to differentiate between those (e.g. T_1 weighted) images and absolute quantifications (e.g. T_1 maps) of the same object. In the latter, all other sources of

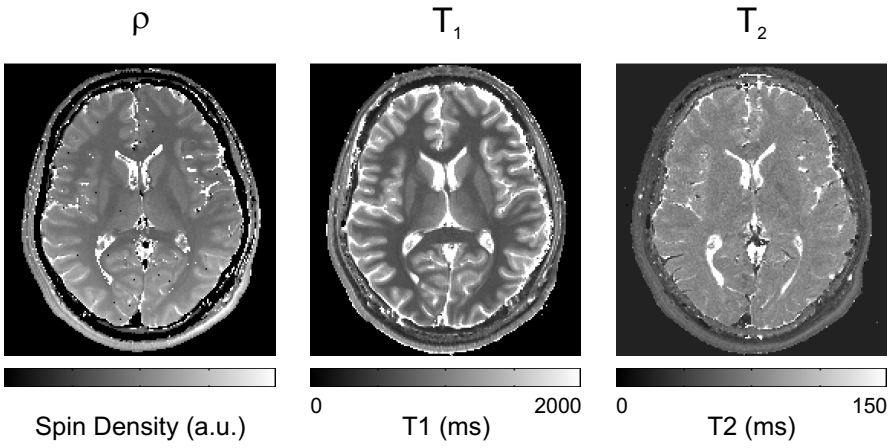

Figure 1.5: Parametric proton density, T_1 and T_2 maps of a volunteer's brain (images courtesy of Rym Djouri)

contrast (i.e. image intensity variations) are eliminated and the image intensity at a given point directly represents the relaxation time in physically significant units (e.g. 1/s), while in the weighted image we only require the effect of the relaxation parameter to be the dominant visible contrast. Paramagnetic substances (or "contrast agents") which shorten the T_1 relaxation time (an idea going back to Bloch's first "Nuclear Induction" paper [7]) and their visualization in T_1 weighted images are also of great importance in the clinical practice, especially to differentiate between different types of pathologies in the brain.

The Bloch equations, when applied to MR imaging, already contain three possible sources of contrast: the longitudinal T_1 relaxation time, the transverse relaxation time T_2 and the proton density (which is represented by the single number M_0 in the Bloch equations, but in MRI varies spatially, as discussed in the preceding subsection, and is commonly designated by ρ). Maps of these three imaging parameters in a volunteer's brain are shown in figure 1.5, the very good contrast between the different tissue types can be appreciated especially in the T_1 map.

To this date, many more sources of contrast in MR images have been found, opening great possibilities in terms of clinical applications. Among the most important are microscopic susceptibility weighted (T_2^*) images, the measurement of molecular diffusion (which is direction-dependent), magnetization transfer contrast, flow quantification, temperature mapping and various techniques based on the selective suppression or enhancement of magnetization with certain relaxation times or chemical shifts.

1.3.4 Signal to Noise Ratio

The signal to noise ratio (SNR) in an MR experiment is generally a complicated function depending on various parameters of the hardware used and the imaging sequence. Vlaardingerbroek and Boer [31] give the following expression for the SNR in terms of practically relevant parameters:

$$\mathrm{SNR} = |\mathrm{M_T}(\mathbf{r})|\Delta V \sqrt{\frac{\omega_0 \mu_0 Q\, t_s}{4kTV_{\mathrm{eff}}}} \sqrt{N_m N_p N_s N_a N_c} \times 10^{-(\delta + \mathrm{F_r})/20}$$

Here, $\mathrm{M_T}(\mathbf{r})$ is the transverse magnetization at the time of data collection and therefore depends on $\mathrm{M_0}$, echo time, relaxation times and the flip angle of the particular pulse sequence used. ΔV is the voxel volume and V_{eff} the effective volume, Q the quality factor of the RF coil and t_s the sampling time. N_m and N_p denote the number of samples acquired in readout and phase encoding directions, respectively, N_s the number of partitions for 3D acquisitions (i.e. the number of samples in slice direction), N_a the number of averages (i.e. how many times any given point in k-space is sampled) and N_c a factor that accounts for the signal improvement when quadrature coils are used (then $N_c = 2$, for a linear coil $N_c = 1$). Finally, the last term accounts for the influence of the receiver circuitry, with δ the power damping (power input divided by power output) and F_r the noise figure of the receiver.

The random noise in an MR system results from losses in the receive circuit and the noise figure of the signal amplifier. The noise from the receive circuit has two main components, the ohmic losses of the coil itself and eddy-current induced losses in the patient, which are inductively coupled to the RF coil. In a well-designed high-field system the latter should dominate [31]. The measured noise by in MR images is usually well described by a Gaussian distribution in both real and imaginary parts [32], which results in a non-Gaussian distribution if magnitude images are measured. In that case, the measured noise is distributed according to the Rician distribution [32]:

$$p_M(M) = \frac{M}{\sigma^2} \exp\left(-\frac{M^2 + A^2}{2\sigma^2}\right) I_0\left(\frac{AM}{\sigma^2}\right)$$

Here, A is the image pixel intensity in the absence of noise, M the measured pixel intensity, I_0 is the modified zeroth order Bessel function of the first kind and σ the standard deviation of the Gaussian noise in the real and imaginary parts (which is assumed to be equal). In image regions where only noise is present, this simplifies to the Rayleigh distribution:

$$p_M(M) = \frac{M}{\sigma^2} \exp\left(-\frac{M^2}{2\sigma^2}\right)$$

For the Rayleigh distribution, the mean and standard deviation are given by $M = \sigma\sqrt{\pi/2} \approx 1.253\,\sigma$ and $\sigma_M^2 = (2-\pi/2)\sigma^2 \approx 0.429\,\sigma^2$. To measure the SNR in-vivo, where perfectly homogeneous tissue regions can generally not be found, it is advantageous to calculate the SNR by dividing the mean signal intensity for the given tissue type by the standard deviation σ estimated from one of these formulas. To that end, either the mean M or the standard deviation σ_M are measured in the magnitude image outside the object in a region free of artifacts.

In many practical cases, it is not the SNR but the detectability of the difference in brightness of two particular tissue types (the contrast) that is the major concern. The contrast to noise ratio (CNR) is then the relevant figure, defined as $\mathrm{CNR} = \mathrm{SNR_A} - \mathrm{SNR_B}$ for two tissues types A and B.

1.3.5 Gradient Echo Sequence

The possibility to use a magnetic field gradient reversal to generate an echo (as described in section 1.3.1) was first described by Hahn [33] in 1960 (cited according to [34]). When MR imaging was developed, most techniques used direct sampling of the FID signal instead of a gradient echo. The first imaging technique to use gradient reversal was Mansfield's planar imaging [35] described in the following subsection 1.3.6. The single echo variant, much like the gradient echo sequence as we understand it today, was proposed by Edelstein et al. [36]. They used the Fourier encoding principle of Kumar et al. [25] together with gradient refocused echoes. In contrast to Kumar et al., they applied phase encoding gradients on all axes simultaneously and varied them in strength instead of duration, which proved advantageous in the presence of field inhomogeneities. They also described an optional inversion recovery preparation to generate $\mathrm{T_1}$ contrast. The repetition time (TR) was long (around 1 s) to allow for signal recovery.

In 1986, Haase et al. [37] introduced the "fast low angle shot" (FLASH) technique as the second "fast" imaging sequence (after STEAM). It was basically the same as the above sequence by Edelstein (also with non-refocused phase encoding gradient, no special spoiling gradient, no RF spoiling), but with low flip angle and a short TR, which led to much improved scan-time efficiency (and potentially intrinsic $\mathrm{T_1}$ contrast). With the short TR, however, the remaining transverse magnetization from previous excitations had a strong influence on the measured signal. In the image, it induced artifacts in the form of a bright band around the center and along the readout direction [38]. Wood et al. [39] tried to reduce those artifacts by dephasing the remaining magnetization at the end of the readout using additional dephasing (or "spoiler") gradients. They tried different axes and sizes for the spoiler gradients and found, based on measures of image homogeneity, that spoiler gradients with changing size (decreasing, for each phase encoding step, from G_0 to 0) along the slice selection axis were most effective at

obtaining a homogeneous image of a spherical phantom.

Later, Frahm et al. [40] realized that the phase encoding gradients which differed for each repetition, were the major source of these image artifacts. They proposed variable spoiling of a gradient echo sequence with each phase encoding step. Similar to the later results of Wood, they preferred a sequence with a variable z gradient ("spoiled FLASH"), which they found to give the best T_1 contrast, but also discussed "refocused FLASH" with a balanced phase encoding gradient, which they found to give a mixed contrast (the read gradient still returned to zero at the k-space edge, no further gradient and also no RF spoiling).

The FLASH sequence is today commonly understood to include a balanced phase encoding gradient and "RF spoiling" [41], which consists of a quadratic phase increment applied to the RF pulses between repetitions, which is more effective than gradient spoiling alone at suppressing refocused transverse magnetization (and thereby reduces artifacts improves T_1 contrast).

Apart from the repetition time, the contrast in a gradient echo sequence depends on the echo time. Since local field inhomogeneities are not refocused in the gradient echo (as opposed to the spin echo) sequence, this dephasing is not purely due to Bloch's T_2 relaxation, as recognized already by Hahn in 1950 [11]. He found that the decay envelope of the MR signal following an on-resonant 90° pulse was exponential with a time constant T_2^*which relates to the transverse (spin echo) relaxation time T_2 as

$$\frac{1}{T_2^*} = \frac{1}{T_2} + \frac{1}{T_2'}$$

where T_2' is the decay time due to static field inhomogeneities within the sample. In gradient echo imaging, because T_2^* is usually much shorter than T_2, it is the major source of image contrast.

For a repeated gradient echo sequence, the signal behavior (based on the assumption of purely longitudinal magnetization before each pulse, i.e. an ideally spoiled sequence) was described by Ernst in his famous "Fourier Spectroscopy" paper [13]. He calculated the optimal excitation flip angle α for a repeated pulse experiment, given by $\cos(\alpha) = \exp\left(-\frac{TR}{T_1}\right)$ (the "Ernst angle").

1.3.6 Echo Planar Imaging Sequence

Historically, Mansfield's echo planar imaging (EPI) sequence, then termed "multi-planar image formation" technique [35, 42] (cited according to [34]), was one of the very first imaging sequences. However, it became practical only years later, when special gradient hardware was developed to reach the very fast gradient switching times necessary to acquire a sufficient number of echoes before all the signal dephased. Also, image artifacts were a severe

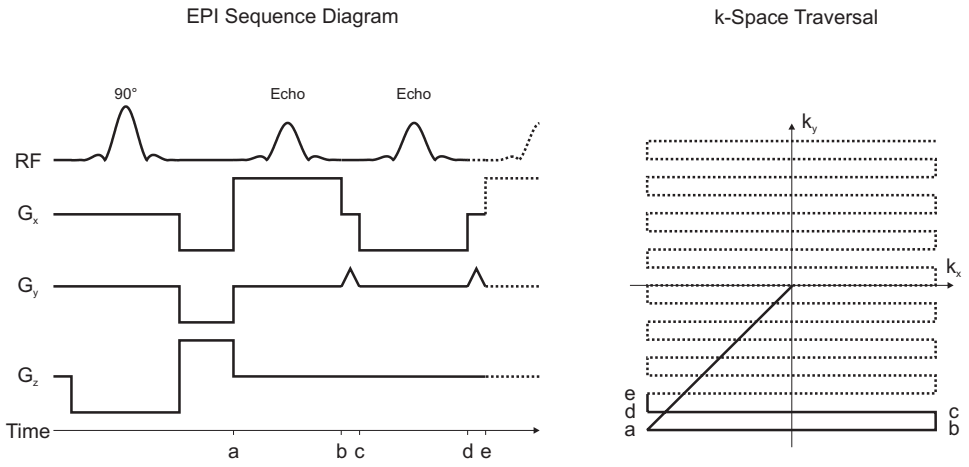

Figure 1.6: Sequence timing diagram and corresponding k-space traversal for an echo planar imaging (EPI) sequence. Corresponding time points in the two diagrams are denoted with letters a to e.

problem in the early days of EPI, according to Mansfield's Nobel Prize lecture [43], it was only with the development of actively shielded gradient coils that EPI came into practical use.

The EPI sequence builds on the principles of a gradient echo sequence. Instead of refocusing just one echo, the polarity of the readout gradient is inverted at the end of the first echo acquisition and a second echo read out. This procedure can be extended infinitely, as long as it is conducted more rapidly than the signal decay with T_2^*. These echoes are then phase encoded, in the original EPI sequence with a constant gradient in y direction [35]. With the improved hardware available today, the phase encoding gradient is usually applied in small gradient steps between the readouts, the "phase encoding blips". The sequence diagram and the corresponding k-space traversal of a modern EPI sequence are shown in figure 1.6. The phase encoding of the echoes can be extended to three dimensions, as Mansfield already recognized in his original 1977 Paper [35]. Also, echo-planar imaging can be combined with the spin echo sequence (SE-EPI), as developed by Mansfield's co-worker Pykett [44], with the full echo amplitude reached if the center line of the phase encoding scheme coincides with the echo time of the spin echo [44]. The SE-EPI method retains much of the susceptibility insensitivity of spin echo while being extremely fast as well, Pykett advocated its use especially for abdominal imaging.

The echo acquisition on both positive and negative gradient lobes in EPI gives rise to a typical $N/2$ ghosting artifact. Even the slightest phase accumulation due to imperfect gradient wave-shapes will be repeated for every positive (or negative) gradient, resulting in a phase difference between even and odd lines, which in turn results in a ghost image shifted by half

the image size in y direction due to the Fourier reconstruction. There are different ways to avoid or solve this problem (see, e.g. Hennel [45]), the easiest being to reconstruct only even or odd echoes. Today's standard technique is to assume a linear phase accumulation over the phase encoding lines and to correct it with three non phase encoded echoes acquired prior to the EPI readout train. This technique was pioneered by Wong [46] (who used only two echoes but was the first to acquire them repeatedly prior to each readout train) and Jesmianowicz [47].

Chapter 2

Introduction to Auditory fMRI

2.1 The BOLD Effect

2.1.1 Basic Principle

The blood oxygenation level-dependent (BOLD) effect makes use of the deoxygenated blood – which is paramagnetic in contrast to the diamagnetic oxygenated blood – as an MR contrast agent. The paramagnetic deoxyhemoglobin in the red blood cells (erythrocytes) induces a magnetic field distortion in the surrounding tissue. In an MRI experiment, these microscopic field distortions induced by the presence of many deoxygenated erythrocytes lead to an accelerated coherence loss of the excited transverse magnetization and hence to a more rapid (T_2 and T_2^*) signal decay.

Since its discovery, the BOLD effect has opened an entirely new dimension of non-invasive measurement of brain activation and sparked huge interest among researchers. Today, a Medline search for "BOLD" returns almost 2500 references, and of the 6500 containing "fMRI", it can be assumed that most are measured using the BOLD technique.

2.1.2 Historical

The early ancestors of the BOLD effect were the experiments conducted by Roy and Sherrington [48] in 1890. They used invasive measurement of the blood flow induced changes in brain volume in dogs upon electrical stimulation to show that cerebral blood flow changes are intricately coupled to changes in neuronal activation.

The oxygenation dependence of the transverse NMR relaxation time T_2 in blood was discovered in 1982 by Thulborn et al. [49]. They conducted NMR measurements of fresh animal blood samples dependent on oxygenation state and found a large T_2 effect which quadratically depended on the

magnetic field strength B_0.

The feasibility of using the BOLD effect for in-vivo detection of brain activity was first demonstrated in the ground-breaking animal studies by Ogawa et al. [50, 51]. The MRM paper [50] first described the measured oxygenation sensitive contrast in rodent brain at 7 and 8.4 T. It was found to be much greater with gradient echo rather than spin echo imaging. Based on these measurements, Ogawa concluded that the BOLD effect arose from the susceptibility effect of the deoxygenated blood. In the PNAS paper [51], they verified the BOLD contrast behavior in pharmacologically modified oxygenation states in rat brain.

The application of the BOLD effect to the measurement of human task-induced brain activation states was achieved independently by three groups in 1992 [52–54]. Kwong et al. [52] used visual as well as sensomotor stimulation experiments and compared the dependence of the BOLD signal changes on stimulation frequency with PET (with excellent agreement). They also pioneered the use of multislice echo planar imaging (EPI) for fMRI data acquisition, which is used by nearly all studies today. Ogawa et al. [53] used a FISP sequence with TR = 10 s and a TE of 8 or 40 ms to record the BOLD signal change induced by a visual alternating checkerboard stimulus. They observed the BOLD signal to be TE-dependent (i.e. originating from a T_2^* effect) and also advocated the use of EPI as a more time-efficient data acquisition technique. Bandettini et al. [54] described a single slice gradient echo EPI fMRI experiment using a finger-tapping task. They recorded the time course in the activated voxels and found the signal to change by 4.3% during the activation phase.

2.1.3 Hemodynamics

The reliance of the BOLD effect on the paramagnetic deoxyhemoglobin implies that the measured signal change is due to hemodynamics (the local control of blood flow, blood volume and oxygenation). What exactly acts as the driving force behind this control mechanism is still controversial. Questions such as whether the hemodynamic changes are driven directly by the energy need of the neurons or by some neurotransmitter related signaling mechanism and whether the pre- or postsynaptic activity is the major energy consumer in the brain are topics of ongoing research, as described in the following subsection 2.1.4.

However, there is a growing consensus on how the sequential regulations take place in response to an event of local neuro-electric activity (this description follows [55]). After such an event, there is an initial increase in oxygen consumption due to the increased metabolic demand which may be uncompensated by the vasculature, thereby leading to a brief decrease in the MR signal due to the increase of deoxy- vs oxyhemoglobin (the so-called "initial dip" in the BOLD response, which remains controversial to this day).

After a delay of about two seconds, the cerebral blood flow (CBF) in the vicinity of the active site increases rapidly. This increase is roughly proportional to the metabolic demand, but actually delivers more oxygenated blood to the active area than is metabolized, thereby giving rise to the (comparatively large) positive MR signal increase which is usually associated with the term "BOLD effect". Also, local vasodilation of the venules and veins leads to a marked increase in venous blood volume .

According to Logothetis and Wandell [56], it is still unclear why this oxygen oversupply occurs. They give two hypothetical explanations: If the blood delivered a constant ratio of oxygen and glucose optimal for aerobic metabolism, anaerobic processes during brain activation could account for the oxygen oversupply. On the other hand, if the oxygen extraction from the blood matched the local demand, an inefficient oxygen delivery process (as has been suggested for high blood flow rates) could be the explanation for the oxygen oversupply in the blood.

2.1.4 Neurophysiological Foundation of the BOLD Effect

Electrical activity of neurons can be measured in living animals by single microelectrode measurements. If an microelectrode with a small tip is placed very near an active neuron, the so-called mean extracellular field potential is measured, consisting of the weighed sum of the spiking activity of a small number of neighboring neurons (up to about 100 µm distance). Sub-threshold neuro-electric activity is buried under the much larger spiking potentials and is therefore not accessible with this technique. Additionally, it suffers from a strong biased toward neurons with larger size and toward certain cell types (this and the next paragraph according to the excellent review papers by Logothetis and Wandell [56], Logothetis and Pfeuffer [57]).

If an electrode with sufficiently large tip (i.e. low impedance) is placed with its tip farther from the site of neuronal activity, the action potentials do not predominate the measured signal, but the summed potential of many surrounding cells is measured. It consists of high frequency (> 400 Hz) multi unit spiking activity (MUA) from a large number of surrounding neurons (up to 300 µm from the electrode) and the low frequency (< 300 Hz) local field potentials (LFPs), which most likely reflect synaptic potentials, spike after-potentials and voltage-gated membrane oscillations (about 0.5-3 mm from the electrode). Event though LFPs certainly do not directly and solely relate to the synaptic activity, LFPs arguably still are the best available (electrical) indicator of synaptic activity in the brain [58].

Recently, it was shown by combined fMRI and electrical recording in monkeys [59] that the BOLD signal timecourse more closely follows the LFP than the MUA timecourse, when convoluted with a hemodynamic response function model. This means that most likely, the BOLD fMRI technique measures the integrative synaptic potentials represented by the LFP rather

than the action potentials. Mukamel et al. [60] measured both LFP and MUA in human subjects undergoing cerebral surgery. They compared those two electrophysiological recordings in response to an auditory movie stimuli in two patients, compared to BOLD data from a (n=11) average of healthy volunteers. They found a robust linear relationship between LFPs and the BOLD timecourse. However, in their experiments, the MUA and LFP timecourses were also highly correlated, so that their data does not allow to separate between MUAs and LFPs as the driving forces behind the BOLD signal.

Research into the biochemical processes that lead to the vascular regulation has been increasingly rewarding in very recent times. For example, Attwell and Iadecola [61] argued on the basis of data measured earlier, that the CBF changes are locally regulated by glutamate-mediated signaling processes and globally by amine- and acetylcholine signaling and are thus not directly driven by the energy need of the neurons. Takano et al. [62] very recently showed in experiments with astrocyte-labeled transgenic mice that astrocytes play a very important role in the local vasodilation. Selective increase of Ca^{2+} in the glutamaergic astrocytic synapses was consistently associated with vasodilation. Further, they were able to show that astrocyte-mediated vasodilation is primarily driven by cyclooxygenase-1 (COX-1) signaling. Interestingly, nitric oxide (NO), which had earlier been suggested to play an important role in the regulation of CBF [63] showed no effect. A further study from the same lab [64] added additional evidence to the key role of the astrocytic glutamaergic Ca^{2+} response discussed in above paper by Takano. Their in-vivo mouse experiments showed that astrocytic Ca^{2+} is indeed up-regulated in response to whisker stimulation, as a direct function of the sum of LFP signals and with an average delay of 3 s. This up-regulation was strongly inhibited by blocking glutamate signaling with mGluR antagonists. Interestingly, local inhibition of AMPA and NMDA receptors did not reduce the Ca^{2+} increase despite effectively suppressing excitatory postsynaptic currents.

2.1.5 Spatial resolution of BOLD fMRI

The spatial extent of the BOLD response to an experimental stimulus depends on a number of factors, such as the sequence used for data acquisition and the stimulation paradigm. It is therefore advisable to separately look at different aspects of this matter.

The first question we may ask is how accurate the blood flow is regulated in the brain. By optical microimaging of cat visual orientation columns, Malonek and Grinvald [65] found that the early hemodynamic response ($t < 3$ s) is highly localized (down to the columnar level), while at later times, it spreads to the surrounding tissue with final extent of 3-5 mm. For fMRI, this means that using short stimuli and / or measuring only the first few seconds

of the BOLD response should lead to an order-of-magnitude improvement in localization accuracy. Using perfusion-based fMRI (FAIR), Duong et al. [66] were able to accurately detect cat visual orientation columns with a full width at half maximum (FWHM) of the point spread function estimated as 470 µm. Using segmented gradient echo EPI at 4 T, Menon and Goodyear [67] were able to successfully detect activation of human ocular dominance columns with stimulus durations of 2 and 4 s. Using no other measures to increase the spatial specificity of their fMRI technique, they measured ocular dominance columns separated by as little as 700 µm. On a similar line, Thompson et al. [68] have reported the "initial dip" of the BOLD fMRI response to be better localized to the site of neuronal activation than the later (positive) BOLD response (measured by simultaneous single unit activity and extravascular tissue oxygenation). However, it has to be cautioned that the "initial dip" has been notoriously difficult to measure in human fMRI in practice. In a later paper by the same group [69], they simultaneously measured oxygen partial pressure and multi-unit extracellular neural activity in the retinotopically organized lateral geniculate nucleus of cats using a dual-purpose electrode. They measured robust "initial dips" which correlated with the local MUA in timing and magnitude (depending on the stimulus size in the visual field) while the positive oxygen showed the usual delay of the hemodynamic response and did not correlate with the magnitude of the neuronal response (it increased monotonically with stimulus extent). The coupling between the CBF and oxygen extraction fraction is therefore dependent both on the size and extent of the neuronal response, which further complicates the interpretation of BOLD fMRI data. However Thompson et al. admit that their electrode oxygenation measure is much more sensitive and specific to localized changes in tissue oxygenation than BOLD fMRI.

A different approach at limiting the spread of the BOLD signal is to use a "differential mapping" of stimuli known to activate different (ideally orthogonal), but closely spaced areas. The difference contrast then eliminates the (nonspecific) common activation from the further analysis. This method was pioneered by Engel et al. [70, 71] who used a continuous series of visual stimuli to excite a "traveling wave" response in the retinotopically organized cortex. Using this method, they were able to localize activation with an accuracy of 1.1 mm, even though the vascular response point spread function they measured (based on a linear model) was of 3.5 mm FWHM using 1.5 T gradient echo EPI. The advantage of the differential mapping approach has been beautifully illustrated in optical imaging experiments in the visual cortex of macaque monkeys by Grinvald et al. [72].

To determine the spatial resolution of fMRI, it is also very important to quantify the relative contributions of intra- and extravascular processes to the total BOLD signal and what size the blood vessels have that are responsible for that effect. A signal originating from large vessels would be rather unspecific, since they are not present in high densities throughout

the brain [73]. The extravascular BOLD signal originates in the dephasing effect of local susceptibility variations in the tissue surrounding blood vessels. The relative contribution of different size vessels depends on the acquisition sequence, with gradient echo sequences weighted toward larger vessels, the spin echo sequence dominated by the contribution of capillaries. The intravascular signal also contributes to the measured BOLD signal and is generally not desired, because it increases for larger vessels. However, the contribution of the intravascular signal quickly diminishes with increasing field strength, due to the rapid shortening of blood T_2 (from about 100 ms at 1.5 T to around 18 ms at 4.7 T [74]).

Experimental support for above considerations has come from a number of authors. Boxerman et al. [75] studied the intra- and extravascular BOLD signal changes in both a Monte-Carlo simulation and asymmetric spin echo fMRI. They concluded that at 1.5 T, the intra-vascular compartment largely dominates the observed BOLD signal change. The other pioneering study came from Song et al. [76] who studied gradient echo fMRI with additional diffusion gradients of varying strength. They found that at 1.5 T, a relatively small diffusion gradient of $b \leq 100\,\mathrm{s/mm^2}$ effectively suppresses the intravascular BOLD signal, which they found to dominate the BOLD signal. At higher field strengths and for spin-echo fMRI, the extravascular signal is more important, with almost no intravascular signal remaining for 9.4 T spin-echo fMRI according to Lee et al. [77] (based on the relatively constant BOLD signal they measured across different diffusion b values). According to his paper, it is generally accepted that the intravascular signals from large vessels are reduced at b values as small as $20 - 30\,\mathrm{s/mm^2}$.

Accordingly, the spatial resolution of BOLD fMRI is generally reported to be better at higher fields and better for spin echo than gradient echo fMRI. High resolution human fMRI at 4 T was demonstrated already in 1993 by Ugurbil et al. [78], who showed fMRI maps of the visual cortex at $0.6 \times 0.6\,\mathrm{mm^2}$ in-plane resolution using gradient echo EPI. Duong et al. [79] used spin echo EPI at 4 and 7 T to reproducibly generate fMRI maps of $1 \times 1 \times 2\,\mathrm{mm^3}$ and even $0.5 \times 0.5 \times 2\,\mathrm{mm^3}$. For gradient echo fMRI, the effective spatial resolution has been measured to be around 3.5 mm at 1.5 T, 2 mm at 4.7 T and 1.6 mm at 9.4 T, according to Harel et al. [80]. Parkes et al. [74] measured the point spread function at 3 T using both gradient echo and spin echo and estimated it as 3.9 mm for gradient and 3.4 mm for spin-echo. Still, she suggests that at 3 T, gradient echo sequences will lead to a higher effective resolution due to the about threefold better contrast-to-noise ratio.

Another aspect influencing the size of a measured activation is the signal to noise ratio of the images. Saad et al. [81] showed that the number of activated voxels in an fMRI experiment depends crucially on the amount of averaging. In their experiments, they found that the number of activated voxels monotonically increases with the number of session averages, without

reaching a plateau or upper bound for the range of 1 to 22 averages in a visual task. They found a logarithmic model to fit the above relationship relatively well. They concluded that in a typical experiment, many low-SNR activated voxels remain undetected.

2.1.6 Localization, and correspondence with neural activity

In animals, the co-localization of neural activity and BOLD fMRI activation is relatively well established. Logothetis et al. [59], for example, simultaneously measured different aspects of the neuroelectrical response and fMRI and found the BOLD response to be confined to centers of neuroelectric activity. In an impressive paper, Duong et al. [82] compared calcium dependent manganese fMRI with BOLD and CBF in the same animals (rats) at 9.4 T. They found excellent co-localization of the neuronal activity (as detected by the Mn-fMRI) with CBF and BOLD measurements. However, even at the ultra high field strength they used, remaining draining-vein effects were found in the gradient echo BOLD activation maps (as voxels with large percent signal change, but low statistical significance), whereas the CBF measurements did not show such an effect.

In human subjects, where invasive electrophysiological measurements are more problematic, the number of studies are lower. Where comparisons of BOLD fMRI with intra-surgical recordings were conducted, however, they generally reported good agreement for the co-localization of activated regions. Puce et al. [83], for example, found "good" co-localization between the intra-operative electrophysiological recordings and fMRI in the sensory and motor areas of four patients. Yousry et al. [84], found "identical" localization of hand areas in six patients in a similar comparison of electrophysiological recordings and fMRI.

2.2 Analysis of fMRI Data

2.2.1 Making Inferences about Activation

Inferences about activated regions in the brain are most commonly made using a general linear model (GLM) of the form $X = G\beta + \varepsilon$. The aim of this procedure is to model the behavior of the time series data X as a linear combination of "predictor functions", which form the rows of G, with weights β , where the entries of the vector ε represent error terms assumed to be independent, and from a zero mean normal distribution [85]. The predictors commonly consist of the stimulus function convolved with an assumed hemodynamic response function (HRF), which models the delay and dispersion of the BOLD signal with respect to the underlying neuronal activity. Alternatively, additional predictors such as the time derivatives of the above predictors can be included to account for possibly variable, region

specific delay or dispersion properties of the HRF. In actual fMRI data, the noise arising from physiological processes (in contrast to instrumental random) is temporally (and spatially) correlated, which makes an extension of the above situation necessary [86, 87].

Then, the significance of a specific compound of effects modeled in G (a "contrast") can be assessed using the t statistic under the null hypothesis that the observed effects are not significant. By thresholding the t values calculated for each voxel, inferences can be made about regions in which the modeled effect is significant. To give actual probability levels such an observation, a multiple comparison test (such as the Bonferroni correction or, better, Gaussian random field theory) has to be employed to account for the spatial correlations in the data.

One fundamental assumption behind the general linear model is that the BOLD signal measured in response to a stimulus is proportional to a measure of local neuronal activity, averaged over a certain spatial and temporal extent and possibly with a delay. This assumption, referred to as the "linear transform model", has three important implications. The first is that the response to a long stimulus can be predicted by the summation of responses to shorter stimuli, assuming that this temporal summation holds up for the underlying neuron-electrical activity. While this has proved a useful model, departures from this temporal linearity can be measured for many areas of the brain (as discussed in the following section 2.2.2). A second implication of the linear transform model is that the BOLD signal timecourse can be accurately predicted by convolving the neuroelectric response with a constant (but possibly region-specific) impulse response function, the HRF. This has recently been confirmed in the visual cortex of monkeys by a combination of invasive electrical measurements and fMRI [59], where the neuroelectrical signal could explain up to 90% of the variance in the BOLD signal, but with large regional differences. A third implication is that a BOLD signal change should be observed only in areas where there is neuronal activity. This is relatively well established, as discussed in section 2.1.6.

2.2.2 Nonlinearity of the BOLD response

Nonlinearities in the BOLD response can be observed both with respect to the stimulus amplitude (the second implication of the linear transform model of section 2.2) and with respect to its duration (i.e. departures from the temporal summation, the first implication of above linear transform model). If nonlinear behavior with respect to a certain aspect of a stimulus is observed, however, this does not necessarily mean that the observed nonlinearities stem from the vascular response, it could also be a property of the underlying neuroelectric response to stimuli (in which case the linear transform model would not be violated).

According to Vazquez and Noll [88], the nonlinearity of the BOLD re-

sponse in human V1 is strongest with respect to stimulus duration (for stimulus durations $< 4\,\mathrm{s}$), but also to a lesser extent with respect to amplitude (starting from about 40% contrast). A paper by Soltysik et al. [89] quantifies the nonlinearities in the BOLD response of visual, auditory and sensomotor areas concerning the temporal additivity. By studying how well the BOLD response to short stimuli can predict longer stimuli and how well the impulse responses of short and long stimuli agree, they comes to the conclusion that the "hemodynamic response is nonlinear for stimuli less than 10s in the primary auditory cortex, nonlinear for tasks less than 7s in the primary motor cortex, and nonlinear for stimuli less than 3s in the primary visual cortex.

Specifically in the auditory cortex, Talavage and Edmister [90] showed that the BOLD response to an orchestral music stimulus and recorded scanner noise do not add up linearly in the auditory cortex (measured with the sparse sampling technique of section 3.7 and functionally defined regions of interest). A similar approach was used by Langers et al. [91] to study interactions between scanner sound and acoustic stimuli. They also used a sparse sampling paradigm (cf. sec. 3.7) and nonlinear systems analysis and found a decrease in the BOLD amplitude from 1.3% to 0.9% due to the interaction of scanner noise. From the fact that scanner noise preceding the stimuli by several seconds caused such nonlinear behavior, they concluded that they must be of vascular (rather than neuronal) origin.

Regarding the question of whether these nonlinearities originate from hemodynamic or neuronal processes, Kellman et al. [92] reported that the second-order nonlinear response they observed in the activation timecourse to visual stimulation were probably due to neuronal, not vascular effects. Also, combining invasive electrophysiological recordings with fMRI, Logothetis et al. [59] found pronounced nonlinearities in the amplitude of the BOLD signal with respect to the magnitude of the neuroelectrical signal in monkey visual cortex.

2.3 Auditory System

2.3.1 From the Cochlea to the Brain

The auditory system is one of the most sensitive and responsive sensory systems in the human body. At its heart lies an array of acoustical detectors the size of a pea. They are able to detect vibrations as small as the diameter of an atom and they respond three orders of magnitude faster than visual photoreceptors ([93], entire subsection). The audible frequency range extends from about $20\,\mathrm{Hz}$ to $20\,\mathrm{kHz}$. In fact, the sound frequency is an important characteristic of an auditory signal already at the stage of transduction from a physical into a neuronal signal. This transduction takes place in the cochlea, a fluid-filled, spiral shaped structure (the Latin cochlea

translates to snail) in the inner ear, which maps incoming sounds of different frequencies to different spatial modes of vibration. This decomposition of frequencies into spatially separate neuronal signals is referred to as tonotopy and is preserved throughout the central auditory pathway up to the cortex (see figure 2.1).

Another main organizational principle of the auditory system is its parallel organization, which becomes apparent once the neuronal information from the hair cells in the cochlea enters the brainstem. Here, it branches to innervate three sections of the cochlear nucleus and from there via different pathways to the superior olivary complex, the lateral lemniscus and the inferior colliculus. From there, the auditory information is integrated and relayed to the medial geniculate complex of the thalamus, where it is finally passed on to the primary auditory cortex (again, see figure 2.1).

The first station of auditory processing occurs at the cochlear nucleus, where the signals from the auditory nerve are modulated in three different sections, the dorsal, the posteroventral and the anteroventral chochlear nuclei with different populations of neurons which have different properties, each maintaining the tonotopic organization.

In the superior olivary complex, auditory information from both ears meets for the first time. Already at this stage, information processing occurs to decode spatial information from the sounds. In humans, two different strategies are used for sound localization, depending on the sound frequencies. For frequencies below about 3 kHz (or 1.5 kHz, according to a more recent study [94]), timing differences are used; above that frequency, intensity differences are used for sound localization. This twofold strategy illustrates the usefulness of parallel processing. The computation of timing differences occurs in the medial superior olive, which is able to detect timing differences as small as 10 µs, allowing for sound localization with an accuracy of about 1°(!). For higher frequencies, intensity differences of the sounds arriving at both ears are evaluated in the lateral superior olive and in the medial nucleus of the trapezoid body.

In the midbrain, the auditory information is processed and integrated in the inferior colliculus. Here, complex temporal patterns as well as spatial information are analyzed and integrated. Some neurons in the inferior colliculus respond only to frequency-modulated sounds, some only to sounds of a specific duration. In barn owls, which extensively use hearing to obtain spatial information, the inferior colliculus exhibits a spatial representation of location in space. In mammals, however, such auditory space maps have not been found to this date.

All ascending information reaching the cortex has to pass the medial geniculate complex (or medial geniculate body), which receives most of its input from the inferior colliculus, but some axons also directly connect it to the lower brainstem. In some mammals, such as in echolocating bats, the medial geniculate complex departs from the strict tonotopic organization

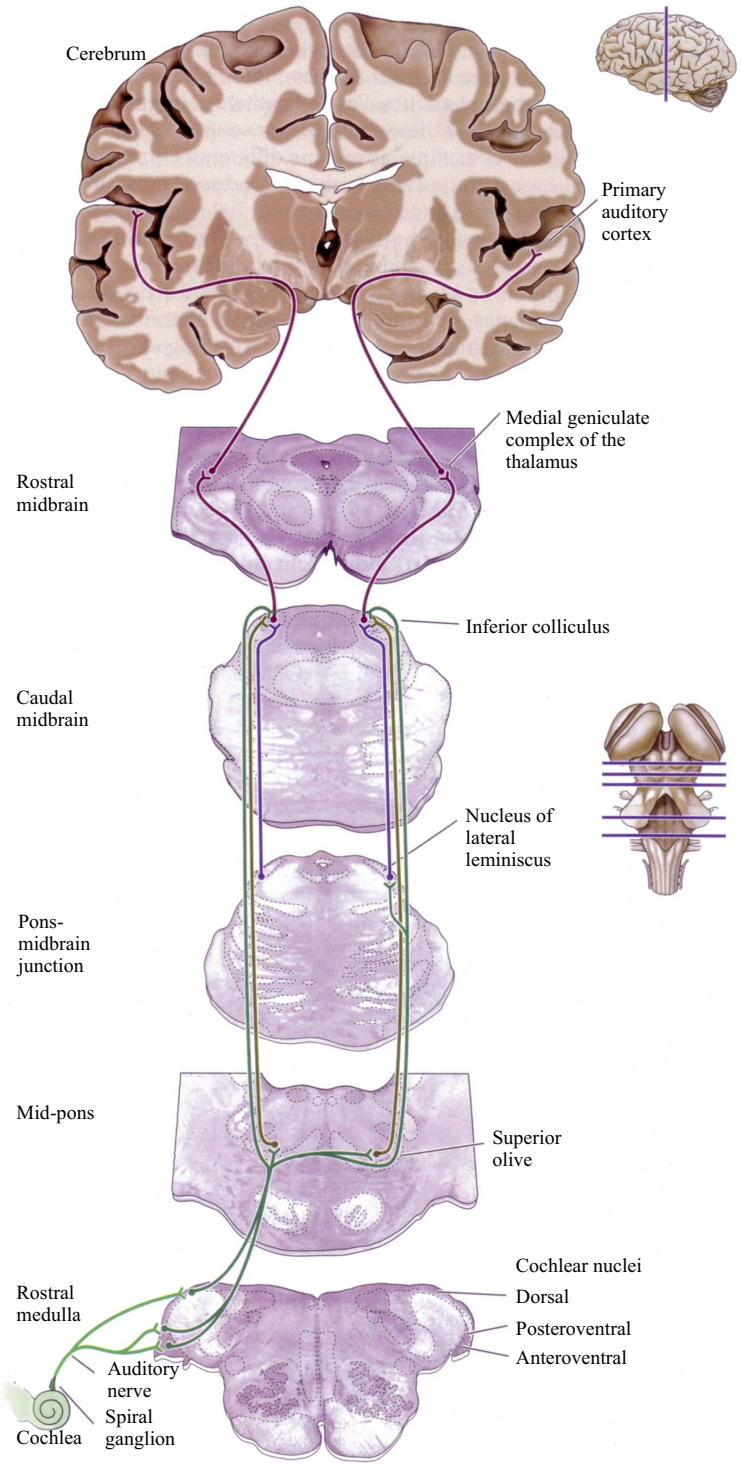

Figure 2.1: Auditory Pathway (reproduced from [93])

and comprises neurons responding specifically to certain combinations of frequencies. In any case, it seems to mediate the detection of specific spectral and temporal combinations of sounds.

The final target for auditory information is the auditory cortex, to be described in the following section.

2.3.2 Architecture of the Auditory Cortex

The architecture of the auditory cortex is much better understood in animals than in humans, for the obvious reason that direct (i.e. invasive) measurements are problematic in humans. For a long time, the cat was the animal of choice for auditory neurobiological research, which has now changed in favor of nonhuman primates [95]. In the monkey, these research findings have converged to form a "consensus model" of a auditory cortex architecture (see figure 2.2) comprising a primary "core" region and a secondary, peripheral "belt" region [95–98].

The primary cortex of the core region is distinguished from its surroundings by a dense, granular ("koniocortical") layer IV. It comprises two or three subdivisions which are each laid out tonotopically, with mirror-symmetrical frequency gradients (their isofrequency bands are oriented medio-laterally) [96]. Further, the core region is characterized by sharp frequency tuning [95] and responds well to pure tones [98].

The surrounding belt region consists of seven or eight subdivisions and a lateral parabelt region comprised of at least two fields [95, 96]. The belt region receives the majority [96] or all [95] its input from the core area and is less clearly tonotopically organized [95] (while some of the parabelt regions seem not to be tonotopically organized at all [96]). Also, the belt region responds only weakly and non-specifically to pure tones, but exhibits stronger responses to more complex stimuli such as bandpass noise bursts [98].

In humans, the primary auditory cortex (designated PAC, A1 or Brodmann's area 41, defined by the koniocortical cytoarchitecture and its dense myelination [100]) is located on the supratemporal plane of the superior temporal gyrus (STG) [95]. Its location at least partly coincides with one or several small transverse gyri posterior to the first transverse sulcus (FTS) of the STG , commonly referred to as Heschl's gyrus or gyri (HG) [101]. A secondary peripheral region, homologous to the "belt" region in the monkey is located around the primary area. Specifically, it includes the caudally located planum temporale and the ventrally located planum polare and also the lateral and posterior parts of Heschl's gyrus [101].

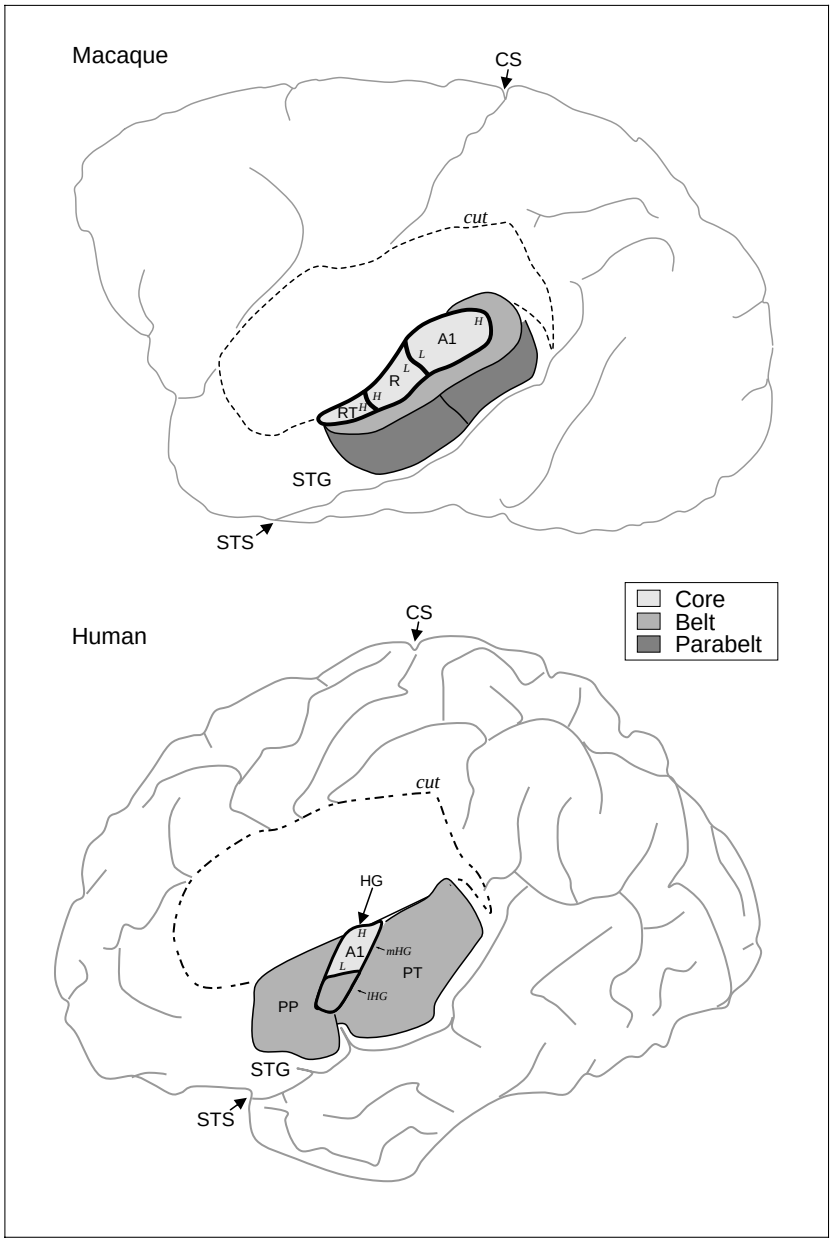

Figure 2.2: Auditory Cortex Architecture, modified from [97]. The naming of the two subsections of human Heschl's gyrus (mHG and lHG) according to [99], addition of tonotopic gradients in the human according to [100] (also, cf. [95]). Abbreviations used: CS central sulcus, STS superior temporal sulcus, STG superior temporal gyrus, PP planum polare, PT planum temporale, A1 primary auditory cortex, R and RT rostral and rostrotemporal areas in the monkey, HG Heschl's gyrus, mHG and lHG medial and lateral HG, H and L high and low ends of tonotopic frequency gradients.

2.3.3 Anatomical Variability in Human Auditory Cortex

The great inter-individual anatomic variability in the region of the primary auditory cortex and the possibility of left-right asymmetries have been known for almost 100 years [102]. The number of transverse (Heschl's) gyri following the FTS, for example, varies from a single gyrus to three or more. Yousry et al. [103] in 100 control hemispheres found 66 single Heschl's gyri, 33 with two and one with three HG, Rademacher et al. [104] reported a single HG in 70%, two in 24% and three in 6% of 54 hemispheres studied.

A larger volume of the left auditory cortex, which could be expected from the left-dominant language processing, has been reported, for example, by Penhune et al. [102], who found it to result from a larger white matter volume (n=20). They also found the right HG to be localized more anterio-medially. This shift has also been reported by Rademacher et al. [104], who measured an average of 7 mm in the anterior and 5 mm in the lateral direction (n=27), although they found no overall volume asymmetry (despite up to twofold asymmetries in individual brains). On the other hand, Schneider et al. [105], in a computerized average of 87 subjects, found no asymmetry neither in size nor position, except for an enlargement of the left planum temporale.

The localization of the primary auditory cortex (A1), as defined by the cytoarchitecture, is also subject to large inter-individual variability. Rademacher et al. [104], in a combined MR and cytoarchitectonic study on human post-mortem brains (n=27), report that the volume of A1 ranged from 16 to 92% of the HG volume (mean 54%) but also frequently extended beyond the borders of HG. Further, they found no correlation between the volume of A1 and the volume of HG or the number of transverse gyri. Their probabilistic atlas of the location of the A1 in the human brain is shown in figure 2.3. Rademacher et al. concluded that "the precise location and absolute size of area Te1 [i.e. A1] cannot be reliably inferred from the macroanatomic landmarks." Still, in their measurements, the A1 always covered portions of the HG, and was on averages located on the medial two-thirds of HG.

Very interesting correlations have been found to exist between the volume of various parts of HG and musical ability in two studies by Schneider et al. In a first paper [99], they found that, averaged over both hemispheres, the anteromedial part of the HG gray matter volume was larger in professional musicians by $130 \pm 23\%$ compared to non-musicians ($p<0.0001$). In a more recent publication [105], they reported that the volume of lateral HG (lHG) correlates to a standardized test of musical listening ability (AMMA test, $r=0.71$, $p<0.0001$). The structural right-left asymmetry of lHG strongly correlated with "pitch asymmetry" (as determined by a psychometric test for pitch perception based on fundamental frequency versus spectral pitch) ($r=0.77$ $p<0.0001$). They concluded that the lHG is a pitch processing center.

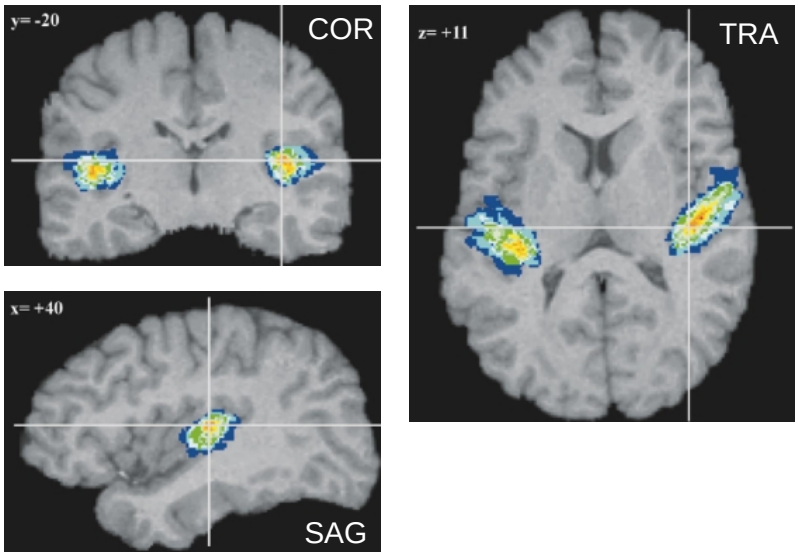

Figure 2.3: Anatomic variability of the human auditory cortex: Probabilistic map of the location of the cytoarchitectonically defined A1. Probabilities range from 10% in dark blue to 100% in dark red. (slightly modified from [104]).

2.3.4 Architecture-Related Evidence from fMRI Studies

Naturally, the question whether and to what extent the "core-belt" architecture in the monkey is homologous to the situation in human auditory cortex has been the subject of intense research. Rivier and Clarke [106] used cytochrome oxidase (a marker for metabolic activity [97]) and acetylcholinesterase staining (used to differentiate functionally distinct areas within auditory cortex), together with cytoarchitectonic measures, to identify the primary and seven distinct higher level auditory areas in the human brain. For functional, in-vivo measurements, fMRI has proved a very important tool. From the core-belt architecture model, it can be expected that the core responds better to simple stimuli (pure tones, temporal modulations) while the belt areas preferentially respond to more complex stimuli (harmonic sounds, broadband noise, speech, spectral modulations). Evidence for such a spatial segregation was found, for example, by Wessinger et al. [107], who showed that pure tone stimuli activate a smaller region in the human auditory cortex than bandpass noise. They used sparse sampling (see section 3.7) and counted the number of activated voxels for the two stimuli, when the statistical maps were thresholded at the same value. Hall et al. [108] similarly used four stimuli consisting of the combinations of either a 500 Hz sine tone or a harmonic equivalent and a 5 Hz frequency modulation or continuous tone presentation. They found a larger area for

the contrast of frequency modulated stimuli versus static tones surrounding a smaller activation volume for the harmonic versus pure tone contrast.

Another research focus has been on the number and location of tonotopically organized regions within the human auditory cortex. First investigations on this topic go back to 1996, when Talavage et al. [109] attempted to measure tonotopy in the human AC using frequency-swept bandpass noise. The results were interpreted as indications of tonotopy but were not conclusive. Further studies with simpler stimulation protocols followed. Both Wessinger et al. [110] and Talavage et al. [111] used fMRI of two different frequency stimuli to calculate "centers" of activation based on frequency dependent activation maps which gave support to the tonotopic organization principle. Also, using a sparse sampling design (see section 3.7) to eliminate the influence of scanner acoustic noise, Bilecen et al. [112] measured frequency-dependent activation maps with two pulsed tones of 500 Hz and 4 kHz. Still, all those studies remained somewhat unsatisfactory in that they "failed [...] to display the expected functional complexity for the auditory cortex" [98]. The situation changed in 2003, when Formisano et al. [100] were able to demonstrate the existence of mirror-symmetric tonotopic maps by high field fMRI. That study was conducted on a 7 T system using a silent event-related paradigm (i.e. sparse sampling). Six subjects were measured using 8 Hz pulsed sine tones of 3 s duration at two to six different frequencies between 0.5 and 3 kHz. They found two mirror-symmetric tonotopic maps sharing a low-frequency border following the length of Heschl's gyrus, with marked inter-individual differences in extent and shape, but very similar to the well established maps in nonhuman primates (see figure 2.2).

2.3.5 Auditory BOLD Response: The Importance of the Sound Temporal Envelope

The importance of the time-dependent amplitude modulations of sounds, the sound temporal envelope, in the processing of auditory signals can already be anticipated based on simple psychoacoustic experiments. For example, repeated burst of noise presented at a low rate (e.g. < 10 Hz) can be separately resolved (Miller and Taylor 1948, Symmes 1955, cited according to Harms and Melcher [113]), while bursts presented at a higher rate fuse to form a single, modulated percept. Neurophysiological experiments in animals have shown that the highest repetition rates at which neurons respond faithfully to each successive sound in a train tends to decrease from brain stem to thalamus to cortex. In the cortex, the neuronal coding of low and high rates may be accomplished by different populations of neurons, one coding low-rate stimuli through stimulus-synchronized activity and the other coding high rates in the overall amount of discharge activity (all according to [113]).

Consistent with above animal data, Harms and Melcher [113] found the

percent signal change in their human BOLD fMRI experiments to be maximal for frequencies which decreased from brainstem to cortex. They used 25 ms white noise bursts presented at various repetition rates and found the preferred rates to be ≥ 35 /s for the inferior colliculus, 20 /s for the medial geniculate body, 10 /s for Heschl's gyrus and 2 /s for the superior temporal gyrus (n=9). In an earlier paper, Giraud et al. [114] had come to similar results. Using white noise stimuli, amplitude modulated (AM) at 4 to 256 Hz, they found preferred AM frequencies to decrease from 256 Hz in the brainstem to 4-8 Hz in the cortex.

In Heschl's gyrus, the situation is somewhat controversial. Seifritz et al. [115] found a monotonic decrease in percent signal change BOLD response when compared across different repetition rates. They used 50% duty cycle 1 kHz sine tones at repetition rates of 2.5, 5, 10, 15, 20, 25 and 30 Hz and a sparse sampling (sec. 3.7) design to eliminate the influence of the scanner sound. Giraud et al. [114]'s results (also using energy-equated stimuli) largely agree with this finding. In contrast, they contradict Harms and Melcher [113]'s peak at 10 Hz and a similar 5 Hz peak BOLD percent signal change measured by Tanaka et al. [116] (who compared 1 kHz sine tones of 30 ms duration presented at rates of 0.5, 2, 5, 10 and 20 Hz). However, these preference peaks can be attributed to the latter two studies using fixed-length stimuli in contrast to the energy-equated stimuli used in the first two papers (according to Seifritz et al. [115]).

The sound repetition rate (or temporal envelope) also has a striking influence on the observed response timecourse. In the above mentioned study published in 2000, Giraud et al. [114] found that the time course of the hemodynamic responses differed depending on the AM frequency, with sustained response for lower frequencies (less than about 16 Hz) and transient response for higher frequencies. To separate between the two, they simply analyzed their (28 s on $-$ 28 s off) block design data with either an event or an epoch related model.

In two very careful and convincing studies, Harms et al. further detailed these findings. In the first [113] (mentioned above), they also recorded response waveforms depending on repetition rate (in a 30 s on $-$ 30 s off block design experiment). In the inferior colliculus, the response amplitude increased with increasing rate while the response waveshape remained unchanged (i.e. sustained). In the medial geniculate body, increasing rate produced an increase in onset amplitude up to a point where a further increase in rate instead produced a change in waveshape (from a largely sustained response to one showing a distinct peak just after train onset). In Heschl's gyrus, the site of the primary auditory cortex, onset amplitude changed somewhat with rate, but the most striking change occurred in response waveshape. At low rates, the waveshape was sustained, while at high rates it was strongly phasic (in that there were prominent response peaks just after train onset and offset). In the superior temporal gyrus, which

includes secondary auditory areas, onset amplitude showed no systematic dependence on rate, whereas response waveshape showed a strong and dramatic rate dependence paralleling that in HG. Especially because of the observed offset response, they interpreted the phasic responses as resulting from an underlying neuronal response pattern, rather than a hemodynamic effect [113].

In a second paper [117], Harms et al. entirely focused on the auditory cortex and expanded the range of stimuli used. Again, they employed a (30 s on − 30 s off) block design and white noise bursts of varying duration (i.e. varying duty cycles) and rates, but also narrowband noise bursts, continuous noise, trains of clicks, human speech and orchestral music stimuli. They found that both in HG and STG, the average response to 100 /s clicks and 35 /s noise bursts was highly phasic, whereas the response to 2 /s noise bursts, speech and music was primarily sustained. The responses evoked by 35 /s clicks, 10 /s noise bursts, and continuous noise were "intermediate" in waveshape (figure 2.4a). The waveshapes of low-rate stimuli was sustained equally in both HG and STG, while the response to higher rate stimuli (and continuous noise) was more phasic in the STG than HG. The phasic versus sustained nature of the BOLD response was quantified in a waveshape index based on the fit of the data to a five-predictor model of the hemodynamic response function. Using this metric, the waveshape was significantly more phasic for 35 /s than 10 /s noise bursts in both HG and STG. This was true both for equal noise burst duration and equal (50%) sound time fractions (STF, equivalent to the stimulus duty cycle). When keeping the rate constant at 35 /s and increasing the STF, the BOLD timecourses continuously approached the waveshape found for a continuous tone (i.e. a phasic response pattern, figure 2.4c). Even a change of 50 to 88% STF produced a significant difference in waveshape index. Interestingly, they found that sound levels in the range of 40 to 70 dB above the hearing threshold resulted in no change of waveshape (and almost no change in amplitude!) of the BOLD response with sound level (figure 2.4b). Also, there was no dependence of waveshape on the stimulus bandwidth (i.e. broadband noise bursts versus narrowband noise bursts or tone bursts).

Especially important for the work presented in this thesis is the BOLD response to continuous noise or tones. As discussed above for the study by Harms et al. [117], it is highly phasic in nature and can be seen as the limit of very high repetition rates or high sound time fractions (while the rate is kept constant).

This has also been shown for 50% duty cycle amplitude modulated 1 kHz tones compared to a continuous 1 kHz tone in a sparse sampling task (sec. 3.7) by Seifritz et al. [115]. They found an initial peak of 3.3% ΔT_2^* about 5-6 s after stimulus onset and a sustained plateau (2.2%) for pulsed tones, in contrast to a peak of 1.9% about 2 s earlier and virtually no (0.5%) sustained response for the continuous tone. Simultaneous measurement of blood vol-

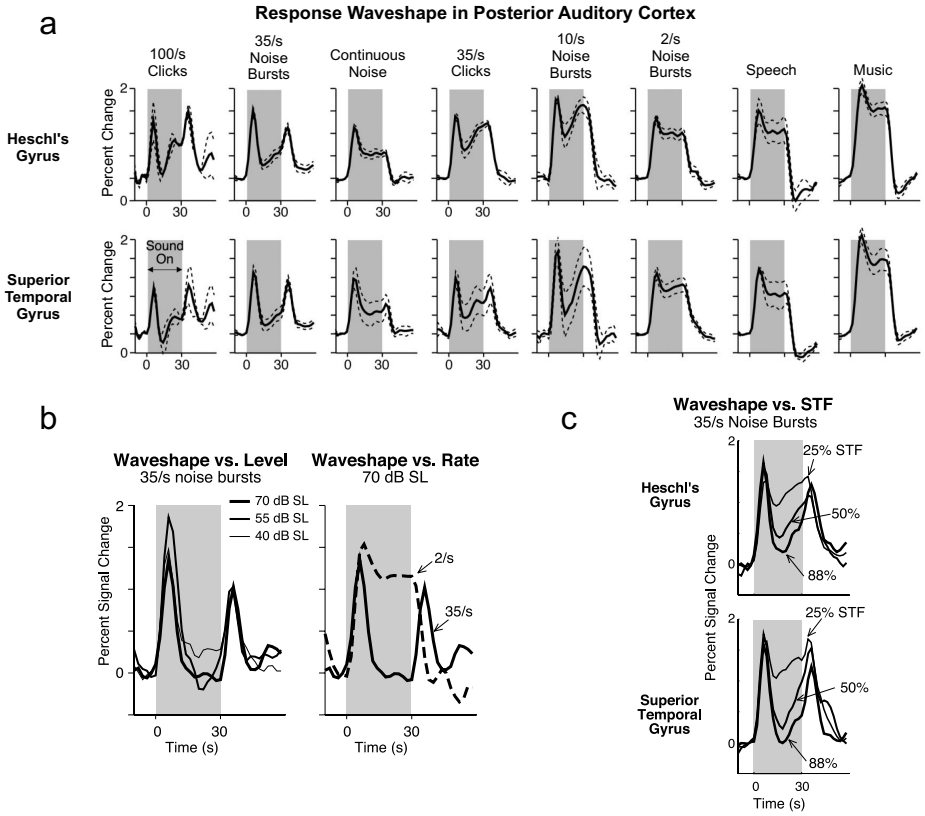

Figure 2.4: Influence of repetition rate on the BOLD timecourse in the human auditory cortex. (a) BOLD response timecourses for different kinds of stimuli. The repetition rate of a stimulus is a key factor in terms of the response shape it evokes, with higher rates resulting in a more phasic, lower rate stimuli in a sustained response. (b) The repetition rate, but not sound level (nor stimulus bandwidth, not shown) determines the waveshape of the BOLD response in posterior Heschl's gyrus. All responses from the same imaging session. (c) Effect of sound time fraction (i.e. stimulus duty cycle) on the response waveshape. Data is from seven sessions using a broadband noise stimulus presented at 55 dB above hearing threshold. (all figures reproduced from Harms et al. [117])

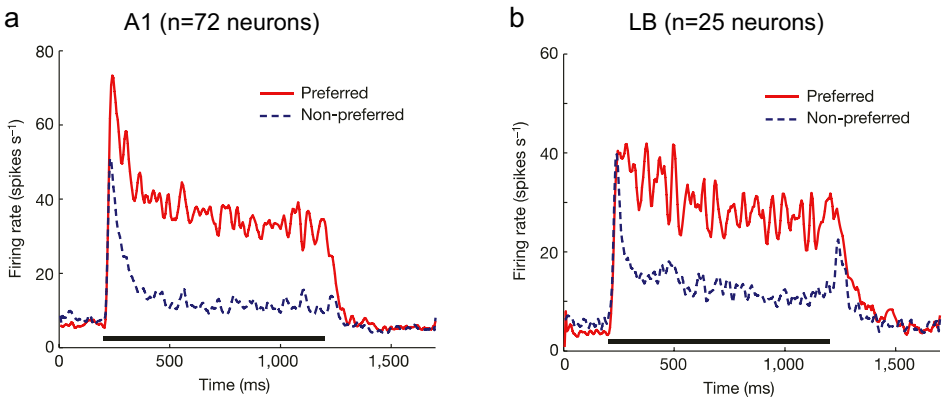

Figure 2.5: Sustained firing of (marmoset monkey) neurons in the primary auditory cortex (A1) and lateral belt (LB) in response to preferred (best modulation frequency, BMF) and non-preferred (modulation frequency f with lowest firing rate for which $f > \text{BMF}$). Note the neuronal offset response to the LB non-preferred stimulus. (reproduced from Wang et al. [118])

ume changes suggested that the rate-dependent modulation of BOLD signal during the sustained phase was indeed due to sustained firing, and not to a vascular effect.

Neurophysiological evidence for sustained neuronal firing in response to an extended stimulus has indeed been found by other researchers. In a study in awake marmoset monkeys, Wang et al. [118] showed that neurons in the primary auditory cortex and the lateral belt respond to preferred stimuli with sustained firing, and a more phasic response to non-preferred stimuli (figure 2.5). They showed that even single neurons fire repeatedly in response to preferred stimuli. These findings were in contrast to earlier studies in anesthetized animals, but according to Wang et al. [118], anesthesia conditions strongly influence electrophysiological response patterns. In the experiments of Wang et al., lateral belt neurons of marmoset monkeys as well as macaque monkeys responded more strongly to noise stimuli than to pure tones. On the other hand, most primary auditory cortex neurons were more strongly driven by amplitude- or frequency-modulated tones than by pure tones, and typically showed preference for a particular, or 'best' modulation frequency. In some cases, off-responses were observed for non-preferred stimuli in LB neurons.

Chapter 3

Principles: Continuous EPI

3.1 Acoustic Gradient Noise

3.2 Problem description

In functional Magnetic Resonance Imaging (fMRI) of the auditory system, one of the most fundamental problems is the interference of the scanner's acoustic noise with the experimental stimulus. In most studies, EPI sequences are used because of their speed and high signal-to-noise ratio. However, the rapidly switched gradients in these sequences lead to very high sound pressure levels . More importantly, the spectral characteristics of the EPI gradient noise, especially the low-frequency pulsation, result in a particularly effective stimulation of the auditory system and thus largely mask the experimental stimulus.

3.3 Origin and Characterization

The gradient acoustic noise originates in the Lorentz forces that act on the gradient coils. Any conductor carrying an electric current $\mathbf{I}$ in an external field $\mathbf{B}$ feels a force $\mathbf{F} = \mathbf{B} \times \mathbf{I}$. In the gradient coils of an MR system, these forces cause the gradient coils to bend and buckle depending on the current that passes through them, or transmit that force over their supports to the rest of the MR system. This means that the rapidly switched gradients result in vibrations of the entire system, much as if the currents used to switch the gradients were passed to a loudspeaker (see, for example [119, 120]).

As a direct consequence of the Lorentz force equation, it can be expected that the acoustic noise during MR scanning increases with the field strength of the magnet and the strength of the gradient field (which, in turn, determines how fast a given imaging sequence can be run). The linear dependence of acoustic noise level on the B_0 field was validated in a study by Moelker [121] for magnetic field strengths of 0.5, 1, 1.5 and 2 T. In a survey of of

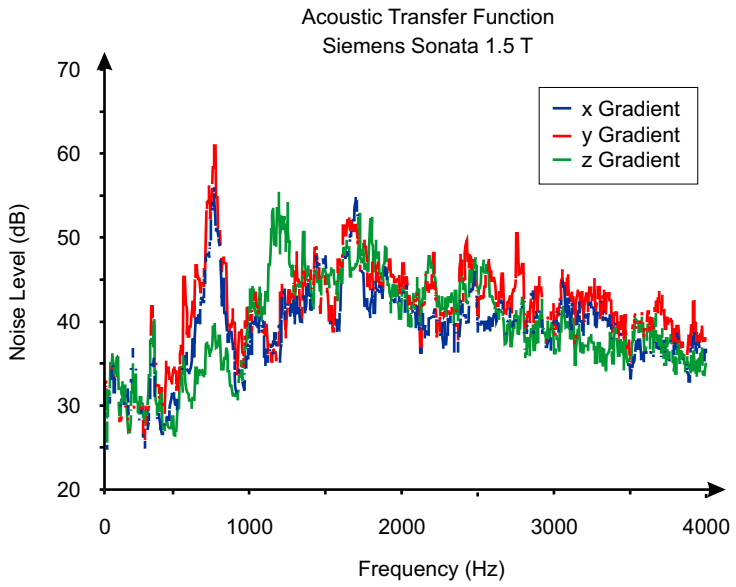

Figure 3.1: Acoustic transfer function for a 1.5 T Siemens Sonata system.

acoustic noise levels of fifteen different scanners, Price [122] found both the increase of noise levels with B_0 field and gradient field strength confirmed.

The scanner's gradient system is a linear electromechanical system to a good approximation, the acoustic noise spectrum $P(f)$ thus directly relates to the frequency spectrum of the gradient waveform $G(f)$ through the relation $P(f) = H(f) \cdot G(f)$, where $H(f)$ is called the acoustic transfer function [123]. In order to estimate the acoustic noise frequency spectrum for a given sequence, a measured acoustic transfer function (obtained using a white-noise gradient pattern or a frequency-swept sine tone) can therefore be multiplied by the gradient waveform spectrum. Good correspondence of measured acoustic noise spectra with the spectra of the applied gradient waveforms has been reported, for example, by Foster [124]. For the Siemens Sonata system, such a measured acoustic transfer function is shown in figure 3.1. For frequencies less than about 300 Hz, the acoustic damping is very good, with a sound attenuation of about 25 dB relative to the peak at about 800 Hz (i.e. the main acoustic resonance of the gradient system). The acoustic transfer functions are qualitatively similar to the above example for most MR scanners. This means that slow gradient waveforms (with frequencies below about 300 Hz) result in low sound levels, while sequences with gradient switching frequencies around 800-1000 Hz can be extremely loud and are even forbidden by the scanner software in some cases.

3.4 Sound Pressure Levels

Acoustic sound levels during MR scanning are frequently reported in terms of the sound pressure level (SPL). The SPL is a logarithmic measure of the pressure exerted by airborne acoustic waves, relative to a standardized reference sound pressure $P_0 = 20\,\mu\text{Pa}$ [121]:

$$\text{SPL} = 10 \cdot \log(P^2/P_0^2) = 20 \cdot \log(P/P_0)$$

Since the human auditory system is not equally sensitive to all frequencies, a (frequency-dependent) weighting is also commonly used when reporting noise levels relevant to human subjects. The "A" weighting curve reflects measurements of perceived equal loudness in human subjects. It strongly attenuates sound frequencies outside the 1-10 kHz range and is applicable for relatively low-intensity sounds . The "C" weighting has a flatter response profile in the low frequencies and is intended for louder sounds.

Several studies have reported gradient acoustic noise levels during EPI scanning with sequence settings similar to those used in fMRI. Ravicz et al. [119], for example, reported noise levels of 115 dB SPL at 1.5 T and 131 dB SPL at 3 T. These values changed less than one decibel when A or C weighting was used instead of the SPL. Other researchers reported similar values, 103.2 dB(C) [125], 115 dB(A) [126] and 90-117 dB SPL [120] at 1.5 T, 122-131 dB SPL [124] and 105-133 dB SPL [120] at 3 T.

The actual sound pressure levels vary according to the position within the magnet bore and can be higher when a patient lies in the magnet, compared to the empty bore [122] (by up to 3 dB [124]). Even when no scanning is performed, the scanner room can be a noisy place, with the cryogen pump as the main source of background noise. Background noise levels of 45-71 dB(A) [120] and even 78 dB(A) [126] and 80 dB(C) [125] have been reported.

In order to protect human subjects from the dangerously high sound levels during EPI scanning, protective ear defenders and / or ear plugs are commonly used. Depending on how well they are used, ear plugs attenuate the acoustic noise levels by about 10-30 dB [127] to 30-35 dB (Ravicz, according to [128]).

3.5 Influence of Gradient Acoustic Noise on the Auditory System

The acoustic noise of the MR scanner can be expected to result in a reduced dynamic range of auditory BOLD responses and in acoustic masking of experimental stimuli [128]. Auditory activation by scanner-generated noise was demonstrated by several groups [129–133]. Scarff et al. [134] showed that the BOLD response is attenuated for pure tone stimuli close to the scanner's acoustic resonance frequencies compared to tones with frequencies

outside the scanner noise spectrum. As already mentioned in section 2.2.2, Talavage and Edmister [90] as well as Langers et al. [91] were able to show that experimental stimuli and the scanner acoustic noise do not add up linearly, which means that the BOLD response measured in a conventional fMRI experiment is different from what the response to the same stimulus would be in absence of scanner noise.

3.6 Reduction of Acoustic Noise in MRI

In the past, several approaches have been taken to reduce the influence of scanner acoustic noise on the activation in the auditory cortex. The most obvious strategies are the acoustical damping and / or optimization of the gradient system and ear protection such as ear plugs or ear defenders. Both strategies are applied for practically every MR scan performed at a typical site and shall therefore be excluded from the further discussion.

The application of active noise cancellation techniques ("antinoise") has been successfully demonstrated in the context of MR scanning by Goldman et al. [135]. They routinely obtained a sound level reduction in the order of 10 dB. However, this technique has not come into common use, probably mainly because of safety concerns, as slight misadjustments in the feedback circuitry could potentially lead to a sudden (and potentially dangerous) doubling in sound amplitude compared to the unmodified scanner noise.

On the imaging sequence side, various strategies can be used to lower the acoustic noise levels generated during scanning. Because the scanner acoustic noise spectrum is approximately equal to the gradient waveform, convolved with the scanner's acoustic transfer function (see section 3.3), the optimization of gradient switching can lead to very large reductions in acoustic noise levels. For EPI, where the rapidly switched readout gradient is the main source of acoustic noise, simply changing the bandwidth of the readout can have a large effect on the noise levels. Tomasi and Ernst [136], for example, reported a 12 dB reduction in acoustic noise during EPI scanning at 4 T using this method.

A more sophisticated approach based on the same principle is the optimization of gradient ramp shapes. It is based on the fact that typically, vibration frequencies below about 300 Hz are very efficiently damped by commercial gradient coil setups (see figure 3.1), so that band-limited "soft" gradient waveforms can greatly reduce sound levels. The use of sinusoidally shaped gradient ramps for both spin-echo and gradient echo sequences has been pioneered by Hennel et al. [137]. It can also be applied to faster imaging sequences such as turbo spin echo and FLASH [138] and spiral imaging [139]. In those cases, where rapid gradient switching is desired to maintain good image quality and scan time efficiency, compromises have to be made with regard to the noise reduction obtainable. The application of

such "soft" gradient shapes to auditory fMRI has been demonstrated by Loenneker et al. [140]. Their intrinsically lower scan time efficiency can be partly compensated by using simultaneous multislice excitation (SIMEX) pulses[140] or parallel imaging techniques [141].

Finally, and still based on a similar strategy, imaging sequences with a reduced number of gradient pulses such as BURST [142] can been used. This approach will be separately discussed in section 6 of my thesis.

3.7 Sparse Sampling

The idea to temporally separate the (auditory) stimulus presentation from the data acquisition by taking advantage of the delay of the BOLD response, was pioneered in two ISMRM abstracts by Bilecen et al. [143] and Scheffler [129] in 1996 and 1997, respectively. In both abstracts, they acquired single volumes of image data following auditory stimulation (or rest), and then in a 10-13 s pause allowed the BOLD response to return to baseline. In a series of papers from the same group, the principle was worked out in its full generality. Bilecen et al. [130], similar to the conference abstract, directly measured an EPI-like gradient sound generated by the MR scanner using this technique. In a second paper [112], they found early evidence for tonotopic mapping in the human auditory cortex using above scheme. Scheffler et al. [144] measured the BOLD response to acoustic stimulation in monaurally deaf patients compared to a healthy control group.

The method became quite popular in the following years, with one of the few papers based on above works published by Eden et al. [145] in 1999. In his "behavior interleaved gradients" technique, he used a 4 s EPI acquisition interleaved with 8 s compared to a time-shifted but otherwise identical scheme and a continuous (conventional) acquisition scheme. "New" methods equivalent to this technique came form a number of groups in the same year. Edmister et al. [128] simply compared fMRI using two different EPI multislice acquisition schemes, one acquiring all slices at the beginning (or end) of a TR, the other distributing the slices equally over the TR. The first technique, termed "clustered volume acquisition" was shown to yield more activated pixels and more percent signal change in those voxels. Talavage et al. [131] measured the auditory cortex activation in response to EPI gradient noise (an EPI sequence without RF pulses) using a similar scheme. For them, the main focus was on the question whether, by adjusting the timing to suitable values, the clustered acquisition could be used to get images unaffected by the scanner noise. They concluded that by using a "sufficiently long" TR and an acquisitions time of no more than 2 s, this was the case. Hall et al. [146], who coined the term "sparse temporal sampling" for the technique, referred to the technique by Talavage but extended it by adjusting the timing so that the hemodynamic response to the

stimulus was expected to be at its maximum during the data acquisition window. They acquired single volumes of eight slices using 3 T gradient echo EPI in just 0.5 s with a TR of 14 s. Also, they varied the stimulus timing to acquire a full timecourse of the evoked BOLD response. Two other noteworthy papers were by Belin et al. [147], who extended the work of Edminster to "event-related" fMRI and Bandettini et al. [132], who measured the activation pattern of a fMRI gradient sound (without RF pulses) by subtraction (gradient-silence), implicitly corrected for the T_1 dependent saturation during the multi-volume datasets they acquired. To avoid such T_1 effects in multi-volume sparse sampling designs, continued slice-selective excitation pulses during the silent periods can be used, with the slice selection gradients ideally switched at a lower slew rate than normal to make them (almost) inaudible [148].

Where it is used, the technique is nowadays most often cited with reference to the paper by Hall et al. [146]. It continues to be re-invented, so that in 2003, Yetkin et al. [149], building on Yang et al. [150]'s "first implementation of an event-related silent fMRI sequence", was still able to publish a study with the aim "to evaluate the utilization of a new silent fMRI design in the assessment of the auditory cortex activation" (using a technique equivalent to the above). On the other hand, the sparse sampling strategy has found numerous fruitful applications in auditory neuroscience, with Formisano et al. [100]'s conclusive demonstration of tonotopic mapping in the human auditory cortex arguably the most important one.

3.8 Continuous EPI: Previous Work

The continuous-sound EPI sequence (or Continuous EPI for short), was first proposed in a conference abstract by Scheffler and Seifritz [151]. It builds on the finding that continuous sounds (or noise) evoke a highly phasic BOLD response in the auditory system (see section 2.3.5) with only a very weak sustained component. In contrast to that, the acoustic gradient noise of a typical EPI fMRI scan is dominated by the readout gradient switching (compare section 3.3), which is repeated at a rate determined by the acquisition time for one slice, about 10 Hz for a typical 1.5 T scan using an echo time of 50 ms. As discussed in section 2.3.5, repetition rates of this order result in particularly salient stimulation of the auditory system, with a largely sustained BOLD response to that stimulus. By re-arranging the EPI gradient pattern to a quasi-continuous waveform (see figure 3.2), Scheffler and Seifritz [151] were able to reduce the spurious auditory activation by the gradient acoustic noise significantly, thereby increasing the sensitivity (and dynamic range) of the sequence for experimental auditory stimuli.

In a full paper from the same group [152], the properties of this sequence were studied on a great number of auditory stimuli. A first experiment

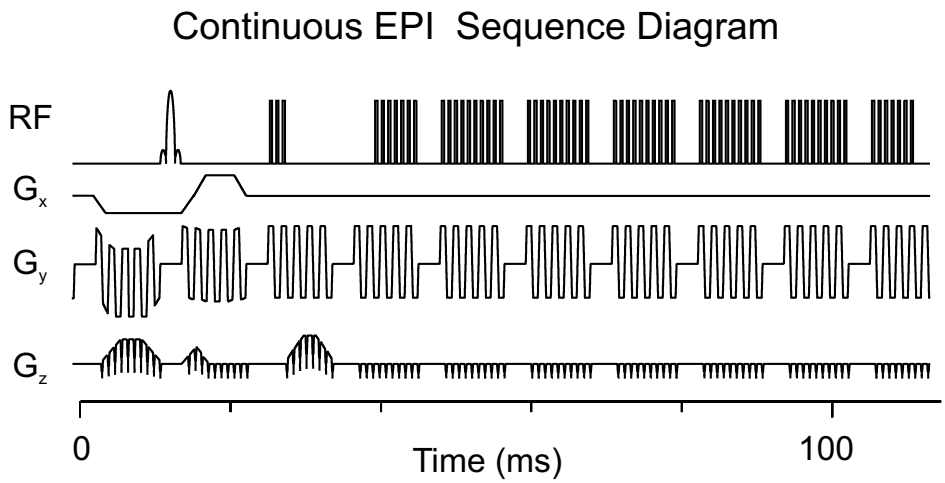

Figure 3.2: Sequence timing diagram for the Continuous EPI sequence as implemented by Seifritz and Scheffler (reproduced from Seifritz et al. [152]

showed that recorded scanner noise of conventional EPI yielded a significantly greater BOLD response than that of Continuous EPI (figure 3.3, measured using a sparse sampling task). Further, comparing the two sequences in both an auditory and a visual task, Seifritz et al. [152] were able to show that the evoked BOLD response was significantly larger using the Continuous EPI in the auditory task but equal to that using conventional EPI in the visual task (figure 3.4). This strongly improved sensitivity of Continuous EPI held for a large number of auditory stimuli (figure 3.5), in addition to the comparisons of modulation depth, bandwidth and spectral frequency shown in figure 3.5, orchestral music and an event-related paradigm showed similar gains in sensitivity. Finally, the measurement of tonotopic frequency gradients was demonstrated to be possible with Continuous EPI at 1.5 T while the same paradigm and data analysis procedure did not yield intelligible results for the data acquired using conventional EPI (not shown here).

In the time since its inception, the Continuous EPI sequence has been applied to a (non-auditory) working memory task by Haller et al. [153], who found that small differences can be observed in the activation pattern of an n-back task that can be attributed to increased attentional demands in the presence of pulsed EPI noise.

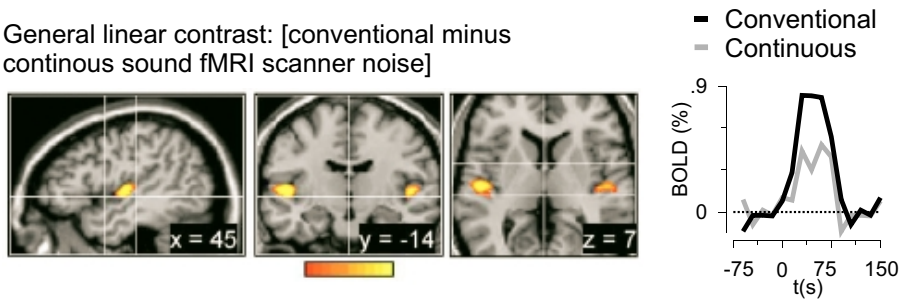

Figure 3.3: Auditory response to conventional EPI and Continuous EPI recorded scanner noise, measured with a sparse sampling paradigm. (reproduced from Seifritz et al. [152]

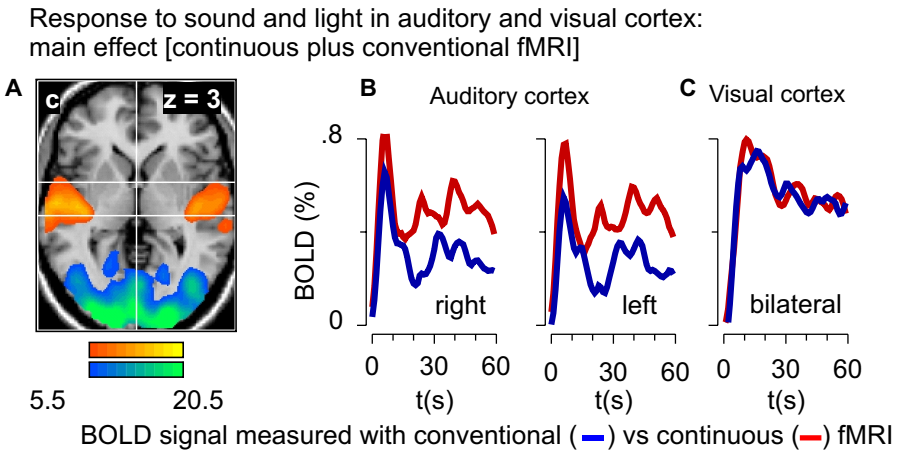

Figure 3.4: Sensitivity of conventional and Continuous EPI compared in a visual and an auditory stimulation experiment. The auditory stimulus was a 50% duty-cycle 5 Hz pulsed 1 kHz sine tone of 90 dB SPL, the visual a 5 Hz flickering LED array, both in a 60 s on – 60 s off block design. (reproduced from Seifritz et al. [152]

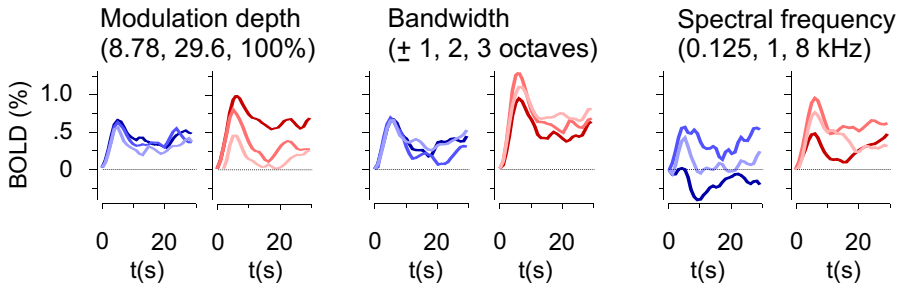

Figure 3.5: BOLD timecourses for conventional EPI (blue) compared to Continuous EPI (red) for different auditory stimuli. All auditory stimuli were pulsed at 5 Hz with 50% duty cycle, presented at 90 dB SPL and measured using a (30 s on−30 s off) block design. Modulation depth stimuli were 1 kHz sine tones with AM depths yielding contrasts of 100, 29.6 and 8.78%. Bandwidth stimuli were bandpass white noise with graded bandwidth of ±1, ±2 and ±3 octaves. Spectral frequency stimuli were sine tones graded in spectral frequency yielding pitches of 0.125, 1 and 8 kHz. (reproduced from Seifritz et al. [152]

Chapter 4

Implementation of Continuous EPI

4.1 Overview

In the course of this work, the Continuous EPI sequence was designed, implemented and tested on five different clinical scanner systems ranging from 1.5 T to 7 T with five different software versions. The intricacies of porting an MR sequence to different scanner software versions (such as the necessity to re-program the otherwise simple superposition of two gradient shapes on the same gradient axis as a single arbitrary shape gradient due to a software bug on one system) shall not be further mentioned. Apart from such complications, the implementation of an imaging sequence from scratch gave rise to a number of questions and necessitated design decisions that shall be described in this chapter. It focuses on the principles and questions that were considered in the implementation state and leaves the characterization of the imaging properties and the results of the fMRI experiments using this sequence to the next chapter.

4.2 Continuous Sound

In this section, it is examined how the gradient sound of an EPI sequence can be modified such as to be perceived as continuous. It shall be assumed that this "continuous sound" property can be defined based on the subjectively perceived characteristic of the noise. The disadvantage of this physiologically motivated definition (based on the processing in the human auditory system) is that it is difficult to quantify. Also the correctness of this assumption can be evaluated only retrospectively, based on fMRI data.

An immediately measurable quantity such as the frequency spectrum or the temporal variation of the frequency spectra over short time windows would be an attractive alternative, but also has disadvantages. The hu-

man auditory is very sensitive to small changes in a repeated sound pattern which may have very little effect on low-frequency contributions to the sound spectrum, such as short gaps in a broadband noise stimulus. Conversely, the perception of isolated sound-events can be masked by other events, which means that sound events that do modify the frequency spectrum might go unnoticed in the perceived sound as heard by human subjects [154]. For these reasons, the present work is based on the above hypothesis that the subjectively perceived sound characteristic is the relevant measure for the effect this sound has on the BOLD response in the auditory cortex.

The perception of amplitude modulated acoustic stimuli depends strongly on the modulation frequency. If a sine-tone of 1 kHz is modulated at a rate lower than about 20 Hz, the increasing and decreasing loudness of the stimulus is perceived. If the modulation rate is between 20 and about 150 Hz, the stimulus is perceived as continuous with a "roughness" depending on the modulation frequency. Above 150 Hz, the stimulus is increasingly perceived as a combination of three different tones (all according to [155]). The transition between these different modes of perceiving amplitude modulated sounds is gradual and cannot be fixed to specific modulation frequency.

4.3 Methods to Achieve Continuous Sound

The fundamental principle used in making the sound of an EPI sequence continuous is the elimination or acoustic masking of all gradient shapes that correspond to amplitude modulation rates below about 30 Hz. To this end, gradients of large magnitude are repeated periodically with a repetition rate above 30 Hz. Smaller gradients may also be acoustically masked by lowering their slew rates.

The alternating readout gradients are the most noticeable component in the sound of a typical EPI sequence. When the readout pulse train is repeated for multiple slices or acquisitions, pulsation is inevitably introduced into its acoustic noise by the requirement that no gradients in read direction can be active during RF excitation. Continuous sound for the readout gradients is therefore achieved by breaking the EPI readout train into several smaller blocks that form an almost periodic gradient pattern. In-between these blocks, a gradient-free interval of the same duration as the one required during RF excitation is repeated, as shown in figure 4.1.

Taking only the gradients on the x axis (readout direction) into consideration, this already forms an almost periodic pattern. Only the dephasing gradient at the beginning of the readout train breaks this symmetry. However, when it is switched with the same slew rate as the full readout gradients, the imperfection in the periodicity of the sound perceived only lightly (figure 4.2a). Still, the effect can be further reduced by ramping it up even more slowly and masking it by superposition with additional readout

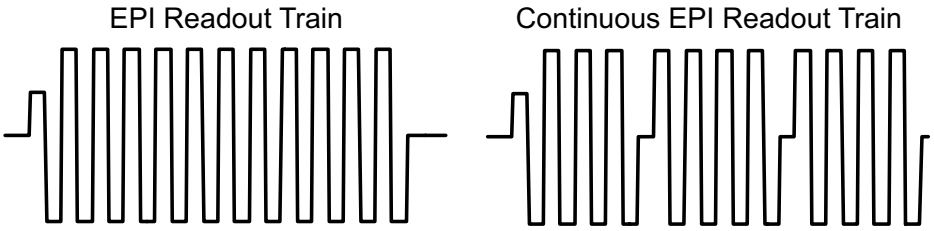

Figure 4.1: Elimination of pulsating acoustic noise by breaking the readout train into quasi-periodic blocks of readout gradients.

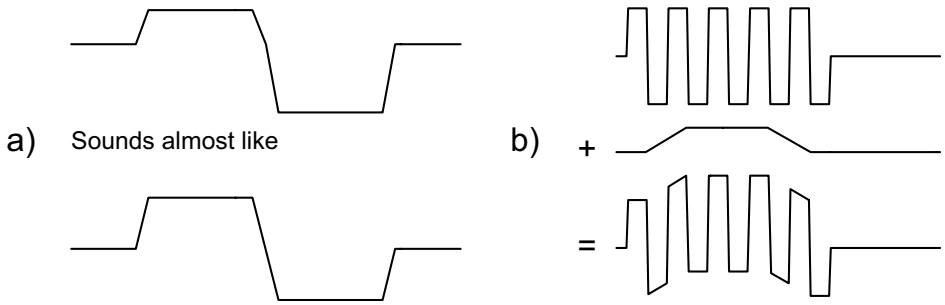

Figure 4.2: Techniques to acoustically mask non-periodic gradient forms: (a) Masking gradients by superposition with balanced pairs of gradients (b) Substitution of an unbalanced gradient pair with a balanced pair or vice versa.

gradients, as demonstrated in figure 4.2b. While at the beginning, the first approach was taken (up to the first fMRI experiment of section 5.3), the later versions use the second approach.

As a next step, we consider the gradients in the z (slice) direction. For slice-selective RF excitation, a slice-select gradient and a subsequent refocusing gradient are needed. The shorter the duration of the RF pulse, the larger the amplitude of the corresponding slice-select gradient for the same slice thickness. Several strategies can be used to form a z-gradient pattern which does not disrupt the perceived periodicity of the gradient sound. One approach is to select a relatively long RF pulse (e.g. 2.5 ms duration) and chose long ramp times (i.e. a low slew rate) compared to the readout gradients which masks the non-periodic slice-select gradients with the much louder read-gradients. This is the technique used in the original Continuous EPI sequence by Scheffler and Seifritz [151]. However, this also increases the size of the refocusing gradient. Taken together, this approach sacrifices quite a lot of time before the center of k-space is read out and thus not only reduces the scan time efficiency of the sequence but also increasing the minimal echo time that can be used.

A different, more time-efficient approach is to use a short RF pulse (e.g.

0.5 to 1 ms) and higher slew rates for the slice-select and refocusing gradients and to make them quasi-periodic by repeating balanced pairs of z-gradients with the same total moment and equal slew-rate during the x-gradient-free intervals (compare figure 4.2a). Again the pulsation of the sequence sound can be perceived lightly, but is normally well masked by the much louder readout gradients. The addition of balanced z gradient pairs makes the sequence slightly more susceptible to flow and motion artifacts (and diffusion) but does not lower image quality noticeably under typical conditions. When water selective excitation is selected (binomial 1-1 pulses on alternating polarity z gradients, see section 4.5), the repetition of balanced pairs of gradients on the z axis is even more natural. In this case (as for the sequence shown in figure 4.3), only the refocusing pulse after the slice select gradients has to be masked using a suitably low slew rate.

Finally, the blipped gradients in the y (or phase encoding) direction are repeated with every gradient in read direction, wherever possible (also see figure 4.3). To balance the additional blips as well as to pre-phase the phase encoding, long, very low slew rate pulses overlaid with blips are used. Only the three navigator echoes are not phase-encoded and therefore do not tolerate phase-blips in-between. For typical settings, these missing phase-encoding blips are acoustically masked by the gradients in slice and read direction.

The resulting gradient waveforms for typical settings as used in fMRI experiments at 1.5 T is shown in figure 4.3. Here, water excitation pulses are used, and a period of three additional readout gradients introduced to mask the rephasing gradient following the excitation pulses as well as for the phase encoding pre-phasing gradient.

4.4 Sine-Shaped Gradient Ramps and Frequency Tuning

As described in section 3.6, "soft" gradient ramps can lead to a significant reduction in acoustic noise levels [137]. For rapid sequences such as EPI (and also Continuous EPI), where gradient switching is intrinsically fast and very little time can be sacrificed for longer gradient ramps, this method alone is normally not sufficient to suppress frequencies outside the acoustically well damped range of about 0-300 Hz (compare figure 3.1). Rather, typically used readout bandwidths of 750-2000 Hz per pixel lead to gradient switching frequencies no more than a factor two lower (350-1000 Hz), which may well include the scanner's own acoustic resonance frequencies (at which scanning is loudest and may even be forbidden to prevent unnecessary helium boil-off). Therefore for EPI sequences, the effect of tuning the readout bandwidth so that the readout gradient switching frequency falls between the peak resonance frequencies of the scanner [136] is usually much more efficient at

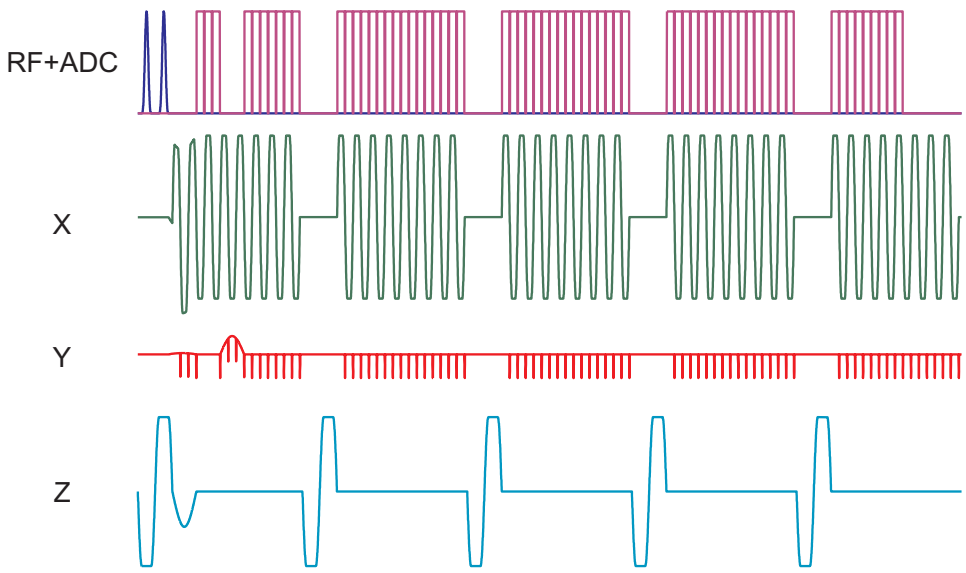

Figure 4.3: Continuous EPI Sequence Timing Diagram (typical settings for a 64×64 matrix at 1.5 T)

reducing the generated acoustic noise.

Still, in the present implementation of Continuous EPI, sinusoidal gradient ramps were used for all gradients in the sequence with the exception of the phase encoding blips (where modified ramp shapes would have been difficult because of software limitations). The reasoning behind this decision was that the above tuning of the readout bandwidth might be much more effective if higher-order harmonics due to trapezoidal gradient waveshapes were suppressed. Of course, effective tuning of the fundamental gradient sound frequency necessitates the other timing parameters of the sequence to be flexible enough to accommodate changes in the readout bandwidth over a broad range. This flexibility was therefore one of the main design criteria in the implementation process, but was not always trivial to fulfill because additionally, the continuity of the generated sound had to be ensured at the same time.

For the readout gradients, data is acquired already when the read gradient is still ramped up. This "ramp sampling" technique, which is used in all current commercial EPI sequences as well, makes it necessary to correct for the non-equidistant k-space sampling by a one-dimensional regridding procedure. To fully sample the field of view, the total gradient moment during the readout has to be equal to that used with a constant gradient. In the current implementation, the fraction of time spent on the ramps relative to the readout gradient's total duration is made selectable to the user as a custom sequence parameter. On the standard resolution phantom, it was found that even to for fully sinusoidal readout gradients, no noticeable

degradation of image quality could be observed.

4.5 Fat Suppression Strategy

In EPI based fMRI, the suppression of the fat signal is an important issue, because the low readout bandwidth in phase encoding direction leads to a very noticeable chemical shift artifact for fatty tissue. The chemical shift for fat with respect to the water resonance frequency is about 3.5 ppm [156], which results in an off-resonance frequency of about 214 Hz at 1.5 T. In images of the brain, this is apparent as a bright contour of the head (resulting from the subcutaneous fat), which is shifted with respect to the rest of the image by several pixels in phase encoding direction. This observed "fat shift" has the result that the fat signal can sometimes be shifted into regions of interest, where the bright fat signal can distort BOLD signal change measurements and additionally makes the images more sensitive to motion artifacts.

The most common fat suppression strategy in EPI is the saturation of fat spins by a frequency-selective saturation pulse. To achieve a relatively sharp frequency profile, long pulses of about 10 ms are usually applied with strong spoiler gradients to ensure that any on-resonant transverse magnetization from that pulse is fully dephased before the imaging sequence starts. It is because of the length of this saturation pulse and the necessity for strong spoiling gradients that this fat suppression technique is not compatible with Continuous EPI. The gradient-free interval during the application of the fat saturation pulse would need to be repeated at a suitably high frequency throughout the sequence, leading to a very inefficient use of scan-time, and the strong gradient pulses would be very difficult to mask using the techniques described above.

However, composite spectral-spatial excitation pulses [157], such as "binomial" pulses (as proposed for the use in EPI by Schick et al. [156]) can be incorporated into a quasi-continuous gradient pattern. A binomial pulse designed to excite on-resonant spins by a total flip angle α is given by a series of n on-resonant pulses regularly spaced at a time interval τ with flip angles

$$q_{n,m} = \binom{n}{m} \frac{\alpha}{m} = \frac{n!\,\alpha}{(n-m)!\,m!\,m}$$

which result in a frequency response $S_n(f) = \cos^n(\pi f \tau)$ where f is the (off-resonance) frequency[158]. The first null of this function is at $1/(2\tau)$, giving a pulse spacing of about 2.34 ms for an off-resonance of 214 Hz to be suppressed at 1.5 T. The workings of binomial spectrally selective excitation can easily be illustrated with rotating-frame vectors for a 1-1 90° excitation pulse (figure 4.4). Alternatively, the frequency selectivity of a

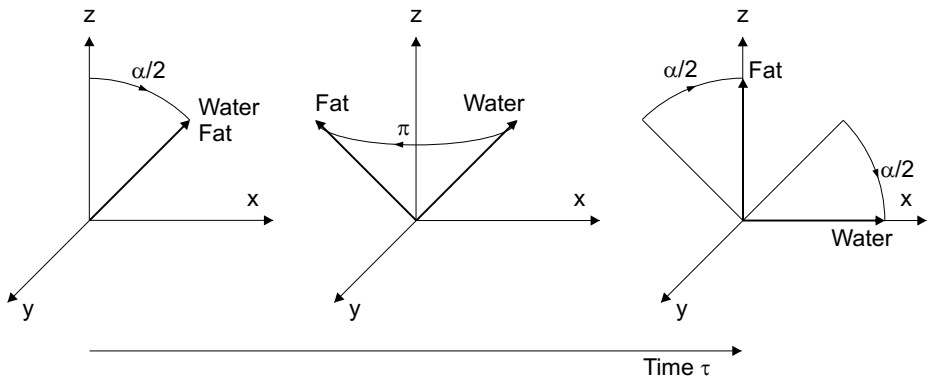

Figure 4.4: Illustration of the working principle of a water selective binomial 1-1 excitation pulse. The time τ is chosen so that the off-resonant fat spins acquire a phase of π during time τ.

binomial pulse train can be understood to result from its similarity with a DANTE sequence, where the slice-selective sub-pulses give rise to the spatial selectivity and the different amplitudes of the sub-pulses suppresses the aliasing of the frequency profile [159]. According to Schick et al. [156], the spatial-spectral fat suppression method using binomial pulses is superior to the more conventional spectral saturation technique in terms of its greater B_1 field insensitivity and the lesser specific absorption rates (SAR) associated with these pulses.

In the context of Continuous EPI, the scan-time efficiency as well as the need to acoustically mask (or repeat) all gradients makes the use of slice-select gradients with alternating polarity (as proposed by Zur [160]) highly attractive. Also, the use of 1-1 pulses instead of higher order pulses, which would have more favorable frequency selectivity, seemed advantageous. For such a pulse, the slice select gradient is already balanced and can therefore be periodically repeated without any modifications, and only the slice rephasing gradient has to be masked by using a long, low slew rate gradient pulse (compare figure 4.3). In spite of these advantages, when using two slice-select gradients with opposite polarity, any imperfection in gradient waveform gives rise to a specific artifact that causes a sinusoidal intensity modulation over the slices in a multi-slice experiment, and can be corrected only on an empirical, system-specific basis, as discussed in section 5.2.1. A possible further optimization strategy, which has not been pursued in the present work, is the use of Shinnar–Le Roux pulse design methods to further improve the frequency and spatial selectivity of the composite pulses [160].

4.6 Advanced imaging methods

The design of Continuous EPI can be naturally extended to advanced imaging concepts such as partial Fourier reconstruction and parallel imaging. Both techniques were successfully implemented in the context of the present work; they have the same benefits and shortcomings for Continuous EPI as for conventional EPI.

The shorter slice acquisition times that can be achieved using these methods can be "invested" into different aspects of sequence performance. On the one hand, the shorter echo time possible with these methods can be used to minimize distortions and signal losses (as suggested, for example, by de Zwart et al. [161] for parallel imaging). On the other hand, the reduced number of readout gradients can be switched more slowly (with lower gradient slew rate) at any given echo time, thereby reducing the acoustic sound levels (here, reductions in SPLs of 11 dB have been shown to be possible using conventional EPI with a SENSE factor of 2 [141]).

Chapter 5

Results: Continuous EPI

5.1 Overview

In this central chapter, the imaging properties of the Continuous EPI sequence and its application to auditory fMRI are discussed. The emphasis lies on the comparison of the Continuous EPI implementation described in the previous chapter to a "matched" conventional EPI sequence. To ensure a fair comparison, the conventional EPI sequence used was also specially implemented, to allow for the use of the exact same fat suppression pulses and sinusoidal readout gradients as in the Continuous EPI sequence. In the following, the term "conventional EPI" refers to that sequence. Much care was also taken in matching the imaging parameters of the two sequences for each comparison. Where not explicitly mentioned, this consisted of adjusting the echo and repetition times, the readout bandwidth, the amount of ramp sampling, the shape of the readout gradient ramps, the excitation pulse timing and shape as well as the geometry, position and ordering of the imaging slices of the conventional EPI to that of the Continuous EPI sequence.

In the first section of this chapter, several aspects of image quality and signal stability of Continuous EPI are compared to the conventional EPI sequence. It also includes the results of acoustic measurements comparing different Continuous EPI variants to conventional EPI. In the following sections, the results of seven auditory fMRI experiments comparing the two sequences are presented. For the fMRI data, I have chosen a chronological order, since each experiment was motivated by the results of the preceding experiment. Consequently, the results of each experiment are discussed separately, with a summary of all experiments and an outlook on possible further research added in a separate section at the end of this chapter.

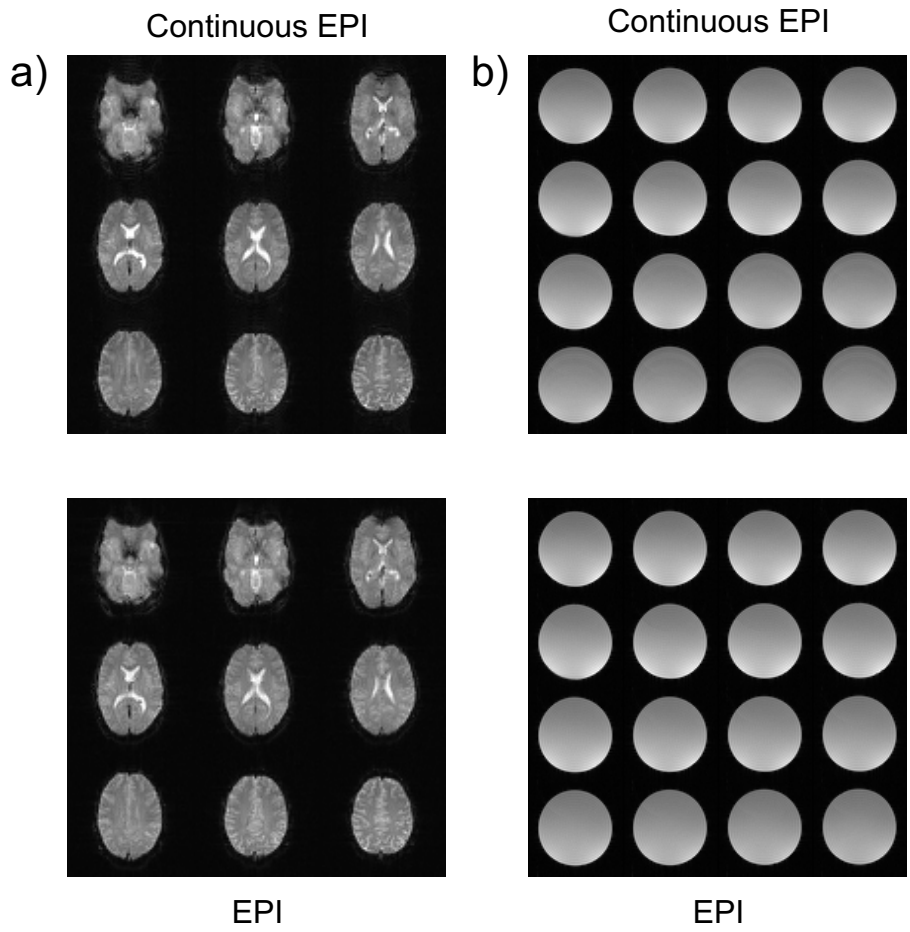

Figure 5.1: Comparison of image quality in Continuous EPI and conventional EPI in (a) nine contiguous slices of a volunteer's brain (b) 16 contiguous slices through a water bottle phantom.

5.2 General Characterization of Continuous EPI

5.2.1 Image Quality

Images acquired with continuous EPI are very similar in image contrast compared to conventional EPI both in vivo and in a standard water bottle phantom, as shown in figure 5.1. The water bottle phantom contained 1.25 g $NiSO_4 \times 6 \cdot H_2O$ and 5 g NaCl per 1 kg H_2O dest. to obtain physiological relaxation times. Image parameters were: **(a)** for the in vivo experiment in figure 5.1a: TE=52 ms, TR=1.0 s, 9 slices of 4 mm thickness, image matrix 64×64, bandwidth 941 Hz/px, FOV=25.2 cm, **(b)** for the phantom experiment in figure 5.1b: TE=55.5 ms, TR=1.78 s, 16 slices of 4 mm thickness, image matrix 64×64, bandwidth 1000 Hz/px, FOV=15 cm.

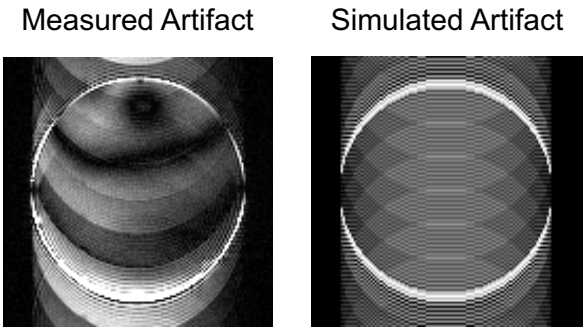

Figure 5.2: Characteristic artifact of Continuous EPI due to the irregular echo spacing in the readout train (T_2^* effect). Left: difference image of Continuous EPI minus EPI for a 128×128 matrix, TE=192 ms, scaled from zero (black) to 1/10 of the mean signal intensity (white) of the mean signal in the conventional EPI image. Right: simulation of a T_2^* signal decay over an irregularly spaced Continuous EPI readout train.

When the echo train becomes longer, or the T_2^* of the tissue shorter, however, the irregular echo spacing leads to a noticeable artifact. When a conventional EPI image with identical parameters is subtracted from a Continuous EPI image, this effect of the irregular echo spacing is seen very clearly, as shown in figure 5.2. This artifact arises because, when the echo train is divided into blocks of equal length, the signal decay due to T_2^* is no longer uniform over the echoes, but has periodic "steps" wherever a gap is introduced between readouts. It is this periodic modulation of an otherwise smooth decay process that leads to a kind of multiple ghosting artifact, as seen in figure 5.2, left. In this figure, the difference image Continuous–conventional EPI is shown for a rather extreme example of a 128×128 image matrix with TE=192 ms, bandwidth 545 Hz/px and 18 blocks of 6 readouts with water excitation pulses on alternating slice selection gradients with a duration of 4.34 ms. The phantom in the image was the same water bottle phantom as used above, with relaxation times of approximately T_1=300 ms and T_2=250 ms. The difference image in figure 5.2 is scaled from zero (black) to 1/10 of the mean signal intensity (white) of the mean signal in the conventional EPI image. This artifact is very similar to a numerical simulation calculating the effect of such a step-wise T_2^* signal decay over the k-space lines (figure 5.2, right). Here, the Fourier transformed image of a white circle on black background was multiplied once with an exponential decay in y-direction and for another with an exponential with additional steps of similar relative weight as in the experiment. The subtraction of the two reconstructed images shows an artifact that is very similar to the one actually measured.

5.2.2 Temporal Signal Stability

Temporal signal stability is a very important issue in fMRI since it effectively determines how sensitive a given sequence is to detect functional activation over an image time-series. The temporal signal stability can also be thought of as the temporal signal to noise ratio (see, for example Triantafyllou et al. [162]). In the development of a new or modified sequence for fMRI, it is therefore crucial to assess temporal stability, as compared to the standard technique.

In the context of the present work, temporal signal stability was compared for image time series of the same length and using the same sequence parameters as in the fMRI experiments. The same water bottle phantom as described in above was used. For a given image time series, the relative standard deviation was calculated for each voxel v as $\mathrm{std}(v(t))/\mathrm{mean}(v(t))$. Since this value is largest for the background, where only noise is present, masking of the phantom or brain was applied using the Matlab `im2bw` function, eroded with a circle of 3 voxel radius as the kernel for the `imerode` function. Also, in order to remove signal drift and to take into consideration only at those aspects of temporal stability that are actually relevant for the detection of functional activation, the same high-pass filter as used in the fMRI analysis (with a cut-off frequency of 1/128 Hz) was applied to the stability time-series. Histograms of the voxel-wise relative standard deviation have been used as measures of the temporal signal stability of fMRI sequences by various authors and have proved useful to compare different fMRI data acquisition techniques [163]. In the present work, the stability histograms computed with this method were found to depend very little on the size of the mask used (i.e. the size of the `imerode` kernel). This because the background and edge voxels usually have a relative standard deviation that is much larger than for the inner voxels and forms a distinct distribution in the histograms.

Figure 5.3 summarizes the stability measurements using this method. The histograms of the voxel-wise relative standard deviation vary markedly between different systems (and field strengths), but are remarkably similar for Continuous EPI and conventional EPI. On the 1.5 T system, sudden signal amplitude changes from one to the next image occurred frequently (and were present in all stability measurement runs with varying amount of relative signal change). These steps, which are probably due to external factors, were largely responsible for the larger temporal variance in the 1.5 T data, compared to 3 T and 7 T. Image parameters were: **(a)** On the 1.5 T Siemens Avanto system: TE=56.6 ms, TR=1054 ms, 9 slices of 5 mm thickness, image matrix 64×64, bandwidth 940 Hz/px, FOV=15 cm, flip angle 65°, water excitation pulse, 5 blocks of 16 readouts for the Continuous EPI sequence. **(b)** On the 3 T Siemens Allegra system: TE=38.6 ms, TR=953.4 ms, 12 slices of 4 mm thickness, image matrix 64×64, bandwidth

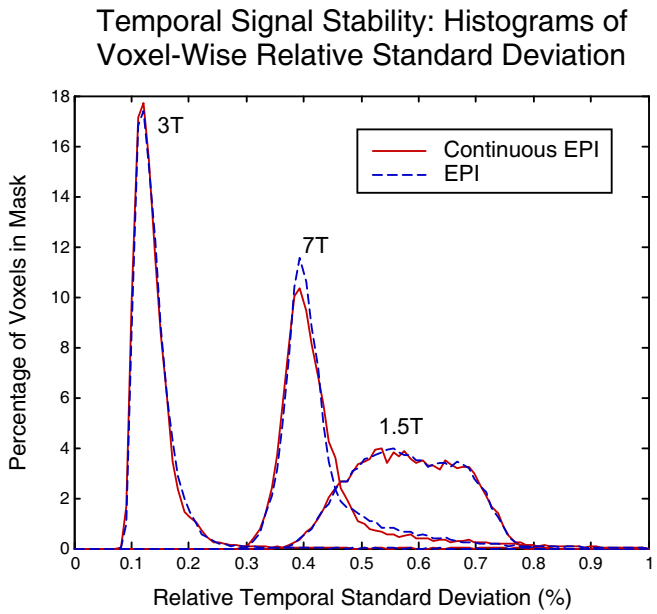

Figure 5.3: Temporal signal stability in a phantom for continuous EPI compared to EPI as measured by histograms of the voxel-wise relative standard deviation.

1302 Hz/px, FOV=22 cm, flip angle 70°, water excitation pulse, 3 blocks of 28 readouts for the Continuous EPI sequence. **(c)** On the 7 T Siemens / Magnex Scientific system (MGH, Boston USA): TE=28.8 ms, TR=1262 ms, 16 slices of 4.2 mm thickness, image matrix 128×128, partial Fourier 6/8, bandwidth 1698 Hz/px, FOV=22 cm, flip angle 60°, water excitation pulse, 4 blocks of 28 readouts for the Continuous EPI sequence.

5.2.3 Spatial Aspects of the Temporal Stability

Naturally, it is also of interest whether the observed distribution of the voxel-wise relative standard deviation (of the previous section) is spatially uniform, as could be expected for a homogeneous phantom. Figure 5.4 shows a comparison of these relative standard deviation maps for the 1.5 T system (for the same data as shown in figure 5.3). Both sequences exhibit a relatively uniform distribution of temporal fluctuations. If no masking were applied, higher values would be observed for voxels very close to the edge of the phantom or near water-air interfaces. The Continuous EPI data show a hint of the multiple ghost like intensity modulation which is inherited from the artifact due to the irregular echo spacing (see section 5.2.1).

Another question that can be asked regarding the spatial characteristics of temporal signal variations is how large the spatial correlation is among the temporal fluctuations of the signal. Such an analysis was proposed by

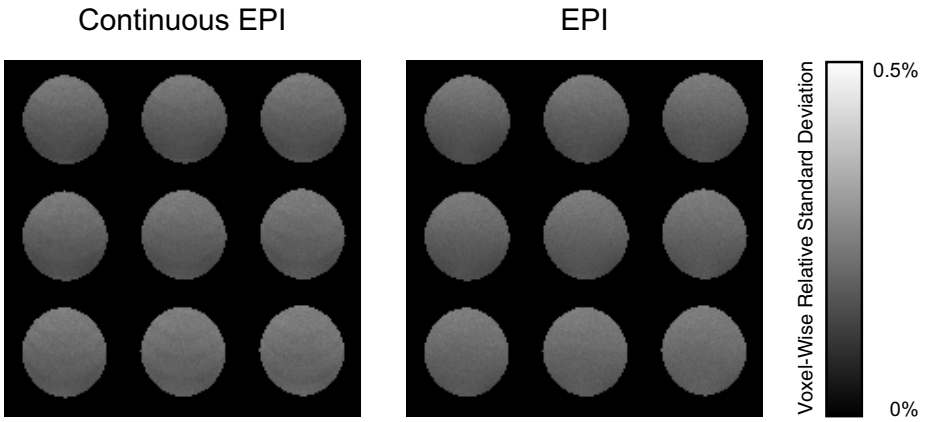

Figure 5.4: Spatial distribution of voxel-wise relative standard deviation for the same 1.5 T dataset used for the histogram in figure 5.3.

Weisskoff [164]. In his method, Weisskoff selected two "relatively large" regions of interest (ROI), one in the middle of the phantom and one in the background (outside the phantom and away from any image artifacts). On each image i, he measured the mean m_i of the image ROI, and the standard deviation s_i of the background ROI and determined theoretical (best) signal to noise ratio SNR_0 as

$$\mathrm{SNR}_0 = \frac{\sum_i m_i}{1.53 \cdot \sum_i s_i}$$

where the factor 1.53 (the factor $1/\sigma_M$ in section 1.3.4) corrects for the different statistics of the background, relative to the image noise distributions. Then, for a series of ROIs of $n \times n$ pixels, the relative fluctuation F_n is defined as

$$F_n = \sqrt{\frac{1}{N-1}\sum_i (m_i^n - \overline{m^n})^2} \;/\; \overline{m^n}\,, \quad \text{where} \quad \overline{m^n} = \frac{1}{N}\sum_{i=1}^{N} m_i^n$$

and m_i^n is the mean of the $n \times n$ ROI of image i. Ideally, in the absence of scanner instabilities, the fluctuation F_n should scale with n as $F_{n,t} = 1/(n\mathrm{SNR}_0)$. Now, the spatial correlations can be visualized by plotting F_n versus n. In such a plot, F_n departs from $F_{n,t}$ for large n and asymptotically approaches a certain value which is characteristic for a given system.

What is not accounted for in the analysis proposed by Weisskoff [164] is the dependence of the results of such an analysis on the selection of a particular ROI, especially when the phantom is not perfectly homogeneous. Therefore, for the analysis shown in figure 5.5, the mean of all possible

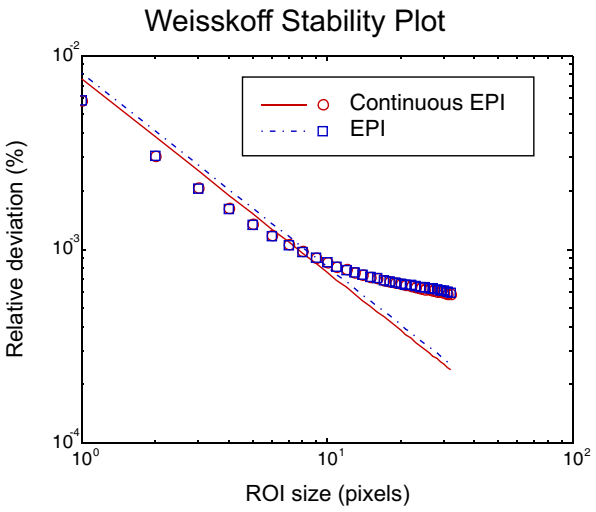

Figure 5.5: Weisskoff stability plot calculated for the 1.5 T stability time series, giving a measure of spatial correlations in the temporal signal fluctuations.

locations of the $n \times n$ ROIs within a 32×32 ROI in the center of the phantom (which was used to determine m_i) was used instead of F_n.

The result of this analysis on the stability data for Continuous and conventional EPI is shown in figure 5.5. Again, the same 1.5 T dataset was used as in the stability histograms of figure 5.3 and de-trended using the above high-pass filter with a cutoff frequency of 1/128 Hz. From this figure it can be concluded that spatial correlations in the temporal fluctuations are equal for Continuous and conventional EPI.

5.2.4 Scan-Time Efficiency of the Sequence

Regardless of the implementation details, the modification of a sequence necessary to obtain a continuous sound pattern will result in a decreased scan-time efficiency. The scan-time efficiency of a sequence can be defined as the total data acquisition time for one slice (i.e. the summed duration of all readouts) divided by the repetition time for that slice. Conventional EPI Sequences, without fat saturation, can achieve very high efficiencies of up to 90% (if TE and TR are set to minimal values given the other parameters). EPI sequences with spectral fat saturation and parameters typically used for fMRI usually have scan-time efficiencies of about 75%. For Continuous EPI, the scan-time efficiency depends strongly on the parameters used, especially on how many readouts are used in each block (a setting that directly affects the acoustic fundamental frequency of the sequence sound). In the current implementation, for parameters as used in the fMRI experiments presented

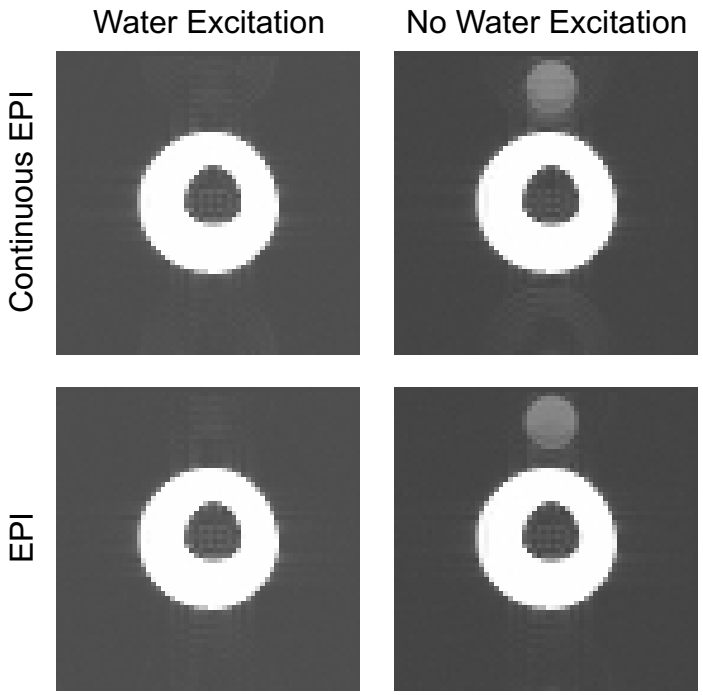

Figure 5.6: Fat suppression using binomial 1-1 water excitation pulses on alternating polarity slice select gradients. Images were acquired on a 3 T system using a water bottle phantom with a smaller tube of oil inserted in the middle.

here, the scan-time efficiency was about 65% without fat signal suppression and around 60% with 1-1 water excitation pulses. For comparison, the scan-time efficiency of the original Continuous EPI implementation by Scheffler and Seifritz [151] was about 45%.

5.2.5 Fat Suppression

The efficiency of binomial 1-1 pulses with alternating polarity slice select gradients (as described in section 4.5) was evaluated for the conventional and Continuous EPI sequences in figure 5.6. The phantom consisted of a water bottle with a smaller tube of sunflower oil inserted in the middle. Note the shift of the fat signal in phase encoding direction by almost half the field of view. These images show that the binomial 1-1 pulses, while not completely eliminating the fat signal, attenuate it very strongly. All images were acquired on a 3 T Siemens Allegra system.

At higher fields, the close spacing of the two sub-pulses can severely limit the maximum achievable gradient amplitude for those pulses. This limitation is particularly acute at 7 T, where the spacing between the two sub-pulses is only 584 µs. Here, the obtainable bandwidth-time product

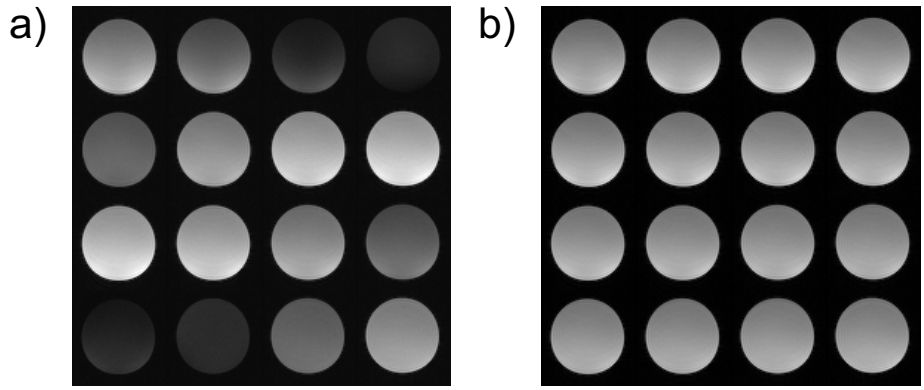

Figure 5.7: (a) Sinusoidal signal modulation over the slices of a multi-slice Continuous EPI scan of a water bottle phantom at maximum slice select gradient amplitude. This artifact results from an imperfect gradient shape in the two opposite polarity slice select gradients and can be corrected (b) by empirically biasing the amplitude of the second gradient lobe, here by −2%.

(BTP) of the RF pulse was limited to about 1.0 even with the very high slew-rate of 80 mT/m on that particular system. At such a low BTP, the pulse shape and with it the slice profile was nearly Gaussian. For ultra-high fields, it would therefore be advisable to consider the implementation of RF pulses on time-varying gradients (e.g. using the Shinnar–Le Roux pulse design method [165]) to replace the simple apodized sinc pulses used here.

Additionally, when large slice-select gradient amplitudes are used, the effect of gradient imperfection (similar to the $N/2$ ghost in EPI) can be observed. In multi-slice images, it leads to a sinusoidal signal modulation over the slices, as demonstrated in figure 5.7. This effect is system specific but, for a given set of measurement parameters, can be corrected empirically by using a selectable bias on the amplitude of the second gradient lobe. For example, the strongly affected 1.5 T image shown in figure 5.7a could be corrected by decreasing the amplitude of the second gradient lobe by −2%, as demonstrated in figure 5.7b.

5.2.6 Acoustic Sound Level Measurement

In the course of this work, several sound recordings were performed. One absolute sound level measurement was conducted in the preparation for fMRI experiment 1 (see section 5.3). For this measurement, the MR compatible condenser microphone of a Brüel and Kjær sound level meter was placed at the side of a spherical water phantom in the scanner head coil and connected to the sound level meter outside the MR cabinet with a long coaxial cable. Four sequences were compared: **(a)** the Continuous EPI sequence with settings as in the fMRI experiment, **(b)** a matched EPI sequence used

for comparison in the fMRI experiment, **(c)** a product EPI sequence without spectral fat saturation and **(d)** the original Continuous EPI implementation by Scheffler and Seifritz [151]. Sequence parameters were as follows: **(a)** for the Continuous EPI sequence: TE=58.5 ms, TR=2048 ms, 16 slices of 5 mm thickness, image matrix 64×64, bandwidth 930 Hz/px, FOV=23 cm, flip angle 90°, fully sinusoidal readout gradients, no fat suppression, 8 blocks of 10 readouts, fundamental frequency of the sequence sound 61.9 Hz. **(b)** for the EPI sequence: TE=58.5 ms, TR=2048 ms, 16 slices of 5 mm thickness, image matrix 64×64, bandwidth 930 Hz/px, FOV=23 cm, flip angle 90°, fully sinusoidal readout gradients, no fat suppression. **(c)** for the product EPI sequence: TE=59 ms, TR=2050 ms, 16 slices of 5 mm thickness, image matrix 64×64, bandwidth 930 Hz/px, FOV=23 cm, flip angle 90°, trapezoidal readout gradients, no fat suppression. **(d)** for the Continuous EPI sequence, Scheffler: TE=60.83 ms, TR=1770 ms, 16 slices of 5 mm thickness, image matrix 64×64, bandwidth 1280 Hz/px, FOV=23 cm, flip angle 90°, trapezoidal readout gradients, no fat suppression, 10 blocks of 10 readouts, fundamental frequency of the sequence sound 90.4 Hz. The sound level measurements are summarized in the following table:

	Sequence Type	Sound Level
(a)	Continuous EPI	86.2 dBA
(b)	EPI	90.0 dBA
(c)	Product EPI	91.7 dBA
(d)	Continuous EPI, Scheffler	92.0 dBA

The effect of sinusoidal readout gradients in both the conventional and Continuous EPI sequence, as well as the acoustically relatively well damped readout frequency due to the lower bandwidth result in an about 2 dB lower sound level for these two sequences. The larger difference between Continuous EPI and EPI of 4 dB is due to the fact that in the Continuous EPI sequence, all gradients (with the exception of the phase encoding blips) were sinusoidal and used a slew rate smaller or equal to that of the readout gradient, while the conventional EPI sequence used trapezoidal slice select and phase encoding gradients at the highest slew rates possible.

5.2.7 Acoustic Sound Frequency Spectra

To demonstrate the effect of (quasi-)continuous gradient switching on the scanner sound, sound recordings were performed for conventional and Continuous EPI sequences for the same sequence parameters as in the signal stability measurements on the 3T system (compare section 5.2.2): TE=38.6 ms, TR=953.4 ms, 12 slices of 4 mm thickness, image matrix 64×64, bandwidth 1302 Hz/px, FOV=22 cm, flip angle 70°, water excitation pulse, 3 blocks of 28 readouts for the Continuous EPI sequence.

In addition, the effect of the sinusoidal gradients was evaluated by varying the ramp fraction (rfr), defined as the time spent to ramp up and down the gradient divided by the gradient's total duration. Setting this value to 1 means that the gradient is fully sinusoidal while, for example, a value of 0.5 corresponds to a gradient which is constant for half its duration. For all sequences, the scanner's acoustic noise was recorded using the headset microphone while the headset was put over a water-filled sphere phantom, with a recording time of 2 min for each measurement.

The recorded sound waveforms were normalized to the same power level (mean of the squared amplitudes) and the absolute value of the waveform low pass filtered with a cut-off frequency of 1 kHz to demodulate the alternating readout gradient signal. The entire 2 min sample was then divided into 10 s blocks, for which power spectra were calculated and then averaged to obtain a mean power spectrum for each sequence sound recording. Figure 5.8 shows 1 s samples of the sound waveform and the mean power spectra for the frequency range of 0-100 Hz. The sound levels at the first six peak frequencies of the conventional EPI sequence, corresponding to the first six harmonics of the slice repetition rate of 12.8 Hz are shown as dotted lines in figure 5.8. The attenuation of sound levels at those frequencies, relative to the sound level of EPI at the Continuous EPI fundamental frequency of 37.8 Hz are listed in the following table.

Seq	rfr	Attenuation of the peak at ... (dB)					
		12.6 Hz	25.2 Hz	37.8 Hz	50.3 Hz	62.9 Hz	75.5 Hz
EPI	0.5	6.9	5.7	0	-19.5	-5.5	-4.3
Cont. EPI	1.0	-22.2	-23.4	0	-27.2	-22.2	-13.0
Cont. EPI	0.2	-36.1	-31.2	-23.6	-39.3	-31.6	-20.1
Cont. EPI	0.5	-28.8	-36.9	-14.6	-32.6	-29.6	-17.4

For the conventional EPI sequence, the pulsation at the slice repetition frequency of 12.6 Hz is 6.9 dB louder than its third harmonic at 37.8 Hz. For Continuous EPI, on the other hand, the pulsation at the slice repetition frequency is attenuated by -22.2 dB for rfr=1, -14.2 dB for rfr=0.5 and -12.5 dB for rfr=0.2, relative to their respective sound levels at the fundamental frequency of 37.8 Hz. From these data, it can be concluded that fully sinusoidal readout gradients are really beneficial to obtain a continuous scanner sound with good acoustic masking of the pulsation at the slice repetition rate.

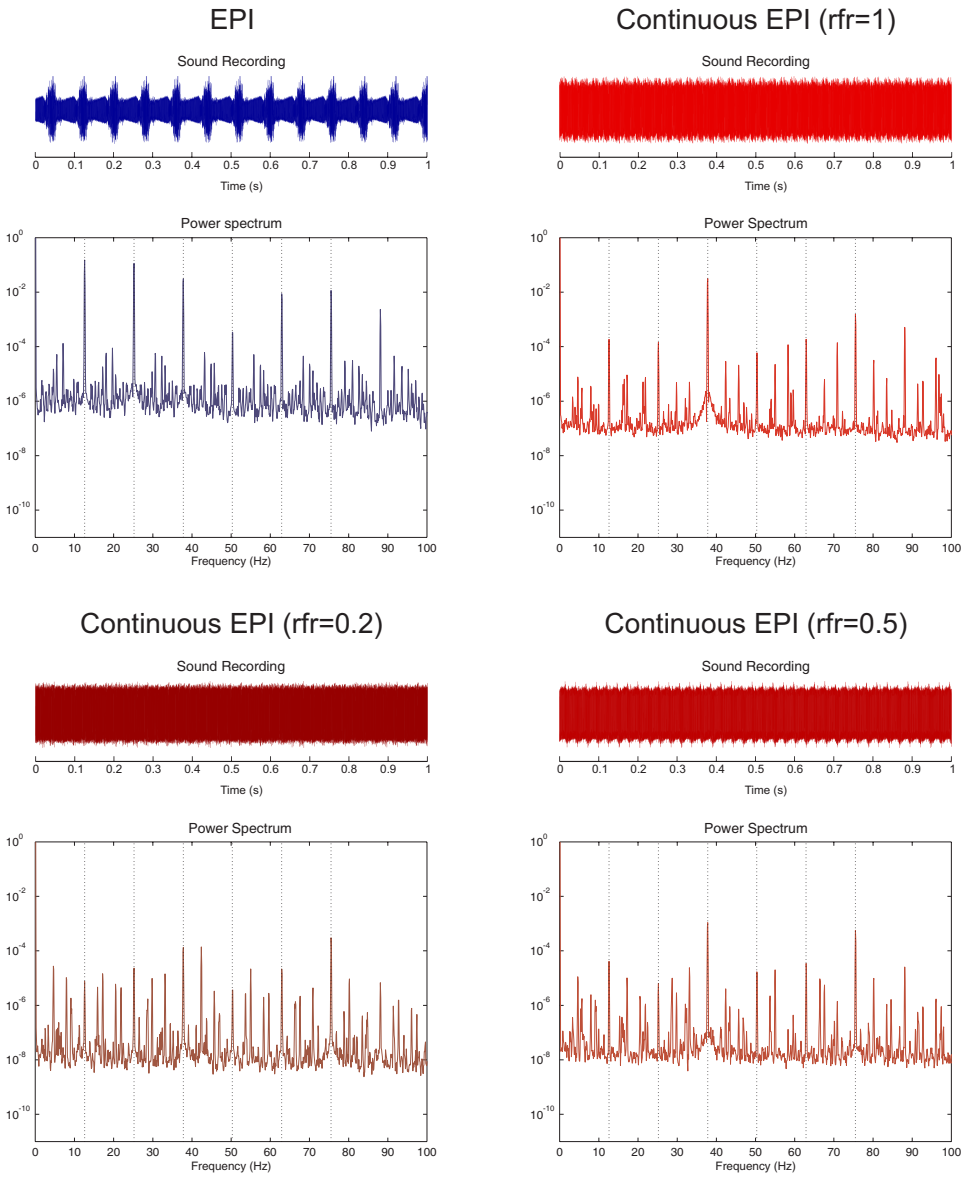

Figure 5.8: Recorded sound waveforms and acoustic power spectra for EPI and three (otherwise equal) Continuous EPI sequences with different readout gradient ramp shape. The "ramp fraction" (rfr) is defined as the time of the (sinusoidal) ramp up and ramp down periods of the gradient divided by the total gradient duration.

5.3 fMRI Experiment 1: Pulsed Tones

5.3.1 Experiment Design and Stimulus

The aim of this first fMRI experiment was to obtain a proof of concept for the newly implemented Continuous EPI sequence. Therefore, as very simple stimulation paradigm was chosen, consisting of a 20 s epoch block design and a 1 kHz sine tone stimulus pulsed at 5 Hz. The beginning and end of each tone (of 100 ms duration) was modulated with a sine squared function, thus giving smoothed ramps of 10 ms duration. The stimulus waveform was generated in Matlab and recorded on a CD, which was manually synchronized with the start of the imaging sequence. The stimulation paradigm consisted of 7 cycles plus an additional baseline period at the beginning for a total time of 5 min. The stimulus was delivered using the scanner's default headphone system, consisting of a piezoelectric transducer connected to the headphones by an air-filled tube. The sound level was adjusted individually to be perceived as very loud but not painful.

Four volunteers were recruited, all male, age 33.1 ± 3.9 years (mean $\pm$ standard deviation), three right handed, one left handed. Volunteers were instructed to relax, keep their eyes open and listen attentively to the stimuli. For each subject, a sagittal localizer was first acquired, followed by four functional runs which alternated between conventional EPI and Continuous EPI. Two subjects were scanned with conventional EPI in the first run, two with Continuous EPI to minimize session effects. After the functional runs, a T_1 weighted MPRage (magnetization prepared rapid gradient echo [166]) dataset with 1 mm^3 isotropic resolution was acquired.

5.3.2 Imaging Sequence

This experiment was conducted on a 1.5 T Siemens Sonata machine using the standard birdcage head coil.

At this stage, fat suppression was not implemented yet, but the slice select gradients were still repeated, using a balanced pair of gradients with equal average gradient moment instead of the (non-balanced) slice selection gradient and rewinder pair. The timing diagram for the Continuous EPI sequence used in this experiment is shown in figure 5.9. The EPI sequence used for comparison was a self implemented EPI sequence with matched TR, TE, bandwidth and readout gradient wave-shape (i.e. also fully sinusoidal).

Sequence parameters were: **(a)** for the Continuous EPI: TE=58.5 ms, TR=2048 ms, 16 slices of 5 mm thickness, image matrix 64×64, bandwidth 930 Hz/px, FOV=23 cm, flip angle 90°, fully sinusoidal readout gradients, no fat suppression, 8 blocks of 10 readout gradients, fundamental frequency of the sequence sound 61.9 Hz. **(b)** for the conventional EPI: TE=58.5 ms, TR=2048 ms, 16 slices of 5 mm thickness, image matrix 64×64, bandwidth

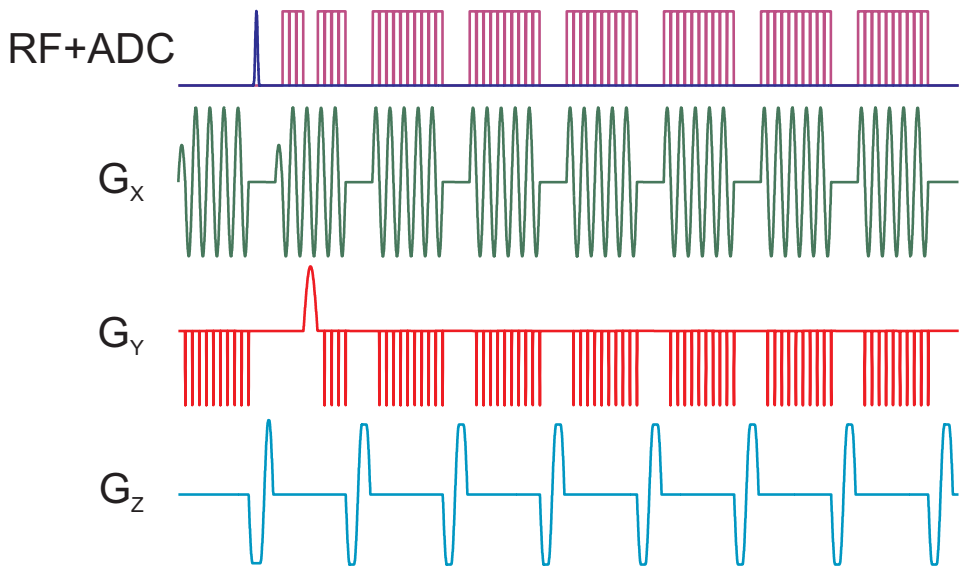

Figure 5.9: Sequence timing diagram for the Continuous EPI sequence used in fMRI experiment 1. Note that no fat saturation was used and the smaller read dephasing not specially masked.

930 Hz/px, FOV=23 cm, flip angle 90°, fully sinusoidal readout gradients, no fat suppression.

5.3.3 Results and Discussion

Image data were analyzed using BrainVoyager QX. The preprocessing consisted of 3D motion correction, slice time correction, 3 cycle high pass filtering as well as 4 mm spatial smoothing.

Activation patterns consistent with the anatomical location of auditory cortex were found in all runs, both for conventional and Continuous EPI. The main effect, when computed for all subjects with individual predictors for each run, is shown in figure 5.10 at a threshold of $t = 20$, $p < 0.001$ Bonferroni corrected. The activation patterns are overlaid on the averaged anatomical images of the four subjects, with the three orthogonal views centered on right Heschl's gyrus at Talairach coordinates x=36, y=−22, z=13 (white cross).

The activation patterns were slightly different for the conventional, compared to the Continuous EPI sequence, as shown in figure 5.11. At the same threshold $t=10$, $p<0.001$, the number of activated voxels was slightly larger for Continuous EPI, and the difference contrast Continuous EPI minus conventional EPI showed only positive resulting voxels at a threshold of $t=5$, $p<0.03$.

Event related averages were computed for both the conventional and

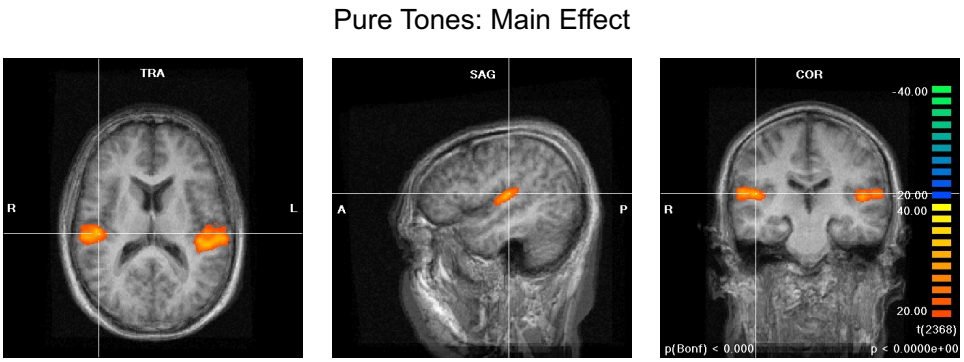

Figure 5.10: Main effect activation pattern for fMRI experiment 1, thresholded at $t=20$, $p<0.001$ Bonferroni corrected. Here displayed for the right auditory cortex at Talairach x=36, y=−22, z=13 (white cross).

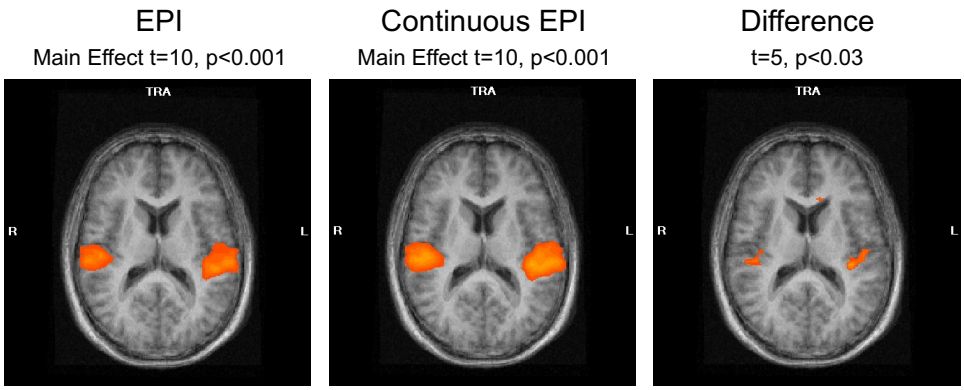

Figure 5.11: Difference in activation patterns obtained with conventional EPI and Continuous EPI in fMRI experiment 1, both thresholded at the same value $t=10$, $p<0.001$. The rightmost pattern was obtained with a difference contrast Continuous EPI minus conventional EPI, thresholded at $t=5$, $p<0.03$. Displayed slice at Talairach z=13.

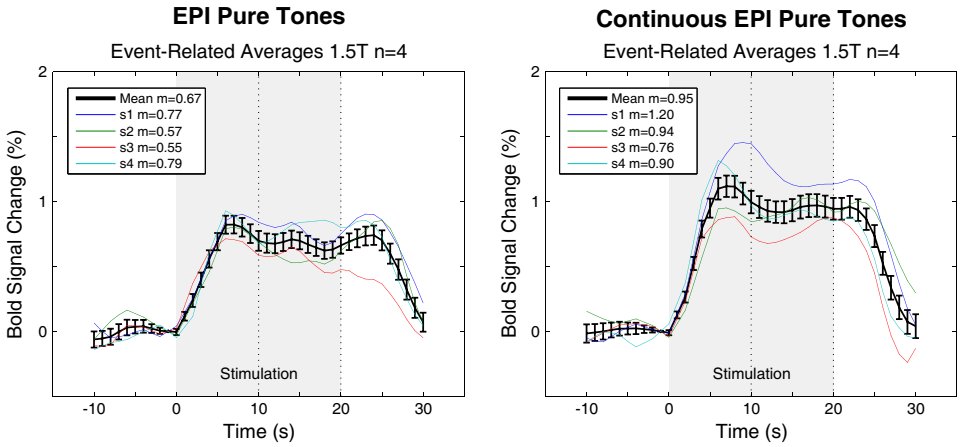

Figure 5.12: Event-related averages for fMRI experiment 1, based on a volume of interest defined by the main effect GLM of all runs (both conventional and Continuous EPI), thresholded at $t = 20$.

Continuous EPI runs for the group of all subjects and for each subject individually. When evaluated for a functionally defined volume of interest based on above main effect thresholded at $t = 20$, the group event related response as well as all th individual event related averages had a larger percent signal change BOLD response for Continuous EPI, compared to conventional EPI (see figure 5.12).

The mean BOLD percent signal change values for the time interval 10 to 20 s after stimulus onset (dotted lines in figure 5.12) are summarized in the following table and graphically depicted in figure 5.13, where the crosses correspond to individual subjects and the bars to the group average.

Frequency	Subject 1	Subject 2	Subject 3	Subject 4	Mean
conv. EPI	0.768	0.573	0.550	0.792	0.671
Cont. EPI	1.204	0.936	0.763	0.898	0.950
Change	+56.9%	+63.5%	+38.7%	+13.3%	+41.7%

The advantage of Continuous EPI, as clear as it seems from the results of this experiment, is not statistically significant. A paired non-parametric (Wilcoxon rank sum) test gives a probability of $p = 11\%$ for this result to be occurring by chance.

So far, the analysis exactly followed the procedure used in the Seifritz et al. [152] paper. One thing that could be questioned in this method is the selection of the functionally defined volume of interest. The activated area computed by the main effect GLM with one predictor for each run will be biased toward the run for which the activation is strongest (in terms of z value when using BrainVoyager QX defaults, or alternatively percent signal

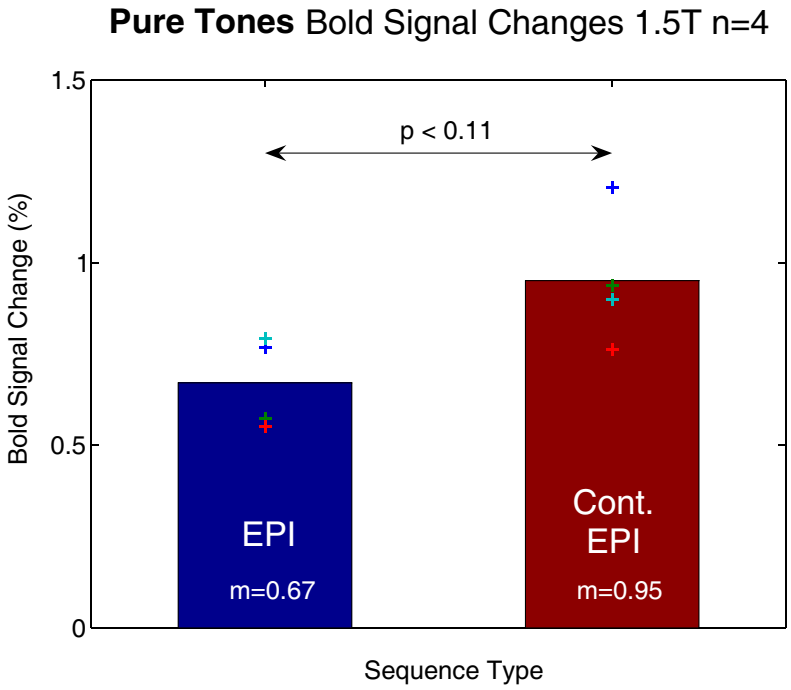

Figure 5.13: Group comparison of percent signal changes in fMRI experiment 1. Percent signal changes were computed for a VOI based on the main effect activation at $t = 20$, and the time courses for that VOI averaged over the interval 10 to 20 s after stimulus onset. Crosses correspond to individual subject values, bars to the group results.

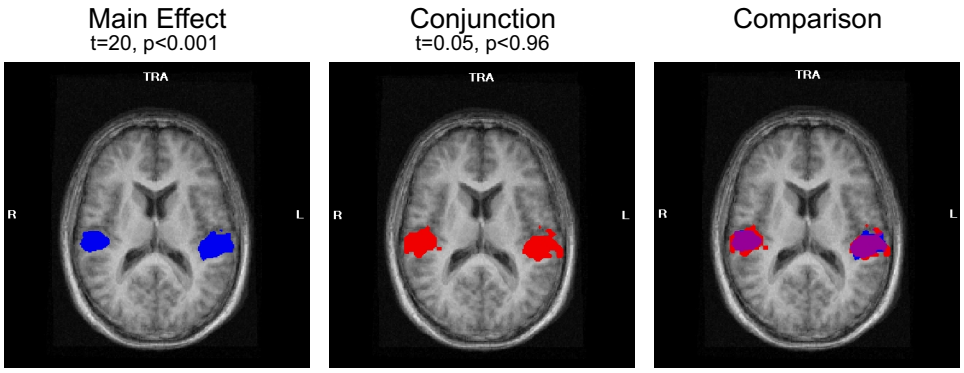

Figure 5.14: Two possible definitions of a functionally defined volume of interest. Left, the above definition based on the main effect GLM, thresholded at $t = 20$, in the middle, the VOI based on a conjunction analysis of all runs at $t = 0.05$, on the right a comparison of the two. Displayed slice at Talairach z=13.

change). When event related averages are computed for that volume of interest, the result will also be biased toward that specific run, which is likely to increase the variance between the measured percent signal change values for the different runs. Also, it should be noted here that such a main effect GLM is not the same as a random effect group analysis, because multiple runs from the same subjects and runs from different subjects are analyzed together in the same model. For these reasons, it seemed appropriate to compare above results with a differently selected volume of interest which more evenly accounts for the different runs. For this, a conjunction analysis was carried out over all the runs (both conventional and Continuous EPI) and all subjects. The voxels surviving this test are then known to be consistently activated over all runs (figure 5.14, note the similar localization). Naturally, such an analysis leads to much smaller activated areas at the same threshold, or very low thresholds for a similar activation volume. The percent signal changes evaluated in the conjointly activated area ($t = 0.05$, $p < 0.96$, averaged 10-20 s after stimulus onset) are listed in the following table and graphically displayed in figure 5.15.

Frequency	Subject 1	Subject 2	Subject 3	Subject 4	Mean
conv. EPI	0.572	0.512	0.458	0.681	0.556
Cont. EPI	0.935	0.784	0.639	0.774	0.783
Change	+63.3%	+53.0%	+39.7%	+13.7%	+40.9%

As expected, the percent signal changes computed for the conjunction VOI have a standard deviation (computed over Subjects 1-4) that is smaller than for the above main effect based VOI (0.096 versus 0.127 for the conventional and 0.121 versus 0.185 for the Continuous EPI sequence). Even

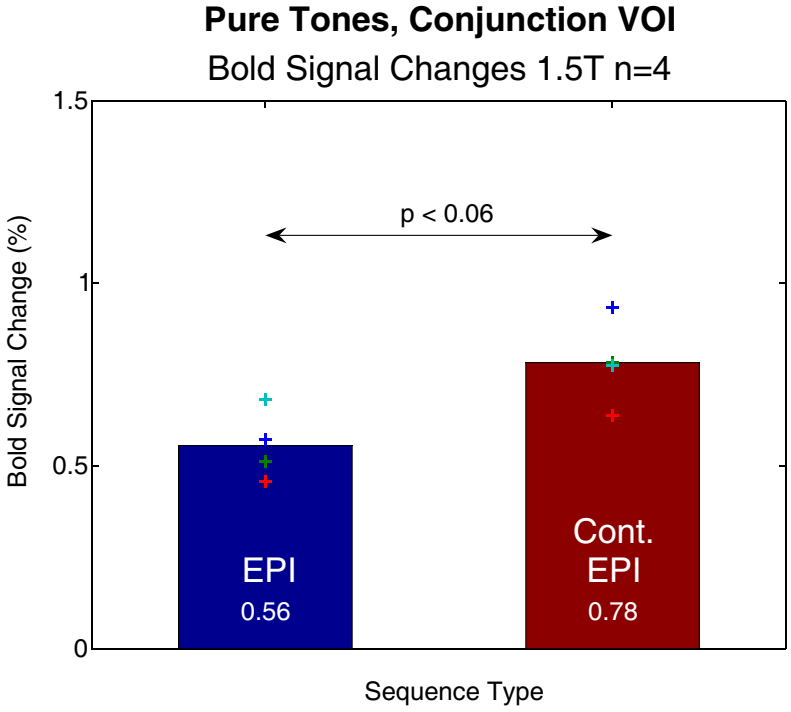

Figure 5.15: Group comparison of percent signal changes in fMRI experiment 1, analyzed using a conjunction test VOI at $t = 0.05$, time courses averaged over 10 to 20 s after stimulus onset. Crosses correspond to individual subject values, bars to the group results.

though the mean advantage of Continuous EPI over conventional EPI is around 41% in for both methods, the reduced variance in the conjunction VOI approach leads to an almost statistically significant result, with $p<0.06$, Wilcoxon rank sum test (compared to $p < 0.11$ for the main effect based VOI). It can therefore be concluded that the selection of a functional volume of interest based on a conjunction analysis more evenly accounts for the different runs and may be regarded as superior to the main effect based selection of a VOI.

5.4 fMRI Experiment 2: Auditory Stimulation Using the Gradient Sound

5.4.1 Experiment Design and Imaging Sequence

An interesting possible extension of the Continuous EPI sequence is to introduce an audible irregularity into the gradient pattern in a place where it does not modify the image contrast. When switching this modification on and off periodically, the gradient noise of the sequence intrinsically represents an auditory stimulus which can be used to trigger functional activation in the auditory cortex.

The difficulty in such an approach lies in the very high sensitivity of the data analysis procedure to minute changes in contrast between the periods where the additional gradients are on and the "normal" (or rest) condition periods. This problem precluded the theoretically very rewarding direct comparison of the activation states of conventional versus Continuous EPI scanner noise by simply switching between acquisition periods with either sequence. However, by introducing an additional block of readout gradients into the quasi-continuous pattern of the Continuous EPI sequence prior to the excitation pulses, the gradients of this block could be changed more or less arbitrarily, as shown in figure 5.16.

In this experiment, this additional block of gradients was periodically switched between a resting state condition, where it replicated the other readout gradient blocks, or a stimulation condition where it was exchanged for a 1 kHz triangular gradient shape of maximum amplitude of 15 ms duration. The last 7 ms of the stimulation gradient block were identical to the resting state block to minimize the effect of eddy currents (induced by the very rapid gradient switching) on the image contrast. The duration of this identical period was determined empirically in phantom experiments, as described in the following subsection. The difference in scanner sound was subjectively perceived as very obvious, with the stimulation gradients sounding like a loud, pulsed beep tone overlaid on the otherwise continuous gradient sound.

The stimulus was switched on and off in a block design pattern with 10

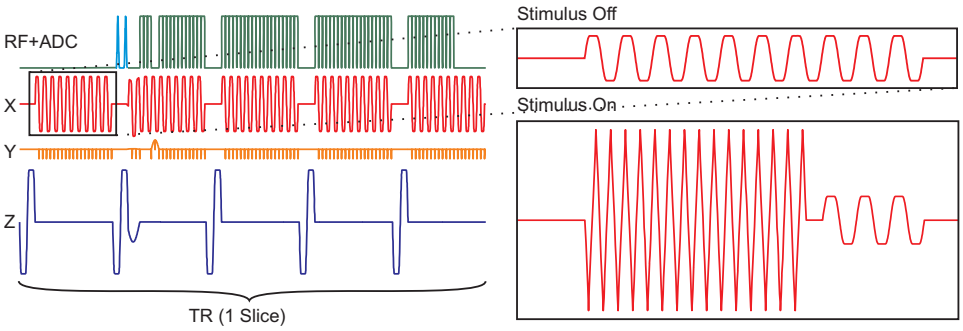

Figure 5.16: Sequence timing diagram for fMRI Experiment 2. The additional readout gradient block inserted before the excitation pulses (magnified on the upper right) can be modified arbitrarily. If it is periodically exchanged for a rapid, large amplitude triangular pattern (of 1 kHz frequency, 15 ms duration and maximum gradient amplitude, shown on the bottom right), the different gradient sound of the two periods leads to a stimulation of the auditory cortex (figure 5.18).

volumes "on" and 10 "off", equivalent to 12 s epochs. Seven cycles were measured for a total acquisition time of 3:09 min, with both the first and last 10 volumes rest condition. Synchronization of the image acquisition and the stimulus was in this case given intrinsically, a clear an advantage of this approach.

For this experiment, one single right handed of 34 years volunteer was measured. The only instruction in this case was to lie very still and relax. A T_1 weighted MPRage anatomical image was acquired prior to the functional run. The experiment was conducted on a 1.5 T Siemens Sonata system using the standard birdcage head coil.

Sequence parameters were: TE=52 ms, TR=1261 ms, 9 slices of 4 mm thickness, image matrix 64×64, bandwidth 942 Hz/px, FOV=25 cm, flip angle 90°, ramp fraction 0.6 (sinusoidal), fat suppression using 1-1 binomial water excitation pulses, 5 blocks of 20 readout gradients, fundamental frequency of the sequence sound 35.7 Hz.

5.4.2 Results and Discussion

As discussed above, it was of crucial importance for this experiment that image contrast was identical for the "stimulation" and "rest condition" gradient patterns. This was ascertained by acquiring phantom images of a water bottle phantom (containing 1.25 g $NiSO_4 \times 6 \cdot H_2O$ and 5 g NaCl per 1 kg H_2O dest.) with the same block design gradient pattern, and then looking at the pixel-wise intensity variations over the time series. By this procedure, it was found that when continuing the 1 kHz stimulation gradients over the entire block, strong variations were apparent, especially toward the edges of the

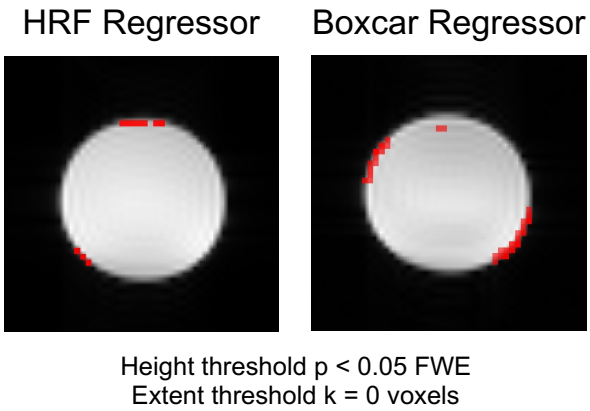

Figure 5.17: Remaining (eddy current induced) changes in image contrast between stimulation and rest periods in fMRI experiment 2. The falsely activated pixels in read are determined using the same analysis as for the in vivo fMRI data.

phantom, which were most likely caused by eddy currents induced by the strong and rapidly switched stimulation gradients. They could be reduced below visibility by leaving the last 7 ms of the gradient pattern identical for both stimulation and rest conditions.

To evaluate the influence of remaining changes in image contrast on the fMRI data, the phantom time series were analyzed with the identical fMRI analysis procedure as the in vivo data. Some falsely "activated" voxels were still found near the edges of the phantom at a thresholding level with a family wise error (FWE) of $p < 0.05$, but none survived a threshold of $p < 0.01$ (see figure 5.17, left). However, the analysis based on a physiological hemodynamic response function (HRF) as a predictor could be expected not to be very sensitive to (very rapid) contrast changes (through eddy currents, or any other effects). Therefore, a second analysis was based on a boxcar predictor, but also gave only relatively few falsely activated voxels near the phantom edges (figure 5.17, right) at the same threshold.

The in vivo fMRI data were analyzed using SPM2, with 3D motion correction, slice scan time correction, default high pass filtering and 8 mm spatial smoothing. The activation pattern found for a canonical HRF-convolved stimulus boxcar function is shown in figure 5.18, left, and conforms well to the anatomically expected location of the auditory cortex (threshold $t = 7.22$, $p < 10^{-6}$ FWE). Any remaining false activation due to image contrast changes could be expected to fit better to a boxcar function than to the HRF convolved predictor. Such an analysis (figure 5.18, right) gave activation near the expected location of the auditory cortex only at the very edge of the brain and a few small clusters in other areas at the same threshold of $t = 7.22$. The time course data for the activated areas in the

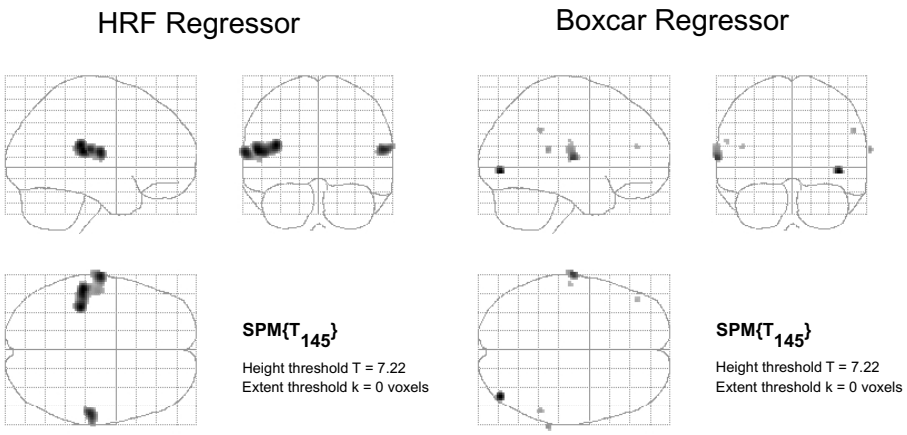

Figure 5.18: Activation pattern evoked by scanner generated gradient sound in a volunteer measured for fMRI experiment 2. The hemodynamic response function convolved predictor is expected to predominantly reveal true activation (due to hemodynamic regulation) while the boxcar predictor can be expected to include remaining contrast changes induced by the sequence.

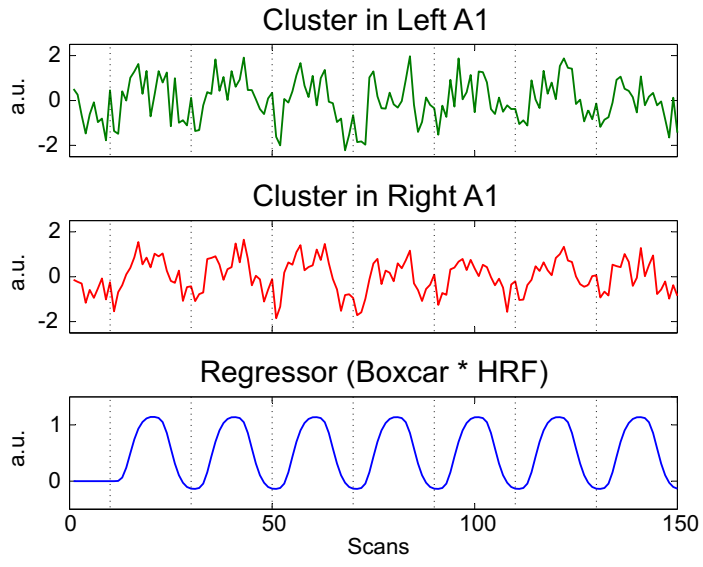

Figure 5.19: Timecourse data from the activated region from figure 5.18, left of fMRI experiment 2. The contrast to noise ratio is relatively poor.

HRF based analysis were also extracted, they are shown in figure 5.19, and give an indication that the contrast to noise ratio was not very high for this relatively short acquisition. In conclusion, the use of the scanner's gradient sound as an auditory stimulus overlaid on the otherwise continuous sound of a (modified) EPI sequence has been demonstrated. Although this may be a useful technique in terms of its ease of use and intrinsic stimulus–sequence synchronization, the main problem of this approach are remaining image contrast differences between stimulation and rest periods.

5.5 fMRI Experiment 3: 7T Tonotopy Paradigm

5.5.1 Stimulus and Experiment Design

The main goal of this experiment was to demonstrate the generality of the Continuous EPI principle by extending it to high field imaging at 7 T. To this end, is was important to select a robust, and at the same time general, experimental paradigm.

To ensure robust activation, a block design experiment was used, with a relatively long acquisition time of about 15 min to obtain sufficient statistical power. As a stimulus, pure sine tones were chosen because of their fundamental role in auditory perception. The tonotopic organization principle lies at the heart of the human auditory system, as discussed in section 2.3, therefore pure tones (containing only one frequency component) are very basic and fundamental auditory stimuli. Also, pulsed tones with repetition rates on the order of 5 to 10 Hz were known to result in a stronger activation than continuous tones (see section 2.3.5). On the other hand, it seemed advisable to use more than one frequency for the sake of generality. For example, it could be argued that if a 1 kHz tone was used and the scanner sound generated by the sequence had a strong frequency component in that range, auditory masking of the stimulus could not be neglected in the explanation of the observed BOLD response.

Fortunately, such experimental paradigms had already been used in a number of published studies and could therefore be regarded as robust. For example, Formisano et al. [100], in their first conclusive demonstration of tonotopic mapping in the human auditory cortex, had used 3 s blocks of 8 Hz pulsed sine tones of two to six different frequencies. Also, an on-going study by the Seifritz group used a similar tonotopy paradigm with 3 s epochs of pulsed sine tones at three different frequencies. The relatively short stimulation interval was chosen with the aim of obtaining a higher spatial specificity (as the early BOLD response is known to be better localized to the site of neuronal activation, as discussed in section 2.1.6). Additionally, such short stimulation intervals help to avoid the problem of finding an appropriate hemodynamic response function (sustained or transient, see section 2.3.5). The pilot study by the Seifritz group was already completed when

the present experiments were planned, they had observed robust activation of the auditory cortex and been able to generate tonotopic maps for all of their subjects.

For these reasons, the above tonotopy paradigm used by Seifritz et al. was used for this experiment (as well as for fMRI experiments 4 and 5 described below). Stimulation periods of 3 s were interleaved with 16 s rest periods, with an additional rest period at the beginning of the scan. Stimuli were generated by Matlab and recorded to CD, presented over a dedicated MR compatible headset and manually synchronized with the sequence start. They consisted of 5 Hz pulsed sine tones of 333, 1000 and 3000 Hz, with smoothed ramps of 10 ms. For the 7 T experiment only, the stimulus was synchronized to the (protocol) TR of the sequence. However, for that measurement, the protocol and actual TR were different in the EPI sequence (due to a programming error), so that the analysis was performed on a time basis and not based on volumes in the time course. The different frequency tones were presented in a pseudo-random order based on a 3×3 Latin square $[bac, acb, cba]$ repeated five times, where a corresponded to the 333 Hz, b to the 1 kHz and c to the 3 kHz tone. The total scan time for each run was 14 : 31 min. Again, the sound level was adjusted to be perceived as very loud but not painful.

Due to scan time limitations on the 7 T system at the MGH, Boston, only one single volunteer was measured. He was male, right handed and 40 years old. The volunteer was instructed to keep his eyes open and not to move during the scan. A T_1 weighted 3D MPRage image was acquired prior to the two functional runs, where the Continuous EPI scan preceded the conventional EPI scan. The functional slices were positioned parallel to the Sylvian fissure, centered on Heschl's gyrus.

5.5.2 Imaging Sequence

The 7 T system at the Martinos Imaging Center of the MGH (Massachusetts General Hospital, Boston USA) consisted of a Magnex Scientific magnet connected to a Siemens console. It was equipped with an extremely fast and strong gradient system with 80 mT/m/s slew rate and 80 mT/m maximum gradient amplitude. A custom built birdcage head-coil was used.

The adaption of the sequences to the 7 T system was relatively straight forward and mainly consisted in adapting the sequence parameters for a suitable TE and favorable acoustic properties, the adjustment of the binomial water excitation pulse spacing and the removal of problems introduced by the different software version. The very close spacing of the two water excitation sub-pulses (584 µs) made very short RF pulses with almost Gaussian frequency profile and very large slice selection gradients necessary, leading to a noticeable artifact (see section 5.2.5) which was correctable based on an empirical bias in the amplitude of the second slice select gradient.

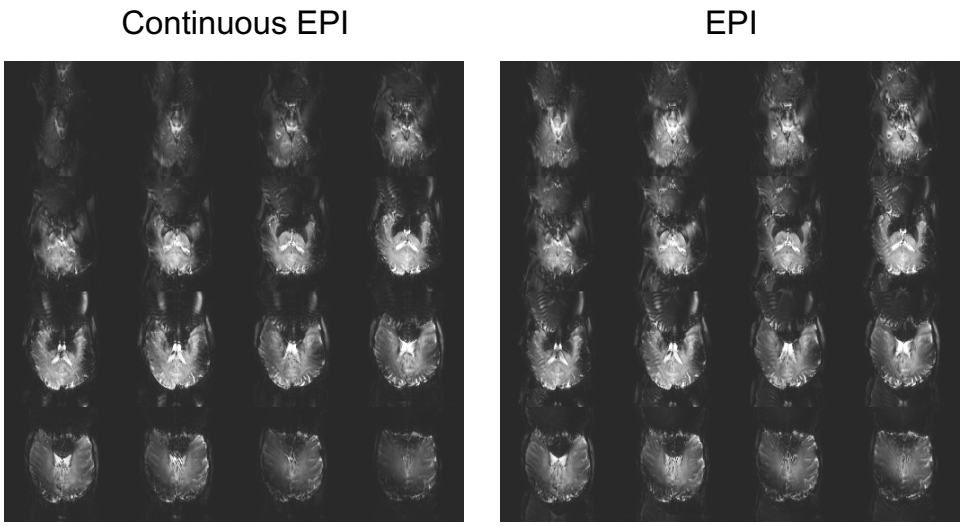

Figure 5.20: Image quality using conventional compared to Continuous EPI at 7 T in fMRI experiment 3. Significant distortions, signal drop-outs and remaining ghosting artifacts are observed in both images.

Sequence parameters were: **(a)** for the Continuous EPI: TE=28.8 ms, TR=1262.3 ms, 16 slices of 4.2 mm thickness, image matrix 128×128, partial Fourier 6/8 reconstruction, bandwidth 1700 Hz/px, FOV=22 cm, flip angle 60°, fully sinusoidal readout gradients, binomial 1-1 pulse water excitation, fundamental frequency of the sequence sound 50.7 Hz. **(b)** for the EPI sequence: TE=28.8 ms, TR=1262.3 ms, 16 slices of 4.2 mm thickness, image matrix 128×128, partial Fourier 6/8 reconstruction, bandwidth 1700 Hz/px, FOV=22 cm, flip angle 60°, fully sinusoidal readout gradients, binomial 1-1 pulse water excitation.

5.5.3 Results and Discussion

The raw first images from both the conventional and Continuous EPI time series are displayed in figure 5.20. Image quality is not very good, there were remaining ghosting artifacts in the images as well as severe distortion and signal drop-out artifacts. Also, the effect of a strongly inhomogeneous B_1 field and or coil sensitivity is visible as a higher signal intensity in the middle of the images, compared to the peripheral regions. Even the T_1 weighted anatomical scan was severely affected by distortion (and motion) artifacts, as seen in figure 5.21.

The functional data were analyzed using BrainVoyager QX. Preprocessing consisted of 3D motion correction, slice time correction, 3 cycle high pass filtering, but no spatial smoothing as event-related averages could be expected to be similar for smoothed and non-smoothed data.

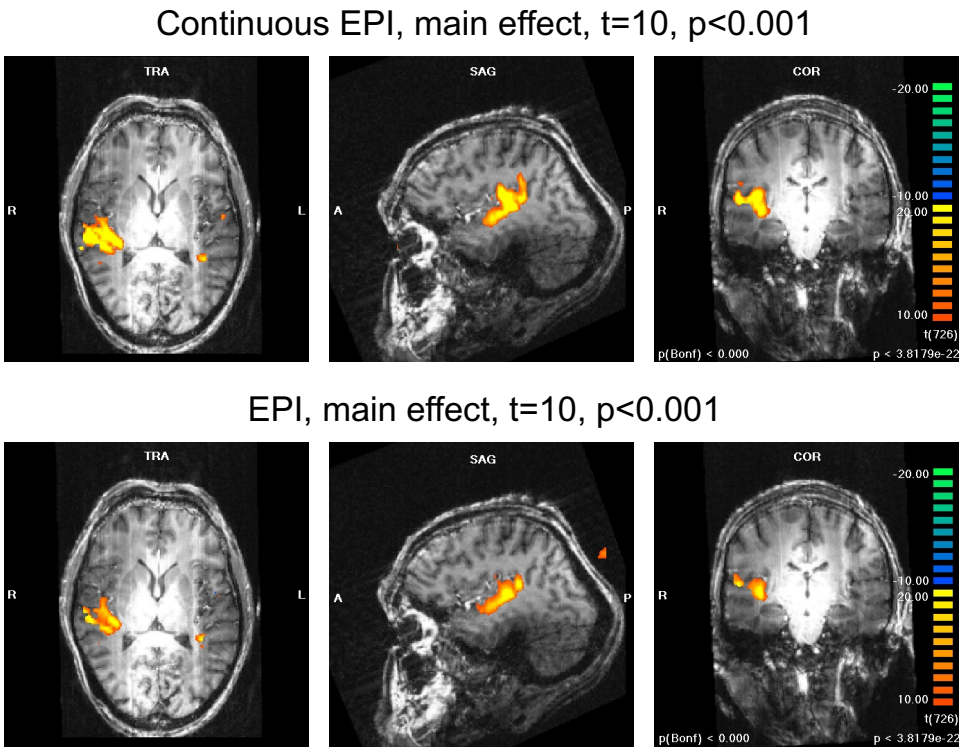

Figure 5.21: Main effect activation pattern for the conventional and Continuous EPI runs in fMRI experiment 3. Statistical maps are thresholded at $t = 10$, $p < 0.001$ Bonferroni corrected. The three orthogonal slices are displayed for the right auditory cortex at Talairach x=40, y=−18, z=8. The left auditory cortex was almost completely absent in the raw images due to signal drop-outs. Note the false "activation" outside the brain for the conventional EPI sequence due to the strong ghosting artifact.

Activation patterns of the main effect (all three stimulus frequencies) are shown in figure 5.21, thresholded at $t = 10$, $p < 0.001$ Bonferroni corrected. Highly significant activation was found at the location expected for the right auditory cortex. There was no activation of the same significance level at the site of the left auditory cortex. From the raw functional images, where the expected site of the left auditory cortex was strongly affected by signal drop-outs, it can be concluded that these drop-out due to the rather long echo time and thick slices were the most likely reason for the failure to find activation at this location. In the maps from the conventional EPI, there is false "activation", offset by half the field of view (along the oblique slices) from the main activation site, which can be attributed to the more pronounced ghosting artifact for that sequence, compared to Continuous EPI.

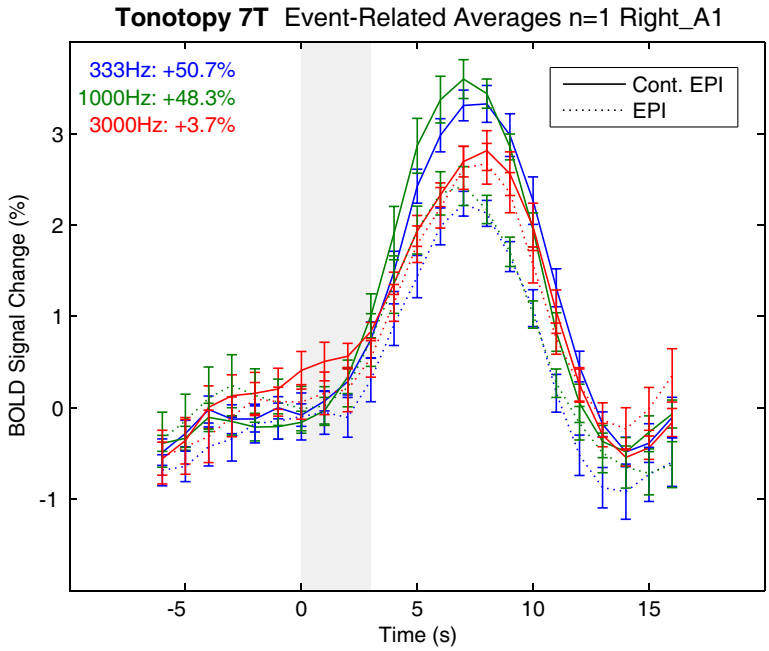

Figure 5.22: Event related average time courses evaluated for the conjointly activated region ($t = 10$) in fMRI experiment 3 using conventional and Continuous EPI. The Continuous EPI sequence yielded larger BOLD percent signal changes for all three frequencies.

From these activation maps, a functionally defined volume of interest (VOI) was computed based on the conjoint activation in both runs, also thresholded at $t = 10$ (which was similar in extent and shape to the activation patterns shown in figure 5.21). Event related averages evaluated for that VOI are displayed in figure 5.22. At all three frequencies, the Continuous EPI sequence yielded larger percent signal changes. When compared to the time courses acquired using the conventional EPI sequence, the measured BOLD percent signal changes were larger by 50.7% for the 333 Hz tone, 48.3% for the 1 kHz tone and 3.7% for the 3 kHz tone. These values were determined by fitting a quadratic polynomial onto the five time points surrounding the maximum. Fits were visually inspected and found to be satisfactory. The baseline was determined in the event related averaging procedure from the average of the time points 2 to 0 s before stimulus onset. If only the largest time point is used, its corresponding standard error (error bar in figure 5.22) can be used to calculate the standard error for the "advantage" of Continuous over conventional EPI, based on the error propagation in the calculation. Using this method, the BOLD signal change is found to be larger by $49 \pm 11\%$ for the 333 Hz tone, $48 \pm 12\%$ for the 1 kHz tone and $6 \pm 10\%$ for the 3 kHz tone for the Continuous EPI run.

The question why the difference between the two sequences was so much smaller for the 3 kHz tone than for the other two frequencies cannot be answered with any certainty. Judging from the event related average data, it can probably be attributed to a poor statistics for for the Continuous EPI 3 kHz predictor, which shows an otherwise unexplained early increase at times 0 to 2 s after stimulus onset. Auditory masking would be another possible explanation for such an effect.

It has to be cautioned that the stronger ghosting artifact observed for the conventional EPI sequence resulted in the signal from the auditory areas to be distributed between the image and the ghost. This lead to activated voxels observed in the ghost image outside the brain. While this can be expected to result in a poorer contrast to noise ratio for the conventional EPI time series (which was not clearly visible in the data), it should not have any direct influence on the measured percent signal change values.

It could be argued that the observed difference in response amplitude between the two sequences was not due to the different acoustic characteristics of the two sequences, but to a session effect, such as the decreasing attention of the subject throughout the scanning session (which lasted a little more than one hour). Based on the limited data in this experiment, such a session effect cannot be ruled out.

Based on these data, the Continuous EPI sequence can be concluded to result in larger BOLD percent signal changes in response to pulsed sine tones at 7 T, over the three frequencies tested and for the single volunteer measured. Apart from the not ideally chosen echo times and slice thickness settings (signal drop-outs), the limitation of having measured only one subject and the possibility of a session effect were the main shortcomings of this experiment.

5.6 fMRI Experiment 4: 3T Tonotopy Paradigm

5.6.1 Stimulus and Experiment Design

Similar to the 7 T experiment, the same well established tonotopy paradigm was used to compare Continuous and conventional EPI in this experiment at 3 T (3 s epochs interleaved with 16 s rest periods, 5 Hz pulsed sine tones of 333, 1000 and 3000 Hz, presented in Latin square pseudo-randomized order, each stimulus repeated a total of 15 times, scan time 14:31 min). Again, the stimulation waveform was generated using Matlab, recorded to CD and synchronized manually to the sequence start. The stimulus was delivered using a high fidelity MR compatible head set which had been previously used for the Continuous EPI paper by Seifritz et al. [152].

For this experiment, four volunteers were recruited, all male, all right handed, age 33.3 ± 0.7 (mean±standard deviation). Volunteers were asked to lie very still throughout the scan, relax and keep their eyes open. The

sound level of the stimuli was individually adjusted to be perceived as very loud, but not painful and of equal loudness on both ears. For each volunteer, two sessions were measured on different days, one with the Continuous EPI sequence measured first, one with conventional EPI first. In each session, a T_1 weighted 3D MPRage image was acquired prior to the two functional runs and used to position the slices for the functional runs obliquely, parallel to the Sylvian fissure and including the entire superior temporal plane.

5.6.2 Imaging Sequence

Image data was acquired on a 3 T Siemens Allegra system with a birdcage head coil. As in the earlier experiments, the Continuous EPI sequence (adapted to the 3 T system) was compared to a matched EPI sequence in terms of echo and repetition times, bandwidth, excitation pulse and readout gradient waveshape. Since the Allegra system was equipped with a rather fast gradient system of 40 mT/m/s, a 96×96 matrix size for a 2.3 mm^3 isotropic resolution could be used together with a RF pulse bandwidth time product of 2.0 for a reasonably rectangular slice profile.

Sequence parameters were: **(a)** for the Continuous EPI: TE=30.96 ms, TR=1342.2 ms, 21 slices of 2.3 mm thickness, image matrix 96×96, bandwidth 2365 Hz/px, FOV=22.08 cm, flip angle 76°, ramp fraction 0.85, binomial 1-1 pulse water excitation, 3 blocks of 38 readouts, fundamental frequency of the sequence sound 46.9 Hz, sound level 86.0 dB(A). **(b)** for the conventional EPI: TE=30.96 ms, TR=1342.2 ms, 21 slices of 2.3 mm thickness, image matrix 96×96, bandwidth 2365 Hz/px, FOV=22.08 cm, flip angle 76°, ramp fraction 0.85, binomial 1-1 pulse water excitation, sound level 85.4 dB(A).

5.6.3 Results and Discussion

The data analysis procedure was very similar to that in fMRI experiment 3. The functional data were analyzed using BrainVoyager QX with preprocessing consisting of 3D motion correction, slice time correction, 3 cycle high pass filtering, but no spatial smoothing. Functional time series were co-registered onto the anatomical scan and transformed into standard anatomical space.

Consistent, highly significant ($t = 6$, $p < 0.001$ Bonferroni corrected) activation at the expected location of the auditory cortex was observed in all runs and for all subjects. Still, the inter-individual differences in the precise location of the activation were quite noticeable, so that less than 9000 voxels (of $1 \times 1 \times 1$ mm^3) survived a conjunction analysis over both sequences and all eight sessions at a threshold of $t = 0.05$. This volume was used to generate event-related averages for each run (it is depicted in figure 5.23, overlaid on the average of the eight anatomical images).

As in fMRI experiment 3, event related averages were computed. The

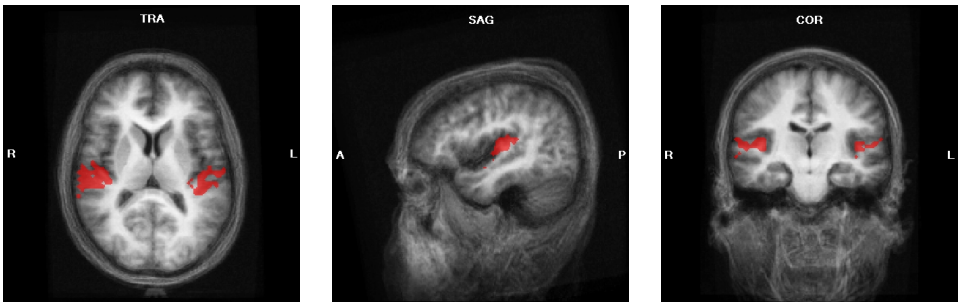

Figure 5.23: The volume of interest used for event-related averaging in fMRI experiment 4. It was determined by conjunction analysis of all runs (of four subjects, each with two sessions of two runs) thresholded at $t = 0.05$. The three orthogonal slices are centered at the right auditory cortex at Talairach x=43, y=−19, z=10.

resulting time courses for the group, averaged over all eight sessions are shown in figure 5.24. Based on the fit of a quadratic polynomial to the five points next to the time point with maximum amplitude, the Continuous EPI sequence yielded larger percent signal change responses by 11.9% for the 333 Hz tone, 16.5% for the 1 kHz tone and 25.6% for the 3 kHz tone.

Event related average time courses for the two sessions (s1 and s2) of each individual subject largely resembled the group average in shape and the trend towards a larger BOLD response when measured with the Continuous EPI. Percent signal change values, computed using the same fit of quadratic polynomials to the maxima, were:

Sequence	Freq.	Subject 1		Subject 2		Subject 3		Subject 4	
		s1	s2	s1	s2	s1	s2	s1	s2
conv.EPI	333 Hz	1.09	1.14	1.00	0.92	1.07	1.13	1.30	1.46
	1000 Hz	1.19	0.97	1.08	1.13	1.11	1.02	1.18	1.19
	3000 Hz	1.17	0.57	1.05	0.84	0.86	0.82	0.84	0.90
Cont.EPI	333 Hz	1.64	1.06	1.11	0.79	1.18	1.55	1.52	1.30
	1000 Hz	1.25	0.98	1.26	0.88	1.32	1.56	1.63	1.38
	3000 Hz	1.07	0.70	1.03	1.11	1.08	1.27	1.10	1.26

These results are also depicted graphically in figure 5.25, where the bars are calculated percent signal changes of the group average, stars are individual subject values from session one (Continuous EPI measured before the conventional EPI) and crosses from session two (inverse order). The advantage of Continuous EPI calculated from above group event related averages is rather similar to the mean of the individual runs, which is 11.4% for the 333 Hz tone, 15.7% for the 1000 Hz tone and 21.8% for the 3000 Hz tone. The larger BOLD response amplitude measured using Continuous

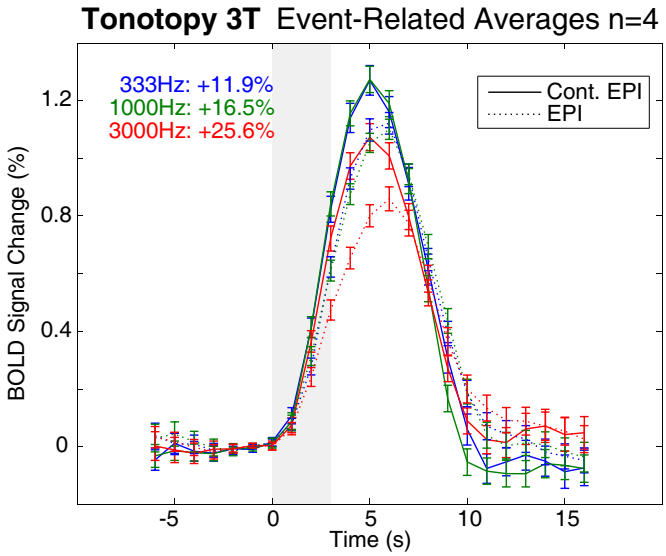

Figure 5.24: Group event related averages in the functionally defined volume of interest of figure 5.23 in fMRI experiment 4. All eight sessions from four volunteers were considered. The BOLD response measured with Continuous EPI are larger than those measured with conventional EPI by more than 30% for all three frequencies.

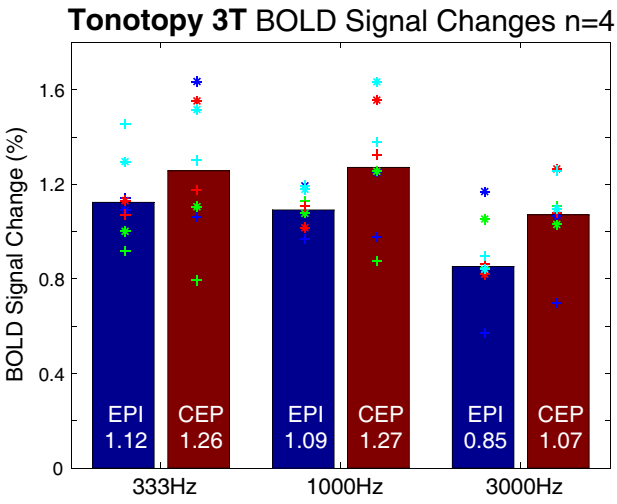

Figure 5.25: Graphical summary of BOLD percent signal changes in the individual runs of fMRI experiment 4. Bars are based on group event related averages, stars indicate the values for the first session (Continuous EPI measured first) and crosses those from the second session (with inverse sequence order).

EPI, compared to conventional EPI at 3 T is demonstrated rather clearly by these results for all three stimulus frequencies measured. When the percent signal changes (PSC) from both sessions are averaged for each subject, four statistically independent pairs of samples are obtained, which can be used to test the null hypothesis of no difference in mean PSC between the two sequences. Using a paired, non-parametric (Wilcoxon rank sum) test, the probability for the observed results to occur by chance under the null hypothesis is $p<0.67$, $p<0.34$ and $p<0.06$ for the three frequencies, respectively. The advantage of Continuous EPI, clear as it may seem, is therefore not statistically significant, but almost so for the highest frequency. Clearly, when using a (parametric) t-test or pooling the three frequencies, higher significance levels would result.

Because for each subject, two sessions were measured, one with Continuous and one with conventional EPI first, a session effect (e.g. decreasing attention over the session) can be ruled out as an explanation of the observed result. By comparing the first functional run in each session to the second in the same manner as the Continuous – conventional EPI comparison described above, this session effect can even be quantified from these data. The first run on average resulted in a larger BOLD response amplitude by $17 \pm 6\%$ for the 333 Hz tone, $14 \pm 5\%$ for the 1 kHz tone but a $1 \pm 7\%$ smaller BOLD response amplitude for the 3 kHz tone, compared to the second run. Here, the percent signal change values and the corresponding standard errors were simply determined from the time-point with maximum amplitude and its standard error. In conclusion, session effects, while not resulting in an equally strong effect as the difference between Continuous and conventional EPI, cannot be neglected for this experiment.

One could argue that delayed BOLD responses are likely to occur even in in a primary area like the auditory cortex (see, for example [167]) and that temporal derivative predictors should be used for the short stimulation epochs used in this paradigm to minimize any amplitude bias induced by such delays (as proposed in [168]). However, since only time courses in a common ROI are compared, such a bias would have no effect on the comparison of BOLD amplitudes as here described. While the inclusion of temporal derivative predictors might also increase the robustness towards small time shifts which could be caused by the manual synchronization of sequence and stimulus, this was omitted in the present analysis to avoid the complication in the interpretation of the results.

5.7 fMRI Experiment 5: 1.5T Tonotopy Paradigm

5.7.1 Experiment Design and Stimulus

The goal of this experiment was to complete the comparison of Continuous and conventional EPI sequences for the tonotopy paradigm used in fMRI

experiments 3 and 4. The stimulus and experiment design was exactly the same as in fMRI experiment 4 (see section 5.6). If a similarly clear effect was observed in this experiment as could be expected from the two preceding ones, this might have concluded the comparison the new Continuous EPI implementation and conventional EPI. But then things were not quite as clear, as described in the following.

5.7.2 First Trial

5.7.2.1 Subjects and Sequence Parameters

For this experiment, four volunteers were measured, three male, one female. Their age (mean ± standard deviation) was 29.2 ± 6.8, three were right handed, one left handed but writing with his right hand.

The scanner used was a 1.5 T Siemens Avanto system, with standard (TIM) four-channel head coil. Stimuli were delivered over the same high-fidelity MR headphone system as in fMRI experiment 4, again using a manually synchronized stimulus recorded on CD. The stimulus volume was adjusted individually to be perceived as very loud but not painful. Subjects were instructed to lie very still, relax and keep their eyes open during the functional scans. For all subjects, an anatomical T_1 weighted MPRage scan was first acquired, followed by the conventional EPI sequence and then the Continuous EPI. Again, slices for the functional runs were positioned parallel to the Sylvian fissure, to include all of the superior temporal plane. A second session with the Continuous EPI sequence measured before the conventional was planned, but not carried out due to the surprising results found in the first session.

Sequence parameters were: **(a)** for the Continuous EPI: TE=53.13 ms, TR=1271.0 ms, 12 slices of 4.5 mm thickness, image matrix 64×64, bandwidth 1085 Hz/px, FOV=25.6 cm (resulting in a voxel size of $4{\times}4{\times}4.5\,\mathrm{mm}^3$), flip angle 75°, ramp fraction 0.4, binomial 1-1 pulse water excitation, 5 blocks of 16 readouts, fundamental frequency of the sequence sound 47.2 Hz, sound level 78.7 dB(A). **(b)** for the conventional EPI: TE=53.13 ms, TR=1271.0 ms, 12 slices of 4.5 mm thickness, image matrix 64×64, bandwidth 1085 Hz/px, FOV=25.6 cm (resulting in a voxel size of $4{\times}4{\times}4.5\,\mathrm{mm}^3$), flip angle 75°, ramp fraction 0.4, binomial 1-1 pulse water excitation, sound level 75.2 dB(A). The wider spacing of the water excitation pulses made a good rectangular slice profile possible, with the same bandwidth time product of 5.22 equal as used in the vendor EPI sequence.

5.7.2.2 Results and Discussion

The data analysis procedure was identical to that used in experiment 4. Functional data were analyzed using BrainVoyager QX with preprocessing consisting of 3D motion correction, slice time correction, 3 cycle high pass

filtering, but no spatial smoothing. Functional time series were co-registered onto the anatomical scan and transformed into standard anatomical space.

In both the anatomical and functional images, strong RF artifacts were present. While the same setup of the stimulation system was used as in the 3 T fMRI experiment 4, it was the unfiltered (RS-232) cable connecting the sound amplifier to the transducer inside the magnet room which caused these artifacts. At the time, no connectors for this cable were present on the filter plate of the scanner cabinet, the cable was therefore simply introduced through a tube in the wall between scanner and the console rooms (the same method as used on the 3 T system).

Pronounced and unambiguous activation at the expected location of the auditory cortex was only found in three runs from two subjects (both runs of subject 2 and the Continuous EPI run of subject 4). The conventional EPI run for subject 4 and both runs of subject 1 also showed significant, albeit less extended, bilateral activation in the region of the auditory cortex, but also very few isolated negatively activated voxels at locations unrelated to auditory processing. Part of an explanation for the latter three runs could be the reduced signal (and contrast) to noise ratio due to the RF artifacts, which were strongest for subject 1 at least in the anatomical scan.

Subject number 3 displayed a completely unexpected activation pattern, consistent over both runs. The conjoint activation for both runs of that volunteer (right handed, female) is shown in figure 5.26, thresholded at $t = 6$, $p < 0.001$ Bonferroni corrected. No significant activation is seen at the expected location of the auditory cortex (the three orthogonal slices are centered on the right Heschl's gyrus at Talairach coordinates x=36, y=−28, z=11). On the other hand, highly significant negative "activation" is seen for most other regions that were included in the functional volumes. One possible explanation for such a result might be a synchronization problem between the stimulus and the imaging sequence, however, the consistency of the effect observed in both runs makes such an explanation seem unlikely. However, in trying to explain this result, I was made aware that subject 3 was affected by thalassemia, an uncommon variation in the shape and number of erythrocytes. An effect of this condition on BOLD fMRI response has not been reported in the literature, as far as I am aware of, but could be a possible explanation for this effect (and might be a fruitful subject for future research).

For the present experiment, subject 3 was excluded from the further analysis (it would have rendered the determination of a conjointly activated volume of interest impossible). For the three remaining subjects, such a conjoint activation over all runs was readily found at a threshold of $t = 1.0$, it agreed relatively well with the expected location of the auditory cortex, as shown in figure 5.27.

Similar to the previous experiment, event-related averages were computed and evaluated for this volume of interest, the resulting time courses

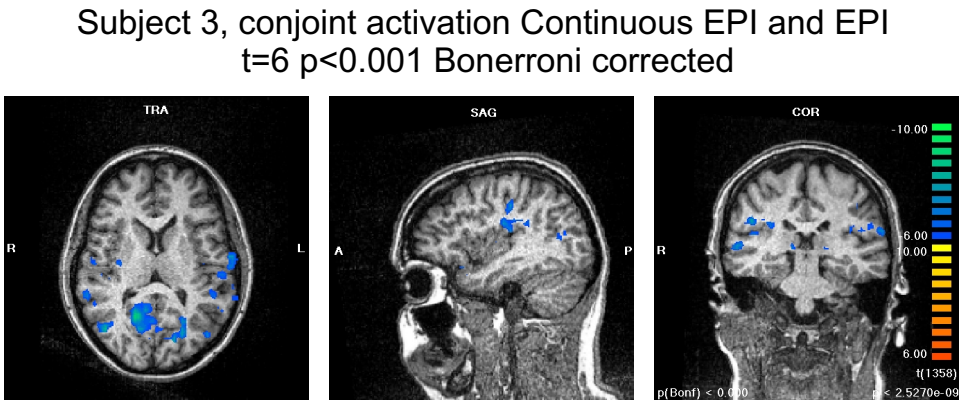

Figure 5.26: Unexpected, highly significant ($p<0.001$ Bonferroni corrected) activation pattern found in subject 3 of fMRI experiment 5, trial one. The maps represent the conjoint activation in response to the tonotopy stimulus for both functional runs (Continuous and conventional EPI), thresholded at $t=6$. The three orthogonal slices are centered on the right Heschl's gyrus at Talairach x=36, y=−28, z=11.

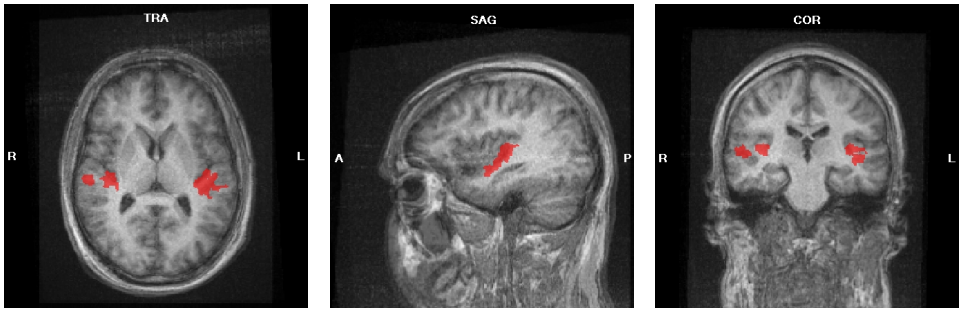

Figure 5.27: Conjointly activated volume for subjects 1,2 and 4 in fMRI experiment 5, trial one. The maps were centered around the expected location of the right auditory cortex at Talairach coordinates x=36, y=−22, z=8 and thresholded at $t=1.0$.

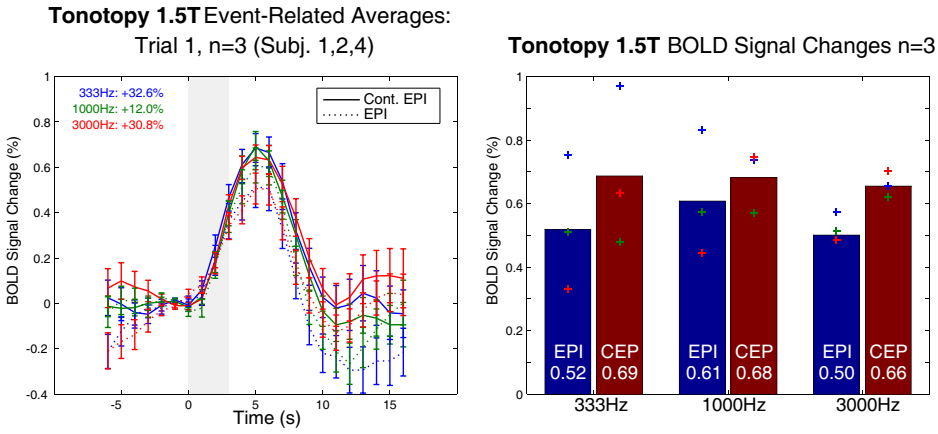

Figure 5.28: Group event related averages (left) and summary of individual subject results (right) for subjects 1,2 and 4 in fMRI experiment 5, trial one. Again, runs measured with Continuous EPI result in a larger BOLD response amplitude than the runs with conventional EPI.

are shown in figure 5.28, left. Again, the runs measured with Continuous showed a larger percent signal change BOLD response than the runs measured using conventional EPI, in this experiment by 32.6% for the 333 Hz tone, 12.0% for the 1 kHz tone and 30.8% for the 3 kHz tone (fit of a quadratic polynomial to the five points surrounding the maximum). This result is still compatible with an increased BOLD response of about 25 to 30% when using Continuous EPI, as could be expected from the previous experiments. From the non-negligible session effect observed in fMRI experiment 4, it could be expected that the advantage in BOLD amplitude measured for Continuous EPI in this experiment is a slight underestimation of the "true" effect, due to decreasing attention levels or similar effects.

The BOLD percent signal change values, calculated using the same method as above for the three individual subjects, are listed in the following table and graphically depicted in figure 5.28, right.

Sequence	Freq.	Subject 1	Subject 2	Subject 4
conv.EPI	333 Hz	0.75	0.51	0.33
	1000 Hz	0.83	0.57	0.44
	3000 Hz	0.57	0.52	0.49
Cont.EPI	333 Hz	0.97	0.48	0.63
	1000 Hz	0.74	0.57	0.75
	3000 Hz	0.66	0.62	0.70

As expected for only three subjects, the trend towards a larger BOLD response amplitude using the Continuous EPI sequence is not significant in this case, with the 3 kHz frequency showing the smallest variance and

therefore the highest significance level ($p < 0.1$ Wilcoxon rank sum test).

In conclusion, this experiment showed a greater BOLD response percent signal change in response to the tonotopy paradigm when using Continuous compared to conventional EPI. Although one subject had to be excluded from the analysis and all subjects were measured with the conventional preceding the Continuous EPI run, the results showed a clear trend towards an advantage when using Continuous EPI of the same order as in experiments 3 and 4 (which used the same stimulus at 7 and 3 T). Shortcomings of this experiment were the strong RF artifacts in both anatomical and functional images, a highly unusual, not fully explained activation pattern observed in subject 3, a possible session effect (biased in favor of the conventional EPI sequence) and a poor statistics (n=3).

5.7.3 Second Trial

5.7.3.1 Experiment Design

In an attempt to resolve the problems and shortcomings of the first trial, the experiment was repeated with the same experimental set-up and paradigm, but more subjects and the auditory stimulation transducer connected over the filter plate of the MR cabinet. For the transducer cable, a custom connector was built which split the RS-232 cable onto six individual filtered connections. Again, the 1.5 T Siemens Avanto system was used with standard (TIM) four-channel head coil and the same stimulation system as in the first trial.

Six volunteers were recruited for this experiment, five male, one female, five right-handed one left age 35.2 ± 4.3 (mean $\pm$ standard deviation). None of them had participated in trial one. Each volunteer participated in two sessions on different days, one with conventional and one with Continuous EPI measured first. In all sessions, a T_1 weighted MPRage scan was acquired prior to the functional runs and used to position the functional slices parallel to the Sylvian fissure including the entire superior temporal plane, as in the previous experiments. Again, the stimulus volume was adjusted for each subject individually, so that the stimulus was perceived as loud but not painful. For the functional scans, subjects were instructed to relax, lie very still and keep their eyes open.

Sequence parameters were slightly changed with respect to the first trial. Thinner slices were used (3.4 mm instead of 4.5 mm) to reduce signal dropouts, especially in vicinity of the air-filled cavities of the temporal bone, and a better spatial resolution ($3.4\,\text{mm}^2$ instead of $4\,\text{mm}^2$) achieved by a reduction in field of view. As in the first trial, the same rectangular slice profile as in the vendor EPI sequence could be used (BTP 5.22).

Sequence parameters were: **(a)** for the Continuous EPI: TE=47.32 ms, TR=1515.4 ms, 16 slices of 3.4 mm thickness, image matrix 64×64, band-

width 1280 Hz/px, FOV=21.76 cm (resulting in an isotropic voxel size of 3.4 mm^3), flip angle 75°, ramp fraction 0.6, binomial 1-1 pulse water excitation, 5 blocks of 16 readouts, fundamental frequency of the sequence sound 52.8 Hz, sound level 77.8 dB(A). **(b)** for the conventional EPI: TE=47.32 ms, TR=1515.4 ms, 16 slices of 3.4 mm thickness, image matrix 64×64, bandwidth 1280 Hz/px, FOV=21.76 cm (resulting in an isotropic voxel size of 3.4 mm^3), flip angle 75°, ramp fraction 0.6, binomial 1-1 pulse water excitation, sound level 81.4 dB(A).

5.7.3.2 Results

The same data analysis procedure as in the first trial was used with the only difference that in this case, the co-registration of functional and anatomical datasets was carefully controlled. In the earlier experiments, an automated two-step procedure consisting of a pre-alignment based on the slice header and a least-squares based automated fine alignment (six parameter rigid body registration) was used. Here, and for all later experiments, an additional manual fine-adjustment (translations only) was introduced between those two steps, based on visually guided alignment of the ventricles and prominent sulci in a blended composite anatomical-functional image. Typically the subsequent automated least-squares fine alignment procedure converged after a much shorter time and fewer iterations. In cases where the automated fine alignment resulted in a large translation (more than about two Talairach coordinates) and, or rotation (more than about two degrees) or where excessive numbers of iteration steps (more than 10) were necessary, the manual and automatic fine alignment steps were repeated. Using this approach, satisfactory results according to above criteria were obtainable in for all subjects (here and in the following experiments).

The RF artifacts and marked noise in anatomical and functional runs were reduced below visibility in this setup with filtered connection of the stimulation system, greatly simplifying the precise localization of Heschl's gyrus and the co-registration procedure as well as the transformation into standard anatomical space.

Activation Patterns The activation patterns observed in this experiment were very different between subjects, with lots of unexpected effects.

Subject 1 In the first subject, all four functional runs resulted in extended, highly significant activation bilaterally along Heschl's gyrus (at $t = 6$, $p < 0.001$ corrected). Subject movement was minimal, with no sudden movement events larger than 0.3 mm or 0.3°.

Subject 2. Data from the first session, in which conventional EPI was measured before Continuous EPI gave highly significant activation along Heschl's gyrus (figure 5.29), but mostly in the lateral two thirds of it (thus excluding the most likely location of the primary auditory cortex). In the

second session, where the Continuous preceded the conventional EPI sequence, the conventional EPI gave a highly significant activation along the full length of Heschl's gyrus, while the Continuous EPI run gave almost no highly significant ($p < 0.001$ Bonferroni corrected) activation except for some negative activation along left Heschl's gyrus (which increased in extent and was found bilaterally for a significance level of $p < 0.02$ Bonferroni corrected). While subject motion was very small (< 0.5 mm and $0.5°$), event-related averages calculated for this run was shifted in time and began to rise before the stimulus onset time, as displayed in figure 5.30 (evaluated for a main-effect VOI, as described below). This effect was very likely due to an synchronization problem in the stimulus delivery, such as the CD player suddenly jumping to a different time point in the stimulus track. Such a "jump", although it has been noticed in no other experiment earlier or later, is supported by the localization of significant negative activation along Heschl's gyrus. Also, the raw time course data evaluated for the same functional VOI exhibits the expected response delay of about 2 s for about the first 3 min, from whereon it peaks synchronously with the stimulus offset (as far as can be told from the relatively noisy signal). For this reason, the second session was repeated for that subject under identical conditions but on a different day. Unfortunately, the activation patterns observed in that session were even harder to explain. For the conventional EPI run, there was highly significant activation along Heschl's gyrus, but also some spurious activation medially near the ventricles and also isolated voxels in white matter regions. For the Continuous EPI run, highly significant and extended (positive and negative) activation ($p < 0.001$ Bonferroni corrected) was found in different areas of the brain, but not at the expected location of the auditory cortex. For example, positive activation was found in the thalamus, corpus callosum as well as outside the brain laterally of the pons, and negative activation in large parts of the superior occipital lobe. In this case, the full time course data evaluated for the above VOI revealed no indications of bad synchronization, it just showed periods of very low response to the stimuli alternating with strong, normal appearing responses.

Subject 3. For the third subject, highly significant activation along Heschl's gyrus was found in all four runs. However, in the activation pattern for the conventional EPI sequence found in the second session, where Continuous EPI was measured before the conventional EPI, the extent of the activated area was very small and included only the lateral-most parts of Heschl's gyrus. For that specific run, subject head motion was largest, with three events of sudden motion of up to 1 mm displacement and $0.5°$ rotation. This seems a likely explanation for the lower significance of activation found in that run. The other runs for that subject were also affected by head motion, but at lower levels, with sudden movements below 0.5 mm or $0.5°$.

Subject 4. Subject number four showed conspicuous activation patterns

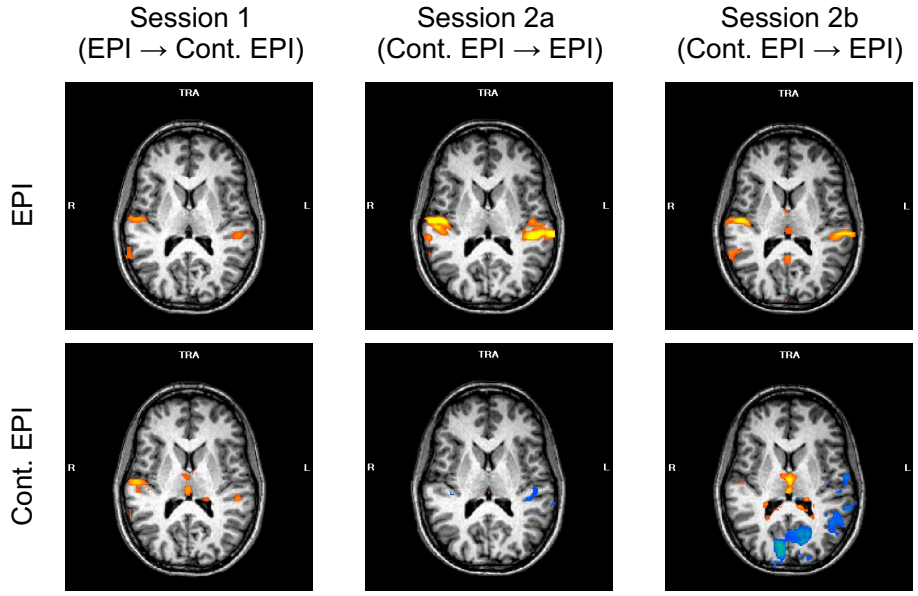

Figure 5.29: Activation patterns for subject 2 in fMRI experiment 5, trial two. Session 2 was repeated, because the Continuous EPI run of session 2a showed a negative time shift presumably due to an error in the synchronization of sequence and stimulus. For the conspicuous activation pattern observed in the Continuous EPI run of session 2b, no obvious explanation has been found.

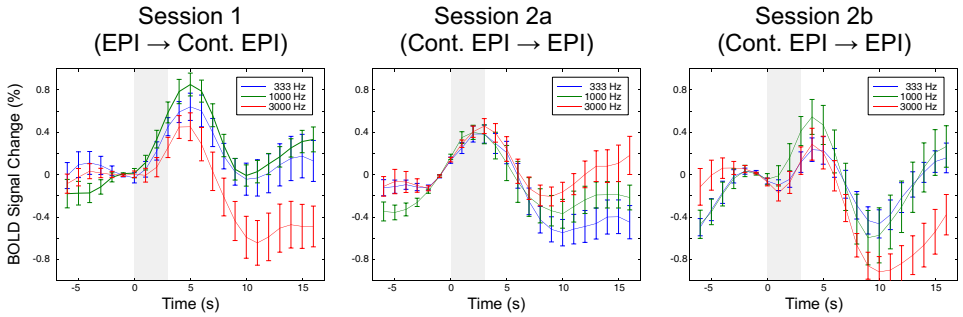

Figure 5.30: Event related averages for the Continuous EPI runs of subject 2 in fMRI experiment 5, trial two. The averages were evaluated in volume of interest based on a main effect GLM over all subjects and runs ($t = 4$). Note the time shift in session 2a, where the BOLD response begins to rise before the stimulus interval (gray shaded area).

in all four runs (figure 5.31). While highly significant activation along Heschl's gyrus was found in all four runs (in the conventional EPI run of session 1 only on the left hemisphere), there were also extended activated areas in other areas of the brain at the same threshold of $t = 6$, $p < 0.001$ Bonferroni corrected. Subject head movement was generally rather low, with no sudden motion events larger than 0.5 mm or 0.5°. The two Continuous EPI runs were more strongly affected than the conventional EPI runs, and especially in the Continuous EPI run of session 2 (the first functional run of that session) motion was repeatedly synchronous with the stimulus onset, as shown in figure 5.32. Such a synchronization can be easily explained by the subject being startled by the beginning of the (loud) auditory stimulus and might explain false activation in areas of high image contrast, such as near the ventricles. Stimulus-correlated motion was also present in the other runs and may at least partly explain the spurious activation found in this subject. Sudden motion events were of extremely low amplitude (less than 0.2 mm and 0.2°) for the conventional EPI run of the first session, combined with gradual motion of only 0.5 mm. It was precisely this run, however, that showed the smallest extent auditory activation. Also, the relatively consistent negative activation in the visual cortex remains somewhat worrying. In the conventional EPI run of the first session, where this area is most clearly negatively activated, the time-course data from this area shows large amplitude fluctuations, which follow the auditory stimulation only incidentally (in contrast to the low amplitude but relatively consistent activation in the auditory areas).

Subject 5. In subject 5, highly significant auditory activation was found in all but the conventional EPI run of the second session (figure 5.33). While the Continuous EPI run of the first session showed extended activation along Heschl's gyrus and areas in the planum temporale and planum polare ($t = 6$, $p < 0.001$ corrected), the EPI run of the second session (where it was the first functional run) revealed no activated pixels at the same threshold. At a lower, but still significant threshold of $t = 5$ ($p < 0.029$ corrected), activation was found bilaterally along Heschl's gyrus, albeit of somewhat limited extent. That run had a relatively large motion event near the middle of the time series (of about 0.4 mm) which may partly explain the lower significance in activation. The Continuous EPI run of the first session follows a similar pattern. Here, activation is restricted to right Heschl's gyrus at $t = 6$ but is found bilaterally at $t = 5$ ($p < 0.033$ Bonferroni corrected). This run was also affected by two sudden motion events of about 0.3 mm displacement, which were additionally both synchronous with the stimulus onset. Finally, in the Continuous EPI run of the second session, where highly significant activation is only seen for the right Heschl's gyrus at Talairach $z = 7$, activation along left Heschl's gyrus was also found at the same threshold of $t = 6$, but located somewhat more superior and posterior (centered at Talairach x=−43, y=−26, z=14).

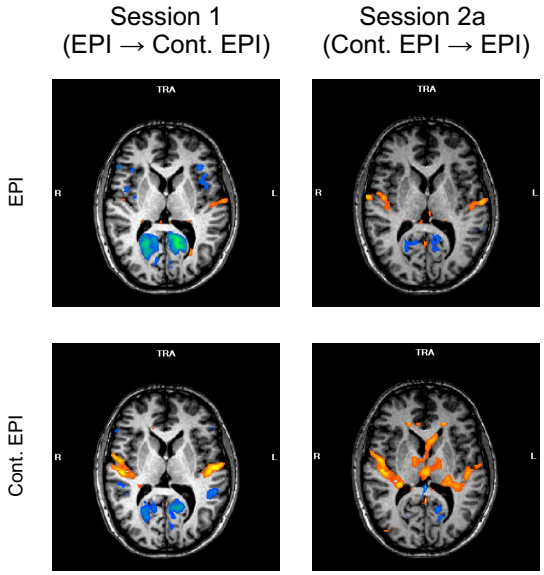

Figure 5.31: Conspicuous activation patterns found in all four runs of subject 4 in fMRI experiment 5, trial two. All maps are thresholded at $t = 6$, $p < 0.001$ Bonferroni corrected and located at Talairach z=7.

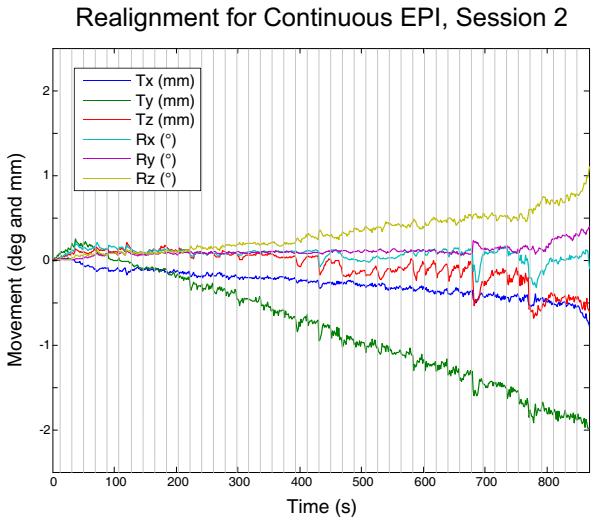

Figure 5.32: Estimated subject head motion for subject 4 in fMRI experiment 5, trial two. Motion parameters were calculated from the image time-series during preprocessing in BrainVoyager QX. Note the motion events synchronous with the stimulus onset (gray lines) especially for times 600-700 s after the beginning of the scan.

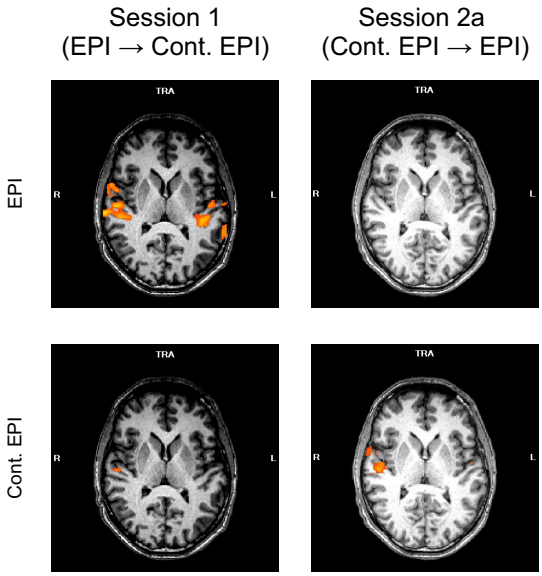

Figure 5.33: Activation patterns for subject 5 in fMRI experiment 5, trial two. All maps are thresholded at $t = 6$, $p < 0.001$ Bonferroni corrected and located at Talairach z=7.

Subject 6. In subject 6, spurious activation was present in all four runs (figure 5.34). Interestingly, the two runs from the first session, where relatively consistent activation is found along Heschl's gyrus bilaterally, were also afflicted with the most extensive head motion of all subjects and runs (figure 5.35). In the case of the conventional EPI runs, these motion events were sometimes even synchronous with stimulus onset, and in one case almost 1 mm in translation and more than 1° rotation. While a certain amount of head motion can be expected for a scan of 15 min, subject head motion was nowhere as severe as in these runs in any of the earlier experiments (with the same paradigm). The head motion may well explain the spurious activation near the centerline and at the border of the ventricles in these runs, rather it seems a bit mysterious why the auditory activation was seen here so clearly. For the runs of the second session, which were also showing relatively strong head motion, but less than the runs of session one, there was positive as well as negative highly significant ($t = 6$, $p < 0.001$ corrected) activation in different areas of the brain. Along Heschl's gyrus, activation was found only for the Continuous EPI run in the right hemisphere. At $t = 5$, $p < 0.33$ corrected, both runs revealed bilateral activation along Heschl's gyrus among quite numerous other activation sites. Somewhat similarly to subject 4, predominantly negative activation was found in the occipital lobe, while areas near the thalamus and at the superior border of the ventricles were positively activated. It has to mentioned that due to

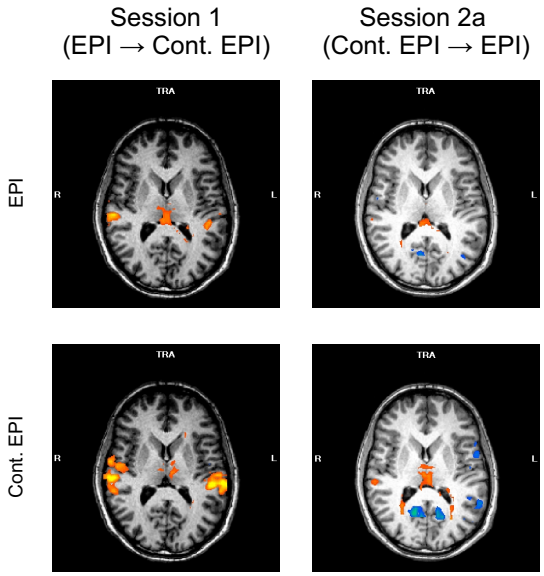

Figure 5.34: Activation patterns for subject 6 in fMRI experiment 5, trial two. All maps are thresholded at $t = 6$, $p < 0.001$ Bonferroni corrected and located at Talairach z=9. Strangely the runs of the first session were afflicted by worse head movement than the second and still showed activation patterns closer to what was expected.

an operating error, the sequence was stopped for the conventional EPI run of the second session after 529 of 574 volumes. Therefore, the two runs of that session were analyzed only for the first 529 volumes, with two repetitions of the 1 kHz tone, one 333 Hz tone and one 3 kHz tone omitted. While there is no a priori reason while such shortened runs should have resulted in such spurious activation, the lessened statistical averaging may have worsened whatever problems were responsible for these patterns.

Event-Related Averages The activation patterns observed were so different between subjects and runs that less than 500 voxels (of $1\times1\times1\,\mathrm{mm}^3$) survived the conjunction analysis over all runs even at the lowest possible threshold of $t=0.05$ (a software limitation). It was therefore chosen to conduct the analysis based on the main effect GLM (one predictor containing all three frequencies for each run), thresholded at $t=4$ to obtain a volume of interest for event-related averaging (figure 5.36, containing 17500 voxels). This sort of definition for a functional VOI is different from trial 1 of this experiment as well as both preceding fMRI experiments (3 and 4) with the tonotopy paradigm. On the other hand, it has been successfully used in the Continuous EPI paper by Seifritz et al. [152] and is a valid way to define a functional VOI event though it is biased in favor of the runs containing the

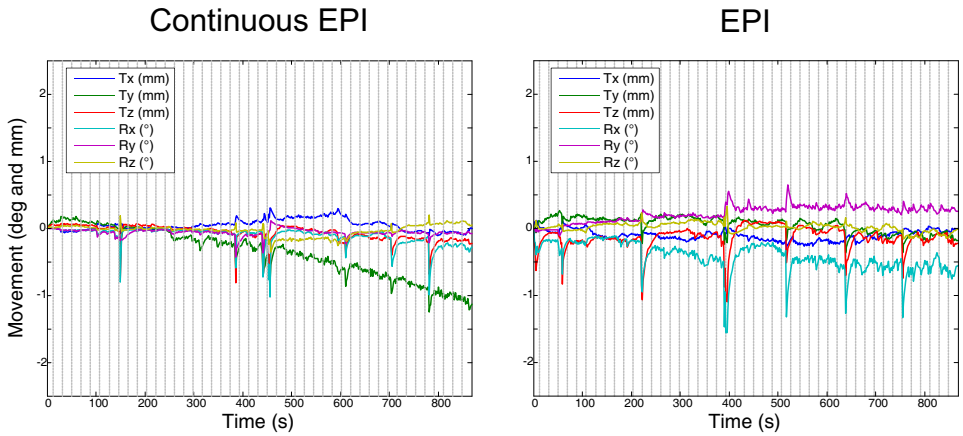

Figure 5.35: Realignment data for the first session of subject 6 in fMRI experiment 5, trial two. Head motion was quite excessive and sometimes synchronous with stimulus onset (especially in the conventional EPI run).

Figure 5.36: Volume of interest used to evaluate event related averages in fMRI experiment 5, trial 2. The volume was defined as the area activated in a main effect GLM over all subjects and runs, thresholded at $t=4$.

strongest activation (which was a desired effect in this case).

Group event related averages over all subjects and sessions are shown in figure 5.37. Because all datasets but that of the first subject contained problems of some sort, it was hard to define exclusion criteria. Therefore, all runs were included in the analysis, with the exception of session 2a from subject 2 (which contained the synchronization error). Here, the BOLD response to the tonotopy paradigm is not clearly different measured with Continuous versus conventional EPI. The trend still goes towards a larger percent signal change for Continuous EPI, but is hardly compatible with the approximately 25–30% measured in the three previous experiments. When measured using a quadratic polynomial to fit the five time-points nearest to the maximum, the group event related averages give a higher BOLD response for the Continuous EPI by 3.8% for the 333 Hz tone, 11.5% for the 1 kHz tone and 3.6% for the 3 kHz tone.

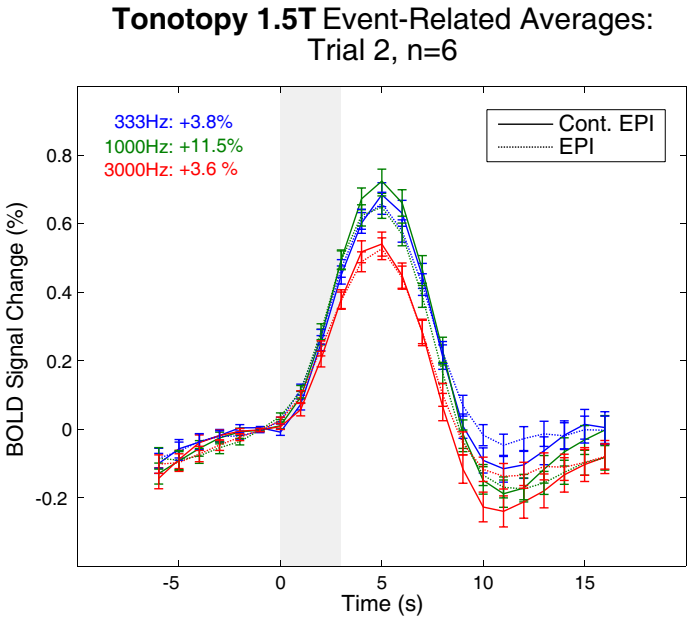

Figure 5.37: Group event related averages over all subject of fMRI experiment 5, trial 2. Here, the BOLD response to the tonotopy paradigm measured with Continuous EPI tends to be larger but is not clearly different from that measured with conventional EPI.

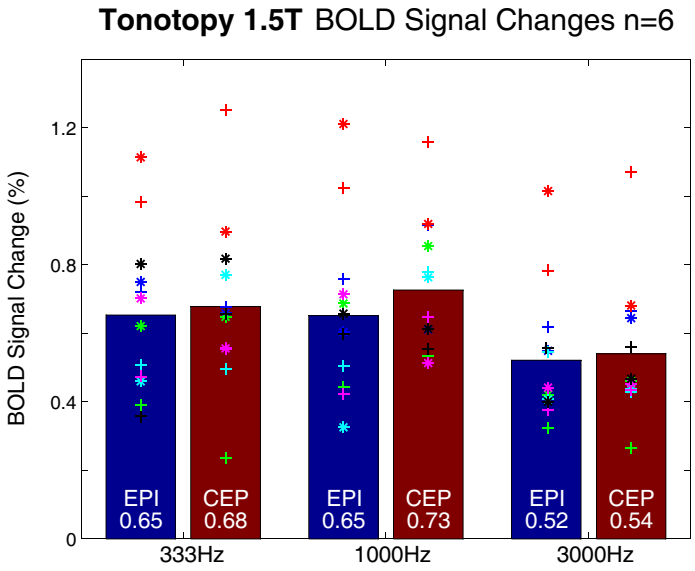

Figure 5.38: BOLD percent signal changes for the group of all subjects (bars) and for the individual subjects of fMRI experiment 5, trial 2. The stars correspond to session 1, in which Continuous EPI was measured after the conventional EPI, and crosses to session 2, with inverse sequence order.

BOLD percent signal changes in the individual subjects graphically displayed in figure 5.38. Here, bars correspond to the above group averages, stars to the first session (in which the Continuous EPI was measured after the conventional EPI) and crosses to the second session values of the individual subjects. Notably, the BOLD percent signal change from subject 3 (red), who showed the most consistent and significant activation patterns, are also consistently higher than for the other subjects. The individual subject percent signal changes, averaged over the two sessions of each subject, are given in the following table.

Sequence	Freq.	Subj.1	Subj.2	Subj.3	Subj.4	Subj.5	Subj.6
conv.EPI	333 Hz	0.74	0.51	1.05	0.48	0.59	0.58
	1000 Hz	0.68	0.57	1.12	0.41	0.57	0.63
	3000 Hz	0.58	0.37	0.90	0.48	0.41	0.48
Cont.EPI	333 Hz	0.67	0.44	1.07	0.63	0.55	0.74
	1000 Hz	0.76	0.69	1.04	0.77	0.58	0.58
	3000 Hz	0.65	0.36	0.88	0.43	0.44	0.51

As the large variance of the subject percent signal changes in figure 5.38 suggests, the trend towards a higher BOLD response amplitude for the Continuous EPI sequence is not statistically significant. The probabilities

of such an effect to be observed by chance under the null hypothesis of no difference between the two sequences, is $p < 0.7$, $p < 0.24$ and $p < 1$ for the three frequencies. Again these values were determined by a paired, non-parametric (Wilcoxon rank sum) test using above session-averaged subject values.

Since two sessions with different sequence ordering were acquired for each subject, it is again possible to quantify a session effect between the first and second functional run. For this, event-related averages were evaluated for the same volume of interest as above, but with all first and all second functional runs (of all sessions) averaged separately. The evoked BOLD response was larger in the first sequence by $22 \pm 7\%$ for the 333 Hz tone, by $2 \pm 7\%$ for the 1 kHz tone but larger by $3 \pm 9\%$ for the 3 kHz tone (mean±standard errors, calculated from mean and standard error of the time point with maximum amplitude). As in the previous experiments, there is a trend for a session effect in the direction of decreasing BOLD amplitudes over an imaging session, compatible with the hypothesis of decreasing attention levels. However, it has to be cautioned that because of the large variance in the BOLD percent signal changes, this effect can also not be regarded as being of any statistical significance.

Discussion In summary, this experiment has extended the observed (and expected) trend towards a larger BOLD response amplitude for Continuous EPI in he previously used tonotopy paradigm to 1.5 T. However, various complications have arisen, ranging from stimulus-correlated subject motion to a very likely stimulus synchronization error in one subject. As a result, the observed activation patterns showed sometimes unexpected patterns, and a volume of interest based on a conjunction analysis could not be used in this case to calculate event-related averages. Instead, a main effect based volume was used. The group event related averages showed a smaller than expected trend towards a larger BOLD response amplitude for the Continuous EPI. Also, this trend was not statistically significant in spite of the larger number of subjects used in this experiment (compared to the earlier experiments). The reason for this is found in the large inter-individual as well as session differences, which are likely due to similar problems as the low significance levels in the functional activation maps. Such a conclusion is supported by the consistently larger BOLD response amplitudes for the subject with the most significant and consistent activation pattern (although it has to be cautioned that that subject very likely contributed disproportionately to the selection of the main effect based volume of interest). In spite of all the advantages of the tonotopy paradigm, its long duration (of 15 min) as well as its sub-optimal statistical power (due to the short stimulation intervals) can be seen as factors contributing to this. On the other hand, the lower contrast to noise ratio of a 1.5 T, relative to higher field systems as well as

the better acoustic damping (higher acoustic contrast between stimulus and sequence sound) of the Avanto system relative to most other 1.5 T machines (including the Sonata used in fMRI experiment 1), can be listed as other possible factors explaining the large variance observed in this experiment.

5.8 fMRI Experiment 6: Possible Non-Acoustic Effects

5.8.1 Experiment Design

Motivated by the very large inter-individual differences and the observation of unexpected activation patterns in the preceding experiment, the aim of this experiment was to pinpoint some of the problems encountered there and test some of the assumptions that had influenced the design of the Continuous EPI implementation but had remained untested to this point.

The experiment was divided into three parts: a visual stimulation experiment to verify the assumption that conventional and Continuous EPI would measure the same amplitude BOLD response in a non-auditory area such as the visual cortex (something that had been shown for the original implementation of Continuous EPI [151] in the Seifritz et al. [152] paper, see figure 3.4). Then, a series of short (3 min) block design auditory experiments (all using the same stimulus) were designed to compare BOLD response amplitudes in the auditory cortex between seven different sequence variants. And finally, a pair of 5 min block design experiments using the same auditory stimulus, but with variations in sound level to test the assumption that the effect of Continuous versus conventional EPI was independent of sound level.

For this experiment, six volunteers were recruited and measured in a single session, but with the order of conventional and Continuous EPI balanced over the subjects (three with conventional and three with Continuous EPI measured first for each pair of sequence comparison runs, as listed below). For each subject, a T_1 weighted MPRage volume was first acquired and used to position the slices in the functional runs. Then, the two runs with visual stimulation were acquired, followed by the seven backwardspeech runs and finally the sound level graded backwardspeech runs. The sequential order of the functional runs is listed in the following table.

Nr.	Subj.1	Subj.2	Subj.3	Subj.4	Subj.5	Subj.6
1	VCE	VEP	VEP	VEP	VCE	VCE
2	VEP	VCE	VCE	VCE	VEP	VEP
3	CKS	EPI	EPI	KSL	CEP	CEP
4	EKS	CEP	CEP	EKS	EPI	EPI
5	KSL	CGN	CGN	CKS	EPD	EPD
6	EPD	EPD	EPD	CGN	CGN	CGN
7	CGN	KSL	KSL	EPD	CKS	CKS
8	CEP	EKS	EKS	EPI	EKS	EKS
9	EPI	CKS	CKS	CEP	KSL	KSL
10	3CE	3EP	3EP	3EP	3CE	3CE
11	3EP	3CE	3CE	3CE	3EP	3EP

Here, additional shorthands VCE and VEP have been introduced for the visual experiment with Continuous and conventional EPI, CEP, EPI, CGN, EPD, CKS, KSL and EKS (explained below) for the seven different sequences in the auditory block design experiments, and 3CE, 3EP for the volume graded backwardspeech runs with Continuous and conventional EPI.

To keep the influence of session effects as low as possible, the order of sequence comparison pairs within the seven backwardspeech runs was interchanged between subjects. As a further measure to keep subject attention at a constant level, a silent cartoon movie was continuously shown during all auditory runs. The movie, "La Linea" by Osvaldo Cavandoli, consisted of short but similar episodes of about two minutes, in which a very simple line drawing of a man experienced various humorous situations. The simplicity of the (mostly two-colored) cartoon was advantageous in this situation, as subjects normally wearing glasses reported having easily been able to follow the story in the cartoons.

One of the volunteers was female, five male, five right handed and one left handed but writing with his right. The age of the subjects was 32.3 ± 6.6 (mean $\pm$ standard deviation). Volunteers were instructed to lie very still throughout the entire experiment and watch the movie, but not to listen specially to the stimulus sounds. The volume of the auditory stimulus was adjusted individually at the beginning of the experiment to be perceived as loud but not painful. The resulting volume was, for subjects 1 through 6 (reading on the amplifier): 50, 50, 60, 60, 61 and 61.

5.8.2 Paradigms and Stimuli

Visual Block Design The visual stimulus was an inverting radial checkerboard flickering at 5Hz. The checkerboard bitmap shown in figure 5.39 (created using Matlab) and a brightness inverted copy were alternated at 5 Hz in ePrime and back-projected onto an acrylic glass screen inserted into the

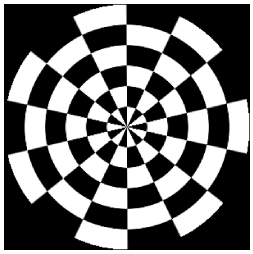

Figure 5.39: The flickering checkerboard stimulus used in the visual task of fMRI experiment 6. The bitmap, back-projected onto a semi-transparent screen in the magnet bore, alternated with its brightness inverted copy five times per second.

head end of the scanner. The video beamer was located along the axis of the magnet, screwed to the wall and encased in a Faraday cage to minimize RF artifacts in the MR images. The subjects viewed the screen over a double mirror attached to the head coil. While the viewing field was somewhat restricted by this setup, a large portion of the stimulus was seen on the screen and visual contrast was high. The lights in the scanner room were turned off for the experiment and subjects were instructed to keep looking at the center of the checkerboard throughout the stimulation periods and at a small fixation cross (on black background) during the rest periods.

Stimulus epochs of 16 s were interleaved with fixation periods of the same duration, with an additional fixation period at the beginning. The paradigm consisted of five stimulation cycles for a total scan time of 3 min. Synchronization of the stimulus and sequence start was again performed manually.

Backwardspeech block design For the auditory experiments, a backwardspeech stimulus was chosen instead of the pulsed sine tones used earlier. The main objective behind this decision was to include a broader range of frequencies in a single stimulus perceived as relatively "interesting" in order to minimize session effects due to decreasing attention levels. While instrumental music (in contrast to, for example, amplitude modulated white noise) would also have fulfilled these requirements, it seemed easier to obtain a natural, yet uniform, amplitude modulation profile ("rhythm") with a speech than a music stimulus. The time reversal was performed in order to exclude content dependent, language specific and emotional components as far as possible.

The stimulus was based on a 5 min excerpt from a German audio book read by a female voice which was digitally time-reversed. Longer pauses were removed manually to maintain a relatively constant frequency spectrum (figure 5.40) while retaining the rhythm of human speech. It covered

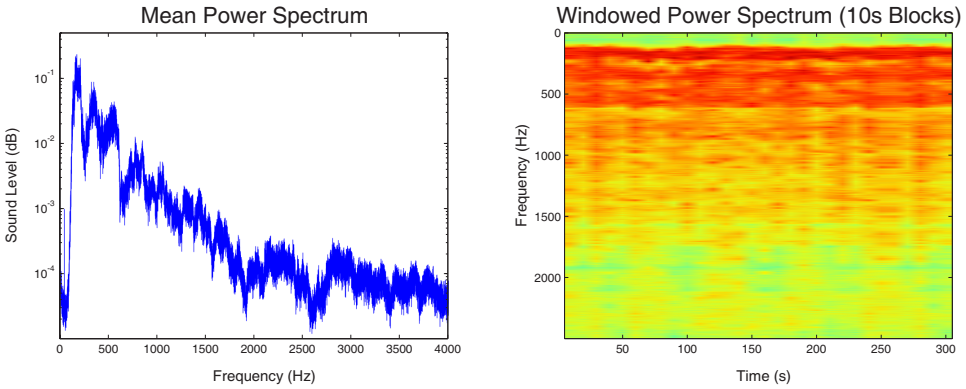

Figure 5.40: Mean frequency spectrum and temporal frequency pattern of the backwardspeech stimulus used in fMRI experiment 6. The left figure shows the mean power spectrum over the entire 5 min excerpt (averaged over 10 s blocks). In the right figure, the logarithmic power spectra over 10 s intervals are color coded to demonstrate the temporal uniformity of the stimulus over its entire duration.

a relatively broad frequency range (fig. 5.40, left), which was relatively constant over the entire length of the sample (fig. 5.40, right). Some of the subjects spontaneously described their experience with the stimulus as feeling as if they should be able to understand the meaning of the words, while not being able to do so.

According to Harms et al. [117], speech stimuli (similar to music) evoke only a relatively mild onset-response but are dominated by as strong sustained response (see figure 2.4). In that respect, speech stimuli are very similar to low-rate amplitude modulated (or pulsed) tones, and make the stimulus function, convolved with a canonical HRF a rather good predictor of the expected BOLD response.

For the block design experiment, five consecutive samples of 16 s from the 5 min excerpt were used, with 16 s silent rest conditions interleaved, and 20 s silence in the beginning. The total scan time for these runs was 3 min. The stimulus was recorded on CD, delivered over the high fidelity MR audio system used in the previous experiments and synchronized manually with the sequence start. The sound level was again adjusted individually to be perceived as very loud but not painful.

Backwardspeech with Graded Sound Levels For the volume-graded paradigm, only the first 16 s sample form the 5 min excerpt was used for all the stimulation periods, to ensure comparability between the different sound levels. Three different sound level stimuli were prepared, (a) one with full volume (individually adjusted to the maximum level that was not perceived as painful), (b) with the waveform scaled with $1/e$ for an attenuation of

$-8.7\,\mathrm{dB}$ and (c) a third attenuated by $-17.4\,\mathrm{dB}$ (waveform scaled with $1/e^2$). The three different stimuli (16 s in duration) were presented in a Latin square pseudo-randomized order [bac, acb, cba], with 16 s silence after each stimulus as well as in the beginning. The total scan time for this paradigm was $5:10\,\mathrm{min}$. As in the other auditory experiments, the stimulus was presented from CD over a high fidelity MR audio system and synchronized manually with the sequence start.

5.8.3 Sequence

For this experiment, seven different sequences were used. For one thing, conventional and Continuous EPI sequences with the same sequence parameters as in fMRI experiment 5, trial two, were used (with only a slightly larger flip angle). In the following, the shorthands **CEP** and **EPI** are used to refer to those sequences. To evaluate the influence of the additional bipolar gradients on the measured BOLD percent signal changes, two specialized sequences were derived from the Continuous EPI and conventional EPI implementations. The first, **CEN**, was equal to the Continuous EPI sequence, using the same water selective binomial 1-1 pulses, but with no repeated bipolar gradients. This made the pulsation with the slice repetition frequency audible again (i.e. the sequence sound was not continuous any more) but to a lesser extent than in the conventional EPI sequence. The other, **EPD**, was the same as the conventional EPI sequence, but had the same number and magnitude of bipolar gradients as in the Continuous EPI sequence added in between the acquisition of the navigator echoes and the beginning of the readout train. Finally, three sequences were used to compare the here described implementation of the Continuous EPI sequence to original implementation by Klaus Scheffler [151] which is denoted by **KSL**. It was compared to a "matched" conventional EPI sequence **EKS**, which used the same echo and repetition times, the same readout bandwidth, the same triangular readout gradients with the same amount of ramp sampling and also no fat suppression technique. The third sequence in this group was a continuous EPI sequence **CKS** with parameters matched to the KSL sequence as far as possible. However, it used water selective 1-1 pulses as above to suppress the fat signal, sinusoidal readout gradients and had a lower fundamental frequency in its gradient sound. In all auditory runs, slices were positioned parallel to the Sylvian fissure and centered on Heschl's gyrus.

For the visual stimulation paradigm, the CEP and EPI sequences were compared with the number of slices increased from 16 to 24 and therefore used a longer TR of 2273.1 ms instead of 1515.4 ms. All other sequence parameters were the same as for the auditory experiments. Slices were positioned parallel to the inferior border of the cerebrum and cerebellum, for almost full brain coverage with inferior-most slices including the posterior

part of the cerebellum.

In the volume graded auditory paradigm, both CEP and EPI sequence were identical to those for the single volume block design paradigm, with the only difference that the flip angle was set to 75° as in fMRI experiment 5 trial 2 instead of 78°.

Sequence parameters were: **(CEP)** for the Continuous EPI sequence: TE=47.32 ms, TR=1515.4 ms, 16 slices of 3.4 mm thickness, image matrix 64×64, bandwidth 1280 Hz/px, FOV=21.76 cm (resulting in an isotropic voxel size of 3.4 mm^3), flip angle 78°, ramp fraction 0.6, binomial 1-1 pulse water excitation, 5 blocks of 16 readouts, fundamental frequency of the sequence sound 52.8 Hz, sound level 77.8 dB(A). **(EPI)** for the conventional EPI: TE=47.32 ms, TR=1515.4 ms, 16 slices of 3.4 mm thickness, image matrix 64×64, bandwidth 1280 Hz/px, FOV=21.76 cm (resulting in an isotropic voxel size of 3.4 mm^3), flip angle 78°, ramp fraction 0.6, binomial 1-1 pulse water excitation, sound level 81.4 dB(A). **(CEN)** for the Continuous EPI sequence without repeated bipolar gradients: TE=47.32 ms, TR=1515.4 ms, 16 slices of 3.4 mm thickness, image matrix 64×64, bandwidth 1280 Hz/px, FOV=21.76 cm (resulting in an isotropic voxel size of 3.4 mm^3), flip angle 78°, ramp fraction 0.6, binomial 1-1 pulse water excitation, 5 blocks of 16 readouts, fundamental frequency of the sequence sound 52.8 Hz, sound level 77.3 dB(A). **(EPD)** for the conventional EPI sequence with additional bipolar (diffusion) gradients: TE=47.32 ms, TR=1515.4 ms, 16 slices of 3.4 mm thickness, image matrix 64×64, bandwidth 1280 Hz/px, FOV=21.76 cm (resulting in an isotropic voxel size of 3.4 mm^3), flip angle 78°, ramp fraction 0.6, binomial 1-1 pulse water excitation, sound level 81.6 dB(A). **(KSL)** for the original Continuous EPI sequence implementation by Klaus Scheffler [151]: TE=60.83 ms, TR=1769.6 ms, 16 slices of 3.5 mm thickness, image matrix 64×64, bandwidth 1280 Hz/px, FOV=22.0 cm (resulting in a voxel size of $3.44 \times 3.44 \times 3.5$ mm^3), flip angle 81°, ramp fraction 0.4, no fat saturation, 10 blocks of 10 readouts, fundamental frequency of the sequence sound 90.4 Hz, sound level 83.0 dB(A). **(CKS)** for the Continuous EPI sequence with parameters as close to those of KSL was possible: TE=60.84 ms, TR=1756.4 ms, 16 slices of 3.5 mm thickness, image matrix 64×64, bandwidth 1280 Hz/px, FOV=22.0 cm (resulting in a voxel size of $3.44 \times 3.44 \times 3.5$ mm^3), flip angle 81°, ramp fraction 0.35, binomial 1-1 pulse water excitation, 8 blocks of 10 readouts, fundamental frequency of the sequence sound 72.9 Hz, sound level 81.7 dB(A). **(EKS)** for the conventional EPI sequence matched to KSL: TE=60.83 ms, TR=1769.6 ms, 16 slices of 3.5 mm thickness, image matrix 64×64, bandwidth 1280 Hz/px, FOV=22.0 cm (resulting in a voxel size of $3.44 \times 3.44 \times 3.5$ mm^3), flip angle 81°, ramp fraction 0.4, no fat saturation, sound level 80.5 dB(A). All sound levels were measured in the scanner room, but away from the magnet bore. The ambient noise level was 49.6 dB(A).

Figure 5.41: Volume of interest used in the visual stimulation runs of fMRI experiment 6 to evaluate event related averages. It is defined as the conjointly activated area in all subjects and runs at $t = 2$ and included 27615 voxels of $1\,\mathrm{mm}^3$ isotropic. The displayed slice is located at Talairach x=9, y=−87, z=−8.

5.8.4 Visual Response

In the visual runs of all subjects, highly significant activation (at $t = 6$, $p < 0.001$ Bonferroni corrected) was found. In some but not all cases, false positive activation at this threshold was also found along the superior sagittal sinus, for one subject these voxels were negatively activated. The conjoint activation over all subjects and runs, thresholded at $t = 2$ (shown in figure 5.41), was used to evaluate event related averages for group of all subjects and for each subject individually.

The group result, shown in figure 5.42 is compatible with the hypothesis of equal BOLD responses for a visual stimulus (individual BOLD amplitudes $p < 1$ Wilcoxon rank sum test), as was expected form the results of Seifritz et al. [152] (who compared the original implementation of Continuous EPI [151] to conventional EPI in a visual task, compare figure 3.4). In the present experiment, the runs with the conventional EPI sequence evoked a slightly larger BOLD amplitude (1.99 versus 1.90 percent signal change), resulting mainly from the low BOLD response amplitude in the Continuous EPI run of subject 2.

In conclusion, the results from the visual paradigm are compatible with the assumption that the BOLD sensitivity of conventional and Continuous EPI sequences should be equal for non-auditory tasks.

5.8.5 Response to the Backwardspeech Block Design

Highly significant activation at a threshold of $t = 6$, $p < 0.001$ Bonferroni corrected, was found along Heschl's gyrus in all 42 runs using the (single sound level) backwardspeech block design paradigm. It was lowest in extent for the CKS and EKS runs of subject 2 (the last two backwardspeech runs in that subject) and in the CGN and EKS runs of subject 4 (the second and

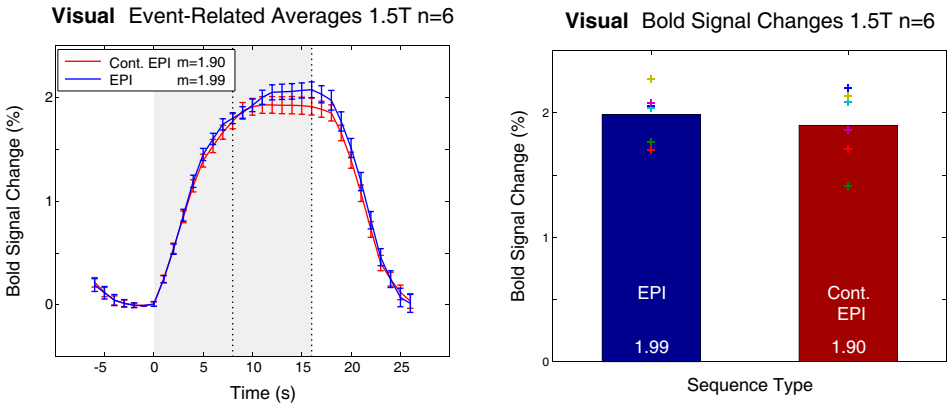

Figure 5.42: Group event related averages (left) and BOLD percent signal changes (right) for the visual task of fMRI experiment 6. Event related averages were evaluated for the conjointly activated area at $t = 2$, BOLD percent signal changes calculated from the individual event related average time courses, averaged over the interval 8 to 16 s after stimulus onset (dotted lines in the left figure)

fourth of seven backwardspeech runs).

In spite of the robust activation over all runs, the differences between runs and especially between subjects was so large that only four significantly activated voxels (of 1 mm^3 isotropic) on lateral left Heschl's gyrus were found in a conjunction analysis over all 42 runs (thresholded at $t = 4.8$, $p < 0.03$ Bonferroni corrected). For the volume of interest to be used in event-related average comparisons, the threshold was lowered to a minimal $t = 0.05$, which resulted in the conjointly activated area depicted in figure 5.43.

Comparison of the Present and Original Implementation One important question addressed by the backwardspeech runs of this experiment is whether the preset Continuous EPI sequence (CEP) shows the same advantage over continuous EPI (EPI) as the original implementation by Scheffler and Seifritz [151] (KSL) over a matched EPI sequence (EKS). Event-related average time courses and BOLD percent signal change values calculated for the time interval 8-16 s after stimulus onset (dotted lines) are shown in figure 5.44. The shape of the response time courses is as expected. For the six subjects measured here, only the larger BOLD response in the original implementation KSL, compared to the matched EKS conventional EPI sequence is statistically significant ($p < 0.03$ Wilcoxon rank sum test). The other two Continuous EPI sequences CKS and CEP also resulted in larger BOLD percent signal changes than the respective conventional EPI sequences (EKS and EPI). However, in those cases the group average difference between

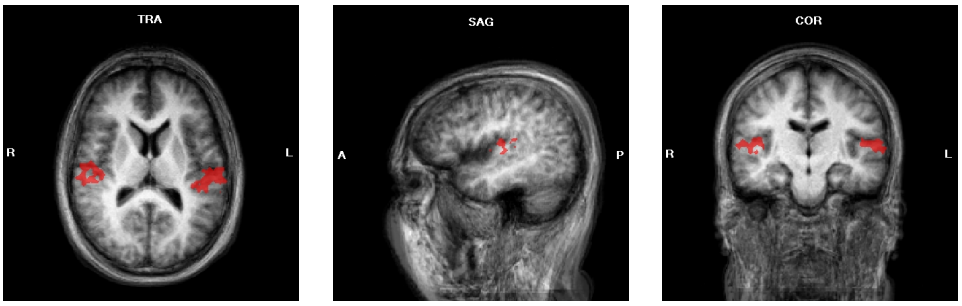

Figure 5.43: Volume of interest used to evaluate event-related averages in the (single sound level) backwardspeech runs of fMRI experiment 6. The volume was determined as the conjointly activated area for all 42 runs at $t = 0.05$. Here shown centered on right Heschl's gyrus at Talairach coordinates x=44, y=−17, z=11.

Continuous and conventional EPI sequences is of smaller magnitude than that observed for the KSL sequence, but also not significantly different from it.

In summary, the comparison of the original Scheffler and Seifritz [151] implementation of Continuous EPI and the implementation developed in the current work did not lead to statistically significant results (with the exception of the previously demonstrated advantage of the original implementation over conventional EPI). Still, the trends seen in the results are worrying, the improvement of the current implementation of Continuous EPI over conventional EPI is only half as large as that of the original implementation over EPI (improvements of 12 versus 28%).

If the non-significant trends seen in this experiment can be seen as indications of the actual sequence performance, a few additional issues can be addressed. The two conventional EPI sequences, "EPI" and "EKS" lead to very similar BOLD response amplitudes, even though the EPI sequence used binomial pulse water excitation while the EKS sequence had no fat suppression. This indicates that the water excitation pulses likely play no role in a potentially smaller BOLD response amplitude in the current, versus the original Continuous EPI implementations. One systematic difference in the CEP, CKS and KSL sequences is the fundamental frequency of the sequence sound. It is lowest for the CEP sequence with 52.8 Hz, followed by the CKS with 72.9 Hz, and the KSL with 90.4 Hz. The fundamental frequency thus correlated with the BOLD percent signal changes measured in this experiment. Although the scanner sound was subjectively perceived as continuous in all three cases, with only the "roughness" (see section 4.2) decreasing in the order of increasing fundamental frequency, this could be interpreted as an indication for a systematic effect which should be further examined (as was subsequently done in fMRI experiment 7).

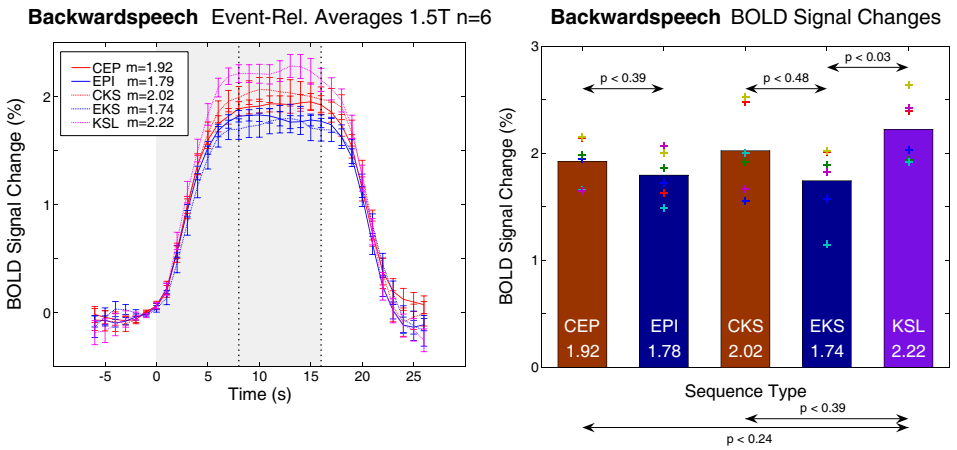

Figure 5.44: Group event related averages (left) and BOLD response percent signal change for the group of all six subjects and for individual subjects of fMRI experiment 6. The only statistically significant difference in BOLD response amplitudes (based on the individual subject percent signal change values) is between the original Continuous EPI implementation KSL and its matched EPI sequence EKS.

Influence of Repeated Bipolar Gradients One of the non-acoustic differences between conventional and Continuous EPI sequences not previously examined is the presence of repeated bipolar gradients to raise the repetition rate of the audible slice selection gradients in the Continuous EPI sequence. Such gradients increase the sequence's sensitivity to motion, flow and molecular diffusion effects. Although these effects could be expected to be of minor importance, two sequences were included in this experiment to test these effects in practice. If, for example, the CEN sequence, equivalent to CEP but with no additional bipolar gradients, resulted in a larger BOLD amplitude in spite of its slightly pulsating sound, then a signal attenuation due to these gradients would be very likely. If no such effect were present, then it could be expected to yield a BOLD amplitude somewhere between CEP and EPI. The EPD sequence (EPI with additional bipolar gradients but clearly pulsed sound), on the other hand, would be expected to result in the same BOLD response amplitude as EPI if these gradients had no influence on the BOLD response amplitude, and a smaller response if such an effect was present.

The results of the comparison of these additional sequences with above standard sequences (based on the same volume of interest and the same data analysis procedure as above) is shown in figure 5.45. The BOLD percent signal change values for CEN and EPI are almost identical, slightly larger for EPD. While the variance among individual subject results is again fairly large, this result supports the hypothesis that the additional bipolar gradi-

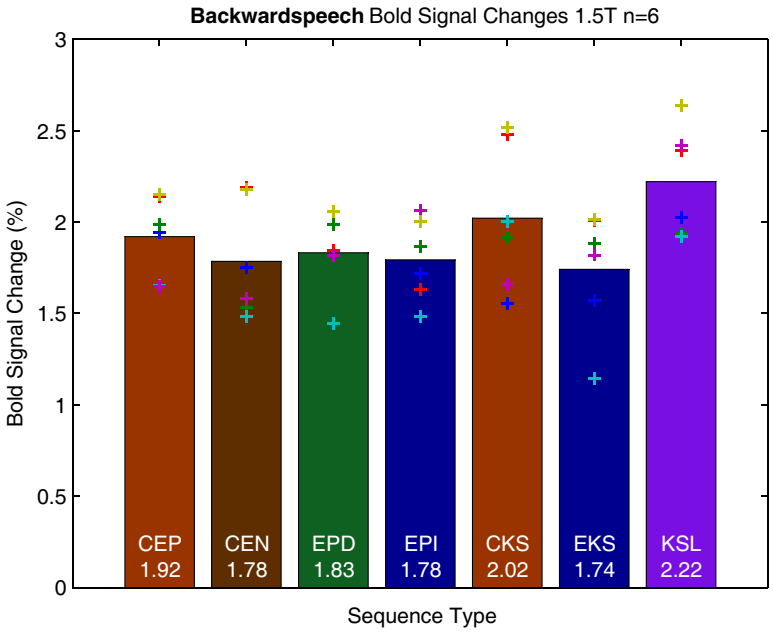

Figure 5.45: Percent signal change values for the CEN and EPD sequences with removed or added bipolar gradients, compared to the sequences of figure 5.44. The bipolar gradients seem to have no direct influence on the measured BOLD response amplitude.

ents have no direct effect on the measured BOLD response magnitudes.

The signal attenuation for moving spins when using the additional bipolar gradients can be expected to be seen most clearly for large vessels with rapidly flowing blood. This was examined for the superior sagittal sinus, which was included in the functional runs of the visual task described above. Figure 5.46 shows the contrast Continuous EPI – conventional EPI , thresholded at a non-significant threshold of $t = 4$. Here, the Continuous EPI indeed gives less task-correlated signal from the sinus vein. Note that voxels from this vein contribution were not present in the volume of interest used to compare the BOLD responses because of the conjunction analysis used to obtain that VOI.

A similarly strong effect in seen neither in the Continuous–conventional EPI contrast for the auditory backwardspeech task nor in the contrast CEP–CEN of the above sequences, which can be attributed to the lack of similarly large draining veins in that region. In conclusion, the use of additional bipolar gradients has no direct influence on the measured BOLD response amplitude in an auditory task. While signal attenuation in a large vein can be found in the comparison of Continuous and conventional EPI for a visual task, no such effect has been found in the auditory experiments.

In any case, an attenuation of flowing spins, especially in draining veins,

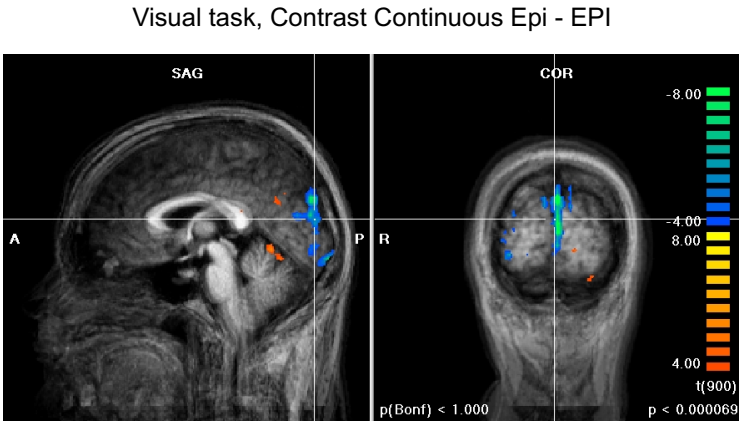

Figure 5.46: Contrast Continuous EPI - EPI in the visual task of fMRI experiment 6. At the non-significant threshold of $t=4$, the Continuous EPI gives less task-correlated signal from the vein, which can be attributed to flow attenuation because of the additional bipolar gradients.

when using Continuous versus conventional EPI, could be seen as both a positive or a negative effect. It could be expected to reduce the BOLD response amplitude (which is larger for the intra- than extravascular signal), but would, on the other hand, lead to an improved spatial accuracy, as BOLD signal from intravascular spins is spatially rather unspecific.

5.8.6 Response to Volume-Graded Auditory Stimuli

One explanation for a smaller than expected difference in BOLD percent signal change between Continuous and conventional EPI could be a generally very high acoustic contrast between the two sequences. It could then be hypothesized that the larger BOLD response for Continuous EPI would be lost because of saturation effects, i.e. that the stimulus was already so clearly audible in the EPI runs that the continuous sound of the Continuous sequence caused no further improvement. One way of testing this hypothesis, the use of different sound levels for the stimuli, was included in this experiment. As described above, the same backwardspeech task as in the other auditory runs was used, but with three sound levels presented in a pseudo-randomized order. If the above hypothesis was true, it could be expected that the difference between Continuous and conventional EPI were largest for the stimulus with the lowest volume. The volume of the loudest stimulus was the same as for the other auditory experiments, the next one was lower by 8.7 dB and the third one by 17.4 dB.

Group event related averages from these two runs are shown in figure 5.47. Here, all the time courses look rather similar, with relatively large error bars and, especially for the lowest volume stimuli, a less-than-perfect return

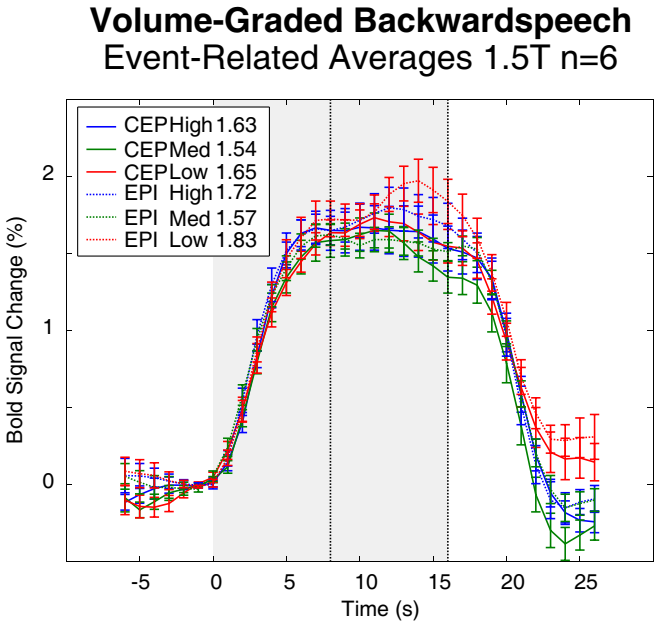

Figure 5.47: Group event related averages for the volume graded backward-speech task of fMRI experiment 6. Response time courses are similar for the two sequences, with a non-significant trend towards a larger response amplitude for the conventional EPI (!) sequence at all three volume levels.

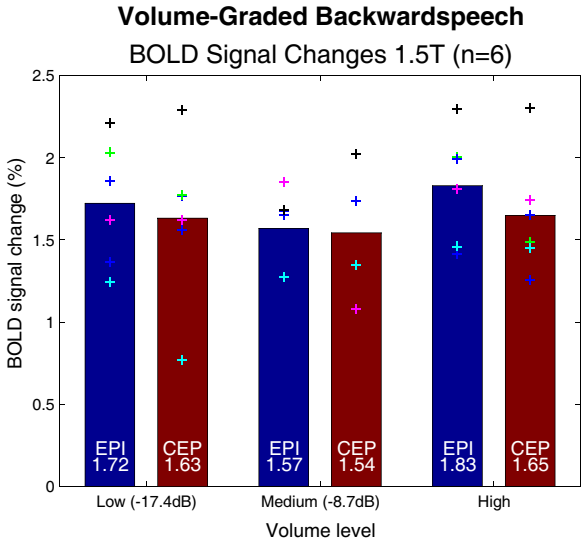

Figure 5.48: BOLD percent signal changes for the volume graded backwardspeech task in fMRI experiment 6. Group averages are plotted as bars, the individual subject values as crosses.

to baseline. Averaged over the interval 8 to 16 s after stimulus onset (dotted lines), there is a trend for the conventional (!) EPI to result in larger BOLD percent signal change at all three volume levels. This is visualized by the bar plot in figure 5.48, where the individual subject values are indicated by crosses. The advantage of conventional EPI, which is in contradiction to the trend observed in the single volume backwardspeech task, amounted to 5.3% for the lowest, 1.7% for the medium, and 10.0% for the highest (or normal) volume stimulus type. As can be guessed from the large variance in the individual subject values, this trend is not nearly statistically significant, with the probability of such a result being observed by chance under the null hypothesis of no effect (Wilcoxon rank sum test) being $p < 0.94$ for the lowest, $p < 0.82$ for the medium and $p < 0.48$ for the highest volume. The low statistical power of the BOLD signal change values found in this experiment can be attributed to the short duration and insufficient averaging in this experiment (every stimulus type was presented only three times per run). If anything, the trend observed here (which for the highest volume stimulus is directly opposed to the opposite trend observed in the single volume experiment) calls into question the predictive power of such non-significant trends.

In conclusion, this experiment with three different volume level stimuli has revealed no statistically significant difference in BOLD response amplitude neither between sequences nor between volume levels. The trend towards a slightly larger BOLD response amplitude for the conventional

EPI sequence (consistent over volume levels), which is at least for the highest volume stimulus in direct contradiction to the opposite trend observed in the single volume paradigm, highlights the danger of over-interpreting such non-significant trends. It has to be concluded that the statistical power afforded by the design of this experiment was clearly insufficient. Either more stimulus repetitions per run (only 3 repetitions per stimulus type in this, compared to 5 in the single volume backwardspeech runs) or more subjects and sessions (or both) would have led to more conclusive results. Also, based on the subjective ratings of the volunteers, it should be noted that even the lowest stimulus was perceived very clearly over the scanner noise background, and a further reduction in the lowest stimulus sound levels might also be advisable in such an experiment.

5.8.7 Influence of Other Effects

Irregular Echo Spacing One inherent difference between Continuous and conventional EPI is the clustering of the readouts in the Continuous EPI into blocks separated by fixed delays. While the influence of this irregular echo spacing on image quality has already been explored in section 5.2.1, its influence on the BOLD sensitivity of the sequence have hitherto not been considered. Because in all experimental comparisons, equal readout bandwidths and equal echo times were used for the conventional and Continuous EPI sequences, the Continuous EPI readout trains were always longer (by the total duration of readout gradient free intervals) and k-space line dependent T_2^* weighting equal only for the central k-space lines in both sequences.

To investigate this effect, a very simplistic numerical simulation was carried out. It consisted of a circular numerical phantom with a T_2^* relaxation time of 65 ms (a literature value for brain gray matter at 1.5 T) with three "activated" areas with a 5% increase in T_2^* relaxation time, corresponding to 1.7% BOLD signal change for an echo time of 48 ms (figure 5.49, left). The "activated" and "non-activated" regions were separately Fourier transformed, and filtered with a T_2^* decay which either corresponded to the constant echo spacing of conventional EPI or the periodically stepped echo spacing of Continuous EPI. After reconstruction, the two images were combined and the reconstruction of a similarly filtered purely circular phantom (without "activated" regions) subtracted to give "activation" maps corresponding to the two sequences.

The "activation maps" were visually indistinguishable and gave about 1.7% signal change in the "active", compared to the "resting" regions (the map corresponding to the regular conventional EPI echo spacing is shown in figure 5.49, right, scaled from black=0 to white=1.8% signal change). The difference image of the maps for conventional minus Continuous EPI echo spacings is shown in figure 5.49, middle. It is scaled from -0.15%

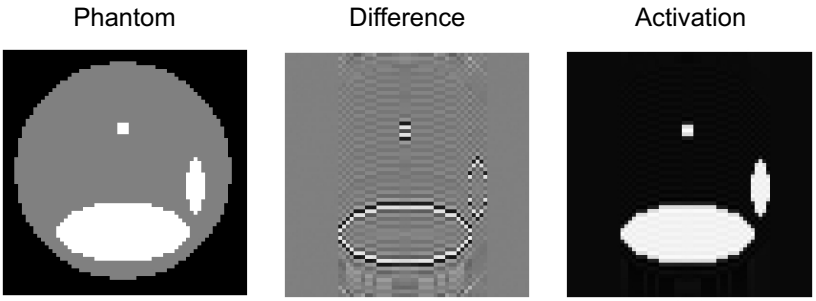

Figure 5.49: Simulation of the effect of a prolonged and irregularly spaced readout train corresponding to the situation in Continuous EPI in the presence of T_2^* decay on BOLD sensitivity. The left image shows the numerical phantom with rest (T_2^*=65 ms, gray) and "activated" regions (T_2^*=68.25 ms, white). In the middle, the difference in activation maps using conventional–Continuous EPI echo trains is simulated (black=0.15%, white=0.15% signal change) and the right image shows the activation map for conventional EPI (scaled from 0 to 1.8% signal change).

signal change (black) to +0.15% (white), the effect is therefore about a factor 10 smaller than the observed signal change between "active" and "resting" regions. Since the same effective echo time (readout time of the central k-space lines) was used, the net signal change in the middle of the largest "active" region is the same for both echo spacings. For the very small area and the borders of the larger ones (high frequency components in the Fourier reconstruction) the Continuous EPI slightly enlarges, or smears out the activated regions. In practice, this effect is negligible and buried in the physiological noise (as, for example, the difference contrast Continuous–conventional EPI in figure 5.46 shows).

Echo Time: Actual Versus Protocol Values A very simple possible source of errors in the comparison of BOLD response amplitudes would be a mismatch between protocol and actual echo time values. This would not immediately be seen from the images, but might, depending on the echo time relative to the T_2^* decay time of the gray matter, result in a non-negligible error in the measured signal change values. Such a mismatch could be caused by simple programming errors that can be difficult to trace, such as a slight error in the summed moments of the phase encoding gradients. The BOLD contrast dependence on echo time follows the difference of the two exponential decay curves for resting state and activated state T_2^* values. This curve has a relatively broad plateau around TE=T_2^* and is steeper towards the short echo times than for echo times longer than T_2^*.

For the seven sequences used in the single volume backwardspeech task, the effective echo time was measured in a spherical phantom placed in the

iso-center of the magnet. The effective echo time was determined as center time of the readout with the largest signal amplitude (the k-space center line). For the 64×64 matrix used, this line number was expected to be 32 for all sequences. In the measurement, this effective echo line was found to coincide with the expected line number 32 for all the conventional EPI sequences in the comparison (EPI, EKS and EPD) and was shifted by one line (number 31) for CEP, CEN, CKS and KSL. Note that this is not an exact measure, as the true k-space center could also be passed between two acquired lines. For two sequences, this seemed to be the case, as the echo amplitude one line from the k-space center had a similar magnitude as the echo line (and was not symmetric towards both sides). These were the CKS sequence, where the k-space center seemed to be between lines 30 and 31 and EKS, with an apparent k-space center between lines 31 and 32.

However, for all sequences the resulting deviation of the effective echo time from the protocol value was less than 1 ms. Assuming a T_2^* value of 65 ms and an echo time of 48 ms, the resulting error in BOLD signal amplitude would be very small, 1.70 instead of 1.71 percent signal change (an error of less than 1%).

VOI Size and Threshold In all of the above comparisons, BOLD signal time-courses were determined by averaging the Talairach-transformed subject data over one common volume of interest (VOI), which was determined either by conjunction analysis or a main effect GLM over all the runs and subjects. While the conjunction method was argued to be less biased towards runs with exceptionally high activation significance or extent, it necessitates the use of extensively small t value in practice. The t values used were in all cases below any significance threshold (the term "conjointly activated" region has been avoided for this reason), because of the large inter-individual and session differences in activation volume and location. This problem worsens with the number of subjects and runs and has, for example, made the selection of a sufficiently low t value for a reasonably large volume impossible in the second trial of the 1.5 T tonotopy experiment (see section 5.7).

Thus, even for the conservative and relatively unbiased volume selection afforded by the conjunction method, voxels are included in the comparison that correspond to t values far smaller than would normally be classified as activated. Whether the inclusion of such voxels has any negative consequences on the BOLD percent signal change comparison in terms of the variance of the signal change over runs has not yet been investigated. Therefore, dependence of the measured BOLD signal change values on t threshold used in the selection of the volume of interest was systematically studied for the Continuous versus conventional EPI comparison in the visual cortex and the original Continuous EPI implementation (KSL) versus its matched

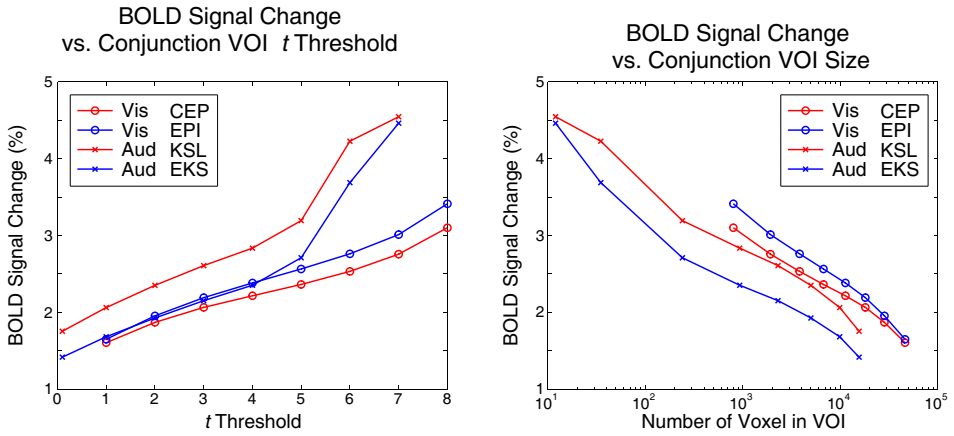

Figure 5.50: BOLD percent signal change values for the visual CEP / EPI and the auditory KSL / EKS comparison plotted against the t threshold used to determine the conjunction VOI (left) and the resulting VOI size (number of voxels, right).

EPI (EKS) in the auditory backwardspeech task.

In figure 5.50, the percent signal changes (averaged over 8 to 16 s after stimulus onset) evaluated for conjunction VOIs at different t thresholds are shown (left). In the right figure, the percent signal changes are are plotted against the resulting number of voxels in that volume of interest, which may be a more stable measure over different experiment when looking at the same functional area.

Of even more interest than the percent signal change values observed for the two sequences of each comparison pair is their relative difference. As in the above experiments, it was determined as the signal amplitude for the Continuous divided by the amplitude for the conventional EPI minus one (figure 5.51).

The latter figure shows that in the visual cortex, where the BOLD response amplitude is expected to be equal for both sequences, their relative difference becomes smaller as the t threshold decreases (and the VOI size increases). For the auditory areas, where a larger amplitude can be expected for the Continuous EPI sequence, this difference becomes larger with decreasing t (and growing size of the corresponding VOI). It can therefore be concluded that the very low t thresholds used in the above comparisons are beneficial in the above comparisons, in terms of showing the expected effect (which is well founded by the data of the Seifritz et al. [152] paper).

To evaluate whether that effect is really due to a systematically larger BOLD amplitude in the auditory areas or just the summation of random values outside any activated voxels, the functional runs from the 3 T tonotopy experiment of section 5.6 were re-examined (where a relatively clear

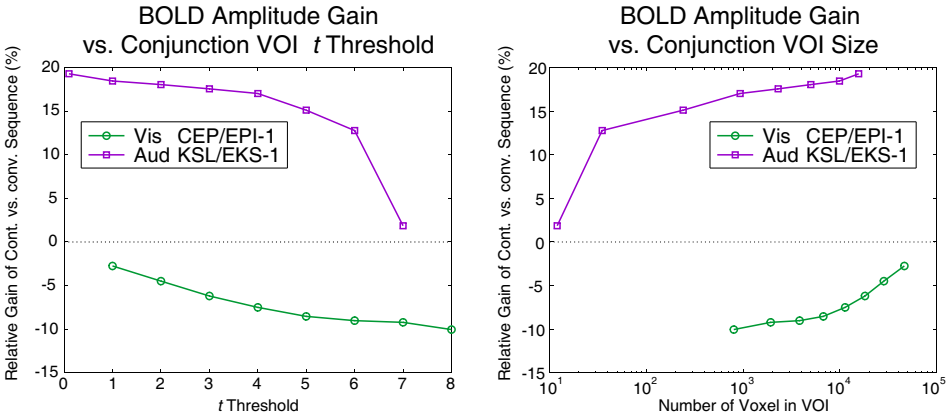

Figure 5.51: Relative advantage of Continuous over conventional EPI plotted against the t threshold used to determine the conjunction VOI (left) and the resulting VOI size (number of voxels, right).

advantage for Continuous EPI was observed). Percent signal change maps of the difference Continuous minus conventional EPI are shown in figure 5.52. Although the units given in those maps (calculated using BrainVoyager) do not correspond well to the percent signal changes of the event related average time courses from those regions and are therefore only loosely related to the values calculated here, they qualitatively show that for the entire region surrounding Heschl's gyrus and even for the planum polare, Continuous EPI results in larger percent signal change values than conventional EPI. The maps shown here for subject 3 of that experiment were qualitatively similar to those of the other subjects.

Different VOI Selection Strategies Completely different strategies for selecting volumes of interest for the percent signal change calculations were also tried. For example, one could argue that for a fair comparison respecting the inter-individual differences in anatomy, subject-specific VOIs should be used, thresholded at a common t value. This was done for the single volume backwardspeech task to compare all seven different sequences in VOIs computed for each run separately at a t threshold of $t = 4$. The resulting BOLD amplitudes are shown in figure 5.53. The larger BOLD amplitudes which can be expected at least for KSL versus EKS with some certainty (from the similarity to the experiments of Seifritz et al. [152]) are not even seen as trends in the data. Such an effect is explainable by the tendency of this process to select larger VOI for runs with higher significance in the activation pattern, which then may equal out BOLD percent signal changes compared to runs with lower significance of activation.

As a second alternative, the main effect approach used by Seifritz et al.

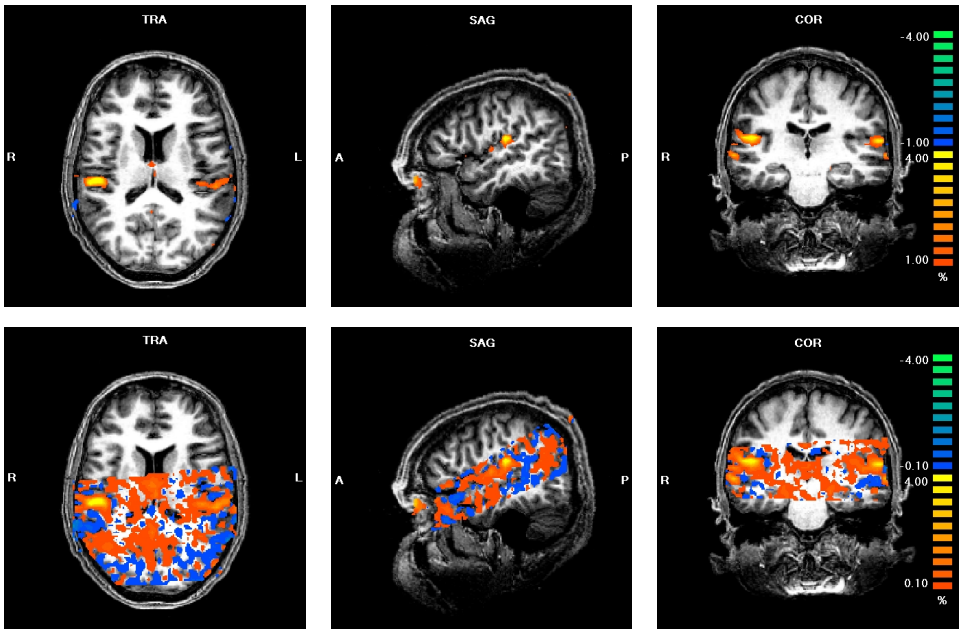

Figure 5.52: Percent signal change maps for the difference Continuous minus conventional EPI for two different thresholds of 1 and 0.1% for subject 3 of fMRI experiment 4 (note that units are not very accurate). The entire region around Heschl's gyrus and most of the planum polare show consistently higher BOLD response amplitudes for Continuous EPI. The displayed slices are centered on right Heschl's gyrus at Talairach x=49, y=-20 and z=16.

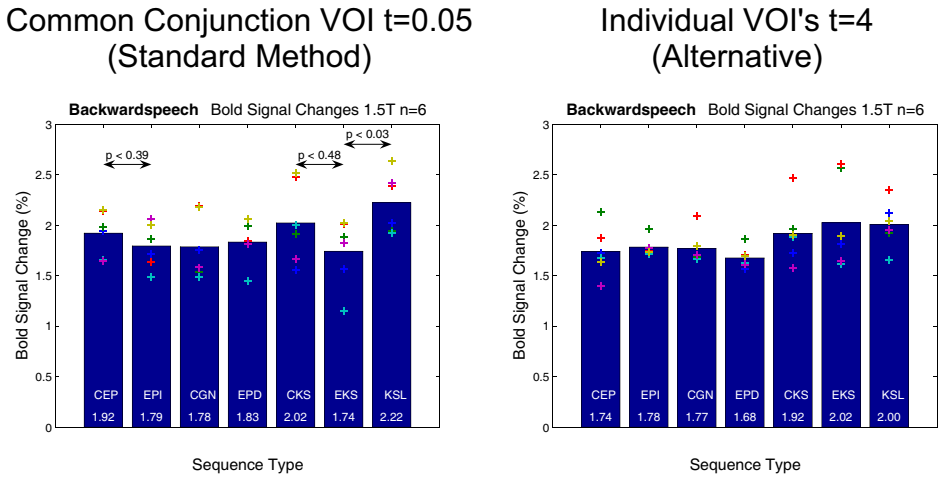

Figure 5.53: BOLD percent signal change for the standard (conjunction) functional volume of interest and per-run individual VOIs.

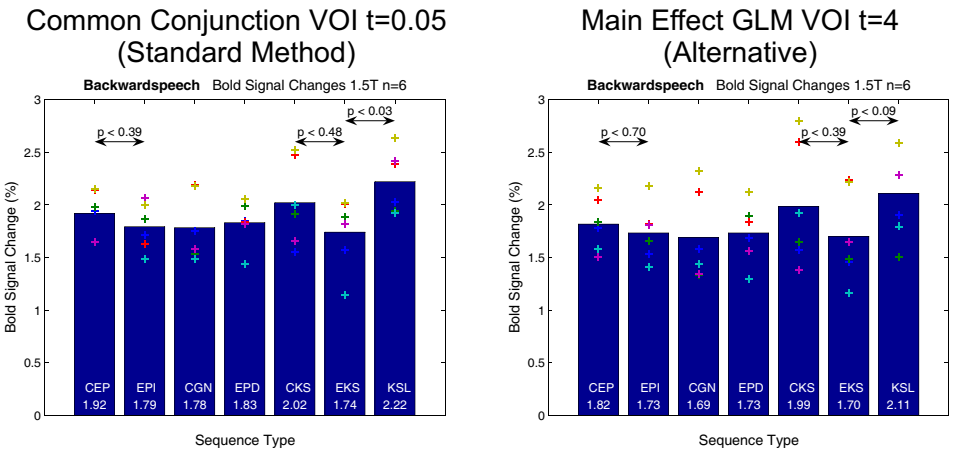

Figure 5.54: BOLD percent signal change for standard (conjunction) and a main effect GLM based VOI.

[152] was also applied to the data from these seven backwardspeech runs. Here, the trend shown by these data (figure 5.54) is again similar to that seen in the conjunction VOI, but with greater variance. Still, this method has been useful in situations where no conjointly activated region could be found even with the lowest obtainable threshold.

In the above analyses, the baseline in the event related averages were was always normalized to time 2 to 0 s before stimulus onset (the BrainVoyager default). For a block design with 16 s rest periods, this could be seen as too little. Therefore, a larger averaging interval from 6 to 0 s before stimulus onset was also tried (figure 5.55) but led to no marked reduction in between-subject variance.

As an alternative to the Conjunction analysis, the same volume should be obtainable by calculating per-run volumes of interest at a common t threshold (here $t=4$ as above) and then computing the voxel-wise intersection of these individual VOIs using an `and` operation. While the resulting volume was not fully identical with that resulting from a conjunction analysis of the seven backwardspeech runs at $t=4$, it was very similar in location and extent (307 vs. 108 voxels). However, in such an approach, apart from being cumbersome, the size of the resulting volume can be hard to estimate a priori, the conjunction method is therefore seen to be much more flexible.

5.8.8 Discussion

In summary, this experiment on six volunteers has not resulted in statistically significant answers to the questions that were posed in the experiment design phase. The main reason of this failure was the large variance in observed BOLD percent signal change values between subjects.

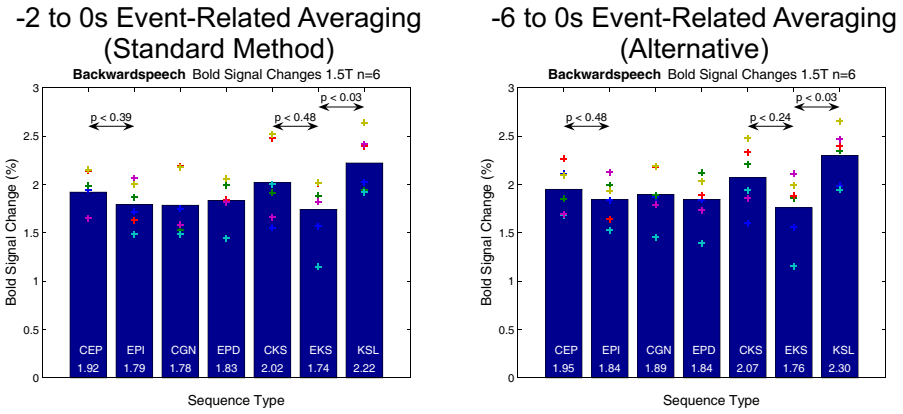

Figure 5.55: BOLD percent signal change for standard (2 to 0 s) and the 6 to 0 s baseline calculation method.

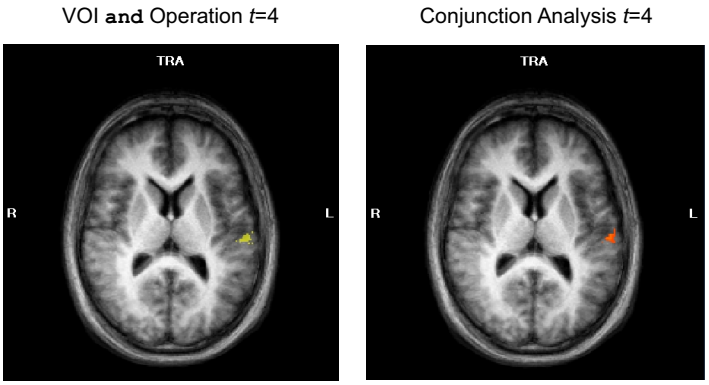

Figure 5.56: Volumes of interest determined based on an "AND" operation on the single-session VOIs (left) or on a conjunction analysis over all sessions (right).

Still, interesting trends were observed in the data. The visual experiments were compatible with the assumption that conventional EPI and the current implementation of Continuous EPI evoke the same BOLD response amplitude in non-auditory areas such as the visual cortex. In the auditory backwardspeech task, there was a trend for all three Continuous EPI variants to yield slightly larger BOLD responses than the conventional EPI sequences. These differences, however, were much smaller than expected from the previous experiments at higher field strength but similar to those seen in fMRI experiment 5 (trial 2). One interesting trend was for the Continuous EPI variants with higher fundamental frequency in the sequence sound to yield higher BOLD signal changes. The volume graded auditory experiment, while showing the largest inter-subject variances due to the quite insufficient averaging (3 times per stimulus type), had an opposite trend for higher BOLD response amplitudes when using the conventional EPI, irrespective of sound level. And finally, indications were found that neither the repeated bipolar gradients nor the irregular echo spacing of the Continuous EPI sequence have any marked influence on measured BOLD percent signal changes.

To increase the statistical significance of the results, either a greater number of subjects could be measured or longer sessions be used. Since the total duration of one measurement session was already 45 min, only the first option seems practicable. Alternatively, the number of sequences used in the comparison could be reduced and multiple runs be planned for each comparison. Of the trends observed, the most interesting one was the tendency of the BOLD response amplitude to increase with sound fundamental frequency.

To obtain a clearer picture of the origin of such a possible effect, a subjective rating of the sequences used plus two CEP variants with higher sound frequency (of 87 and 110 Hz, subsequently used in fMRI experiment 7) was conducted. For each sequence, a five-point rating (1 Very much, 2 Yes, 3 Somewhat, 4 No, 5 Not at all) was applied to the questions: “Is the sound perceived as continuous?” , “Is the sequence sound rough?” and “Is the sequence sound loud?”. The resulting values are listed in the following table, with the fundamental frequencies and sound levels for comparison:

Sequence	Continuous (Rating)	Rough (Rating)	Loud (Rating)	Loud dB(A)	Freq
CEP	1 Very much	3 Somewhat	3 Somewhat	77.8	52.8
EPI	5 Not at all	-	-	81.4	-
EPD	5 Not at all	-	-	81.6	-
CEN	4 No	3 Somewhat	3 Somewhat	77.3	52.8
CKS	1 Very much	4 No	2 Yes	81.7	72.9
EKS	5 Not at all	-	-	80.5	-
KSL	1 Very much	4 No	2 Yes	83.0	-
CEP-87Hz	1 Very much	4 No	1 Very much	84.6	87
CEP-110Hz	1 Very much	5 Not at all	1 Very much	92.5	110

While not being an objective measure of sound properties, this table highlights the multitude of possible factors influencing the perceived sound quality of the sequence, with even more subjective measures such as "How comfortable do you feel in the scanner with this sequence sound?" and "How much did it distract you from the experimental stimulus?" possibly also influencing the BOLD response to an applied auditory stimulus. Finally, the sound properties at this level are highly system specific, and for example depend on the acoustic damping strategy used by the manufacturer, as was very clearly illustrated by the much reduced sound levels on the Avanto compared to the earlier Sonata systems.

Apart from the remaining acoustical differences, only two not previously addressed differences between the KSL sequence (which showed a trend towards a larger BOLD response) and the CEP (and CKS) sequences were found, which seemed unlikely to cause such an effect: That a strong spoiler gradient is present in KSL but not the CEP variants, and that in the KSL and CKS sequences, the echo line was nearly in the middle of a readout block (number 6 of 10) but a bit less so in CEP (number 10 of 16).

5.9 fMRI Experiment 7: Possible Acoustic Effects

5.9.1 Experiment Design and Stimulus

The main goal of this last fMRI experiment was to investigate on the influence of the fundamental frequency of the Continuous EPI sound on the observed BOLD amplitudes. Additionally, the reproducibility of the trends observed in the comparison of different sequences in the same backwardspeech task was investigated by including the same subjects as in the previous experiment. And finally the subject number was increased from 6 to 8 in the hope to obtain more statistically significant results.

To enable a direct comparison to the previous experiment, the same block design paradigm based on the backwardspeech stimulus was used,

again with a cartoon movie to maintain relatively constant attention levels. Continuous and conventional EPI sequences in the present as well as the original implementations were run with the same parameters as in the previous experiment. Additionally, two Continuous EPI runs with matched conventional EPI runs were designed, where the Continuous EPI sound fundamental frequency was increased over the previous (CEP) setting of 52.8 Hz and the Continuous EPI matched to the original implementation (CKS) with 72.9 Hz to a value near the fundamental frequency of 90.4 Hz with 87 Hz and one with an even higher fundamental frequency of 110 Hz.

For this experiment, eight volunteers were recruited and (similar to fMRI experiment 4) measured in one session per volunteer. For each sequence comparison pair (conventional and Continuous EPI) the order of the respective sequences was balanced over the sessions. Also, the order of the comparison pairs was interchanged between sessions, as shown in the following table.

Nr.	Subj.1	Subj.2	Subj.3	Subj.4	Subj.5	Subj.6	Subj.7	Subj.8
1	E11	C11	KSL	E87	C87	CEP	EKS	EPI
2	C11	E11	CKS	C87	E87	EPI	CKS	CEP
3	E87	C87	EKS	E11	C11	KSL	KSL	EKS
4	C87	E87	C87	C11	E11	CKS	E87	CKS
5	EKS	CKS	E87	EPI	CEP	EKS	C87	KSL
6	CKS	KSL	C11	CEP	EPI	C87	E11	E87
7	KSL	EKS	E11	EKS	KSL	E87	C11	C87
8	EPI	CEP	CEP	CKS	CKS	C11	EPI	E11
9	CEP	EPI	EPI	KSL	EKS	E11	CEP	C11

Two of the subjects were female, six male, six right handed, two left (one writing with his right), age 33.8 ± 6.1 (mean $\pm$ standard deviation).

The same cartoon movie was shown over the entire experiment duration in an attempt to keep subject attention levels as constant as possible. As in fMRI experiment 6, the only instruction to the subjects was to lie very still and watch the movie, while not paying special attention to the sound stimuli. The sound level of the auditory stimuli was again adjusted individually to be as loud as possible without being perceived as painful. For subjects 1 to 8, the resulting sound levels (reading on the amplifier were): 60, 70, 70, 70, 70, 60, 70 and 70.

5.9.2 Sequence Settings

Identical sequence settings to those in fMRI experiment 6 (see section 5.8) were used for the Continuous EPI (CEP) and conventional EPI sequence (EPI) as well as the three sequences adapted to the parameters of the original Scheffler and Seifritz [151] Continuous EPI sequence (KSL,CKS and EKS). Parameters are not listed again for these sequences.

The four additional sequences, the Continuous EPI with 110 Hz fundamental frequency **(C11)** and its matched EPI sequence **(E11)** as well as the Continuous EPI with 87 Hz fundamental frequency **(C87)** and the corresponding conventional EPI sequence **(E87)** for the comparison with the above are listed in the following. Parameters were: For the **(C11)** sequence: TE=58.15 ms, TR=1747.2 ms, 16 slices of 3.4 mm thickness, image matrix 64×64, bandwidth 1628 Hz/px, FOV=21.76 cm (resulting in an isotropic voxel size of 3.4 mm^3), flip angle 78°, ramp fraction 0.36, binomial 1-1 pulse water excitation, 12 blocks of 6 readouts, fundamental frequency of the sequence sound 109.9 Hz, sound level 92.5 dB(A). For the **(E11)** sequence: TE=58.15 ms, TR=1747.2 ms, 16 slices of 3.4 mm thickness, image matrix 64×64, bandwidth 1628 Hz/px, FOV=21.76 cm (resulting in an isotropic voxel size of 3.4 mm^3), flip angle 78°, ramp fraction 0.5, binomial 1-1 pulse water excitation, sound level 87.8 dB(A). For the **(C87)** sequence: TE=61.51 ms, TR=1840.2 ms, 16 slices of 3.4 mm thickness, image matrix 64×64, bandwidth 1371 Hz/px, FOV= 21.76 cm (resulting in an isotropic voxel size of 3.4 mm^3), flip angle 81°, ramp fraction 0.34, binomial 1-1 pulse water excitation, 10 blocks of 8 readouts, fundamental frequency of the sequence sound 87.0 Hz, sound level 84.6 dB(A). and for the **(E87)** sequence TE=61.51 ms, TR=1840.2 ms, 16 slices of 3.4 mm thickness, image matrix 64×64, bandwidth 1371 Hz/px, FOV=21.76 cm (resulting in an isotropic voxel size of 3.4 mm^3), flip angle 81°, ramp fraction 0.42, binomial 1-1 pulse water excitation, sound level 85.1 dB(A). The sound levels reported were measured in the scanner room but away from the magnet bore at an ambient noise level of 49.6 dB(A).

5.9.3 Results

The data analysis procedure used for this experiment was identical to that of the previous fMRI experiment (number 6, see section 5.8), with the exception that no slice scan time correction was used in the preprocessing of the fMRI data.

As in the previous experiment, the backwardspeech block design paradigm proved robust, highly significant activation along Heschl's gyrus was again observed in all subjects and runs. The location of the activated region was relatively consistent for the individual runs of a subject, with the extent and significance level of the activation varying over the runs. Event-related averages were again evaluated in the conjointly activated area at a threshold of $t = 0.05$ for all subjects and runs. Compared to the previous experiment, this VOI was similarly located along Heschl's gyrus, but included only 1869 instead of 7232 voxels and was confined to the lateral part of Heschl's gyrus.

The obtained percent signal change values (again averaged over the interval 8 to 16 s after stimulus onset) are visualized in figure 5.57. As in the previous experiment, bars represent group average values, crosses the

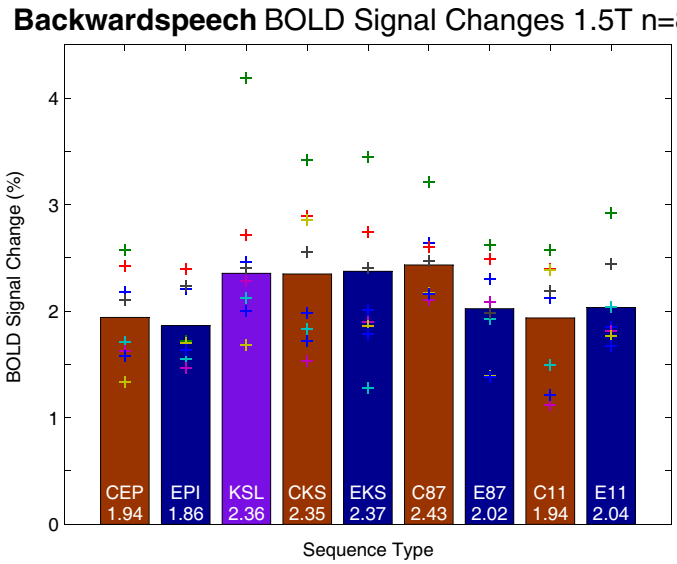

Figure 5.57: Summary of the BOLD percent signal changes for the group of all subjects in fMRI experiment 7 (bars) and individual subjects (crosses).

percent signal change values for the individual subjects. Here, the inter-individual differences are even larger than in the previous experiments, with only the comparison C87 to E87 coming near a statistically significant result with $p<0.08$. Any systematical difference between the other sequences is buried in these scattered values. The variance is especially high for the CKS, KSL and EPI runs. Reading from whatever trends there are left, the increased fundamental frequency does not systematically improve the situation for the Continuous EPI, as the sequence with the highest fundamental of 110 Hz (C11), if anything, shows a trend towards a smaller BOLD amplitude than the E11 (note that the C11 was by far the loudest sequence measured).

Reproducibility of the Results from the Previous Experiment In spite of the not very satisfactory data quality, the question can be asked how well these data reproduce the non-significant trends from the previous experiment. For this, the CEP and EPI sequences as well as the three sequences KSL, CKS and EKS, which were repeated in this experiment from the previous one, the BOLD response amplitudes were compared to those of the previous run, for subjects 1-5 and 7, who had participated in both experiments.

The mean group percent signal changes and the individual subject values are graphically displayed in figure 5.58 for both experiments. While the group values from both experiments in themselves show the same trend

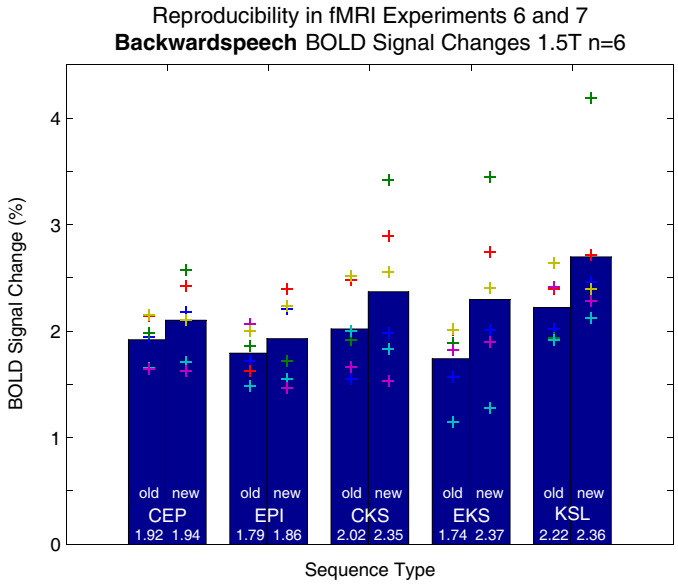

Figure 5.58: Comparison of the CEP and EPI sequences in the present fMRI experiment 7 ("new") and the previous one (fMRI experiment 6, "old"). Only subjects measured in both sessions were included. Note, that different volumes of interest were used for "old" and "new" runs.

(larger BOLD amplitudes for CEP than EPI, larger values for CKS and KSL than EKS, larger value for KSL than CKS), the two sessions show differences in BOLD signal change values far greater than the effect between sequences. This does not really come as a surprise, since different volumes of interest were used.

Interestingly, the situation does not change dramatically when a VOI common to both runs is used. A scatter plot of the BOLD percent signal changes obtained with the conventional EPI versus those with the Continuous EPI sequence is shown in figure 5.59. Here, conjunction at (a still non-significant) $t=2$ over all the repeated runs from both experiments of a subject has been used to generate per-subject volumes of interest in which the BOLD percent signal changes were evaluated. While in such an analysis, the inter-subject differences in anatomy are much better accounted for (at the cost of a complicated inter-subject comparability) this does not lead to much clearer trends.

In conclusion, the trends between the comparison pairs CEP and EPI as well as CKS, EKS and KSL, EKS are similar to those in the previous experiment, although at a different level. The overall BOLD response level obtained in the present experiment seems to be larger, consistent with what can be expected from the smaller VOI used to evaluate the event related averages. From this reproducible trend, it is justifiable to expect

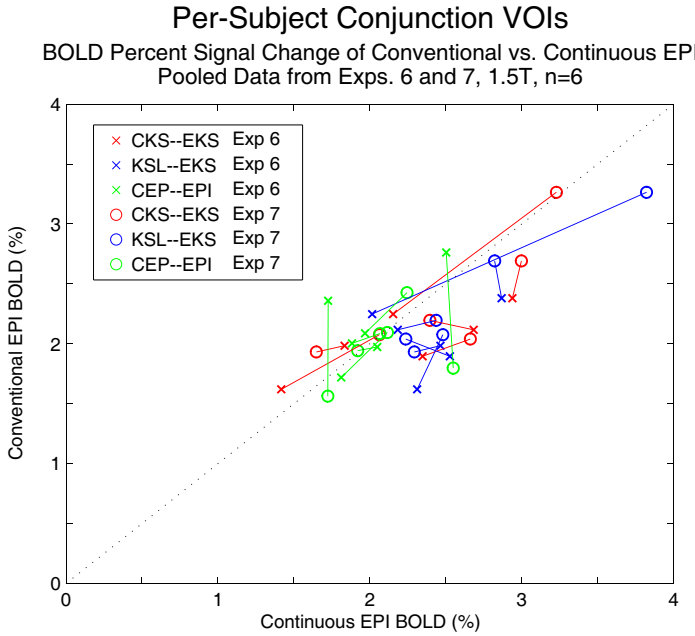

Figure 5.59: Plot of BOLD percent signal change values for conventional vs. Continuous EPI sequences for the repeated runs of fMRI experiments 6 and 7 (only subjects measured in both runs). The line of unity (dotted) is given for reference and the two data points from each subject connected by a solid line. Per-subject conjunction VOIs were used in the evaluation of the BOLD signal changes.

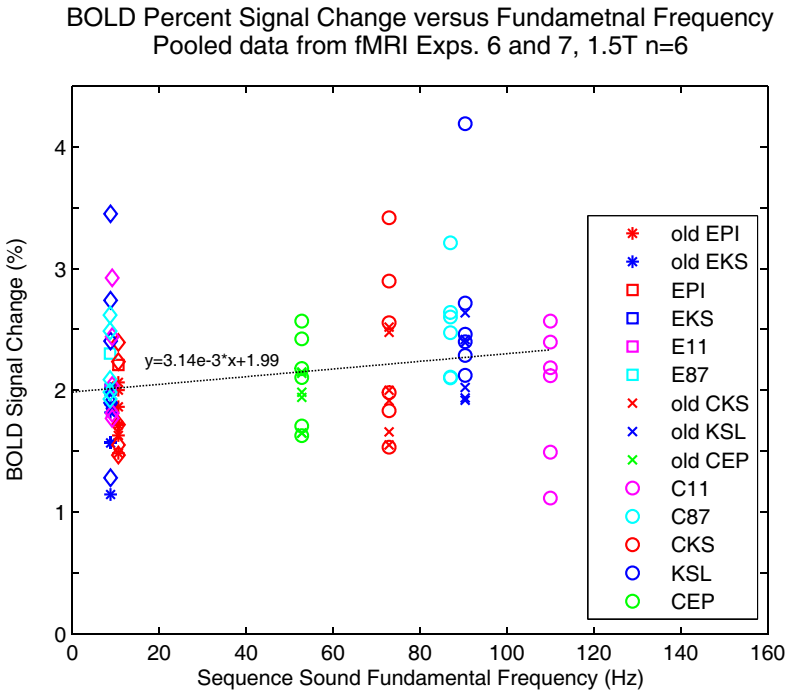

Figure 5.60: Scatter plot of BOLD percent signal change versus sequence sound fundamental frequency for the pooled data of fMRI experiments 6 and 7 (only subjects measured in both experiments). The dotted regression line shows that there is indeed a trend towards higher BOLD response amplitude for higher fundamental frequency.

a fundamental-frequency dependence of the BOLD response amplitude beyond the originally assumed value of about 35 Hz.

Importance of Fundamental Frequency Although the data from this experiment (as those from the previous one), show a much larger session variability than any effect between sequences, an investigation on the dependence of BOLD response amplitude versus fundamental frequency of the sequence sound can be attempted. The percent signal change values for the subjects who participated in both experiments are plotted against the fundamental frequency of the corresponding sequences in figure 5.60. Apart from the consistently low C11 runs, there indeed seems to be a trend towards higher BOLD response amplitudes for higher sound frequencies. The slope of a regression line through all data points is 3.14×10^{-3} percent signal change per Hz.

Pooled Data from the Two Experiments To gain an overview of which sequences and runs resulted in a larger change of BOLD response

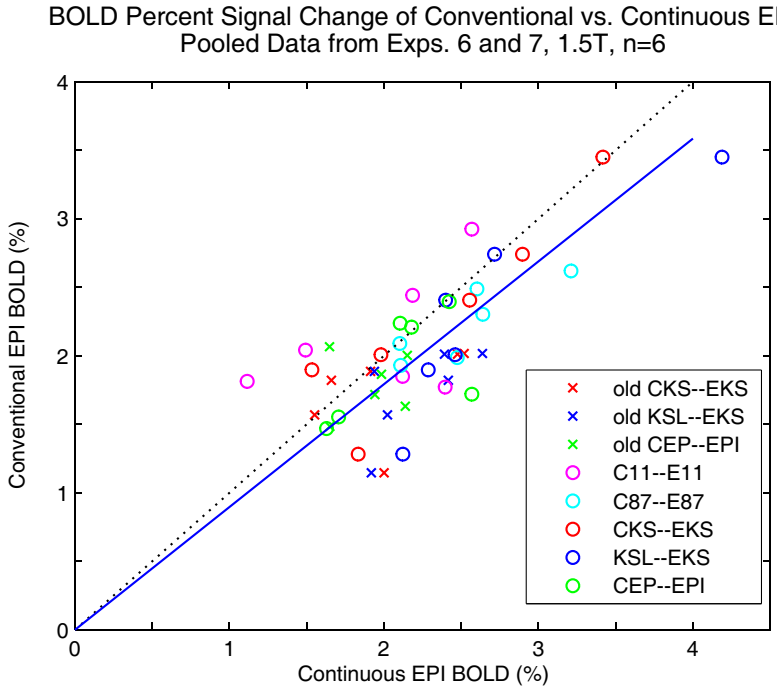

Figure 5.61: Plot of BOLD percent signal change values for conventional vs. Continuous EPI sequences for the pooled data of fMRI experiments 6 and 7 (only subjects measured in both runs). The unity line (dotted) and the regression line (blue, slope 0.896, forced through zero) through all points are included for reference.

amplitudes, it may be useful to plot the magnitude of the BOLD response with the conventional EPI versus the BOLD response using the Continuous EPI sequence in a scatter plot. This has been done in figure 5.61, the dotted unity line has been included to visually guide the judgment of effect. Any sequence pair for which Continuous EPI resulted in a larger BOLD percent signal change than the respective conventional EPI sequence should lie clearly below this line. No clear pattern can be found in these data. The most striking trend is that of the E11 sequence resulting in a larger BOLD response than the C11 sequence. The reason for this trend is unclear, there was no clearly distinct feature in this sequence which was different from the other Continuous EPI sequence configurations except for the considerably higher scanner sound level for C11 (but not E11). The regression line through all data points (forced through zero) gives a slope of 0.896, i.e. a mean increase in BOLD response amplitude of 11.6% when using Continuous versus conventional EPI.

5.9.4 Discussion

The main goal of this experiment, the quantification of an expected dependence of the BOLD response amplitude on the fundamental frequency of the sequence sound, has not led to conclusive results. Even for the increased number of subjects relative to the previous experiment (8 instead of 6), the measured BOLD percent signal changes did not show statistically significant differences between sequence types or settings.A larger BOLD response for higher fundamental frequencies, which could be expected at least for the ($< 35\,\mathrm{Hz}$) EPI sequences compared to the ($> 35\,\mathrm{Hz}$) Continuous EPI sequences based on the Seifritz et al. [152] paper, is found even in the very broadly scattered data of this and the previous experiments, a much clearer effect could have been expected.

With regard to the reproducibility of the trends observed in the sequence comparisons of the previous experiment, the same trends (CEP>EPI, EKS<CKS<KSL) are again found in the data of the present experiment, albeit with even larger inter-individual variance. Additionally, the data from those six subjects who were measured in both experiments highlights the very large session differences, which were of the same order as the inter-individual differences.

In conclusion, while the non-significant trends from the previous experiment were reproduced by the data of the current experiment, the very large inter-individual and session differences call for an extremely cautious interpretation of these trends. Therefore, no significant conclusions can be drawn form these experiments regarding the relative performance of the original versus current implementation of Continuous EPI or the different fundamental frequency settings.

Apart from insufficient statistical averaging (experiment duration, number of repeated runs, number of subjects), one aspect of fMRI experiments 6 and 7 that can be questioned is the robustness of the backwardspeech paradigm. While there were good reasons for the assumption that this stimulus would lead to effective stimulation of the auditory areas (which it did, concluding from the consistent significant activation patterns), its performance and robustness with regard to BOLD percent signal change measurements has not been previously reported. Another aspect is the decision to maintain attention levels only by continuously showing a cartoon movie, instead of an active control condition such as a requested button-press upon a visual cue, which could be a major factor contributing to the very larger inter-session and inter-subject variance (this latter argument hold for all experiments reported in this thesis).

5.10 Summary

The aim of the work presented in this chapter was to characterize the spatial and temporal imaging characteristics of the Continuous EPI sequence compared to the standard (conventional) EPI sequence, and to compare and optimize its performance in relation to conventional EPI for the use in auditory fMRI experiments.

Characterization Two characteristic image artifacts which appear in the Continuous EPI sequence were identified and characterized. One, based on the irregular echo spacing of the readout train, results in a multiple ghosting artifact, which is hardly noticeable under practical conditions. The other, resulting from gradient shape imperfections in the water excitation slice select gradients, leads to an intensity modulation over multi-slice images and can be corrected by a system-specific bias on the second of the two slice selection gradients.

Further, the fat suppression using these water selective binomial pulses was shown to be equally effective when applied to conventional and Continuous EPI sequences.

For fMRI applications, the temporal signal stability of a sequence is a crucial factor influencing the detection efficiency of functional activation. Based on histograms of the voxel-wise relative standard deviation, the temporal stability of Continuous EPI could be shown to be equal to that of matched conventional EPI sequences at 1.5, 3 and 7 T. Finally, based on sequence sound recordings, the use of "soft", sinusoidally shaped gradient ramps (which occupy a large part of the gradient duration) are beneficial for the suppression of the pulsating sound component.

fMRI experiments The second part of this chapter consisted in the results of seven auditory fMRI experiments in which conventional and Continuous EPI sequences were compared.

In the first experiment, a 5 min pulsed sine tone block design experiment of four volunteers measured on the 1.5 T Sonata system, consistently showed a larger BOLD response amplitude for the Continuous EPI sequence in all subjects, on average by 40%.

The second experiment was a single volunteer 3 min proof-of-concept experiment of an interesting extension of the Continuous EPI, the auditory stimulation evoked by the periodic re-introduction of the pulsating gradient sound component.

The third through fifth experiments compared the BOLD response amplitude using conventional and Continuous EPI at 1.5, 3 and 7 T field strength using a pulsed sine tone stimulus of three different frequencies, which were presented in a pseudo-randomized order over a total duration of 15 min. While in the 7 T experiment, a single run on one volunteer showed a

50% increased BOLD response amplitude for Continuous EPI for two of the stimulation frequencies, but no difference for the third, the predictive power of this result was severely limited by the measurement of only one single session. At 3 T, four volunteers were measured in two sessions per subject. In both sessions both a conventional and a Continuous EPI run was measured, with the order of those runs interchanged for the second session. While the inter-session and inter-individual differences were larger than the difference between sequences, the average BOLD response was greater for the Continuous EPI sequence at all three frequencies by 12 to 25%. At 1.5 T, the observed difference between sequences was even smaller, after complications (RF artifacts and the exclusion of one subject) in the first trial, a second trial on 6 volunteers (again measured in two sessions with interchanged sequence order) gave average improvements for Continuous over conventional EPI of only 3 to 11%, with even larger inter-individual and inter-session differences. These large variations were also reflected by the failure to observe consistently high significance levels in the activation patterns of the individual runs. While some of the variance may be explained by the lower contrast to noise level at 1.5 T and the lower statistical power of the short stimulation epochs (compared to fMRI experiment 1), a part of the more unusual activation patterns could also be traced back to subject motion (both stimulus-correlated and uncorrelated motion was observed).

The last two experiments aimed at exploring some of the sequence parameters in the Continuous EPI sequence that could be expected to influence the acoustic performance as well as testing some of the assumptions that had been used in its implementation. Both experiments, even though measuring 6 and 8 volunteers, respectively, were plagued by insufficient statistical power due to the even more extreme variance between sessions and subjects. They both used 16 s epoch block designs which are known to yield optimum statistical power [169, chapter 1]. Especially with the clear effect seen in the block design fMRI experiment 1 in mind, these experiment could have been expected to yield statistically significant results. Different factors could have contributed to the failure to do so. On the one hand, rather long sessions of around 45 min were used (compared to about 25 min in exp. 1). Although in these experiments an attempt was made to control subject attention by simultaneously projecting a cartoon movie, varying attention levels could be a part of the problem (or the distraction by the movie itself). On the other hand, the backwardspeech stimulus which was used here might not have been an ideal stimulus even though it resulted in consistent activation patterns of high statistical significance. As a third factor, the scanner system itself might have had some unexpected influence on the sequence differences measured in these experiment (and the preceding experiment 4). Compared to the Sonata system, the Avanto system used here is much better damped acoustically (an important selling point, and easily detectable when listening to the same sequence on both scanners). Here, it could be suspected

that the general increase in acoustic contrast between stimulus and scanner sound might have reduced the difference in activation measured with Continuous versus conventional EPI sequences, even though the trends from a volume graded acoustic stimulation experiment do not support (nor contradict) this, and stimulus volume is known to have no direct influence on BOLD response amplitude ([117]). Of the non-significant trends found in these experiment, maybe the most robust one is that of both sequences resulting in the same BOLD response amplitude in a visual task (something that has been shown clearly for the original implementation of Continuous EPI [152]). Another trend, reproducible between the two experiments, was that of an increase in BOLD response for increasing fundamental frequency of the Continuous EPI sequence sound beyond the psycho-acoustically motivated "critical point" of about 30 Hz. However, for the highest frequency setting of 110 Hz measured in experiment 7, very low response amplitudes were measured.

Outlook and General Conclusions Of the open questions remaining, this sound frequency dependence is probably the most important. The experiments here reported have pointed out some of the difficulties in making such a comparison. For one thing, a large number of subjects has to be included in such a study (probably 12 or more for a statistically significant result at 1.5 T). On the other hand, the question of subject attention has to be answered for the necessarily long scanning sessions. Here, an active control, such as the measurement of response times to a simple visual cue might be a better option than the presentation of a silent movie as was done in fMRI experiments 6 and 7. Still, it has to be cautioned that it is practically impossible to isolate a factor like the sound fundamental frequency from other factors such as sound roughness, sound pressure level and small variations in image parameters, given the constraints imposed by the continuous sound, similar echo times etc. Also, many aspects of the sequence sound are system-specific, they may depend on the acoustic transfer function of the gradient system, the precise imaging parameters that can be realized given a certain gradient performance, the acoustic damping of the scanner room and so on.

Also, a general problem has been to define what a fair comparison between conventional and Continuous sequence pair should be. In this work, all the comparisons have been based on sequences with equal echo and repetition time, equal readout bandwidth and readout gradient shape, equal slice (and sometimes frequency) selective excitation pulses as well as slice position and geometry. It can be expected that when departing from these constraints, different results would be obtained in the sequence comparisons. For example, a "typical" EPI sequence used for fMRI might use a considerably higher bandwidth than those considered here in the interest

of reducing distortions. Also, the large spoiler gradients which accompany the conventional spectral fat saturation pulses are normally clearly audible. Both factors can lead to much higher sound pressure levels for EPI sequences in typical fMRI experiments than those reached in the conventional EPI runs of this work. In the context of the present experiments, the Continuous EPI sequence was sometimes louder than the conventional EPI sequence (depending on the sequence parameters) because of the relatively large repeated pairs of slice select gradients. However, the sound level difference between scanner sound and stimulus did not lead to a clear difference in BOLD response amplitude in fMRI experiment 6 .

A final concern throughout these experiments has been the selection of a volume of interest for the comparison of BOLD signal changes. It was in all cases functionally defined based on the activated areas found in the individual runs. While the comparison of the Seifritz et al. [152] paper (the only source of Continuous EPI reference data) has been based on a VOI determined by thresholding a main effect GLM over all runs, this has been compared to a VOI based on a conjunction analysis over all runs, thresholded at a (non-significantly) low threshold in the present work. At comparable volume, the localization of the VOIs based on the two methods has been found to be similar but not equal. The conjunction VOI was argued to be less biased towards runs with a very strong activation, which was reflected by a smaller inter-session and inter-subject variance when using the conjunction method. At the same time, the mean percent signal changes were similar for both methods. In the sense maximizing the statistical power of the comparisons, the conjunction method was therefore considered superior to the previously proposed one. For the context of this thesis, the direct comparability with the existing data of Seifritz et al. [152] was crucial and a functional definition of the volumes of interest therefore the only appropriate choice. Still, completely different strategies for selecting a comparison volume could be considered. Most importantly, an anatomically constrained volume based on manual segmentation of Heschl's gyrus (and maybe secondary auditory areas) might be very rewarding. While the anatomical definition of the primary auditory cortex is in itself problematic because of the large inter-individual variability (e.g. [97]), it is an approach that has been repeatedly used in the literature (Harms et al. [117] being the most relevant example for the current work). Such an anatomically defined analysis would allow for an unbiased estimation of the hemodynamic response shape and might also illuminate the question of whether the difference between Continuous and conventional EPI is restricted to the primary auditory cortex (the focus of the present comparisons) or whether it also extends to secondary ares. Such an analysis might be a rewarding subject for future research.

Chapter 6

Principles: BURST

6.1 Historic development of BURST

BURST imaging was originally proposed by Hennig and Mueri [170] in a 1988 conference abstract and characterized and implemented on a clinical scanner in 1993 [142]. They proposed the use of a series of very low flip angle pulses (e.g. 64 pulses of 1.5° flip angle) over a constant "read" gradient to generate a series of distinct magnetization states which could then be refocused in a number of ways. For imaging, all that was needed in addition to this pulse train was a phase encoding gradient (either constant or blipped) and a slice selection mechanism either by a slice-selective refocusing pulse or by using the BURST train as a refocusing pulse for a preceding slice-selective excitation pulse. Already in the conference abstract, they mentioned the possibility of using non-equidistant pulses to generate a number of echoes greater than the number of pulses used.

At about the same time, the equivalent DANTE ultrafast imaging sequence (DUFIS) was proposed by Lowe and Wysong [171] as the imaging application of the DANTE spectroscopic pulse sequence [172] (an acronym for delays alternating with nutations for tailored excitation).

6.2 The Extended Phase Graph

At the heart of the BURST sequence lies the generation of separate magnetization states by a series of low flip angle pulses and their subsequent refocusing. This process can be described in a number of ways; for example, the BURST excitation can be seen as a composite RF pulse or as the equivalent of a rapidly repeated low flip angle gradient spoiled gradient echo experiment. Whichever interpretation is used, the vector model which is so useful in other situations is not very helpful in this case.

In multi-pulse experiments, the generated patterns of magnetization in the vector representation become intractable after only a few pulses. Even in

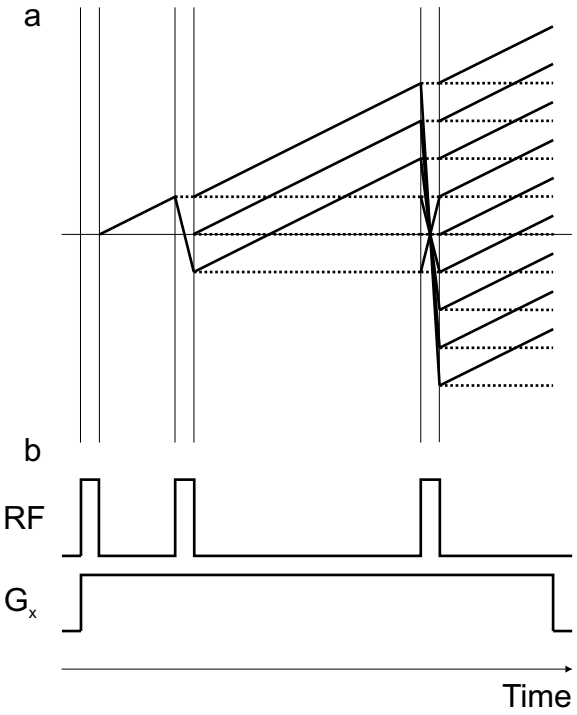

Figure 6.1: Example of a phase graph diagram (a) that describes the effect of a three-pulse sequence (b) in terms of the dephasing due to the gradient (on the vertical axis) versus time (on the horizontal axis). Dotted lines represent longitudinal magnetization, solid lines transverse magnetization.

numerical simulations, a great number of isochromats have to be calculated with different positions along the gradient axis, which – although possible – is time-consuming even on modern computers. Here, it is advantageous to keep tract of the different echoes by sorting them according to their total dephasing history, usually in a diagram with the time axis in the horizontal and the dephasing on the vertical axis. This is called the phase graph. A simple example of a three-pulse sequence is shown in figure 6.1. Note that the RF pulses have the effect of "mixing" the different magnetization compartments (or "states"), which is schematically shown in this figure but conventionally omitted in phase graph diagrams.

Figure 6.1 already makes it clear that the number of magnetization pathways can increases very rapidly with the number of RF pulses, depending on the time between the pulses. In the extreme case (as in figure 6.1), after the application of n RF pulses $2/3 \cdot 3^n$ pathways have to be followed. However, if the RF pulses are equally spaced, all but n of those paths coincide in terms of their dephasing and can be treated as a single "dephasing state". It is this different viewpoint, the calculation of magnetization in terms of its momen-

tary dephasing instead of its dephasing history, that really makes the phase graph (or, to differentiate, the "extended" phase graph formalism) really efficient. This extended phase graph and its corresponding calculation formalism was introduced into MRI by Hennig [173] in 1988 and subsequently detailed in two papers by Hennig [174] and Scheffler [175]. It is based on a similar argument by Kaiser et al. [176] and closely related to the complex magnetization calculations given by Woessner [177], and makes use of the matrix treatment of the Bloch equations developed by Jaynes [178] and Bloom [179]. Although initially motivated by the need to calculate echo amplitudes of RARE (and BURST) type sequences, it is also very successfully used to calculate the behavior of steady-state sequences [41, 175, 180].

In the following introduction into the extended phase graph formalism, the distribution of magnetization to different dephasing states is calculated under the assumption that an applied RF pulse is fully characterized by its flip angle α and its phase ϕ (i.e. instantaneous rotation) and that the dephasing due to the gradient in-between two RF pulses is always a compete dephasing by an angle $\pm\pi$.

To calculate the effect of a single RF pulse on the magnetization vector $\mathbf{M}$, it is advantageous to introduce a complex transverse magnetization $F = M_x + iM_y$, with its complex conjugate $F^* = M_x - iM_y$. From the Bloch equations, it then follows ([175], entire section):

$$F \longrightarrow F^+ = \cos^2(\alpha/2)F + e^{2i\phi}\sin^2(\alpha/2)F^* - ie^{i\phi}\sin(\alpha)M_z$$

$$M_z \longrightarrow M_z^+ = -\frac{i}{2}e^{-i\phi}\sin(\alpha)F + \frac{i}{2}e^{i\phi}\sin(\alpha)F^* + \cos(\alpha)M_z$$

The condition of complete dephasing between RF pulses implies that $\phi_G = \pm\pi$ at the edge of one imaging voxel, where $\phi_G = \gamma GT$, with γ the Larmor constant, G the gradient strength in Tesla per Meter, and T the duration of the gradient. For an arbitrary position $\mathbf{r}$ within the voxel, the n-fold application of the gradient therefore results in a dephasing by $e^{in\phi_G\mathbf{r}}$. Now, we can decompose the total transverse magnetization according to the number of dephasing gradients it has seen as

$$F = \sum_{n=-\infty}^{\infty} F_n \int_{\mathbf{r}} e^{in\phi_G\mathbf{r}} d\mathbf{r}$$

And similarly for the longitudinal magnetization $Z = M_z$:

$$Z = \sum_{n=-\infty}^{\infty} Z_n \int_{\mathbf{r}} e^{in\phi_G\mathbf{r}} d\mathbf{r}$$

where $Z_n = Z_n^*$ since the longitudinal magnetization is real valued. Inserting these definitions into the complex Bloch equations results in [175]:

$$\begin{pmatrix} F_n \\ F_{-n}^* \\ Z_n \end{pmatrix} \longrightarrow \begin{pmatrix} F_n \\ F_{-n}^* \\ Z_n \end{pmatrix}^+ = \begin{pmatrix} \cos^2(\frac{\alpha}{2}) & e^{2i\phi}\sin^2(\frac{\alpha}{2}) & -ie^{i\phi}\sin(\alpha) \\ e^{-2i\phi}\sin^2(\frac{\alpha}{2}) & \cos^2(\frac{\alpha}{2}) & ie^{i\phi}\sin(\alpha) \\ -\frac{i}{2}e^{-i\phi}\sin(\alpha) & \frac{i}{2}e^{i\phi}\sin(\alpha) & \cos(\alpha) \end{pmatrix} \cdot \begin{pmatrix} F_n \\ F_{-n}^* \\ Z_n \end{pmatrix}$$

This equation describes the effect of an RF pulse on the states (or configurations) of the magnetization and is the mathematical formulation of the behavior described by the phase graph. All that remains to be done in order to arrive at a complete description of the magnetization behavior is to account for the relaxation processes in-between pulses. Due to the dephasing, a transverse state F_n^+ evolves into the F_{n+1} state multiplied with a transverse relaxation term $E_2 = e^{-\mathrm{T_R}/\mathrm{T_2}}$ (with $\mathrm{T_R}$ the time between RF pulses):

$$F_n^+ \longrightarrow F_{n+1} = E_2 F_n^+$$

The longitudinal states are not affected by the gradient dephasing, but experience longitudinal relaxation (with $E_1 = e^{-\mathrm{T_R}/\mathrm{T_1}}$):

$$Z_n^+ \longrightarrow Z_n = E_1 Z_n^+ \qquad \text{for} \quad n \neq 0$$

$$Z_0^+ \longrightarrow Z_n = E_1 Z_0^+ + M_0(1 - E_1)$$

This formalism is very fast and efficient at calculating echo amplitudes of multi-pulse sequences but cannot be applied directly to sequences with irregular RF pulse spacings or incomplete gradient dephasing.

6.3 Simulation of the BURST Sequence: Bloch Equations and Extended Phase Graph

Because of the complexity of the signal formation process in multi-pulse sequences (see previous subsection), numerical simulations are an important tool to describe the signal behavior of BURST sequences. This can happen either by the direct numerical solution of the Bloch equations or by an implementation of the extended phase graph formalism.

For the numerical solution of the Bloch equations, several strategies can be used. In almost any case, a formulation of the problem in the rotating reference frame (rotating with $\omega_0 = \gamma \mathrm{B}_0$ around the z axis) is advantageous. Also the formulation of the cross product in matrix form is convenient, as proposed by Jaynes [178]. Also, his re-formulation of the Bloch equations in an "axial" representation using Pauli spin matrices can sometimes be helpful. For the case of a constant (circularly polarized) RF field term, Madhu and Kumar [181] were able to derive an analytical Cartesian-space solution. On the other hand, the Bloch equations can be numerically integrated using any

ordinary differential equation solver. One numerical method merits special consideration because of its close relation to the situation in the digital waveform generators that are used in the MR system. This is the small tip angle (or "hard pulse") approximation [182, 183] (cited according to [184]). It approaches the Bloch equations by simply discretizing time into very small intervals in which the RF and gradient fields can be regarded as constant (which is actually the case for digitally synthesized waveforms), and regards RF rotation, gradient dephasing and relaxation as separate events which are interchangeable within that time step (an approximation). The simulation then consists in repeatedly calculating the effect of these "events" on the magnetization at each spatial location. This very simple approximation (equivalent to Euler integration of the Bloch equations), even though computationally inefficient and numerically highly simplistic, can be very useful for simulations because of the ease of implementation.

The extended phase graph technique, on the other hand, is relatively straight forward to implement. The natural structure for such a simulation program is a loop over the applied RF pulses. The transition due to an RF pulse can be formulated as a matrix acting on the four components F_n, F_n^*, Z_n and Z_n^* for each dephasing state. The dephasing due to the gradients shifts the state upward by one state (e.g. $F_n \rightarrow F_{n+1}$) while the relaxation terms are only changing the amplitude of the individual magnetization states. As long as the RF pulses are equidistant, such simulations are computationally very efficient. If anything, they have to be carefully checked against a direct numerical simulation of the Bloch equation to rule out implementation errors.

6.4 Improving SNR: Phase Cycling

One of the intrinsic limitations of the BURST sequence is its relatively low signal to noise ratio (SNR, compare section 1.3.4). This becomes clear when BURST is seen as the imaging equivalent of the DANTE pulse sequence. The DANTE sequence has the explicit aim of generating a narrow frequency profile and a BURST excitation therefore uses only a very thin strip of magnetization within each voxel. This means that only this portion of the magnetization will contribute to the measured signal, leading to a poor SNR. A different way to look at the same problem is to realize that in a BURST excitation, only small flip angle pulses can be used because otherwise, the sub-pulses no longer predominantly convert longitudinal into transverse magnetization but mix transverse magnetization components and transfer back transverse to longitudinal magnetization. In that case, the echo amplitudes will no longer be uniform. The maximum obtainable echo amplitude is M_0/N for a series of N RF pulses (of flip angle $\leq 90°/N$), a formula already given by Anderson et al. [185] in 1955. In that paper, it was

also foreseen that by using phase or frequency modulations, this fraction could be increased to $M_0/\sqrt{N}$.

For the BURST imaging sequence, the use of phase or frequency modulations was pioneered by Le Roux et al. [186], who applied the frequency modulation of a chirp pulse to the BURST excitation pulse train and also obtained $M_0/\sqrt{N}$ for the maximum obtainable echo amplitude. A conceptually different idea was presented by Duyn et al. [187, 188], who proposed spatially shifting the DANTE stripes in-between repetitions of a rapidly repeated (in their case gradient echo) BURST sequence. Van Gelderen et al. [189] instead proposed the application of a quadratic phase increment $\phi = (\pi/N) \cdot n(n+p)$ with p an integer number on the individual BURST sub-pulses, which they showed to come near the theoretical echo amplitude of $M_0/\sqrt{N}$. However, their method induced B_1-sensitive variations in echo phase, which was not practically correctable. To address that issue, they also investigated on the use of on only two phases of 0 and 180° with echo amplitudes almost as high and uniform as for the quadratic phase increment. Yet another approach was described by Zha and Lowe [190], who proposed to break the BURST excitation into blocks with different off-center shifts (equivalent to the frequency-shifted BURST by Duyn et al. [187]) and showed that they thereby approached the theoretical limit of $M_0/\sqrt{N}$ echo amplitude.

Heid [191] in 1997 conducted a very detailed and general mathematical analysis of the phase modulation strategies in BURST. He formally proved the theoretical signal maximum per echo to be $M_0/\sqrt{N}$. To reach that value, the individual pulses should have flip angles α_i of $\sin(\alpha_i/2) = 1/\sqrt{N}\sin(\alpha_{\text{tot}}/2)$ which means that for small total flip angle, it is approaching $\alpha_i \approx 1/\sqrt{N}\,\alpha_{\text{tot}}$ Further, he showed that chirp sequences $\phi_i = \pi(j^2 + 2jk + j)/N$ (i.e. quadratic phase increments) are close approximations to an ideal phase modulation.

All these types of phase modulation have the common effect of making use of more of the M_0 magnetization and are in that sense equivalent [192]. The quadratic phase modulation used in BURST is also similar to RF spoiling in rapid gradient echo imaging [193] in that an RF spoiled FLASH sequence develops the same magnetization pathways as a prolonged BURST excitation with quadratic phases.

Naturally, more general optimizations to improve the SNR are also applicable to BURST imaging. For example, Jakob et al. [194] have shown that when using long BURST excitation trains under realistic relaxation conditions, half Fourier reconstruction can lead to an improved SNR. The same is probably true for parallel imaging methods.

6.5 Implementations and Applications of BURST

The BURST excitation, as described in the original publications [142, 170], is a rather general concept and lends itself to numerous variations and applications. For example, both spin echo and gradient echo methods can be used to refocus the excited magnetization states in a series of echoes. Also, uneven pulse spacing can be used to generate the maximum number of transverse echoes with a given number of pulses, as applied to imaging by Heid et al. [195].

When a BURST excitation is seen as a type of RF excitation pulse, it becomes obvious that it can be combined with traditional imaging sequences to form "hybrid" sequences. The literature lists a large number of these, including a stimulated echo STEAM-BURST hybrid [196], a bSSFP (Truefisp) BURST hybrid [197], multiply refocused spin echoes (TSE-BURST hybrid) [198, 199], EPI / EVI (ultra rapid gradient echo planar / volumar Imaging) [200]. A number of these have been published only in the form of conference abstracts, which sometimes makes finding the appropriate literature a bit difficult. For a recent review of the BURST literature, see the paper by Doran et al. [201].

One interesting aspect of BURST is its inherent diffusion sensitivity, which has already been pointed out in the original paper by Hennig and Hodapp [142]. Doran and Decorps [202] recognized that after a BURST type excitation, the acquired echoes have a linearly increasing diffusion weighting, thus enabling a direct measurement of the exponential signal decay due to molecular diffusion in a single experiment. A subsequent paper by Wheeler-Kingshott et al. [203] extended this method to imaging.

Another interesting property of BURST is that it need very few gradient switching events per image, which means that acoustic noise levels during BURST imaging can be extremely low (for reasons discussed in sec. 3.3). This has been the main motivation to investigate the use of BURST for auditory fMRI in this thesis. The first application of the BURST sequence to BOLD fMRI was published by Jakob et al. [204]. They used a single slice spin echo BURST sequence with slice selective asymmetric spin echo refocusing to acquire images with an effective echo time of 40 ms. A visual experiment with a 10 Hz flashing LED array, auditory experiments using phonemes, pure tone triplets or noise bursts were performed using a 40 s epoch block design paradigm. In addition, an EEG-monitored sleep experiment was conducted, in which BOLD changes between non-REM and REM sleep were contrasted.

This experiment, which would have been difficult to perform with EPI-based fMRI, showed activation of the primary visual cortex in the REM versus non-REM sleep. Doran et al. [201] lists five further publications using BURST for fMRI, but so far, no full paper has been published applying BURST to auditory fMRI (apart from Jakob et al. [204]'s proof of concept).

6.6 BURST Artifacts

BURST type sequences suffer from a number of specific image artifacts. The ways in which they appear in the final images are rather different from other sequences and highly dependent on the specific variant of the BURST sequence used. Compared to the familiar $N/2$ ghost of the EPI sequences, such sequence-specific artifacts are more troublesome and difficult to "mentally disregard" [201].

For phantom images, the dominant sources of artifacts are ghosting or smearing artifacts, signal fall-offs in readout direction and edge artifacts and deformations. [201, 205]. Ghosting artifacts can appear in BURST images because of uneven echo magnitudes or phases. Uneven echo phases and magnitudes are apparent in the final images in different ways depending on the phase encoding strategy used. They are problematic only if they are periodic over the sampled phase encoding range (which is more often the case for phase than for magnitude errors). Signal decrease or fall-off in the readout direction can result from the limited "hardness" (i.e. the only finitely short duration) of the RF pulses applied over a constant gradient. Apart from the limitations imposed by the RF power amplifier, limitations on the specific absorption rate (SAR) allowable for human subjects and a possible preference for high readout bandwidths (because of signal decay and temporal efficiency) can be reasons to make compromises necessary in this respect. Edge artifacts, finally, are induced by the uneven sampling of the magnetization within a voxel in readout direction. As noted by Zha et al. [206], even for frequency or phase modulated BURST excitation schemes, spins from the same voxel but with different locations along the readout gradient do not contribute evenly to the measured signal from that voxel. The artifacts generated by this process are seen as edge bleeding and dislocation artifacts (which are most pronounced for single phase, unmodulated BURST) and edge deformation artifacts (which tend to be stronger in phase-modulated BURST sequences).

For in vivo applications, subject motion is also a major concern. BURST, as any diffusion-weighted sequence is highly susceptible to motion artifacts. Wheeler-Kingshott et al. [207] have shown that rotation parallel to the BURST encoding gradient direction are negligible, while rotations orthogonal to that direction produce significant distortions (quadratically dependent on the line number) which are partly correctable if the amount of motion is known or can be robustly estimated.

Finally, in gradient echo BURST variants, the usual off-resonance image artifacts can be observed and sometimes troublesome, depending on the phase encoding scheme used.

Chapter 7

Implementation of BURST

7.1 Overview

In this short chapter, the criteria that led me in the choice of a BURST sequence variant and the techniques used in the course of its implementation on clinical scanner systems are described. The results of numerical simulations which guided some of the implementation aspects, such as the choice of a suitable gradient spoiling scheme and the calculation of optimal flip angles, are left to the following chapter, with only the simulation techniques described here.

7.2 Choice of a BURST Variant

The aim of the BURST sequence implemented in the course of this work was the measurement of BOLD fMRI in auditory experiments. The objectives in the choice of a BURST variant as well as in the decisions made during the design and implementation phases were therefore, in the order of their relative importance:

1. Inherent T_2^* contrast
2. Very low acoustic noise levels
3. Continuous gradient sound
4. The best possible SNR
5. The best achievable scantime efficiency

The first objective, inherent T_2^* contrast, led to the choice of a gradient echo BURST variant. Here, the URGE sequences developed by Heid et al. [208] seemed most attractive. Another choice would have been to use spin-echo BURST with asymmetric echo as in the fMRI BURST sequence by

Jakob et al. [204], which was considered somewhat inelegant and would not have been as easily compatible with continuous sound.

The goal of very low noise level influenced, for example, the choice of phase encoding gradients. Here, a single phase encoding gradient was chosen (which is kept constant during the entire excitation pulse train). This is known to lead to a slight deformation of the reconstructed images, which is, however, hardly noticeable in practice.

Concerning the continuous gradient sound of the sequence, the URGE sequence seemed a favorable choice, since it already forms a continuous gradient pattern (at least for the readout gradients, which dominates in amplitude). This condition was also met for two further variations of URGE, the URGE-EPI and URGE-EVI hybrid sequences proposed by Heid [200] in a conference abstract. Whichever sequence is used, the continuous sound objective dictates that the repetition time is either chosen as short as possible (to avoid a gap in the readout gradients) or the readout gradient switching continued to the chosen TR (which must then be a multiple of the shortest possible value). Also, a gradient waveform periodicity with a frequency greater than about 50 Hz was desired to ensure the perception of the gradient sound as a continuous tone. This meant that excitation trains no longer than about 10 ms were aimed at.

The objective of a high signal to noise ratio called for a suitable phase or frequency modulation scheme to get as close as possible to the $M_0/\sqrt{n}$ limit for the echo amplitude (in an n pulse excitation pulse train). Naturally, this also implied the choice of an optimal flip angle and a suitable repetition time to compromise between saturation effects and scantime efficiency.

In interest of the scantime efficiency, a hybrid sequence was favorable compared to a pure BURST sequence. Here, the choice fell on the above mentioned URGE-EVI [200] sequence, a hybrid of BURST and echo volumar imaging (EVI). In comparison to URGE-EPI, the simplicity of image reconstruction compared to an constant phase encoding EPI variant (sampling a zig-zag trajectory) and the natural possibility to switch 3D encoding blips during the read gradient reversal at low slew rate and in agreement with the continuous sound requirement made URGE-EVI seem the better choice.

7.3 Numerical Simulations of Steady-State BURST

A numerical simulation to calculate the echo amplitudes of an URGE sequence was implemented using the extended phase graph formalism (see section 6.2). Since the shortest possible repetition times were aimed at for the fMRI sequence, the simulations were conducted in the steady state, which was usually reached after about 30 to 50 repetitions, depending on the repetition time and relaxation parameters. The calculation of a large number of magnetization states for each RF pulse (on the order of the total number

of RF pulses in the simulation) could be achieved in calculation times below one minute (for single configurations, on the order of several minutes for a free parameter, such as flip angle or dephasing). The simulation accounted for the usual relaxation parameters T_1 and T_2 both between repetitions and between the sub-pulses of an excitation train, and included a term for T_2^* decay between the excitation and the echoes. A freely selectable dephasing (or shift) of magnetization states was included between repetitions to simulate the effect on a varying spoiler gradient in read direction (i.e. the direction of gradient encoding during the BURST excitation).

In addition to these relaxation effects, the possibility for an additional signal attenuation due to molecular diffusion was also implemented. However, for the typically very short BURST trains of around eight pulses studied here, this term had only a very small effect and was therefore neglected in the comparisons of experimental and simulated echo amplitudes.

For comparison and debugging purposes, a simulation based on the direct integration of the Bloch equations (using the hard pulse approximation) was also implemented. Numerical results using the two methods agreed to good accuracy. Since the simulation based on the extended phase graph was much more efficient, this method was used for all the comparisons with experimental results.

7.4 Implementation Details

The sequence timing diagram of the URGE-EVI sequence here described is shown in figure 7.1. Sequence parameters for the displayed sequence are similar to those used in the fMRI experiment described in section 8.4. The RF excitation pulses (which in most cases could be limited to 20 µs duration) are switched on a constant read gradient. The consequence of the finite duration of the pulses is a sinc-shaped intensity modulation in the images along the direction of the read gradient. Also, the phase encoding gradient stays on during the RF pulses in the interest of lower demands on the gradient system and lower acoustic noise. Note that the readout gradient (which refocuses multiple gradient echoes similar to an EPI sequence) is almost perfectly periodic with a repetition rate of about 50 Hz. The dephasing at the end of a TR ("spoiling") is effected by the phase encoding gradient which fully dephases the magnetization (by $\pm\pi$).

Both the phase encoding and the slice encoding gradients follow a segmented scheme. The phase encoding gradient is calculated based on the number of RF pulses in a BURST excitation (n) so that its moment between two RF pulses is equal to one n-th of the k-space width. Over repetitions, a variable phase encoding gradient, switched during inversion of the read gradient, encodes the individual lines between those of the segment. In cases where the number of phase encoding lines is not an integer multiple of n,

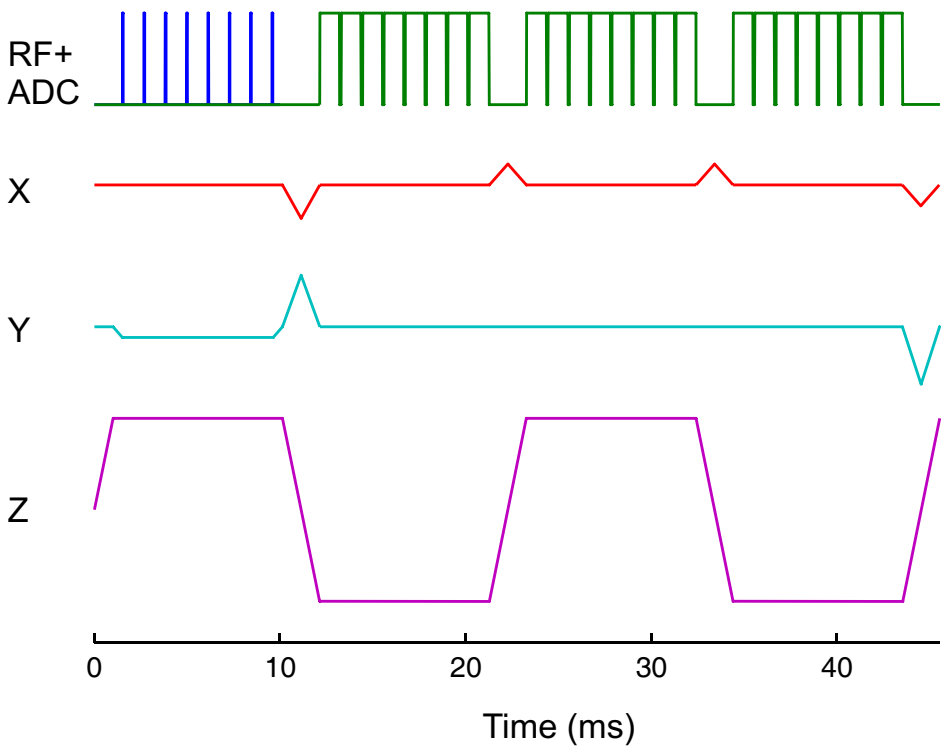

Figure 7.1: Sequence timing diagram of the URGE-EVI sequence implemented in this work. Sequence parameters were similar to those used in the fMRI experiment of section 8.4.

an additional segment with empty lines is used. For the slice (3D) encoding gradients, a similar strategy is used, with n replaced by the number of readout gradient refocusing periods (equivalent to the "EPI factor"). In this case, it is also the first (and the last "re-winder") gradient that is varying in with repetitions and encodes the partitions between the segments, while the inner gradients serve as "blips" to read lines distributed equally across the k-space width in slice direction. The aim of this strategy is to get a monotonic (and especially non-periodic) T_2^* weighting on the echo amplitudes to minimize ghosting artifacts.

The sequence code was tested in phantom experiments on both 1.5 T and 3 T systems. Since considerably larger BOLD response amplitudes could be expected when measuring at 3 T, the application of the sequence to fMRI was conducted at 3 T exclusively, as described in the following chapter. Also, two important questions that arose during the implementation phase regarding the size of the spoiler gradient and the optimal flip angle under steady state conditions are left to be discussed in the next chapter.

Chapter 8

Results: BURST

8.1 Overview

In the first part of this chapter, the results of numerical simulations on the steady state behavior of the URGE sequence are presented. A special emphasis has been placed on the determination of optimum spoiler gradient sizes as well as optimal flip angles in the steady state. Additionally, a not previously described gradient spoiling scheme based on the dephasing of the remaining magnetization on a gradient axis different from the BURST encoding (read) gradient is proposed, which places lower demands on the hardware in practical situations. As a by-product, it is demonstrated that quadratic phase modulations on the excitation sub-pulses (used to improve the SNR) can be combined with a quadratic phase modulation (RF spoiling) over repetitions.

In the second part, the implementation of URGE-EVI which has been described in the previous chapter, is characterized in terms of image quality and temporal signal stability. In an fMRI experiment involving an auditory stimulus, combined with a simultaneous finger-tapping task, the BOLD sensitivity of the sequence and its applicability to auditory fMRI is investigated.

8.2 Theoretical Work

8.2.1 Visualization of Magnetization States

In the following, a simple repeated URGE sequence is considered, as shown schematically in figure 8.1. A BURST excitation consisting of eight regularly spaced pulses is applied over a constant read gradient, which is then inverted to read out eight echoes. The two readout gradients have equal gradient moments, so that after the readout, the total moment of the read gradients is zero. Before the sequence is repeated, an additional spoiler gradient is applied. The size of this spoiler gradient is measured in units of g, the

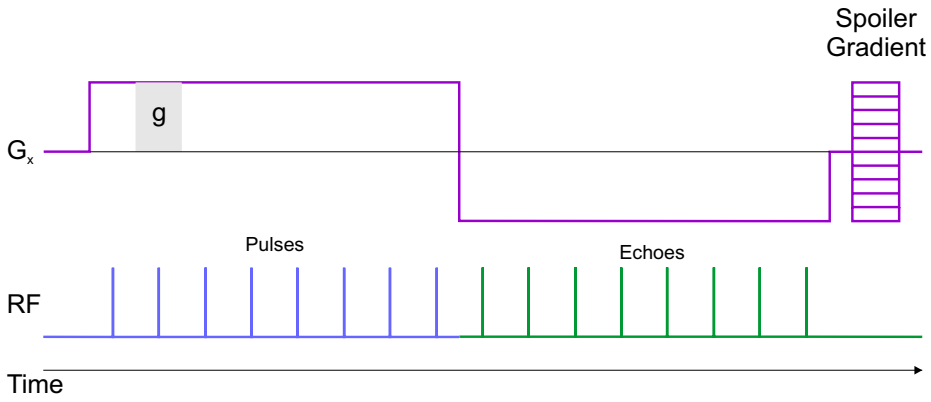

Figure 8.1: Sequence diagram for a simple URGE sequence, as simulated to determine the optimum size of the spoiler gradient. Gradient sizes are measured in units of g, the gradient moment needed to induce a complete dephasing by $\pm\pi$ over one imaging voxel.

gradient moment that is applied between two sub-pulses of the BURST excitation, i.e. the gradient moment that is needed to induce a complete dephasing of $\pm\pi$ over one imaging voxel.

In the limiting case of very low flip angles, where the RF pulses only excite longitudinal magnetization and have no (spin-echo) refocusing effect, the phase graph diagram for such a sequence, where the spoiler gradient is zero, is very simple (figure 8.2). Here, the longitudinal magnetization has also been omitted for simplicity. The remaining transverse magnetization from the previous excitation is superimposed on the consecutive excitation, which leads to a minimum number of only eight magnetization states to be followed at any time point. However, the echo amplitudes, which are the sum of the excited and the remaining magnetization, can already assume a more difficult pattern, depending on the relaxation times and flip angle used. Also, if all magnetization pathways are taken into consideration, the pattern becomes very complicated after only two repetitions (figure 8.3). Again, apart from the complexity of such a plot, the main disadvantage of this representation is that only the existence, but not the relative importance of the magnetization states is displayed.

Here, a color-coded plot of the simulated magnetization states provides a much clearer picture. In figure 8.4, the calculated echo amplitudes of the same sequence as above is shown for five repetitions and two flip angles of 1° (representing the low flip angle limit) and 10° (a more complicated pattern). The other simulation parameters were chosen to be more or less realistic for a phantom experiment using the URGE-EVI sequence: TR=30 ms, T_1=1 s, T_2=0.5 s, T_2^*=50 ms, pulse spacing (and echo spacing) 1.5 ms, first echo time 2 ms, all RF pulses applied at 0° phase. Note that the gradient rephasing

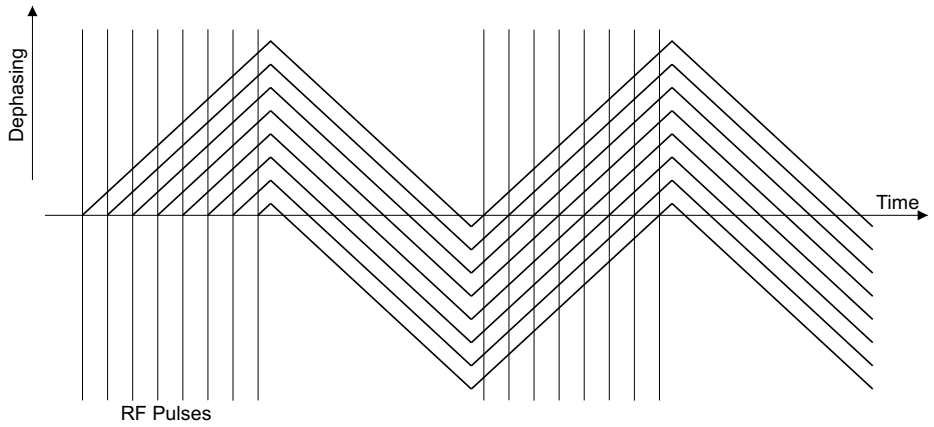

Figure 8.2: Simplified phase graph diagram of an eight pulse URGE sequence (8.1) for the limit of infinitely small flip angles and no spoiler gradient.

during the readout of the echoes is not displayed in these figures, rather, only the magnetization states immediately after the application of the RF pulses is shown. Compared to the above phase graph diagrams, this means that the time in-between the RF pulse trains is simply compressed to the equivalent of one pulse spacing interval. Also, according to the Matlab convention of addressing matrices from top to bottom, in all these diagrams the dephasing increases from top to bottom (i.e. a reflection along the horizontal axis compared to the phase graph diagrams above).

8.2.2 Varying the Spoiler Gradient

Using this visualization technique, the optimum size of the spoiler gradient after the readout of the echoes can be investigated. Again, the above convention (figure 8.1) of measuring the spoiler gradient in units of g is used (i.e. the gradient moment necessary to induce a full $\pm\pi$ dephasing over one imaging voxel). Further, a spoiler moment shall be assigned a positive number when it has the same polarity as the refocusing gradient, a positive number if it has opposite polarity (i.e. the same polarity as the gradient during the BURST excitation).

In the light of the very short repetition times desired to achieve a reasonable scan time efficiency and continuous sequence sound, finding an answer the question of the optimum size for the spoiler gradient is especially important. The literature on this subject is very sparse, while Heid [200] likely used some kind of gradient spoiling, this aspect of the URGE-EVI (and also the URGE [208]) sequence was not discussed in the original papers. Referring to the related question of the size necessary for crusher gradients around a spin echo inversion pulse, Doran et al. [201] stated that "there has been no detailed discussion of the role of these crusher gradients in the BURST

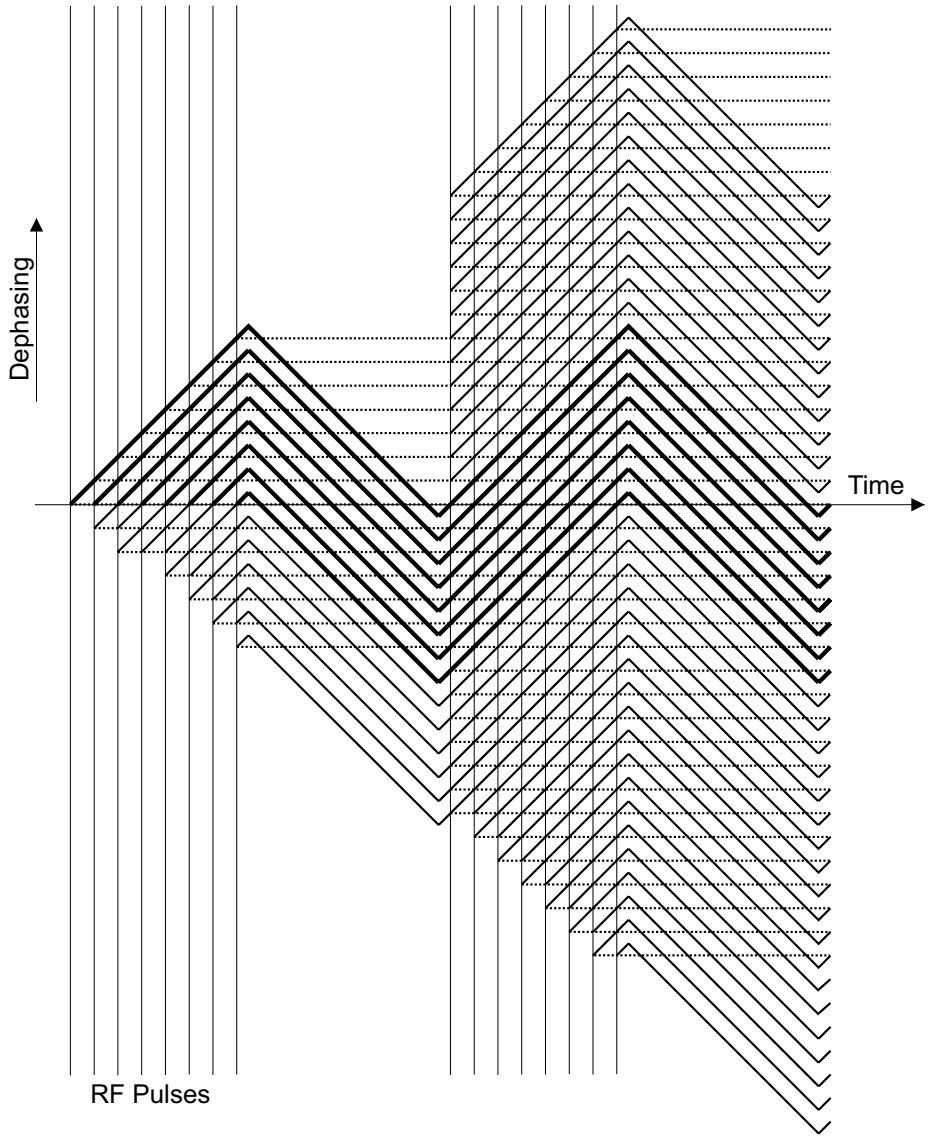

Figure 8.3: Phase graph diagram of an eight pulse URGE sequence (see figure 8.1) showing all magnetization pathways. Bold lines represent the limiting case of small flip angles (figure 8.2), dotted lines longitudinal magnetization.

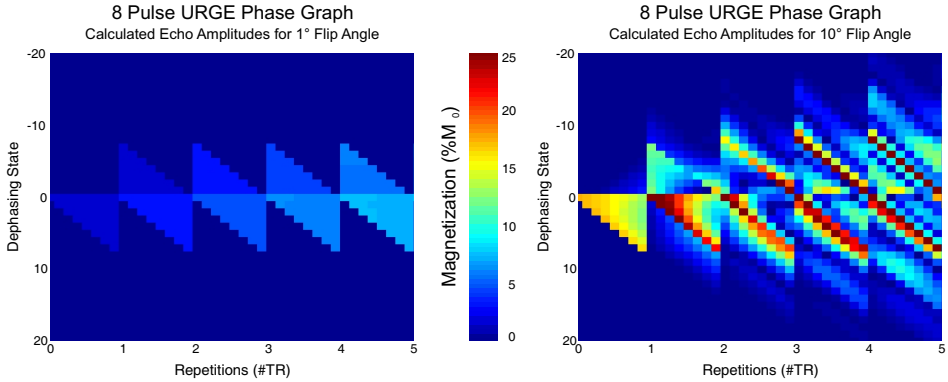

Figure 8.4: Simulated echo amplitudes (phase graph calculation) for an eight pulse URGE sequence as in figures 8.1 to 8.3. Here, the effect of increasing flip angle is seen very clearly (left: 1°, right: 10°). The total gradient moment of the read gradient was zero, i.e. no additional spoiler gradient used.

literature". It was only after the completion of this study that I became aware of one brief conference abstract discussing the question of spoiler gradients by Brenner et al. [209]. They had developed a numerical integration method of the Bloch equations in the steady state, which formed the main part of their abstract, and applied it to study the effect of different size spoiler gradients on gradient echo DUFIS and OUFIS. Similar to the work presented here, they had included relaxation terms and found the necessary size to be at least equal to that of the encoding gradient. In contrast to the present work, they had considered only one polarity for the spoiling gradient (corresponding to positive spoiling gradients, according to above definition) and shown no comparison to measured data.

A natural choice for the spoiler gradient moment for an n pulse URGE sequence is to use an integer multiple of ng. This is the total moment of the (read) gradient present during the BURST excitation train (which can also be thought of as the "slice-selective gradient", if the BURST train is viewed as a selective excitation RF pulse). Figure 8.5 shows the calculated magnetization states for spoiler gradient moments of -8, 0, 8. Simulation parameters were the same as for figure 8.4 (TR=30 ms, T_1=1 s, T_2=0.5 s, T_2^*=50 ms, pulse and echo spacing 1.5 ms, first echo time 2 ms, all RF pulses applied at 0° phase). The flip angle was set to 7°, the optimal flip angle for these parameters (calculated using the method of subsection 8.2.4).

The dependence of the signal amplitudes (mean and standard deviation) on the spoiler gradient size in a rapidly repeated URGE sequence are shown in figure 8.6. Here, all integer multiples of g were considered. Calculations are based on the same parameters as in the previous section: TR=30 ms, T_1=1 s, T_2=0.5 s, T_2^*=50 ms, pulse spacing (and echo spacing)

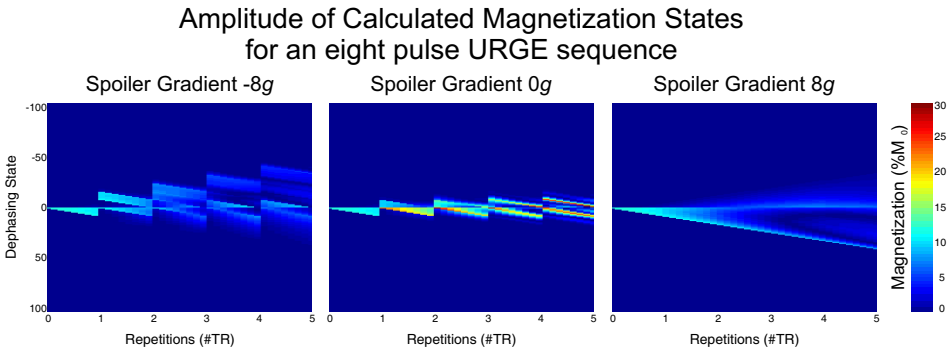

Figure 8.5: Calculated magnetization states for an eight pulse URGE sequence with spoiler gradients of $-8g$ (left), 0 (middle) and $8g$ (right).

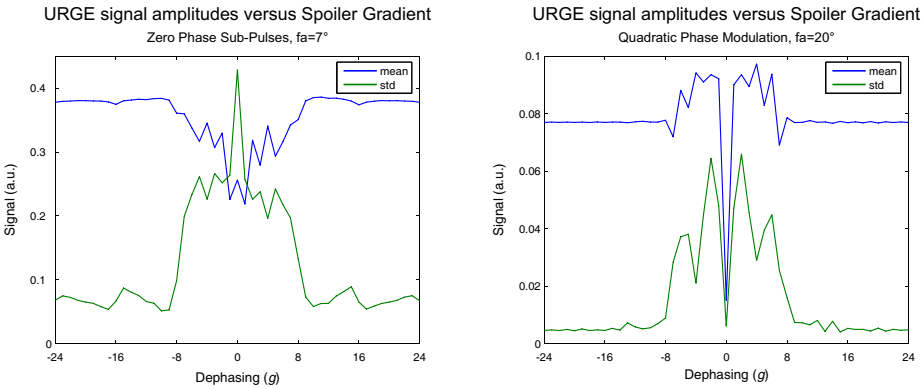

Figure 8.6: Influence of the spoiler gradient on the signal amplitudes in an eight pulse URGE sequence. The plotted values are the mean and standard deviation of the eight steady state echo amplitudes using either 0° pulses (left) or quadratic phase modulation (right).

1.5 ms, first echo time 2 ms. RF pulses are applied either using 0° phase (left) or quadratic phase increments (right, phase of the individual sub-pulses [270, 135, 45, 0, 0, 45, 135, 270] degrees). The flip angles used are 7° for the zero phase variant and 20° for the quadratic phase variant. These values will turn out to be the theoretical optimal flip angles in subsection 8.2.4. The plotted signal values are steady state values after 80 repetitions.

It can be concluded that a spoiler gradient of at least ng should be used for an n pulse URGE sequence. The polarity of the spoiler gradient is not very important, as seen by the almost perfect symmetry of the plots in figure 8.6. However, and especially for the critical value of ng spoiler gradient moment, the negative polarity (not considered by Brenner et al. [209]) shows a slight advantage over the corresponding positive one. In practical situations, a gradient moment equal to that of the encoding and refocusing gradients is already rather large and time consuming, especially if larger numbers of BURST sub-pulses are used.

8.2.3 Spoiling in Phase Encoding Direction

An alternative to using such very large spoiler gradients is to dephased the remaining transverse magnetization along a different gradient axis. For quadratic field of view, the spoiler gradient along the phase encoding direction needed to induce a full dephasing of $\pm\pi$ in each voxel is only of size g, compared to the large multiples of that moment calculated above. Still, it can be assumed to have the same effect on the remaining magnetization. This assumption was tested on the small cylindrical phantom and compared to simulations of large read axis spoilers (figure 8.7). Parameters were: 30 repetitions of TR=25 ms, T_1=404 ms, T_2=292 ms, T_2^*=67 ms, pulse spacing 1.02 ms, first echo time 1.51 ms, echo spacing 1.26 ms, quadratic phase modulation on the BURST sub-pulses (phases were [270, 135, 45, 0, 0, 45, 135, 270]), flip angle 7°, spoiling gradient for the simulation $16g$. The mean of the first eight calculated echo amplitudes was fitted to the mean of the experimentally determined values.

The data, while not being in very good agreement with the simulated values, strongly suggests that the above assumption is true, i.e. that a spoiler gradient in phase encoding direction can be used instead of the very large gradients necessary in read direction. In practice, this is a huge advantage, especially with regard to the objective of quasi-continuous gradient sound. A small gradient in phase encoding direction of moment g can be easily masked, while a n-fold larger gradient (or more) would impose serious problems in this regard. Therefore, this approach was used in the here implemented URGE-EVI sequence.

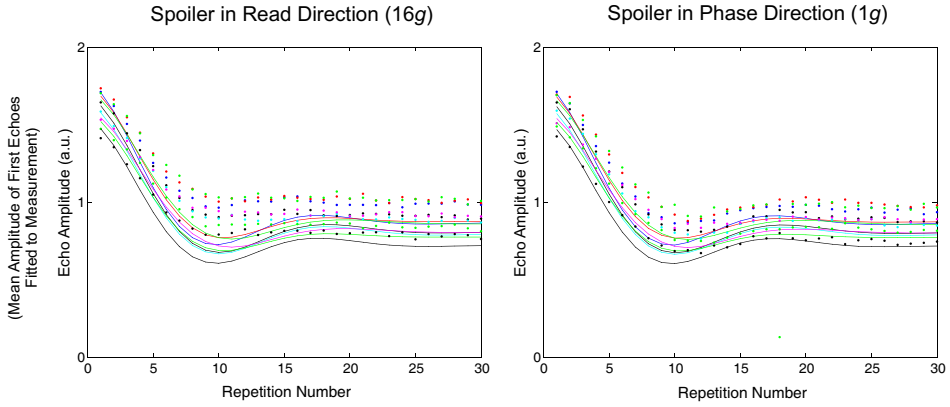

Figure 8.7: Comparison of the spoiling efficiency of large gradient of $16g$ in read direction with a spoiler of g in phase encoding direction. Solid lines correspond to the simulated echo amplitudes, dots to measured data points.

8.2.4 Optimal Flip Angle

Under steady state conditions, it can be expected that the optimal flip angle of an n pulse BURST sequence is considerably smaller than $90°/n$. One reason for such an assumption is the analogy to a single pulse, gradient-spoiled gradient echo sequence (non-RF-spoiled FLASH). Also, the simulation earlier shown in figure 8.4 supports this assumption, where both flip angles (of $1°$ and $10°$) were smaller than $90°/8 = 11.25°$ but the $10°$ pulse train showed highly uneven echo amplitudes. Rather, it can be guessed that the optimum flip angle is given by $\alpha_{\mathrm{opt}} = \alpha_1/n$, where α_1 is the optimum flip angle of the single pulse experiment in the steady state. Then, the echo amplitude reached for a flip angle of α_{opt} could be expected to be M_1/n with M_1 the optimum signal amplitude for the non-RF-spoiled FLASH sequence. Further, it could be expected that for quadratic phase modulations, the above relations might also hold, with n replaced by $\sqrt{n}$ to give $\alpha_{\mathrm{opt}} = \alpha_1/\sqrt{n}$ and $M_{\mathrm{opt}} = M_1/\sqrt{n}$. To test the correctness of these hypotheses, the flip angle dependence of an eight pulse URGE sequence was examined both in simulation and experiment.

The experimental measurement of echo amplitudes was conducted on a small 5 cm diameter spherical phantom containing deionized water doped with about 1:1000 gadolinium DOTA. The relaxation times were measured to be T_1=783 ms, T_2=577 ms. The pulse sequence used was very similar to the URGE sequence schematically depicted in figure 8.1, it used no phase encoding on any axis but simply generated a train of echoes and was repeated at a rate of TR=30 ms. The simulation parameters were adapted to the real timing values used in the experiment: 200 repetitions at a TR of 30 ms, pulse spacing 1.52 ms, first echo time 1.81 ms, echo spacing 1.26 ms (the

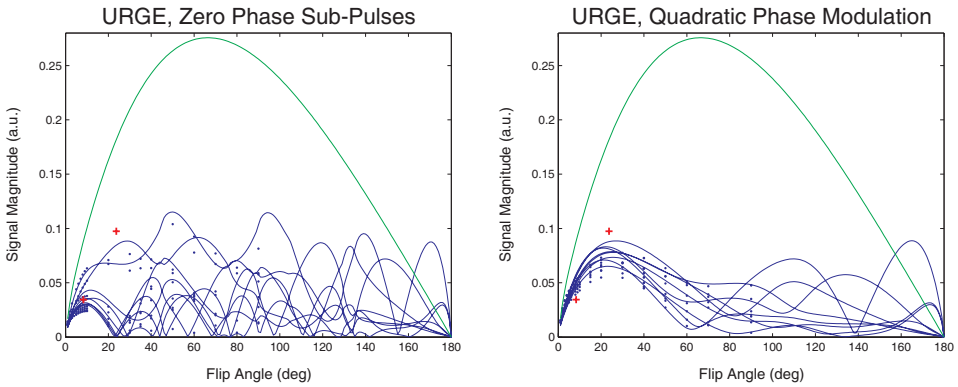

Figure 8.8: Steady state signal amplitudes versus flip angle for an eight pulse URGE sequence with and without quadratic phase modulation. The solid blue lines indicate simulated values, the dots measured echo amplitudes, the red crosses indicate the hypothesized limits and the green line the flip angle dependence of the corresponding single pulse experiment.

encoding and readout gradient were not exactly of the same amplitude). A large spoiler gradient of $16g$ was used. The T_2^* value in the simulation was empirically adapted to the data and set to T_2^*=40 ms.

Figure 8.8 shows the resulting flip angle dependence of the BURST signal in simulation (blue solid lines) and experiment (blue dots). The left figure corresponds to zero phase pulses while in the right figure, a quadratic phase increment was used (the phase of the individual sub-pulses was [270, 135, 45, 0, 0, 45, 135, 270]). For comparison, the flip angle dependence of the single pulse experiment (non-RF-spoiled FLASH) is included in green. The two red crosses indicate the above predictions for zero phase pulses ($\alpha_{\mathrm{opt}} = \alpha_1/n$, $M_{\mathrm{opt}} = M_1/n$) and for quadratic phase increments ($\alpha_{\mathrm{opt}} = \alpha_1/\sqrt{n}$, $M_{\mathrm{opt}} = M_1/\sqrt{n}$). The correspondence between simulation and measurement is relatively good. The assumed limits given by the α_{opt} and M_{opt}, while neglecting much of the complexity of the real signal behavior, are useful indicators of the maximum flip angles for which the echo amplitudes are still more or less equal. It can be concluded that for an n pulse BURST sequence in the steady state, flip angles no larger than $1/n$ of the optimum flip angle of the corresponding single pulse experiment should be used. If quadratic phase modulation is used on the sub-pulses, the flip angle can be increased to about $1/\sqrt{n}$ of optimum value for the single-pulse experiment, with correspondingly larger echo amplitudes and therefore better SNR.

8.2.5 Phase-Modulated URGE and RF Spoiling

Without having any specific application in mind, it was also investigated whether the quadratic phases on the sub-pulses of the BURST excitation

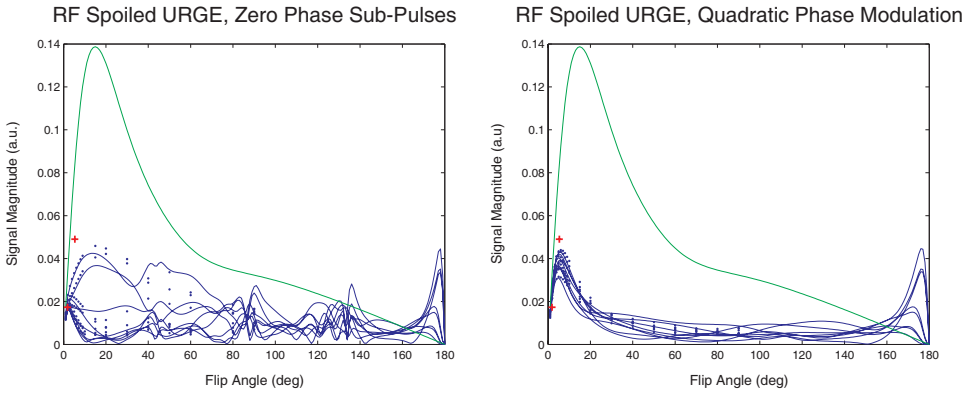

Figure 8.9: Combination of RF Spoiling between repetitions and quadratic phases modulation over the BURST sub-pulses. Again, solid blue lines indicate simulated values, the dots measured echo amplitudes, the red crosses indicate the theoretical limits and the green line the flip angle dependence of the single pulse experiment.

train could be combined with RF spoiling (quadratic phase modulation across repetitions). In FLASH imaging, RF spoiling is standard practice to suppress unwanted signal contributions from the transverse magnetization of earlier pulses [193]. When the BURST excitation is viewed as a composite RF pulse, this question seems natural and it can be expected that such a combination should be possible.

The method for both simulation and experimental verification were identical to the determination of flip angle dependence reported in the last subsection. The only difference was that a quadratic phase term, dependent on the repetition number, was added to the phase of each BURST sub-pulse. The results of this experiment are shown in figure 8.9. Again, the simulation and experiment are in good agreement, and the theoretical limits (where α_{opt} and $\mathrm{M}_{\mathrm{opt}}$ are now replaced with the optimum flip angle and signal for the RF spoiled FLASH) are good approximations of the respective points where the echo amplitudes start to diverge. From this results it can be concluded that it is possible to combine BURST excitation with RF spoiling, even when quadratic phase modulation is already used on the individual sub-pulses of the BURST excitation train.

8.3 Image Quality and Temporal Signal Stability

The present URGE-EVI sequence gives rise to quite pronounced artifacts, as seen in the images of a spherical phantom in figure 8.10. Especially, signal voids (or banding artifacts) are seen near places where magnetic susceptibility effects can be expected. Image parameters images were: TR=52.1 ms,

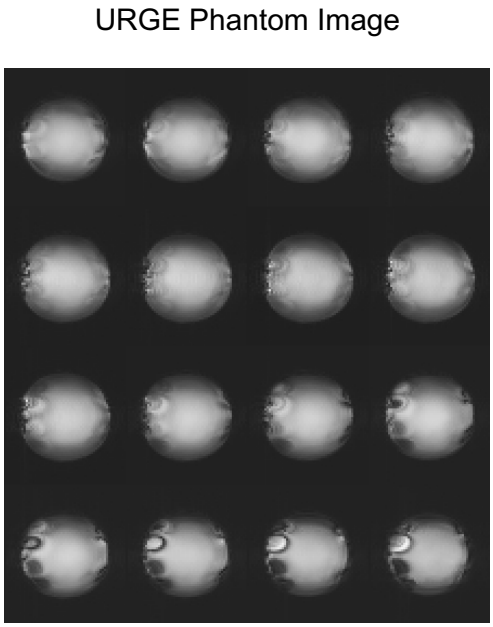

Figure 8.10: Image quality of URGE in a spherical phantom (16 contiguous partitions from a 3D acquisition). Pronounced artifacts can be seen around regions where susceptibility variations can be expected, such as the air bubbles near the top (left in the image) of the phantom.

TE=28.2 ms, matrix size $64 \times 56 \times 32$ (corresponding to $4 \times 4 \times 5$ mm voxel size), flip angle 9°, readout bandwidth 1300 Hz/px, EPI factor 5, 8 pulses per BURST excitation.

In vivo, these artifacts are not as noticeable, as shown in figure 8.11. Here, the last volume of below fMRI experiment using the URGE-EVI sequence is compared to an EPI image of the same volunteer measured on the same system with equal volume TR, TE and voxel size (the fifth volume of a time-series). Note that the EPI sequence used the somewhat exotic sagittal slice positioning to obtain equal voxel dimensions as in the (also sagittally oriented) URGE sequence. Image parameters were: (a) for the URGE sequence: TR=46 ms, volume repetition time 3.55 s, TE=30 ms, matrix size $64 \times 56 \times 32$, field of view $220 \times 192.5 \times 160$ mm (corresponding to 3.4×3.4×5 mm voxel size), flip angle 11°, readout bandwidth 940 Hz/px, EPI factor 3, 8 pulses per BURST excitation, quadratic phase modulation on the sub-pulses, gradient spoiling along the phase encoding direction, (b) for the EPI sequence: TR=3.55 s, TE=30 ms, matrix size 64×64, 36 sagittal slices of 4.5 mm thickness, field of view 22 cm (corresponding to 3.4×3.4×5 mm voxel size), flip angle 90°, readout bandwidth 1370 Hz/px, no fat saturation. Both images were acquired on the 3 T Siemens Allegra system using a birdcage head coil.

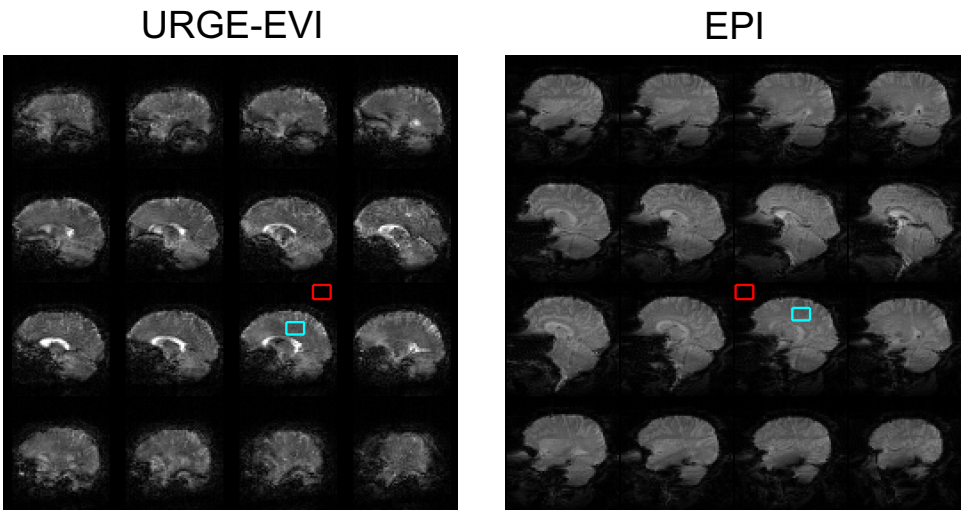

Figure 8.11: In vivo comparison of image quality and SNR for URGE-EVI and a sagittal multislice EPI acquired on the same system for the same volunteer.

The image quality of the URGE sequence seems quite comparable to that of EPI, with distortion artifacts not much more severe than in EPI, but with more pronounced signal drop-outs. The signal to noise ratio is comparable, when measured over rectangular regions of interest of 10×8 pixels (signal ROI blue, noise ROI red), the SNR of the URGE image is 68, compared to 71 for the EPI. However, it has to be cautioned that the parameters were certainly not optimal for the EPI sequence, while the URGE sequence was at its limits. Therefore, SNR per scan time is still expected to be considerably larger for the EPI than the URGE sequence. Also, the selection of the ROI location could be argued to be too optimistic. It is here chosen outside the brain, offset in the readout direction of the sequence, because this was the region of least artifacts (for both sequences). In the phase and 3D encoding directions, ghosting and smearing artifacts were quite strong in the URGE images, which would have led to much higher noise levels (and therefore lower SNR).

Temporal signal stability was measured in the same way as for the comparison of conventional versus Continuous EPI (section 5.2.2). The histograms of relative voxel-wise standard deviation for the present URGE-EVI sequence (at 3 T, compared to EPI at 1.5 and 3 T), is shown in figure 8.12. The stability of the URGE sequence is considerably lower than that of EPI at the same field strength, most likely due to the above artifacts. Still, the temporal stability was considered adequate for fMRI, since it was comparable to that measured for EPI at 1.5 T.

The sound level of the acoustic noise generated by the URGE-EVI se-

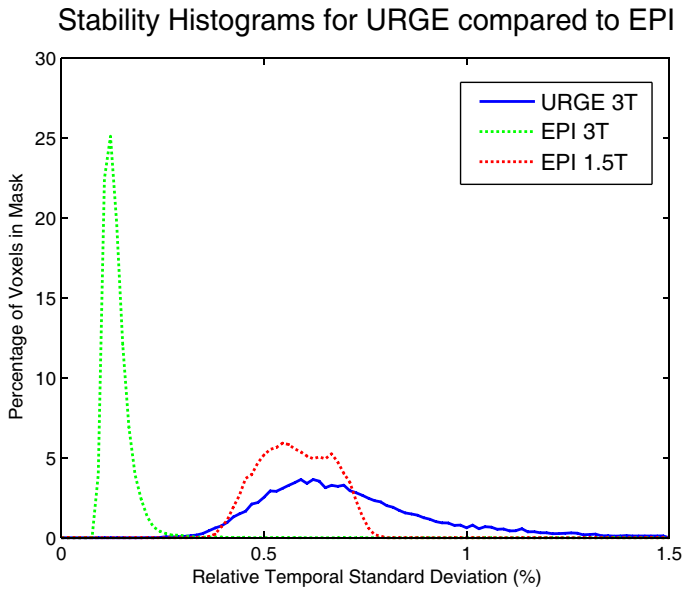

Figure 8.12: Temporal signal stability of the URGE-EVI sequence, compared to EPI at 1.5 and 3 T. As in the conventional – Continuous EPI comparison, histograms of the relative voxel-wise standard deviance are used as a robust measure of temporal signal stability.

quence was, for the sequence settings used in the fMRI experiment, 54.6 dB(A), at a ambient noise level (helium pump etc.) of 48.8 dB(A). In comparison, the EPI sequence used for the in-vivo image quality comparison resulted in a sound level of 82.0 dB(A) and the (conventional) EPI sequence of the fMRI experiment 4 of chapter 5 in 85.4 dB(A). Sound levels in this comparison were measured in the scanner room, but away from the magnet bore.

8.4 fMRI Experiment: Pulsed Tones and Finger-Tapping

To evaluate the use of this sequence for auditory fMRI, a combined auditory and finger tapping experiment was conducted. A single male, right-handed volunteer of 36 years was scanned in 3 sessions of 3 min each. The use of three sessions instead of one longer experiment was necessary because of a software limitation in the image reconstruction system (which limited the product of phase encoding steps, partitions and repetitions). Prior to the functional runs, a T_1 weighted MDEFT dataset was acquired and used both to position the functional sequence and to co-register the functional data during data analysis. All data were acquired on the 3 T Siemens Allegra system using a birdcage head coil.

The paradigm was a block design consisting of five 16 s stimulation epochs interleaved with 16 s baseline periods and an additional baseline period at the beginning (total scantime 3 : 00 min). The auditory stimulus consisted of 1 kHz sine tones pulsed at 5 Hz, with the first and last 10 ms of each pulse smoothed with a cosine-squared function. The auditory stimulus was generated using Matlab and recorded on CD. It was manually synchronized with the sequence start and delivered over a high-fidelity acoustic stimulation system (the same used in the 3 T fMRI experiments of section 5.6). Sound level was adjusted to be perceived as very loud but not painful.

The finger tapping task synchronous with and triggered by the auditory stimulus was included because from preceding trials, it was clear that the contrast to noise ratio of the URGE sequence severely limited the detectability of functional activation. Since sensomotor stimulation results in a very robust and large amplitude BOLD response, which in anatomically well defined regions, this additional task was included as a control condition. The instruction to the subject was simply to open and close both his hands at a freely chosen rate during the auditory stimulation interval.

Image parameters were: TR=46 ms, volume repetition time 3.55 s, TE= 30 ms, matrix size $64 \times 56 \times 32$, field of view $220 \times 192.5 \times 160$ mm (corresponding to $3.4 \times 3.4 \times 5$ mm voxel size), flip angle 11°, readout bandwidth 940 Hz/px, EPI factor 3, 8 pulses per BURST excitation, quadratic phase modulation on the sub-pulses, gradient spoiling along the phase encoding direction. The eight-pulse excitation together with an EPI factor 3 is an empirically determined compromise between long excitation pulse trains which would be beneficial in terms of reduced sound levels but severely lowering SNR, high EPI factors in the interest of efficient scan-time usage (and good SNR) but limited by T_2^* decay (and strong image artifacts) and finally the balance between high resolution desirable for functional localization and the need to obtain volume repetition times on the order of 3-5 s for functional contrast and echo times around 30 ms for sufficient T_2^* weighting. Taken together, these constraints did not leave much space for variation of the image parameters.

As in the Continuous EPI experiments, data were analyzed using BrainVoyager QX, with the standard set of realignment and temporal high-pass filtering steps. In addition, 4 mm spatial smoothing was used. Functional datasets were co-registered to a T_1weighted anatomical dataset and transformed into standard anatomical space (Talairach).

Highly significant activation was found at locations corresponding to left and right primary motor cortex and the supplementary motor area (figure 8.13). All activation maps are thresholded at $t = 6$, $p < 0.001$ Bonferroni corrected. The activation on the left hemisphere (slice at Talairach x=-35) is found somewhat more posterior than anticipated (along the postrather than the precentral gyrus), which is likely to be due to distortion in the URGE raw images. Only the left motor area was consistently acti-

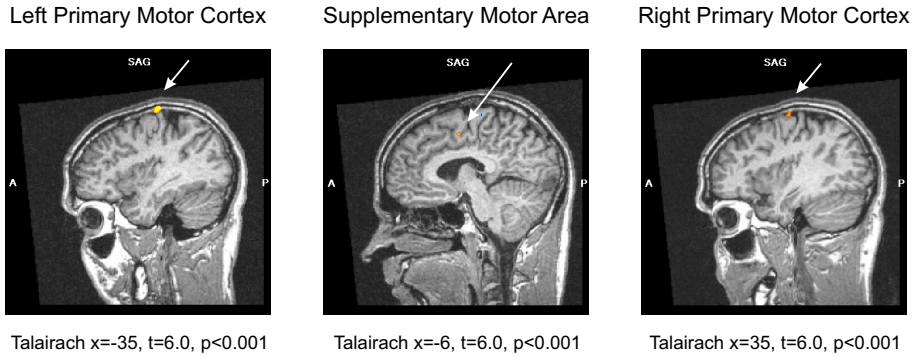

Figure 8.13: Highly significant sensomotor activation in the URGE-EVI fMRI experiment. Shown for three slices corresponding to the expected locations of left and right primary motor cortex and the supplementary motor area ($t = 6$, $p < 0.001$, Bonferroni corrected).

vated across all three runs, as revealed by a conjunction analysis, even for a probability level of $p < 0.05$.

At the expected location of the auditory areas no significant ($p < 0.05$, Bonferroni corrected) activation was found on neither hemisphere. At a non-significant threshold of $t = 2.5$ ($p < 1$ Bonferroni corrected, $p < 0.02$ uncorrected), a bilateral activation pattern was found along the planum temporale (figure 8.14). Whether this reflects auditory activation below the significance level (which would normally be expected along Heschl's gyrus rather than planum polare for pure tones) or false activation cannot be determined from the present data. The latter seems more likely when inspecting these locations in a conjunction analysis, which shows that this activation pattern is no more consistent over the three runs than both positive and negative activation in many other areas unrelated to auditory or sensomotor functions.

Upon inspection of the functional volume, right Heschl's gyrus clearly fell victim to a very pronounced artifact consistently present in all three runs (figure 8.15), which led to an almost complete signal void in that region. For the left hemisphere, the situation was somewhat better, but here, the very bright signal of the CSF extended laterally into that region. Both artifacts seem to include regions where signal is shifted by several pixels towards the left hemisphere. This was the direction of the 3D encoding gradient, the direction of the lowest readout "bandwidth". Most likely, these distortions result from off-resonances in the vicinity of the mastoid (in the temporal bone). Similar off-resonance artifacts can be found in the anterofrontal areas of the brain around the nasal cavities, which supports the conclusion that the distortions indeed arise from (EPI-like) bandwidth-related mis-registration. Choosing a larger bandwidth, for example by reducing

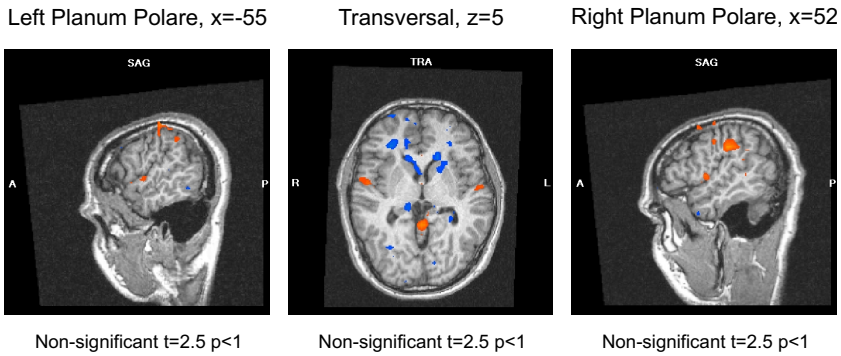

Figure 8.14: Non-significant bilateral activation found in the combined auditory – sensomotor fMRI experiment using the URGE-EVI sequence. The small, but symmetrically located activation clusters could be interpreted as low-CNR auditory activation, but also as an artifact.

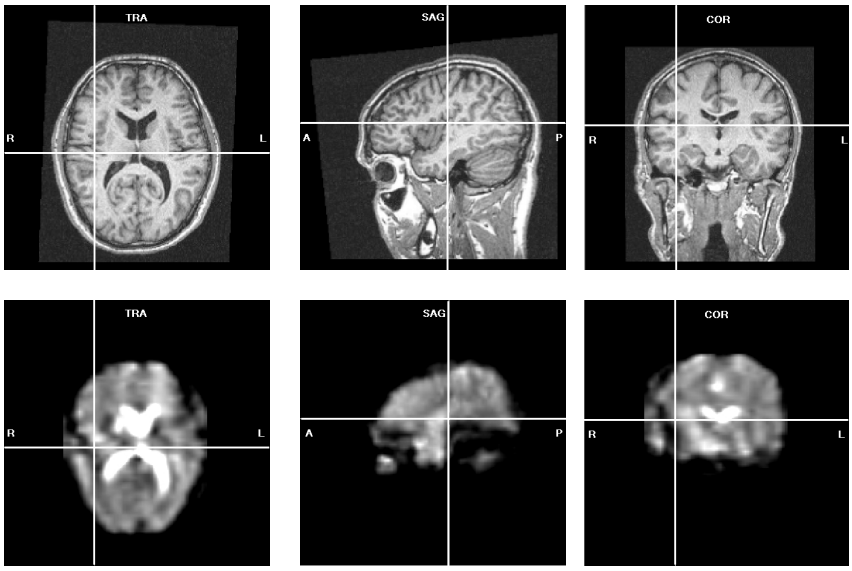

Figure 8.15: Pronounced distortion and signal drop-out artifacts at the location of right Heschl's gyrus in the Talairach transformed URGE-EVI volumes, compared to the co-registered anatomical image. The white cross has coordinates x=40, y=-14 and z=13.

the number of excitation pulses in a BURST, could be expected to reduce this problem, with the limiting case of a pure single pulse EVI sequence. While single pulse EVI does not solve, but only partly relieves this problem, the acoustic properties (i.e. the reduction in acoustic noise) would have been sacrificed by such a modification. Alternatively, the choice of a different phase encoding strategy, such as a purely two-dimensional phase encoding in each segment, might have reduced these artifacts considerably. However, in such a scheme, even slightly uneven echo amplitudes or phases among BURST sub-pulses can be expected to lead to severe ghosting, due to the periodic refocusing of these echoes. Signal drop-outs, on the other hand, could be much reduced if smaller voxel sized could be applied. In the present implementation, the software limitation of the image reconstruction system mentioned at the beginning of this section as well as the necessity to obtain full brain coverage (due to the non-selective RF pulses) at the best possible time resolution has severely limited the minimal voxel size. Here, the upcoming software version (expected next year), which removes the first limitation offers prospects of improvement, especially when additional acceleration with the use of parallel imaging can be implemented.

The time course data from the left and right motor cortex and the supplementary motor area, as defined by the above main effect GLM, thresholded at $t = 6$ ($p < 0.001$ Bonferroni corrected), is shown in figure 8.16. The BOLD percent signal changes of about 2-4% are in the range expected for the field strength of 3 T. Note that the time course was sampled only at 3.5 s intervals, but with a jitter relative to the stimulus onset, since the stimulation cycle of 32 s was not synchronized to the repetition time. The apparently lower percent signal change for the left motor cortex seems somewhat surprising considering more statistically significant activation on that hemisphere the right-handedness of the volunteer but may be an attributed to the relatively low CNR and or the insufficient averaging of the baseline (the event time courses were aligned to the mean of time points 2 to 0 s before stimulus onset).

In conclusion, this experiment has demonstrated the BOLD sensitivity of the current URGE-EVI sequence in that it reliably revealed highly significant activation of (at least the left) primary motor cortex. The failure to find significant activation in the auditory cortex has likely resulted from pronounced off-resonance distortions and signal drop-outs. The strong artifacts and the limited temporal and spatial resolution can be concluded to be the main challenges when applying URGE-EVI to auditory fMRI.

8.5 Summary

In the course of the present work, the steady state behavior of gradient echo BURST (URGE) was examined in detail. An approximate relation for the

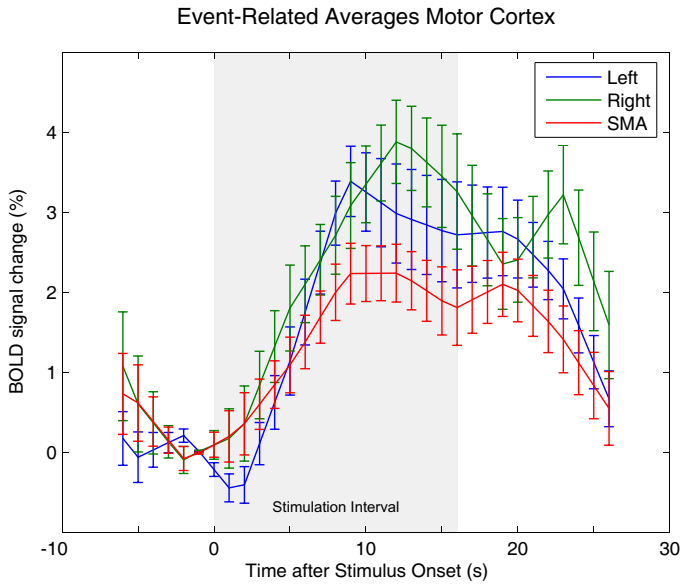

Figure 8.16: Event related averages for the combined auditory – sensomotor fMRI experiment using the URGE-EVI sequence. The averaging is performed for the significantly activated voxels ($t = 6$, $p < 0.001$ Bonferroni corrected) in the left and right motor cortex and the supplementary motor area.

optimal flip angle and the achievable signal amplitude could be given and compared to more exact numerical simulations and phantom measurements. Also, the size of the spoiler gradient necessary to obtain efficient dephasing of remaining transverse magnetization has been determined to be at least as large as the encoding gradient. As an alternative, gradient spoiling along a different gradient axis has been proposed and found to be beneficial in practical situations.

An URGE-EVI sequence was implemented on two clinical 1.5 T and 3 T systems using the above findings. Sound levels during scanning were only 6 dB(A) above the ambient noise level, compared to about 30-35 dB(A) for EPI sequences. Temporal signal stability was found to be reduced, compared to the standard EPI sequence at 3 T, but still in a range where reliable BOLD fMRI measurements should be possible. Also, the signal to noise ratio was found to be comparable to an EPI sequence with similar parameters (which were certainly not optimal for the EPI). In an fMRI experiment combining auditory stimulation with a simultaneous finger-tapping task, the BOLD sensitivity of the URGE sequence was established, as highly significant activation was found in the expected location for the motor cortex and the supplementary motor area. However, this experiment has failed to show activation in the expected location of the primary auditory cortex. This was very likely a result of pronounced distortion and signal drop-out artifacts present in the functional image volumes.

As currently implemented, the usefulness of URGE-EVI for auditory fMRI is therefore seen to be severely limited. The main obstacles are pronounced distortion artifacts similar to those expected for a relatively low-bandwidth EVI sequence and signal drop-outs due to the rather large voxel size. For the currently used 3D segmented phase encoding scheme and given the limitations imposed by the gradient hardware – and especially by a cumbersome limitation in the scanner's current image reconstruction software – these issues are not easy to resolve. The removal of that software limitation in the upcoming version opens prospects of making higher temporal and spatial resolution possible, especially in combination with parallel imaging techniques. This might also reduce the signal drop-out artifacts. While the distortion artifacts might be relieved by using 3D phase encoding scheme using only 2D segments (a stack-of-EPI trajectory), such schemes (which multiply refocus the echoes of a BURST excitation) can be expected to give rise to ghosting artifacts based on phase or magnitude errors in the individual echoes.

Concluding Remarks

The general subject of this thesis has been the design and optimization of dedicated sequences for functional MRI experiments of the auditory system, with the aim of reducing the interference of the acoustic noise generated by the sequence with experimental auditory stimuli. The work on in this direction has been deliberately restricted to two sequences, Continuous EPI and URGE-EVI. The results, which have been summarized and discussed at the end of chapters 5 and 8, have highlighted the great potential, but also some of the intricacies of such an approach. Among the difficulties, the major challenge has been to develop models of the relative importance of a number of acoustical factors that might be considered. The selection of an accurate model is crucial for any work in the direction of optimizing MR sequences for better performance in fMRI. The reason for this is that the effectiveness of the chosen strategy can only be evaluated retrospectively, by measuring a large number of volunteers (eight subjects were insufficient in some of the Continuous EPI experiments) and ideally an equally large number of different experimental stimuli. For this thesis, this meant that some important questions (for example, the scanner sound frequency dependence of the advantage of Continuous EPI over a conventional standard EPI sequence) have not been satisfactorily answered with statistical significance, but only in the form of trends. While this opens possibilities for future research on a number of interesting questions, it also stressed the need to restrict further studies to a small number of carefully selected questions and to accept the expense associated with the measurement of a large number of subjects in order to gain solid results of sufficient statistical significance. Maybe the most interesting possibilities for future research which arose directly from this work are: the exact dependence of the Continuous EPI sequence advantage over conventional EPI on the fundamental frequency of its scanner sound (for which only trends have been found in this work), the characterization of evoked hemodynamic response functions in anatomically defined primary and secondary auditory areas for conventional and Continuous EPI, and the reduction of artifacts and improved temporal and spatial resolutions in the URGE-EVI sequence which could be made possible by future improvements in scanner hard- and software.

At this point, I would like to point out that the two strategies that

were used, the pseudo-continuous sound obtained in the Continuous EPI sequence, and the reduction of sound levels in the URGE-EVI sequence, are very general concepts and can also be applied to other sequences. While a continuous sound pattern is common to many routinely used fast (steady state) sequences, it is relatively difficult to combine with sufficient BOLD sensitivity to be useful for fMRI. Of the steady state sequences that are BOLD sensitive, maybe the most exciting opportunities are held by the frequency sensitive balanced SSFP sequence known as BOSS [210, 211]. Continuous sound could probably also be achieved by partial Fourier EPI sequences at very high fields (of 7 T and higher) and by echo-shifted sequences such as PRESTO. Sound level reductions, on the other hand, can be obtained for most fast sequences by tuning the sequence timing values in such a way as to avoid sound frequencies which are particularly loud on a given scanner system (the scanner's acoustic resonance frequencies). The merits of this technique (which has been previously proposed for EPI [136]) in the context of auditory fMRI has as yet not been quantified in any detail and has failed to be generally applied in auditory fMRI. Although few sequences will allow for similar sound level reductions as BURST techniques, the concept of reducing the number of needed gradients is again very general and the number of possible BURST variants large. For example, an interesting hybrid between frequency sweep and pulsed MR imaging [212] has been recently proposed, which places very low demands on the gradient system but needs modifications to the hardware of the MR system.

Finally, apart from scientific interest, both strategies (continuous sound and reduced sound levels) could be argued to have potential benefits in terms of patient comfort. While these benefits have been previously been advocated for the case of reduced sound levels ([137], for example), the subjectively more pleasant sound of Continuous EPI compared to the pulsed conventional (standard) EPI gradient sound has been spontaneously reported by a number of volunteers involved in the present experiments.

Curriculum Vitae

Personal Data

Name	Christian Boller
Mailing Address	MR-Physics Department of Medical Radiology University Hospital Petersgraben 4 CH–4031 Basel Switzerland
Phone Number	+41 61 265 53 14
Email	christian.boller@unibas.ch
Born	June 16, 1976 in Männedorf, CH

Education

Oct.2003–Dec.2006	Ph.D. student in the group of Prof. Klaus Scheffler in Basel. Postgraduate lectures and seminars by the following people were attended: Prof. Silvia Arber, Prof. Yves-Alain Barde, Prof. Heinrich Reichert, Prof. Markus Rüegg, Prof. Klaus Scheffler, Dr. Valerij Kiselev and numerous guest speakers in the seminars.
2002	Internship at NSLS Synchrotron in Brookhaven, USA, two months duration
1997–2003	Study of experimental physics at the University of Basel, completed with the Diploma in Physics. Diploma thesis entitled "Triboluminescence on Small Scales" in solid state physics, adviser Dr. Roland Bennewitz.
1994–1995	Student exchange year at Layton High School, Layton UT, USA.
1992–1996	Grammar school (Gymnasium) in Oberwil BL, Switzerland, mathematical–scientific orientation (Typus C). Diploma (Maturität) qualifying for university admittance.

Own Publications

Conference Abstracts, Main Author

2004 ESMRMB. Low impact noise acquisition EPI: An optimized sequence for fMRI of the auditory cortex. *Talk.*

2005 ISMRM. Auditory fMRI without an external stimulus: Using the gradient noise of an acoustically modified EPI sequence to stimulate the auditory cortex. *Poster.*

2006 ISMRM. Steady State BURST: Signal Amplitudes and the Influence of Gradient and RF Spoiling. *Poster.*

Conference Abstracts, Contributing Author

2007 ISMRM. Preattentive auditory processing in professional musicians versus non-musicians – an fMRI study. *Submitted.*

2007 ISMRM. Visualization of the paramagnetic markers in interventional MRI using spatial–spectral pulses. *Submitted.*

Acknowledgment

I would like to thank the following people ...

... first of all my advisor, Prof. Klaus Scheffler, for his infectious enthusiasm, for his willingness to answer my questions at any time and for always handling the concerns of his group members with the highest priority.

... my colleagues at the MR-Physics group here in Basel for creating a lively, humorous and productive research environment, and as much for the inspiring scientific discussions as for the social events that we have shared.

... the group members of Prof. Jürgen Hennig's group in Freiburg for theoretical and technical input, especially from Valerij Kiselev and Maxim Zaitsev.

... all the people who have volunteered to be measured in my long, monotonic and sometimes annoying fMRI experiments. Deepest thanks to you.

... to Peter Schneider in Heidelberg for the fascinating discussions about the human auditory cortex.

... to Erich Seifritz, Marcus Herdener, Christoph Lehmann, Caroline Hilti and all the others involved in the MIB measurements, which have been very motivating to me.

... and last but not least to Denise Perret and all my good friends for being at my side and supporting me equally in times good and bad.

Bibliography

[1] F. Bloch, W. W. Hansen, and M. E. Packard. Nuclear induction. *Physical Review*, 69(3-4):127–127, 1946.

[2] E. M. Purcell, H. C. Torrey, and R. V. Pound. Resonance absorption by nuclear magnetic moments in a solid. *Physical Review*, 69(1-2): 37–38, 1946.

[3] II Rabi. Space quantization in a gyrating magnetic field. *Physical Review*, 51(8):0652–0654, 1937.

[4] C. J. Gorter. Negative result of an attempt to detect nuclear magnetic spins. *Physica*, 3:995–998, 1936.

[5] C. J. Gorter and L. J. F. Broer. Negative result of an attempt to observe nuclear magnetic resonance in solids. *Physica*, 9:591–596, 1942.

[6] F. Bloch. The principle of nuclear induction. Technical report, Nobel Prize Lecture, 1952.

[7] F. Bloch. Nuclear induction. *Physical Review*, 70(7-8):460–474, 1946.

[8] F. Bloch, W. W. Hansen, and M. E. Packard. The nuclear induction experiment. *Physical Review*, 70(7-8):474–485, 1946.

[9] H. C. Torrey. A pulse method for nuclear magnetic resonance. *Physical Review*, 75(8):1326–1326, 1949.

[10] H. C. Torrey. Transient nutations in nuclear magnetic resonance. *Physical Review*, 76(8):1059–1068, 1949.

[11] E. L. Hahn. Nuclear induction due to free larmor precession. *Physical Review*, 77(2):297–299, 1950.

[12] E. L. Hahn. Spin echoes. *Physical Review*, 80(4):580–594, 1950.

[13] R. R. Ernst and W. A. Anderson. Application of fourier transform spectroscopy to magnetic resonance. *Review of Scientific Instruments*, 37(1):93–102, 1966.

[14] W. C. Dickinson. Dependence of the f-19 nuclear resonance position on chemical compound. *Physical Review*, 77(5):736–737, 1950.

[15] W. G. Proctor and F. C. Yu. The dependence of a nuclear magnetic resonance frequency upon chemical compound. *Physical Review*, 77 (5):717–717, 1950.

[16] N. F. Ramsey. Magnetic shielding of nuclei in molecules. *Physical Review*, 78(6):699–703, 1950.

[17] N. F. Ramsey. Dependence of magnetic shielding of nuclei upon molecular orientation. *Physical Review*, 83(3):540–541, 1951.

[18] N. F. Ramsey. Chemical effects in nuclear magnetic resonance and in diamagnetic susceptibility. *Physical Review*, 86(2):243–246, 1952.

[19] P. C. Lauterbur. Image formation by induced local interactions - examples employing nuclear magnetic-resonance. *Nature*, 242(5394): 190–191, 1973.

[20] R. Damadian. Tumor detection by nuclear magnetic resonance. *Science*, 171(3976):1151, 1971.

[21] P. Mansfield and P. K. Grannell. Nmr diffraction in solids. *Journal of Physics C. Solid State Physics*, 6(22):L422–L426, 1973.

[22] R. Damadian, L. Minkoff, M. Goldsmith, M. Stanford, and J. Koutcher. Field focusing nuclear magnetic-resonance (fonar) - visualization of a tumor in a live animal. *Science*, 194(4272):1430–1432, 1976.

[23] R. Damadian, M. Goldsmith, and L. Minkoff. Nmr in cancer .16. fonar image of live human-body. *Physiological Chemistry and Physics*, 9(1): 97, 1977.

[24] W. S. Hinshaw. Spin mapping - application of moving gradients to nmr. *Physics Letters A*, A 48(2):87–88, 1974.

[25] A. Kumar, D. Welti, and R. R. Ernst. Nmr fourier zeugmatography. *Journal of Magnetic Resonance*, 18(1):69–83, 1975.

[26] A. N. Garroway, P. K. Grannell, and P. Mansfield. Image-formation in nmr by a selective irradiative process. *Journal of Physics C. Solid State Physics*, 7(24):L457–L462, 1974.

[27] P. Mansfield and A. A. Maudsley. Line scan proton spin imaging in biological structures by nmr. *Physics in Medicine and Biology*, 21(5): 847–852, 1976.

[28] H. Y. Carr. Field gradients in early mri. *Physics Today*, 57(7):83–83, 2004.

[29] H. C. Torrey. Bloch equations with diffusion terms. *Physical Review*, 140(3):563–565, 1956.

[30] N. Bloembergen, E. M. Purcell, and R. V. Pound. Relaxation effects in nuclear magnetic resonance absorption. *Physical Review*, 73(7): 679–712, 1948.

[31] Marinus T. Vlaardingerbroek and Jacques A. den Boer. *Magnetic resonance imaging theory and practice*. Springer, Berlin, 3nd edition edition, 1999.

[32] H. Gudbjartsson and S. Patz. The rician distribution of noisy mri data. *Magnetic Resonance in Medicine*, 34(6):910–4, 1995.

[33] E. L. Hahn. Detection of sea-water motion by nuclear precession. *Journal of Geophysical Research*, 65(2):776–777, 1960.

[34] A. D. Elster. Gradient-echo mr imaging - techniques and acronyms. *Radiology*, 186(1):1–8, 1993.

[35] P. Mansfield. Multi-planar image-formation using nmr spin echoes. *Journal of Physics C. Solid State Physics*, 10(3):L55–L58, 1977.

[36] W. A. Edelstein, J. M. S. Hutchison, G. A. Johnson, and T. Redpath. Spin warp nmr imaging and applications to human whole-body imaging. *Physics in Medicine and Biology*, 25(4):751–756, 1980.

[37] A. Haase, J. Frahm, D. Matthaei, W. Hanicke, and K. D. Merboldt. Flash imaging - rapid nmr imaging using low flip-angle pulses. *Journal of Magnetic Resonance*, 67(2):258–266, 1986.

[38] Y. Zur and P. Bendal. Elimination of the steady state transverse magnetization in short tr imaging. In *Proceedings of the SMRM*, 1987.

[39] M. L. Wood, M. S. Silver, and V. M. Runge. Optimization of spoiler gradients in flash mri. *Magnetic Resonance Imaging*, 5(6):455–463, 1987.

[40] J. Frahm, W. Hanicke, and K. D. Merboldt. Transverse coherence in rapid flash nmr imaging. *Journal of Magnetic Resonance*, 72(2): 307–314, 1987.

[41] Y. Zur, M. L. Wood, and L. J. Neuringer. Spoiling of transverse magnetization in steady-state sequences. *Magnetic Resonance in Medicine*, 21(2):251–263, 1991.

[42] P. Mansfield and A. A. Maudsley. Planar and line-scan spin imaging by nmr. In *Proc XIXth Congress Ampere*, pages 247–252, Heidelberg, 1976.

[43] P. Mansfield. Snap-shot mri. Technical report, Nobel Prize Lecture, 2003.

[44] I. L. Pykett and R. R. Rzedzian. Instant images of the body by magnetic-resonance. *Magnetic Resonance in Medicine*, 5(6):563–571, 1987.

[45] F. Hennel. Two-dimensional deghosting for epi. *MAGMA*, 9(3):134–7, 1999.

[46] E. C. Wong. Shim insensitive phase correcton for epi using a 2-echo reference scan. In *Proceedings of the SMRM*, page 4514, 1992.

[47] A. Jesmianowicz, E. C. Wong, and J. S. Hyde. Self-correcting epi reconstruction algorithm. In *Proceedings of the SMR and ESMRMB*, page 619, Nice, 1995.

[48] C. S. Roy and M. B. Sherrington. On the regulation of the blood-supply of the brain. *Journal of Physiology*, 11:85–108, 1890.

[49] K. R. Thulborn, J. C. Waterton, P. M. Matthews, and G. K. Radda. Oxygenation dependence of the transverse relaxation-time of water protons in whole-blood at high-field. *Biochimica et Biophysica Acta*, 714(2):265–270, 1982.

[50] S. Ogawa, T. M. Lee, A. S. Nayak, and P. Glynn. Oxygenation-sensitive contrast in magnetic-resonance image of rodent brain at high magnetic-fields. *Magnetic Resonance in Medicine*, 14(1):68–78, 1990.

[51] S. Ogawa, T. M. Lee, A. R. Kay, and D. W. Tank. Brain magnetic resonance imaging with contrast dependent on blood oxygenation. *Proceedings of the National Academy of Sciences of the United States of America*, 87(24):9868–72, 1990.

[52] K. K. Kwong, J. W. Belliveau, D. A. Chesler, I. E. Goldberg, R. M. Weisskoff, B. P. Poncelet, D. N. Kennedy, B. E. Hoppel, M. S. Cohen, R. Turner, H. M. Cheng, T. J. Brady, and B. R. Rosen. Dynamic magnetic-resonance-imaging of human brain activity during primary sensory stimulation. *Proceedings of the National Academy of Sciences of the United States of America*, 89(12):5675–5679, 1992.

[53] S. Ogawa, D. W. Tank, R. Menon, J. M. Ellermann, S. G. Kim, H. Merkle, and K. Ugurbil. Intrinsic signal changes accompanying sensory stimulation - functional brain mapping with magnetic-resonance-imaging. *Proceedings of the National Academy of Sciences of the United States of America*, 89(13):5951–5955, 1992.

[54] P. A. Bandettini, E. C. Wong, R. S. Hinks, R. S. Tikofsky, and J. S. Hyde. Time course epi of human brain-function during task activation. *Magnetic Resonance in Medicine*, 25(2):390–397, 1992.

[55] D. J. Heeger and D. Ress. What does fmri tell us about neuronal activity? *Nature Reviews. Neuroscience*, 3(2):142–51, 2002.

[56] N. K. Logothetis and B. A. Wandell. Interpreting the bold signal. *Annual Review of Physiology*, 66:735–69, 2004.

[57] N. K. Logothetis and J. Pfeuffer. On the nature of the bold fmri contrast mechanism. *Magnetic Resonance Imaging*, 22(10):1517–31, 2004.

[58] M. Lauritzen. Reading vascular changes in brain imaging: is dendritic calcium the key? *Nature Reviews. Neuroscience*, 6(1):77–85, 2005.

[59] N. K. Logothetis, J. Pauls, M. Augath, T. Trinath, and A. Oeltermann. Neurophysiological investigation of the basis of the fmri signal. *Nature*, 412(6843):150–7, 2001.

[60] R. Mukamel, H. Gelbard, A. Arieli, U. Hasson, I. Fried, and R. Malach. Coupling between neuronal firing, field potentials, and fmri in human auditory cortex. *Science*, 309(5736):951–4, 2005.

[61] D. Attwell and C. Iadecola. The neural basis of functional brain imaging signals. *Trends in Neurosciences*, 25(12):621–5, 2002.

[62] T. Takano, G. F. Tian, W. G. Peng, N. Lou, W. Libionka, X. Han, and M. Nedergaard. Astrocyte-mediated control of cerebral blood flow. *Nature Neuroscience*, 9(2):260–7, 2006.

[63] U. Dirnagl, U. Lindauer, and A. Villringer. Role of nitric oxide in the coupling of cerebral blood flow to neuronal activation in rats. *Neuroscience Letters*, 149(1):43–6, 1993.

[64] X. Wang, N. Lou, Q. Xu, G. F. Tian, W. G. Peng, X. Han, J. Kang, T. Takano, and M. Nedergaard. Astrocytic ca(2+) signaling evoked by sensory stimulation in vivo. *Nature Neuroscience*, 9(6):816–23, 2006.

[65] D. Malonek and A. Grinvald. Interactions between electrical activity and cortical microcirculation revealed by imaging spectroscopy: Implications for functional brain mapping. *Science*, 272(5261):551–554, 1996.

[66] T. Q. Duong, D. S. Kim, K. Ugurbil, and S. G. Kim. Localized cerebral blood flow response at submillimeter columnar resolution. *Proceedings of the National Academy of Sciences of the United States of America*, 98(19):10904–10909, 2001.

[67] R. S. Menon and B. G. Goodyear. Submillimeter functional localization in human striate cortex using bold contrast at 4 tesla: Implications for the vascular point-spread function. *Magnetic Resonance in Medicine*, 41(2):230–235, 1999.

[68] J. K. Thompson, M. R. Peterson, and R. D. Freeman. Single-neuron activity and tissue oxygenation in the cerebral cortex. *Science*, 299 (5609):1070–2, 2003.

[69] J. K. Thompson, M. R. Peterson, and R. D. Freeman. High-resolution neurometabolic coupling revealed by focal activation of visual neurons. *Nature Neuroscience*, 7(9):919–20, 2004.

[70] S. A. Engel, D. E. Rumelhart, B. A. Wandell, A. T. Lee, G. H. Glover, E. J. Chichilnisky, and M. N. Shadlen. fmri of human visual cortex. *Nature*, 369(6481):525, 1994.

[71] S. A. Engel, G. H. Glover, and B. A. Wandell. Retinotopic organization in human visual cortex and the spatial precision of functional mri. *Cerebral Cortex*, 7(2):181–192, 1997.

[72] A. Grinvald, H. Slovin, and I. Vanzetta. Non-invasive visualization of cortical columns by fmri. *Nature Neuroscience*, 3(2):105–107, 2000.

[73] Editor Johnson, P. C. *Peripheral Circulation*. Wiley, 1978.

[74] L. M. Parkes, J. V. Schwarzbach, A. A. Bouts, R. H. Deckers, P. Pullens, C. M. Kerskens, and D. G. Norris. Quantifying the spatial resolution of the gradient echo and spin echo bold response at 3 tesla. *Magnetic Resonance in Medicine*, 54(6):1465–72, 2005.

[75] J. L. Boxerman, P. A. Bandettini, K. K. Kwong, J. R. Baker, T. L. Davis, B. R. Rosen, and R. M. Weisskoff. The intravascular contribution to fmri signal change - monte-carlo modeling and diffusion-weighted studies in-vivo. *Magnetic Resonance in Medicine*, 34(1):4–10, 1995.

[76] A. W. Song, E. C. Wong, S. G. Tan, and J. S. Hyde. Diffusion weighted fmri at 1.5 t. *Magnetic Resonance in Medicine*, 35(2):155–8, 1996.

[77] S. P. Lee, A. C. Silva, K. Ugurbil, and S. G. Kim. Diffusion-weighted spin-echo fmri at 9.4 t: Microvascular/tissue contribution to bold signal changes. *Magnetic Resonance in Medicine*, 42(5):919–928, 1999.

[78] K. Ugurbil, M. Garwood, J. Ellermann, K. Hendrich, R. Hinke, X. P. Hu, S. G. Kim, R. Menon, H. Merkle, S. Ogawa, and R. Salmi. Imaging at high magnetic-fields - initial experiences at 4-t. *Magnetic Resonance Quarterly*, 9(4):259–277, 1993.

[79] T. Q. Duong, E. Yacoub, G. Adriany, X. P. Hu, K. Ugurbil, J. T. Vaughan, H. Merkle, and S. G. Kim. High-resolution, spin-echo bold, and cbf am at 4 and 7 t. *Magnetic Resonance in Medicine*, 48(4): 589–593, 2002.

[80] N. Harel, K. Ugurbil, K. Uludag, and E. Yacoub. Frontiers of brain mapping using mri. *Journal of Magnetic Resonance Imaging*, 23(6): 945–57, 2006.

[81] Z. S. Saad, K. M. Ropella, E. A. DeYoe, and P. A. Bandettini. The spatial extent of the bold response. *Neuroimage*, 19(1):132–44, 2003.

[82] T. Q. Duong, A. C. Silva, S. P. Lee, and S. G. Kim. Functional mri of calcium-dependent synaptic activity: cross correlation with cbf and bold measurements. *Magnetic Resonance in Medicine*, 43(3):383–92, 2000.

[83] A. Puce, R. T. Constable, M. L. Luby, G. McCarthy, A. C. Nobre, D. D. Spencer, J. C. Gore, and T. Allison. Functional magnetic-resonance-imaging of sensory and motor cortex - comparison with electrophysiological localization. *Journal of Neurosurgery*, 83(2):262–270, 1995.

[84] T. A. Yousry, U. D. Schmid, A. G. Jassoy, D. Schmidt, W. E. Eisner, H. J. Reulen, M. F. Reiser, and J. Lissner. Topography of the cortical motor hand area - prospective-study with functional mr-imaging and direct motor mapping at surgery. *Radiology*, 195(1):23–29, 1995.

[85] K. J. Friston, P. Jezzard, and R. Turner. Analysis of functional mri time-series. *Human Brain Mapping*, 1(2):153–171, 1994.

[86] K. J. Friston, A. P. Holmes, J. B. Poline, P. J. Grasby, S. C. Williams, R. S. Frackowiak, and R. Turner. Analysis of fmri time-series revisited. *Neuroimage*, 2(1):45–53, 1995.

[87] K. J. Worsley and K. J. Friston. Analysis of fmri time-series revisited–again. *Neuroimage*, 2(3):173–81, 1995.

[88] A. L. Vazquez and D. C. Noll. Nonlinear aspects of the bold response in functional mri. *Neuroimage*, 7(2):108–118, 1998.

[89] D. A. Soltysik, K. K. Peck, K. D. White, B. Crosson, and R. W. Briggs. Comparison of hemodynamic response nonlinearity across primary cortical areas. *Neuroimage*, 22(3):1117–27, 2004.

[90] T. M. Talavage and W. B. Edmister. Nonlinearity of fmri responses in human auditory cortex. *Human Brain Mapping*, 22(3):216–28, 2004.

[91] D. R. Langers, P. Van Dijk, and W. H. Backes. Interactions between hemodynamic responses to scanner acoustic noise and auditory stimuli in functional magnetic resonance imaging. *Magnetic Resonance in Medicine*, 53(1):49–60, 2004.

[92] P. Kellman, P. van Gelderen, J. A. de Zwart, and J. H. Duyn. Method for functional mri mapping of nonlinear response. *Neuroimage*, 19(1): 190–9, 2003.

[93] D. Purves, J. J. Augustine, D. Fitzpatrick, L. C. Katz, A. LaMantia, J. O. McNamara, and S. M. Williams. *Neuroscience*. Sinauer Associates, 2001.

[94] S. K. Thompson, K. von Kriegstein, A. Deane-Pratt, T. Marquardt, R. Deichmann, T. D. Griffiths, and D. McAlpine. Representation of interaural time delay in the human auditory midbrain. *Nature Neuroscience*, 9(9):1096–1098, 2006.

[95] M. N. Semple and B. H. Scott. Cortical mechanisms in hearing. *Current Opinion in Neurobiology*, 13(2):167–73, 2003.

[96] M. Schonwiesner, D. Y. von Cramon, and R. Rubsamen. Is it tonotopy after all? *Neuroimage*, 17(3):1144–61, 2002.

[97] D. A. Hall, H. C. Hart, and I. S. Johnsrude. Relationships between human auditory cortical structure and function. *Audiology and Neuro-Otology*, 8(1):1–18, 2003.

[98] F. Di Salle, E. Formisano, E. Seifritz, D. E. Linden, K. Scheffler, C. Saulino, G. Tedeschi, F. E. Zanella, A. Pepino, R. Goebel, and E. Marciano. Functional fields in human auditory cortex revealed by time-resolved fmri without interference of epi noise. *Neuroimage*, 13 (2):328–38, 2001.

[99] P. Schneider, M. Scherg, H. G. Dosch, H. J. Specht, A. Gutschalk, and A. Rupp. Morphology of heschl's gyrus reflects enhanced activation in the auditory cortex of musicians. *Nature Neuroscience*, 5(7):688–694, 2002.

[100] E. Formisano, D. S. Kim, F. Di Salle, P. F. van de Moortele, K. Ugurbil, and R. Goebel. Mirror-symmetric tonotopic maps in human primary auditory cortex. *Neuron*, 40(4):859–69, 2003.

[101] F. Di Salle, F. Esposito, T. Scarabino, E. Formisano, E. Marciano, C. Saulino, S. Cirillo, R. Elefante, K. Scheffler, and E. Seifritz. fmri of the auditory system: understanding the neural basis of auditory gestalt. *Magnetic Resonance Imaging*, 21(10):1213–24, 2003.

[102] V. B. Penhune, R. J. Zatorre, J. D. MacDonald, and A. C. Evans. Interhemispheric anatomical differences in human primary auditory cortex: Probabilistic mapping and volume measurement from magnetic resonance scans. *Cerebral Cortex*, 6(5):661–672, 1996.

[103] T. A. Yousry, G. Fesl, A. Buttner, S. Noachtar, and U. D. Schmid. Heschl's gyrus - anatomic description and methods of identification on magnetic resonance imaging. *International Journal of Neuroradiology*, 3(1):2–12, 1997.

[104] J. Rademacher, P. Morosan, T. Schormann, A. Schleicher, C. Werner, H. J. Freund, and K. Zilles. Probabilistic mapping and volume measurement of human primary auditory cortex. *Neuroimage*, 13(4):669–683, 2001.

[105] P. Schneider, V. Sluming, N. Roberts, M. Scherg, R. Goebel, H. J. Specht, H. G. Dosch, S. Bleeck, C. Stippich, and A. Rupp. Structural and functional asymmetry of lateral heschl's gyrus reflects pitch perception preference. *Nature Neuroscience*, 8(9):1241–7, 2005.

[106] F. Rivier and S. Clarke. Cytochrome oxidase, acetylcholinesterase, and nadph-diaphorase staining in human supratemporal and insular cortex: evidence for multiple auditory areas. *Neuroimage*, 6(4):288–304, 1997.

[107] C. M. Wessinger, J. VanMeter, B. Tian, J. Van Lare, J. J. Pekar, and J. P. Rauschecker. Hierarchical organization of the human auditory cortex revealed by functional magnetic resonance imaging. *Journal of Cognitive Neuroscience*, 13(1):1–7, 2001.

[108] D. A. Hall, I. S. Johnsrude, M. P. Haggard, A. R. Palmer, M. A. Akeroyd, and A. Q. Summerfield. Spectral and temporal processing in human auditory cortex. *Cerebral Cortex*, 12(2):140–149, 2002.

[109] T.M. Talavage, P.J. Ledden, M.I. Sereno, R.R. Benson, and B.R. Rosen. Preliminary fmri evidence for tonotopicity in human auditory cortex. *Neuroimage*, 3(1, Supplement 1):S355, 1996.

[110] C. M. Wessinger, M. H. Buonocore, C. L. Kussmaul, and G. R. Mangun. Tonotopy in human auditory cortex examined with functional magnetic resonance imaging. *Human Brain Mapping*, 5(1):18–25, 1997.

[111] T. M. Talavage, P. J. Ledden, R. R. Benson, B. R. Rosen, and J. R. Melcher. Frequency-dependent responses exhibited by multiple regions in human auditory cortex. *Hearing Research*, 150(1-2):225–44, 2000.

[112] D. Bilecen, K. Scheffler, N. Schmid, K. Tschopp, and J. Seelig. Tonotopic organization of the human auditory cortex as detected by bold-fmri. *Hearing Research*, 126(1-2):19–27, 1998.

[113] M. P. Harms and J. R. Melcher. Sound repetition rate in the human auditory pathway: Representations in the waveshape and amplitude of fmri activation. *Journal of Neurophysiology*, 88(3):1433–1450, 2002.

[114] A. L. Giraud, C. Lorenzi, J. Ashburner, J. Wable, I. S. Johnsrude, R. Frackowiak, and A. Kleinschmidt. Representation of the temporal envelope of sounds in the human brain. *Journal of Neurophysiology*, 84(3):1588–98, 2000.

[115] E. Seifritz, F. Di Salle, F. Esposito, D. Bilecen, J. G. Neuhoff, and K. Scheffler. Sustained blood oxygenation and volume response to repetition rate-modulated sound in human auditory cortex. *Neuroimage*, 20(2):1365–70, 2003.

[116] H. Tanaka, N. Fujita, Y. Watanabe, N. Hirabuki, M. Takanashi, Y. Oshiro, and H. Nakamura. Effects of stimulus rate on the auditory cortex using fmri with 'sparse' temporal sampling. *Neuroreport*, 11(9):2045–2049, 2000.

[117] M. P. Harms, J. J. Guinan, I. S. Sigalovsky, and J. R. Melcher. Short-term sound temporal envelope characteristics determine multisecond time patterns of activity in human auditory cortex as shown by fmri. *Journal of Neurophysiology*, 93(1):210–222, 2005.

[118] X. Wang, T. Lu, R. K. Snider, and L. Liang. Sustained firing in auditory cortex evoked by preferred stimuli. *Nature*, 435(7040):341–6, 2005.

[119] M. E. Ravicz, J. R. Melcher, and N. Y. Kiang. Acoustic noise during functional magnetic resonance imaging. *Journal of the Acoustical Society of America*, 108(4):1683–96, 2000.

[120] A. Moelker and P. M. Pattynama. Acoustic noise concerns in functional magnetic resonance imaging. *Human Brain Mapping*, 20(3): 123–41, 2003.

[121] A. Moelker, P. A. Wielopolski, and P. M. Pattynama. Relationship between magnetic field strength and magnetic-resonance-related acoustic noise levels. *MAGMA*, 16(1):52–5, 2003.

[122] D. L. Price, J. P. De Wilde, A. M. Papadaki, J. S. Curran, and R. I. Kitney. Investigation of acoustic noise on 15 mri scanners from 0.2 t to 3 t. *Journal of Magnetic Resonance Imaging*, 13(2):288–293, 2001.

[123] R. A. Hedeen and W. A. Edelstein. Characterization and prediction of gradient acoustic noise in mr imagers. *Magnetic Resonance in Medicine*, 37(1):7–10, 1997.

[124] J. R. Foster, D. A. Hall, A. Q. Summerfield, A. R. Palmer, and R. W. Bowtell. Sound-level measurements and calculations of safe noise dosage during epi at 3 t. *Journal of Magnetic Resonance Imaging*, 12(1):157–163, 2000.

[125] Z. H. Cho, S. H. Park, J. H. Kim, S. C. Chung, S. T. Chung, J. Y. Chung, C. W. Moon, J. H. Yi, C. H. Sin, and E. K. Wong. Analysis of acoustic noise in mri. *Magnetic Resonance Imaging*, 15(7):815–22, 1997.

[126] F. G. Shellock, M. Ziarati, D. Atkinson, and D. Y. Chen. Determination of gradient magnetic field-induced acoustic noise associated with the use of echo planar and three-dimensional, fast spin echo techniques. *Journal of Magnetic Resonance Imaging*, 8(5):1154–1157, 1998.

[127] M. McJury and F. G. Shellock. Auditory noise associated with mr procedures: a review. *Journal of Magnetic Resonance Imaging*, 12(1): 37–45, 2000.

[128] W. B. Edmister, T. M. Talavage, P. J. Ledden, and R. M. Weisskoff. Improved auditory cortex imaging using clustered volume acquisitions. *Human Brain Mapping*, 7(2):89–97, 1999.

[129] K. Scheffler. Functional imaging of the auditory system. auditory stimulation of defined frequency with b0-gradients. In *Proceedings of the SMRM*, page 1689, 1997.

[130] D. Bilecen, E. W. Radu, and K. Scheffler. The mr tomograph as a sound generator: fmri tool for the investigation of the auditory cortex. *Magnetic Resonance in Medicine*, 40(6):934–937, 1998.

[131] T. M. Talavage, W. B. Edmister, P. J. Ledden, and R. M. Weisskoff. Quantitative assessment of auditory cortex responses induced by imager acoustic noise. *Human Brain Mapping*, 7(2):79–88, 1999.

[132] P. A. Bandettini, A. Jesmanowicz, J. Van Kylen, R. M. Birn, and J. S. Hyde. Functional mri of brain activation induced by scanner acoustic noise. *Magnetic Resonance in Medicine*, 39(3):410–6, 1998.

[133] D. A. Hall, A. Q. Summerfield, M. S. Goncalves, J. R. Foster, A. R. Palmer, and R. W. Bowtell. Time-course of the auditory bold response to scanner noise. *Magnetic Resonance in Medicine*, 43(4):601–6, 2000.

[134] C. J. Scarff, J. C. Dort, J. J. Eggermont, and B. G. Goodyear. The effect of mr scanner noise on auditory cortex activity using fmri. *Human Brain Mapping*, 22(4):341–9, 2004.

[135] A. M. Goldman, W. E. Gossman, and P. C. Friedlander. Reduction of sound levels with antinoise in mr imaging. *Radiology*, 173(2):549–50, 1989.

[136] D. G. Tomasi and T. Ernst. Echo planar imaging at 4 tesla with minimum acoustic noise. *Journal of Magnetic Resonance Imaging*, 18 (1):128–30, 2003.

[137] F. Hennel, F. Girard, and T. Loenneker. "silent" mri with soft gradient pulses. *Magnetic Resonance in Medicine*, 42(1):6–10, 1999.

[138] F. Hennel. Fast spin echo and fast gradient echo mri with low acoustic noise. *Journal of Magnetic Resonance Imaging*, 13(6):960–6, 2001.

[139] C. Oesterle, F. Hennel, and J. Hennig. Quiet imaging with interleaved spiral read-out. *Magnetic Resonance Imaging*, 19(10):1333–7, 2001.

[140] T. Loenneker, F. Hennel, U. Ludwig, and J. Hennig. Silent bold imaging. *Magnetic Resonance Materials in Physics Biology and Medicine*, 13(2):76–81, 2001.

[141] J. A. de Zwart, P. van Gelderen, P. Kellman, and J. H. Duyn. Reduction of gradient acoustic noise in mri using sense-epi. *Neuroimage*, 16 (4):1151–5, 2002.

[142] J. Hennig and M. Hodapp. Burst imaging. *MAGMA*, 1:39–48, 1993.

[143] D. Bilecen, K. Scheffler, N. Schmid, K. Tschopp, and J. Seelig. Cerebral compenstion mechanism of the auditive system detected by fmri. In *Proceedings of the ISMRM*, page 1841, New York, 1996.

[144] K. Scheffler, D. Bilecen, N. Schmid, K. Tschopp, and J. Seelig. Auditory cortical responses in hearing subjects and unilateral deaf patients as detected by functional magnetic resonance imaging. *Cerebral Cortex*, 8(2):156–163, 1998.

[145] G. F. Eden, J. E. Joseph, H. E. Brown, C. P. Brown, and T. A. Zeffiro. Utilizing hemodynamic delay and dispersion to detect fmri signal change without auditory interference: the behavior interleaved gradients technique. *Magnetic Resonance in Medicine*, 41(1):13–20, 1999.

[146] D. A. Hall, M. P. Haggard, M. A. Akeroyd, A. R. Palmer, A. Q. Summerfield, M. R. Elliott, E. M. Gurney, and R. W. Bowtell. "sparse" temporal sampling in auditory fmri. *Human Brain Mapping*, 7(3): 213–23, 1999.

[147] P. Belin, R. J. Zatorre, R. Hoge, A. C. Evans, and B. Pike. Event-related fmri of the auditory cortex. *Neuroimage*, 10(4):417–29, 1999.

[148] C. Schwarzbauer, M. H. Davis, J. M. Rodd, and I. Johnsrude. Interleaved silent steady state (isss) imaging: A new sparse imaging method applied to auditory fmri. *Neuroimage*, 29(3):774–782, 2006.

[149] F. Z. Yetkin, P. S. Roland, P. D. Purdy, and W. F. Christensen. Evaluation of auditory cortex activation by using silent fmri. *American Journal of Otolaryngology*, 24(5):281–9, 2003.

[150] Y. Yang, A. Engelien, W. Engelien, S. Xu, E. Stern, and D. A. Silbersweig. A silent event-related functional mri technique for brain activation studies without interference of scanner acoustic noise. *Magnetic Resonance in Medicine*, 43(2):185–90, 2000.

[151] K. Scheffler and E. Seifritz. Doubling bold signal in auditory cortex by acoustic modification of echoplanar sequence. In *Proceedings of the ISMRM Meeting*, page 521, Kyoto, Japan, 2004.

[152] E. Seifritz, F. Di Salle, F. Esposito, M. Herdener, J. G. Neuhoff, and K. Scheffler. Enhancing bold response in the auditory system by neurophysiologically tuned fmri sequence. *Neuroimage*, 29(3):1013–22, 2006.

[153] S. Haller, A. J. Bartsch, E. W. Radu, M. Klarhofer, E. Seifritz, and K. Scheffler. Effect of fmri acoustic noise on non-auditory working memory task: comparison between continuous and pulsed sound emitting epi. *MAGMA*, 18(5):263–71, 2005.

[154] B. C. J. Moore. *An introduction to the psychology of hearing*. Academic Press, San Diego, 4th edition, 1997.

[155] E. Zwicker and H. Fastl. *Psychoacoustics facts and models*. Springer, Berlin, 2nd updated edition, 1999.

[156] F. Schick, J. Forster, J. Machann, R. Kuntz, and C. D. Claussen. Improved clinical echo-planar mri using spatial-spectral excitation. *Journal of Magnetic Resonance Imaging*, 8(4):960–7, 1998.

[157] C. H. Meyer, J. M. Pauly, A. Macovski, and D. G. Nishimura. Simultaneous spatial and spectral selective excitation. *Magnetic Resonance in Medicine*, 15(2):287–304, 1990.

[158] M. Bernstein, K. F. King, and X. J. Zhou. *Handbook of MRI Pulse Sequences*. Elsevier Academic Press, 2004.

[159] Z. H. Cho, Y. M. Ro, and I. K. Hong. Fm dante fast imaging and variations: Emerging rf-based ultrafast imaging techniques. *Concepts in Magnetic Resonance*, 10(1):33–54, 1998.

[160] Y. Zur. Design of improved spectral-spatial pulses for routine clinical use. *Magnetic Resonance in Medicine*, 43(3):410–20, 2000.

[161] J. A. de Zwart, P. van Gelderen, P. Kellman, and J. H. Duyn. Application of sensitivity-encoded echo-planar imaging for blood oxygen level-dependent functional brain imaging. *Magnetic Resonance in Medicine*, 48(6):1011–20, 2002.

[162] C. Triantafyllou, R. D. Hoge, G. Krueger, C. J. Wiggins, A. Potthast, G. C. Wiggins, and L. L. Wald. Comparison of physiological noise at 1.5 t, 3 t and 7 t and optimization of fmri acquisition parameters. *Neuroimage*, 26(1):243–50, 2005.

[163] J. H. Duyn, Y. Yang, J. A. Frank, V. S. Mattay, and L. Hou. Functional magnetic resonance neuroimaging data acquisition techniques. *Neuroimage*, 4(3 Pt 3):S76–83, 1996.

[164] R. M. Weisskoff. Simple measurement of scanner stability for functional nmr imaging of activation in the brain. *Magnetic Resonance in Medicine*, 36(4):643–5, 1996.

[165] J. M. Pauly, P. Le Roux, D. G. Nishimura, and A. Macovski. Parameter relations for the shinnar-leroux selective excitation pulse design algorithm. *IEEE Transactions on Medical Imaging*, 10(1):53–65, 1991.

[166] J. P. Mugler and J. R. Brookeman. 3-dimensional magnetization-prepared rapid gradient-echo imaging (3dmp-rage). *Magnetic Resonance in Medicine*, 15(1):152–157, 1990.

[167] J. A. de Zwart, A. C. Silva, P. van Gelderen, P. Kellman, M. Fukunaga, R. Chu, A. P. Koretsky, J. A. Frank, and J. H. Duyn. Temporal dynamics of the bold fmri impulse response. *Neuroimage*, 24(3):667–77, 2005.

[168] V. D. Calhoun, M. C. Stevens, G. D. Pearlson, and K. A. Kiehl. fmri analysis with the general linear model: removal of latency-induced amplitude bias by incorporation of hemodynamic derivative terms. *Neuroimage*, 22(1):252–7, 2004.

[169] Richard S. J. Frackowiak. *Human brain function*. Academic Press, San Diego, 2nd edition, 2004.

[170] J. Hennig and M. Mueri. Fast imaging using burst excitation pulses. In *Proceedings 7th SMRM*, page 238, 1988.

[171] I. J. Lowe and R. E. Wysong. Dante ultrafast imaging sequence (dufis). *Journal of Magnetic Resonance. Series B*, 101(1):106–109, 1993.

[172] G. A. Morris and R. Freeman. Selective excitation in fourier-transform nuclear magnetic-resonance. *Journal of Magnetic Resonance*, 29(3): 433–462, 1978.

[173] J. Hennig. Multiecho imaging sequences with low refocusing flip angles. *Journal of Magnetic Resonance*, 78(3):397–407, 1988.

[174] J. Hennig. Echoes - how to generate, recognize, use or avoid them in mr-imaging sequences. part i. *Concepts in Magnetic Resonance*, 3: 125–143, 1991.

[175] K. Scheffler. A pictorial description of steady-states in rapid magnetic resonance imaging. *Concepts in Magnetic Resonance*, 11(5):291–304, 1999.

[176] R. Kaiser, E. Barthold, and R. R. Ernst. Diffusion and field-gradient effects in nmr fourier spectroscopy. *Journal of Chemical Physics*, 60 (8):2966–2979, 1974.

[177] D. E. Woessner. Effects of diffusion in nuclear magnetic resonance spin-echo experiments. *Journal of Chemical Physics*, 34(6):2057, 1961.

[178] E. T. Jaynes. Matrix treatment of nuclear induction. *Physical Review*, 98(4):1099–1105, 1955.

[179] A. L. Bloom. Nuclear induction in inhomogeneous fields. *Physical Review*, 98(4):1105–1111, 1955.

[180] W. T. Sobol and D. M. Gauntt. On the stationary states in gradient echo imaging. *Journal of Magnetic Resonance Imaging*, 6(2):384–98, 1996.

[181] P. K. Madhu and A. Kumar. Direct cartesian-space solutions of generalized bloch equations in the rotating-frame. *Journal of Magnetic Resonance. Series A*, 114(2):201–211, 1995.

[182] D. I. Hoult. Solution of the bloch equations in the presence of a varying b1 field - approach to selective pulse analysis. *Journal of Magnetic Resonance*, 35(1):69–86, 1979.

[183] W. S. Hinshaw and A. H. Lent. An introduction to nmr imaging - from the bloch equation to the imaging equation. *Proceedings of the Ieee*, 71(3):338–350, 1983.

[184] J. M. Pauly, D. G. Nishimura, and A. Macovski. A k-space analysis of small-tip-angle excitation. *Journal of Magnetic Resonance*, 81:43–56, 1989.

[185] A. G. Anderson, R. L. Garwin, E. L. Hahn, J. W. Horton, G. L. Tucker, and R. M. Walker. Spin echo serial storage memory. *Journal of Applied Physics*, 26(11):1324–1338, 1955.

[186] P. Le Roux, J. M. Pauly, and A. Macovski. Burst excitation pulses. In *Proceedings X SMRM*, page 269, San Francisco, USA, 1991.

[187] J. H. Duyn, P. Vangelderen, G. Y. Liu, and C. T. W. Moonen. Fast volume scanning with frequency-shifted burst mri. *Magnetic Resonance in Medicine*, 32(3):429–432, 1994.

[188] J. H. Duyn, P. Vangelderen, P. Barker, J. A. Frank, V. S. Mattay, and C. T. W. Moonen. 3d bolus tracking with frequency-shifted burst mri. *Journal of Computer Assisted Tomography*, 18(5):680–687, 1994.

[189] P. van Gelderen, J. H. Duyn, and C. T. Moonen. Analytical solution for phase modulation in burst imaging with optimum sensitivity. *Journal of Magnetic Resonance. Series B*, 107(1):78–82, 1995.

[190] L. Zha and I. J. Lowe. Optimized ultra-fast imaging sequence (oufis). *Magnetic Resonance in Medicine*, 33(3):377–95, 1995.

[191] O. Heid. Burst excitation pulses. *Magnetic Resonance in Medicine*, 38(4):585–90, 1997.

[192] J. H. Duyn. Burst imaging. In *Ultrafast Magnetic Resonance Imaging in Medicine*, pages 49–53, Kyoto, Japan, 1999. Elsevier.

[193] J. H. Duyn. Steady state effects in fast gradient echo magnetic resonance imaging. *Magnetic Resonance in Medicine*, 37(4):559–68, 1997.

[194] P. M. Jakob, M. A. Griswold, K. O. Lovblad, Q. Chen, and R. R. Edelman. Half-fourier burst imaging on a clinical scanner. *Magnetic Resonance in Medicine*, 38(4):534–40, 1997.

[195] O. Heid, M. Deimling, and W. J. Huk. Quest–a quick echo split nmr imaging technique. *Magnetic Resonance in Medicine*, 29(2):280–3, 1993.

[196] Y. Cremillieux, C. A. Wheeler-Kingshott, A. Briguet, and S. J. Doran. Steam-burst: a single-shot, multi-slice imaging sequence without rapid gradient switching. *Magnetic Resonance in Medicine*, 38(4):645–52, 1997.

[197] O. Heid. Burst imaging with steady-state free precession. In *Proceedings of the ISMRM Meeting*, page 1499, Denver, 2000.

[198] P. van Gelderen, C. T. Moonen, and J. H. Duyn. Susceptibility insensitive single shot mri combining burst and multiple spin echoes. *Magnetic Resonance in Medicine*, 33(3):439–42, 1995.

[199] R. Jerecic, M. Bock, and L. R. Schad. An amplitude optimized single-shot hybrid quest technique. *Magnetic Resonance Imaging*, 18(1): 23–32, 2000.

[200] O. Heid. Ultra rapid gradient echo planar/volumar imaging. In *Proceedings of the ISMRM Meeting*, page 98, Nice, 1995.

[201] S. J. Doran, M. E. Bourgeois, and M. O. Leach. Burst imaging - can it ever be useful in the clinic? *Concepts in Magnetic Resonance*, 26A (1):11–34, 2005.

[202] S. J. Doran and M. Decorps. A robust, single-shot method for measuring diffusion coefficients using the "burst" sequence. *Journal of Magnetic Resonance. Series A*, 117(2):311–316, 1995.

[203] C. A. Wheeler-Kingshott, D. L. Thomas, M. F. Lythgoe, D. Guilfoyle, S. R. Williams, and S. J. Doran. Burst excitation for quantitative diffusion imaging with multiple b-values. *Magnetic Resonance in Medicine*, 44(5):737–45, 2000.

[204] P. M. Jakob, G. Schlaug, M. A. Griswold, K. O. Lovblad, R. Thomas, J. R. Ives, J. K. Matheson, and R. R. Edelman. Functional burst imaging. *Magnetic Resonance in Medicine*, 40(4):614–21, 1998.

[205] L. Zha, W. Zhang, and D. Kramer. Virtues and problems of burst imaging. In *Ultrafast Magnetic Resonance Imaging in Medicine*, pages 61–64, Kyoto, Japan, 1999. Elsevier.

[206] L. Zha, W. Zhang, and D. Kramer. Spatial selectivity induced artifacts and excitation phase modulation methods in burst imaging. In *Proceedings of the ISMRM*, page 327, 1997.

[207] C. A. Wheeler-Kingshott, Y. Cremillieux, and S. J. Doran. Burst imaging: rotation artifacts and how to correct them. *Journal of Magnetic Resonance*, 143(1):161–71, 2000.

[208] O. Heid, M. Deimling, and W. J. Huk. Ultra-rapid gradient echo imaging. *Magnetic Resonance in Medicine*, 33(1):143–9, 1995.

[209] A.R. Brenner, A. Glowinski, J. Kürsch, M. Drobnitzky, T.G. Noll, and R.W. Gunther. Optimization of ultrafast multi-pulse sequences for dynamic mr imaging. In *Proceedings of the SMR*, volume 1, page 638, 1995.

[210] K. Scheffler, E. Seifritz, D. Bilecen, R. Venkatesan, J. Hennig, M. Deimling, and E. M. Haacke. Detection of bold changes by means of a frequency-sensitive truefisp technique: preliminary results. *NMR in Biomedicine*, 14(7-8):490–6, 2001.

[211] K. L. Miller, B. A. Hargreaves, J. Lee, D. Ress, R. C. deCharms, and J. M. Pauly. Functional brain imaging using a blood oxygenation sensitive steady state. *Magnetic Resonance in Medicine*, 50(4):675–83, 2003.

[212] D. Idiyatullin, C. Corum, J-Y. Park, and M. Garwood. Sweep imaging with fourier transform (swift). In *Proceedings of the ISMRM*, page 2433, Seattle, 2006.